

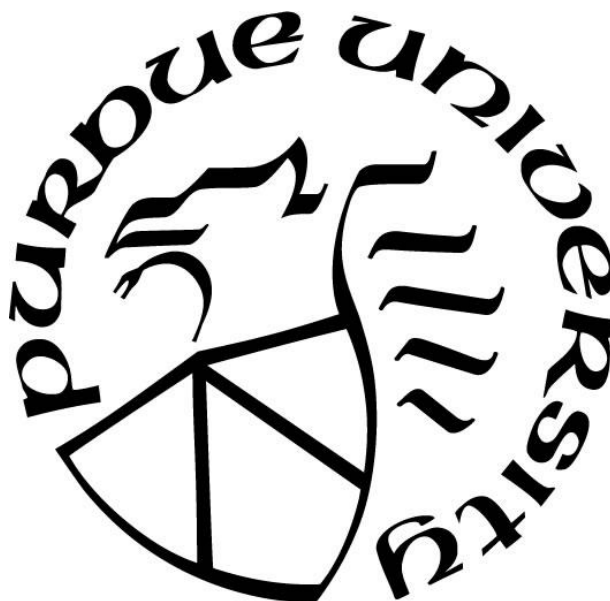
**SPATIAL AND TEMPORAL IMAGING OF EXCITON DYNAMICS
AND TRANSPORT IN TWO-DIMENSIONAL SEMICONDUCTORS
AND HETEROSTRUCTURES BY ULTRAFAST TRANSIENT
ABSORPTION MICROSCOPY**

by
Long Yuan

A Dissertation

*Submitted to the Faculty of Purdue University
In Partial Fulfillment of the Requirements for the degree of*

Doctor of Philosophy



Department of Chemistry
West Lafayette, Indiana
May 2019

THE PURDUE UNIVERSITY GRADUATE SCHOOL
STATEMENT OF COMMITTEE APPROVAL

Dr. Libai Huang, Chair

Department of Chemistry

Dr. Shelley A. Claridge

Department of Chemistry

Dr. Jianguo Mei

Department of Chemistry

Dr. Adam Wasserman

Department of Chemistry

Approved by:

Dr. Christine A. Hrycyna

Head of the Graduate Program

To my beloved family and friends.

ACKNOWLEDGMENTS

First and foremost, I would like to deliver my sincerest gratitude to my advisor, Prof. Libai Huang. I appreciate her for taking me into her lab when she was at the University of Notre Dame in 2014. Since I had a little background on ultrafast spectroscopy before joining her group, she was very patient to guide me to start my project. During my graduate study, I was deeply inspired by her dedication and enthusiasm in the research. She is very supportive to provide various opportunity and valuable advice for my career development. Beyond her professional development, she is also a life mentor and good friend. I am very grateful to Libai for her outstanding mentoring that will benefit me all the time in the future.

I would like to thank my committee member, Prof. Shelley A. Claridge, Prof. Jianguo Mei, and Prof. Adam Wasserman for their advice and interests. I appreciate their time to discuss my research project. Their knowledge and research experiences in the different field always enlighten me with new perspectives that greatly extend my scope and lead to new ideas.

I want to express great gratitude to Dr. Zhi Guo and Dr. Yan Wan, two former postdoctoral researchers in the lab. Zhi helped me a lot in learning how to operate and align the transient absorption microscopy setup after I joined the group. He was always very helpful in providing valuable experiences and resolving my questions. Yan taught me very much on building new optical setup. When I start to build the new transient absorption microscope, his guidance was extremely beneficial that greatly enhance my research skills.

I would like to thank other former group members such as Dr. Tong Zhu, Dr. Ti Wang, Dr. Jordan Snaider, Mingwei Zhou. I was working with Tong together to study a new kind of heterostructures and lead to significant results. Jordan and I were working together on

designing and building new setups such as PL microscope and transient absorption microscope. Jordan is also a good friend of mine and we enjoy the graduate journey together. Mingwei was an undergraduate student working in the lab. He was doing an excellent job of measuring the optical properties of 2D semiconductors during the undergraduate summer research program. I also want to thank a current postdoctoral researcher in the group, Dr. Shibin Deng. Since we had similar research interests, we always had excellent discussions. His suggestions were always very valuable and inspired me very much. I would like to thank other current group members such as Daria Blach, Sona Avetian, Linrui Jin, Wenqing Zhang, Victoria Lumsargis, Thomas Wiles, and Sarath Santhakumar. I am grateful for them to make an active and enjoyable lab environment.

I appreciate all my collaborators during my graduate research. Some of them are Prof. Huili Xing, Prof. Debdeep Jena, Prof. Yong P. Chen, Prof. Jianguo Mei, Prof. Thomas Heine, Prof. Anlian Pan, Dr. Ting-Fung Chung, Dr. Yang Xu, Dr. Agnieszka Kuc, Dr. Yan Zhao, Biyuan Zheng, Dr. Suresh Vishwanath. I thank all your efforts on collaborating with us to explore new physics on two-dimensional materials.

Finally, I owe my deepest gratitude to my family, my mother (Jun Hou), my father (Xiuzhen Yuan), my sister (Yuan Yuan). All my family members always support my decisions and encourage me to overcome various difficulties. During my study abroad, I spent very little time with them. I would like to thank them again for their sacrifices they have made and great love they have offered to me.

TABLE OF CONTENTS

LIST OF TABLES	10
LIST OF FIGURES	11
ABSTRACT	21
CHAPTER 1. INTRODUCTION	25
1.1 Two-dimensional van der Waals materials	25
1.1.1 Overview	25
1.1.2 Excitons in two-dimensional semiconductors	26
1.2 2D van der Waals heterostructures	28
1.2.1 Assemble of 2D van der Waals heterostructures	28
1.2.2 Charge transfer in 2D heterostructures	29
1.2.3 Charge transfer in mixed-dimensional heterostructures	31
CHAPTER 2. OPTICAL MICROSCOPY FOR TWO-DIMENSIONAL MATERIALS CHARACTERIZATION	33
2.1 Ultrafast transient absorption microscopy	33
2.1.1 Description of ultrafast transient absorption microscopy	33
2.1.2 Transient absorption imaging	34
2.1.3 Imaging exciton transport by transient absorption microscopy	34
2.1.4 Factors that limit the spatial precision of exciton transport imaging	35
2.1.5 Noise analysis	36
2.2 Transient absorption spectroscopy	37
2.3 Confocal photoluminescence microscopy	38
2.4 Confocal Raman microscopy	39
2.5 Differential reflection microscopy	39
CHAPTER 3. EXCITON DYNAMICS AND ANNIHILATION IN TWO-DIMENSIONAL SEMICONDUCTORS	41
3.1 Abstract	41
3.2 Background	41
3.2.1 Exciton in two-dimensional transition metal dichalcogenides	41

3.2.2	Bright and dark exciton dynamics	42
3.2.3	Many-body exciton interaction.....	43
3.3	Experiential methods	44
3.3.1	Preparation of WS ₂ monolayers and few-layer samples.....	44
3.3.2	Determination of quantum yield of WS ₂ monolayers and few-layers.....	44
3.3.3	Determination of exciton density.....	44
3.4	Results and discussion	45
3.4.1	Optical characterization of WS ₂ with different thickness.....	45
3.4.2	Exciton dynamics of WS ₂ without the effect of exciton-exciton annihilation.....	49
3.4.3	Bright and dark exciton fine structure and dynamics	52
3.4.4	Defect-assisted recombination in exciton dynamics.....	56
3.4.5	Exciton dynamics of WS ₂ with the effect of exciton-exciton annihilation.....	58
3.4.6	Origin of thickness-dependent exciton-exciton annihilation.....	62
3.5	Conclusion	67
CHAPTER 4. EXCITON TRANSPORT IN TWO-DIMENSIONAL SEMICONDUCTORS.....		68
4.1	Abstract.....	68
4.2	Background.....	68
4.2.1	Strong Coulomb interaction in 2D TMDCs.....	68
4.2.2	2D exciton transport	69
4.3	Experiential Methods	70
4.3.1	Preparation of WS ₂ with different thickness	70
4.3.2	Determination of pump fluence and exciton density.....	71
4.4	Results and discussion	72
4.4.1	Optical Characterization of WS ₂ with different thickness on a quartz substrate	72
4.4.2	Direct imaging of exciton transport using TAM	74
4.4.3	Thickness-dependent exciton dynamics	81
4.4.4	Extrinsic factors in 2D exciton transport.....	83
4.4.5	Intrinsic factors than control 2D exciton transport.....	84
4.5	Conclusion	87

CHAPTER 5. ULTRAFAST CHARGE TRANSFER AND ENHANCED PHOTO-CARRIER GENERATION IN TWO-DIMENSIONAL WS ₂ /GRAPHENE HETEROSTRUCTURES	88
5.1 Abstract	88
5.2 Background	89
5.2.1 Two-dimensional Van der Waals heterostructures	89
5.2.2 Charge transfer transitions	89
5.3 Experiential Methods	90
5.3.1 WS ₂ /Graphene heterostructures fabrication	90
5.3.2 Linear absorption microscopy	92
5.3.3 First-principles calculations	92
5.3.4 Spatial resolution of TAM	93
5.3.5 Determination of pump fluence and exciton density in the TAM measurements	94
5.4 Results and discussion	94
5.4.1 Spatial heterogeneity in WS ₂ /graphene heterostructure	94
5.4.2 Interlayer coupling dependent charge transfer	95
5.4.3 Signature of charge transfer in Raman imaging	100
5.4.4 Transient bandgap renormalization	103
5.4.5 Carrier generation by excitations below the WS ₂ bandgap	109
5.4.6 First-principles calculation of interlayer charge transfer transitions	116
5.4.7 Enhanced carrier generation by excitation above the bandgap	120
5.4.8 Potential to extract carriers generated by the charge transfer states	122
5.5 Conclusion	123
CHAPTER 6. CHARGE TRANSFER EXCITON FORMATION AND TRANSPORT IN TWO-DIMENSIONAL WS ₂ -TETRACENE HETEROSTRUCTURES	124
6.1 Abstract	124
6.2 Background	124
6.2.1 Charge transfer in van der Waals heterostructures	124
6.2.2 Charge transfer exciton transport	125
6.3 Experiential Methods	126

6.3.1	Sample preparation	126
6.3.2	Atomic force microscopy	127
6.4	Results and discussion	128
6.4.1	Charge transfer excitons emission and dynamics	128
6.4.2	Hole transfer from WS ₂ to Tc	135
6.4.3	Electron versus energy transfer from Tc to WS ₂	137
6.4.4	Transport of the delocalized and localized CT excitons.....	143
6.5	Conclusion	153
CHAPTER 7. CHARGE TRANSFER EXCITON DYNAMICS AND TRANSPORT IN TWO-DIMENSIONAL WS ₂ -WSe ₂ HETEROSTRUCTURES		154
7.1	Abstract.....	154
7.2	Background.....	155
7.2.1	Charge transfer in two-dimensional van der Waals heterostructures	155
7.2.2	Moiré superlattice	155
7.2.3	Interlayer charge transfer excitons dynamics and transport	156
7.3	Experiential Methods	157
7.3.1	Second-harmonic generation (SHG) microscopy	157
7.3.2	Determination of exciton density.....	157
7.4	Result and discussions	158
7.4.1	Charge transfer exciton emission in CVD WS ₂ -WSe ₂ heterostructures.....	158
7.4.2	Stacking orientation dependent charge transfer exciton formation in CVD WS ₂ -WSe ₂ heterostructures	165
7.4.3	Stacking orientation dependent interlayer exciton recombination in CVD WS ₂ -WSe ₂ heterostructures.....	168
7.4.4	Moiré trapped interlayer exciton dynamics of CVD WS ₂ -WSe ₂ heterostructures.....	173
7.4.5	Stacking orientation dependent charge transfer exciton transport in CVD WS ₂ -WSe ₂ heterostructures.....	178
7.5	Conclusion	184
REFERENCES		185
PUBLICATIONS.....		214

LIST OF TABLES

Table 7.1 Fitted decay constants of TA dynamics traces shown in Figure 7.11 (a).	169
Table 7.2 Fitted decay constants of TA dynamics traces shown in Figure 7.15.....	172
Table 7.3 First-principle calculations of the band gap, total energy, and interlayer distance for different bilayer stacking registries shown in Figure 7.16.....	174

LIST OF FIGURES

Figure 1.1 Schematic of two types of excitons: (a) Wannier exciton and (b) Frenkel exciton.	26
Figure 1.2 Schematic of excitons in the single layer WS ₂ on a substrate.....	27
Figure 1.3 (a) Schematic of charge transfer in type II WS ₂ -WSe ₂ heterostructures after photo-excitation; (b) Spatially indirect interlayer excitons in WS ₂ -WSe ₂ heterostructures. After charge separation, electrons and holes are residing in WS ₂ and WSe ₂ layers respectively.	29
Figure 1.4 (a) Schematic of 2D WS ₂ -tetracene heterostructures. (b) Band alignment of the 1L-WS ₂ /tetracene heterostructure.	31
Figure 2.1 Schematics of TAM setup. OPO: optical parametric oscillator; AOM: acoustic optical modulator; BBO: beta barium borate.	33
Figure 2.2 Schematics of transient absorption spectroscopy setup. OPA: optical parametric amplifier; YAG: Yttrium aluminum garnet; CCD: charge-coupled device.....	38
Figure 2.3 Schematic illustration of home-built confocal PL microscopy. DM: dichroic mirror; BS: beam splitter; TCSPC: time-correlated single photon counting; CCD: charge-coupled device.	39
Figure 2.4 Schematic illustration of home-built differential reflection microscopy. DM: dichroic mirror; TCSPC: time-correlated single photon counting; CCD: charge-coupled device.	40
Figure 3.1 (a) Optical image of WS ₂ monolayer, bilayer, and trilayer flakes on Si wafer with 90 nm oxide thickness; (b) Raman spectra of WS ₂ monolayer, bilayer, and trilayer flakes. The scale bar represents 5 μm. The dashed lines mark the position of the <i>E2g</i> 1 and <i>A1g</i> positions for the monolayer.	45
Figure 3.2 (a) Differential reflectance spectrum of 1L-WS ₂ . (b) Schematic drawing of the band structure of 1L-WS ₂ and multilayer WS ₂ , with arrows indicating A, B, C, and I excitons.	47
Figure 3.3 (a) PL spectra of WS ₂ monolayer, bilayer, and trilayer. (b) PL spectrum at different locations for monolayer WS ₂	48
Figure 3.4 PL decay without exciton-exciton annihilation for WS ₂ monolayer, bilayer, and trilayer at a pump intensity of 5 nJ cm ⁻² , 0.1 μJ cm ⁻² , and 0.4 μJ cm ⁻² , respectively. The photoluminescence lifetime measurements integrate the entire PL spectra from 500 nm to 850 nm. The black line is the instrument response function (IRF). The red lines are the fitting curves using a single exponential decay convoluted with a Gaussian response function.	49
Figure 3.5 PL dynamics for WS ₂ monolayer at different locations at the pump intensity of 5 nJ/cm ²	50

Figure 3.6 (a) Summary of literature reported bright-dark exciton energy splitting for TMDC monolayers, including both experimental and theoretical values. (b) Schematic illustration of the spin allowed bright exciton (A_B) and spin forbidden dark exciton (A_D) in W-based TMDCs at the K and K' valley. Δ_c is the bright-dark exciton energy splitting. (c) A kinetic model for the dynamics of the bright and dark excitons. (d) Comparison of the temperature dependence of the time-integrated PL intensity of WSe₂ and MoS₂. (e) Temperature-dependent PL lifetime from a suspended monolayer of WSe₂.52

Figure 3.7 (a) TA dynamics of a suspended exfoliated 1L-MoS₂ flake. Redline is a fit using a triexponential function convoluted with an experimental response function. Pump fluence is 0.6 μJcm^{-2} . (b) TA dynamics of exfoliated 1L-WS₂ on SiO₂ substrate and CVD 1L-WS₂ on sapphire. Red lines are fits using a biexponential function convoluted with an experimental response function. Pump fluence is 1 μJcm^{-2}56

Figure 3.8 Integrated PL intensity for WS₂ monolayer as a function of pump intensity. The red line is a guide.58

Figure 3.9 PL decay at different excitation densities for (a) monolayer, (c) bilayer, and (e) trilayer; linearized data using Equation (5) for the PL decay of (b) monolayer, (d) bilayer, and (f) trilayer. The red lines are linear fits to the data. $n(0)$ is the initial exciton density as described in the text.60

Figure 3.10 (a) Evolution of PL spectra in WS₂ monolayer with the pumping intensity. (b) PL spectrum of WS₂ monolayer at pump intensity great than $8.0 \times 10^{11} \text{ cm}^{-2}$. The black dot is experimental data. The red solid line is a fit using a sum of two Lorentz functions as shown in blue and green solid lines.61

Figure 3.11 Schematic summary of the kinetic process of exciton-exciton annihilation. .63

Figure 3.12 Schematic summary of relaxation pathways for WS₂ monolayer and few-layer. (1) Direct exciton recombination; (2) direct exciton-exciton annihilation; (3) indirect exciton recombination; and (4) indirect exciton-exciton annihilation; (5) other nonradiative pathways.64

Figure 3.13 (a) Normalize the decay curves at the low pump intensity (without annihilation) and high exciton density ($1.6 \times 10^9 \text{ cm}^{-2}$) at the long delay time of 2 ns. (b) The subtracted decay curve (green) at the low pump intensity from the high pump intensity which is fitted with a single exponential decay (red).67

Figure 4.1 Experimental design and optical characterizations. (a) optical image of an exfoliated 1L-WS₂ on a fused silica substrate (scale bar represents 5 μm). (b) Differential reflection (black line) and PL spectra (red line) of 1L-WS₂. (c) Schematic description of exciton diffusion measurements. (d) Schematic drawing of band structure and excitonic transitions in 1L-WS₂ along with pump and probe energies for transient absorption measurements.72

Figure 4.2 Raman spectra of 1L-WS₂ on a quartz substrate. The peak energy difference between 2LA and A_{1g} is 65 cm^{-1} which indicates the number of layers to be the single layer.¹²⁰73

Figure 4.3 PL spectra of (a) 2L-WS ₂ and (b) 3L-WS ₂ on a quartz substrate are taken under excitation of 447 nm. We observed both A and I exciton emission. The emission energy of I exciton could be used to identify the number of the layer which is 712 nm (1.74 eV) and 788 nm (1.57 eV) for 2L- and 3L-WS ₂ respectively.	74
Figure 4.4 Transient dynamics of (a) 1L-WS ₂ and (b) 32L-WS ₂ with different pump fluence.	75
Figure 4.5 Transient absorption signal (ΔT) at 0 ps is plotted as a function of exciton density for (a) 1L-WS ₂ and (b) 32L-WS ₂ . Red lines are linear fits.....	75
Figure 4.6 Normalized transient absorption spectra (395-nm pump) with different thickness.	76
Figure 4.7 TAM imaging of exciton propagation in 48L-WS ₂ (pump at 395 nm and probe at 626 nm) with an injected exciton density of $8.6 \times 10^{12} \text{ cm}^{-2}$ at different pump-probe time delays. The color scale is normalized at the maximum ΔT . The normalization factors are indicated on the images. The scale bar represents 1 μm	76
Figure 4.8 Spatial profiles of exciton distribution in 48L-WS ₂ at different pump-probe delays. Solid lines are fits with Gaussian function.	78
Figure 4.9 Exciton diffusion coefficient of WS ₂ with different thickness extracted from time-dependent distribution profiles. Spatial profiles of exciton distribution in (a) 1L-WS ₂ and (b) 100L-WS ₂ with different pump-probe time delays. Solid lines are fits with Gaussian function. (c) The diffusion coefficient is obtained from the linear fitting of the variance of Gaussian profiles. Red lines are linear fits. (d) Extracted diffusion coefficients plotted as a function of the number of layers.	80
Figure 4.10 (a) Transient dynamics of 1L-MoS ₂ with different pump fluence. (b) Spatial profiles of exciton distribution in control 1L-MoS ₂	81
Figure 4.11 Thickness-dependent exciton lifetime. (a) Thickness-dependent transient dynamics are modeled by Equation (3). Fits are shown in red solid lines. (b) Extracted decay constant is plotted as a function of thickness.	81
Figure 4.12 (a) Spatial profiles of excitons in a CVD 1L-WS ₂ at different pump-probe delay times. (b) Diffusion constants of both exfoliated 1L-WS ₂ and CVD 1L-WS ₂ are obtained from the linear fitting of the variance of Gaussian profiles using equation (6). Red lines are the linear fits.	83
Figure 4.13 Extracted decay constant and exciton mobility is plotted as a function of thickness.....	84
Figure 5.1 Optical image of a 2L-WS ₂ /graphene heterostructure.....	91
Figure. 5.2 Determination of spatial resolution of TAM. (a) TAM image of a 2L-WS ₂ /graphene heterostructure. (b) Gaussian function fit of line profile shown in Figure 5.2 (a).	93

- Figure 5.3 AFM measurement of the 2L-WS₂/graphene heterostructure. (a) AFM image of the 2L-WS₂/graphene heterostructure. (b) Line profiles taken along the black and red dashed lines indicated in (a). Scale bar represents 1 μm94
- Figure 5.4 PL spectra (a) and normalized time-resolved PL dynamics (c) of individual 1L-WS₂ and 1L-WS₂/graphene, red lines are exponential fittings.95
- Figure 5.5 TAM image of the 2L-WS₂/graphene measured at 0 ps (pump at 395 nm and probe at 624 nm, pump fluence $\sim 2 \text{ uJ/cm}^2$). (e) TAM image measured at 2 ps.....97
- Figure 5.6 TAM images of a control 2L-WS₂ flake at time delays of 0 ps (a) and 5 ps (b) with 3.14 eV pump and 1.99 eV probe.98
- Figure 5.7 Normalized transient dynamics of the heterostructure at area 1, 2 as marked, and a control 2L-WS₂. Solid lines are the fitting curves with exponential decays convoluted with experimental response function. All scale bars represent 1 μm98
- Figure 5.8 Normalized transient dynamics of position 9 and 10 in 2L-WS₂ indicated in Figure 5.5 with a pump fluence of $8.4 \mu\text{J cm}^{-2}$99
- Figure 5.9 (a) Correlated TAM image of the 1L-WS₂/G heterostructure measured at 0 ps probing the A exciton resonance. Pump photon energy = 3.14 eV and probe photon energy = 1.99 eV (b) Normalized transient dynamics of the heterostructure at areas 1 and 2 as marked, and the control 2L-WS₂ layer. Solid lines are the fitting curves with exponential decays convoluted with the experimental response function. All scale bars represent 1 μm100
- Figure 5.10 (a) Raman mapping of the G band of graphene in 2L-WS₂/graphene. Obvious shift of the G band is due to surface charge transfer doping from underneath WS₂; (b) Comparison of the Raman spectrum of graphene while sitting on a 2L-WS₂ (position 9) and a bare Si substrate (90 nm thick SiO₂). Curves are vertically shifted for clarity. The rising background for the wavenumber above 2600 cm^{-1} originates from the photoluminescence of WS₂; Raman mapping of the position of (c) the strong peak (2LA and E_{12g}¹) and (d) the A_{1g} peak in 2L-WS₂/graphene heterostructure. All scale bars represent 1 μm101
- Figure. 5.11 Raman spectra of 2L-WS₂/G heterostructure (area 1 as shown in Figure 1 (d)) (red line) and control 2L-WS₂ (black line). The enhancement ratio of Raman intensity is about 1.4 times in 2L-WS₂/graphene than control 2L-WS₂.103
- Figure 5.12 (a) TA spectrum of A exciton resonance in 2L-WS₂/graphene (0 ps delay) at different positions as well as for a control 2L-WS₂. Pump photon energy is 3.14 eV and pump fluence of $2 \mu\text{J / cm}^2$. (b) TA spectrum of A exciton resonance in 1L-WS₂/graphene and a control 1L-WS₂ at 0 ps delay.103
- Figure 5.13 TA image (a) and spectrum of A exciton resonance for a strong and a weak coupling location of a 1L -WS₂/graphene heterostructure on a sapphire substrate at 0 ps. Pumped at 3.14 eV.105
- Figure 5.14 Summary of different processes following photoexcitation in WS₂ layers (a) and in 1L-WS₂/graphene heterostructure (b).106

- Figure 5.15 Pump intensity dependent TA spectra of a control 1L-WS₂ flake. Pump photon energy = 3.14 eV.....108
- Figure 5.16 TA signal at 0 ps probed at 1.99 eV (A exciton resonance) for the 1L-WS₂/graphene heterostructure when varying the pump photon energy from 1.2 eV to 1.8 eV, pump fluence $\sim 2 \mu\text{J cm}^{-2}$109
- Figure 5.17 TA spectrum of A exciton resonance in the 1L-WS₂/graphene, 2L-WS₂/graphene heterostructures, and the control 1L-WS₂ at 0 delay time with 1.57 eV pump photon energy, pump fluence $\sim 17 \mu\text{J cm}^{-2}$110
- Figure 5.18 TAM imaging of 2L-WS₂/graphene at 0 ps, scale bar represents 1 μm . 1.57 eV pump and 1.99 eV probe, pump fluence $\sim 17 \mu\text{J cm}^{-2}$111
- Figure 5.19 (a) Schematic showing two possible mechanisms. One possibility is that the graphene layer is excited and hot carrier is subsequently transferred from graphene to WS₂ (mechanism 1), and the other possibility is the direct excitation of interlayer CT transitions (mechanism 2). (b) The amplitude of the TA signal at a 0-ps time delay versus pump fluence for the 1L-WS₂/graphene heterostructure at area 3 showing a linear dependence at three different pump photon energies (probe, 1.99 eV).....112
- Figure 5.20 The amplitude of the TA signal at 0 ps time delay versus pump fluence for the 2L-WS₂/graphene heterostructure at area 1. Pump = 1.57 eV, probe = 1.99 eV.....113
- Figure 5.21 Normalized transient dynamics of the 1L-WS₂/graphene heterostructure at area 3 and the 2L-WS₂/graphene heterostructure at area 1. Pump photon energy is 1.57 eV and probe photon energy is 1.99 eV. Solid lines are fits with a single exponential decay function convoluted with the experimental response function.....115
- Figure 5.22 Band structure of the heterostructure. (A) Commensurate model of a 5×5 graphene/ 4×4 WS₂ supercell (at the PBE level) and (B) incommensurate model of corresponding perfect unit cells (as in a single layer) of each component (at the HSE06/SOC level) along the Γ -K direction. The red arrows indicate interlayer transitions.....116
- Figure 5.23 Band structure of the incommensurate model of the perfect unit cells calculated along the Γ -M directions (at the HSE06/SOC level). No additional transitions between graphene and WS₂ are expected in comparison with the Γ -K directions shown in Figure 5.22.....118
- Figure. 5.24 Raman spectra of the 1L-WS₂/graphene heterostructure and the Fermi level shift of graphene. No obvious change in the position of G peak ($\sim 1586 \text{ cm}^{-1}$) in the two regions, whereas there is a blue shift of the 2D peak ($\sim 15 \text{ cm}^{-1}$) for the graphene layer on WS₂. By analyzing the correlation of the two peaks, we estimate a p-doping density of $2 \times 10^{12} \text{ cm}^{-2}$ in graphene on 1L-WS₂ corresponding to a Fermi level shift of 0.17 eV. Spectra are shifted vertically for clarity.....119
- Figure 5.25 Correlated (a) transmission and (b) reflection images of the same 1L-WS₂/graphene heterostructure on a transparent sapphire substrate. Scale bars: 200 nm.120

- Figure 5.26 Zoomed-in linear absorption (a) and correlated TAM image (D) of the 1L-WS₂/G heterostructure on a transparent sapphire substrate. The TAM image is measured at 0 ps (pump, 3.14 eV; probe, 1.99 eV). Scale bars, 200 nm.122
- Figure 6.1 Identification of numbers of WS₂ layers using photoluminescence spectroscopy. PL spectrum of WS₂ from 1L to 7L is shown from bottom to top.127
- Figure 6.2 AFM line profile of the Tc film thickness.127
- Figure 6.3 (a) Optical image of WS₂ flakes exfoliated on Si/SiO₂ substrate. The 1L-WS₂ is indicated by the dashed line. The dashed square shows the area imaged by AFM in (b). Scale bar represents 10 μm. (b) AFM image of the same 1L-WS₂ flake in (a) with a Tc thin film deposited on top. Scale bar represents 5 μm. (c) Schematic of the formation of CT excitons and the band alignment of the 1L-WS₂/Tc heterostructure, showing the formation of a type II heterojunction.129
- Figure 6.4 Absorption and PL spectrum of Tc film and 1L-WS₂.130
- Figure 6.5 Steady-state PL spectra of a 1L-WS₂, Tc thin film, and a 1L WS₂/Tc heterostructure. The new emission band at 1.7 eV indicates the formation of interlayer CT excitons.131
- Figure 6.6 Photoluminescence excitation (PLE) measurements monitoring CT exciton emission at 1.7 eV.132
- Figure 6.7 (a) PL spectra of a 1L-WS₂/Tc heterostructure, a 3L-WS₂/Tc heterostructure, and a Tc thin film with excitation energy of 2.1 eV and 700-nm long-pass filter selectively exciting WS₂ in the heterostructures and detecting only interlayer CT exciton emission. (b) Time-resolved PL measurements on the interlayer CT exciton in a 1L-WS₂/Tc heterostructure, a Tc film, and a 1L-WS₂ flake. The CT exciton PL decay is fitted with a stretched exponential function, as described in the main text.133
- Figure 6.8 Excitation intensity dependent measurements of PL dynamics of CT exciton emission. Excitation photon energy: 2.1 eV.134
- Figure 6.9 (a) Transient absorption dynamics probed at the A exciton bleach of the 1L-WS₂ before and after Tc deposition with pump energy of 2.1 eV (pump fluence: 50 μJ/cm²). Red solid lines are fittings with a bi-exponential function convoluted with an experimental response function. Inset of band alignment shows the hole transfer process the 1L-WS₂/Tc heterostructure. (b) Transient absorption dynamics probed at the A exciton bleach of 2L-WS₂ before and after Tc deposition with pump energy of 2.1 eV, showing no hole transfer in the 2L-WS₂/Tc heterostructure.135
- Figure 6.10 TAM Dynamics of 4L, 5L, and 7L-WS₂ before and after Tc deposition. TAM dynamics of 4L (a), 5L (b) and 7L-WS₂ (c) before (blue) and after (green) Tc deposition showing no hole transfer in the heterostructures built by thick WS₂ flakes and Tc film. (2.1 eV pump and 2.0 eV probe).136
- Figure 6.11 (a) 1L-WS₂ dynamics before and after Tc deposition. (b) 2L-WS₂ dynamics before and after Tc deposition. Pump = 3.1 eV (pump fluence: 2.2 μJcm⁻²), probe = 2.0 eV.137

- Figure 6.12 Subtraction of 1L-WS₂ dynamics from 1L-WS₂/Tc dynamics fitted with an exponential growth function with a time constant of 2.1 ± 0.2 ps and subtraction of 2L WS₂ dynamics from 2L-WS₂/Tc dynamics yielding a rise time constant of 44 ± 5 ps.139
- Figure 6.13 Energy transfer from Tc to WS₂ measured with TAM (3.1 eV pump and 2.0 eV probe). (a) Transient dynamics of 3L-7L WS₂ before (blue) and after (green) Tc deposition. (b) Subtraction of WS₂ dynamics from WS₂/Tc dynamics yielding rising curves fitted with an exponential function for each WS₂ thickness, indicating energy transfer time constants.....141
- Figure 6.14 Energy transfer rate dependence on numbers of WS₂ layers fitted to the electromagnetic model as described in the main text.142
- Figure 6.15 Schematic illustration of electron and energy transfer processes. In the heterostructures constructed from 2L-WS₂ or thicker, type I heterojunctions are formed and only exciton energy transfer is possible.....143
- Figure 6.16 (a) Exciton population profiles fitted with Gaussian functions at different delay times with the maximum ΔT signal normalized to unity for the control 1L-WS₂. The pump photon energy is 3.1 eV (pump fluence: $4.4 \mu\text{J}/\text{cm}^2$) and the probe energy is 2.0 eV. (b) $\sigma_{1,t2} - \sigma_{02}$ as a function of pump-probe delay time, with a linear fit to equation 3 (line) for the control 1L-WS₂. Error bars of $\sigma_{1,t2} - \sigma_{02}$ are the standard errors estimated from Gaussian fitting to the spatial intensity distributions.....145
- Figure 6.17 TAM image of the same 1L-WS₂/Tc heterostructure shown in Figure 1 taken with spatially overlapped pump and probe beams at 0 ps. Scale bar represents $2 \mu\text{m}$. The pump energy is 3.1 eV (pump fluence: $4.4 \mu\text{J}/\text{cm}^2$) and the probe energy is 2.0 eV.146
- Figure 6.18 Exciton population profile at 1 ns delay fitted with a single Gaussian function (a) and a sum of two Gaussian functions (b) as described in the main text for the 1L-WS₂/Tc heterostructure. The pump photon energy is 3.1 eV (pump fluence: $4.4 \mu\text{J}/\text{cm}^2$) and the probe energy is 2.0 eV. (c) Exciton population profiles fitted with a sum of two Gaussian functions as described in the text at different delay times with the maximum ΔR signal normalized to unity for the 1L-WS₂/Tc heterostructure along the line indicated in Figure 6.17.....148
- Figure 6.19 $\sigma_{1,t2} - \sigma_{02}$ and $\sigma_{2,t2} - \sigma_{02}$ as a function of pump-probe delay time, with a linear fit to equation 3 (line) for the 1L-WS₂/Tc heterostructure.....149
- Figure 6.20 Transient absorption dynamics of a 1L-WS₂/Tc heterostructure measured at different pump fluences. Pump = 3.1 eV, probe = 2.0 eV.150
- Figure 6.21 Power-dependence exciton population profiles (a) pump fluence: $10.0 \mu\text{J}/\text{cm}^2$. (b) pump fluence: $10.0 \mu\text{J}/\text{cm}^2$. $\sigma_{1,t2} - \sigma_{02}$ and $\sigma_{2,t2} - \sigma_{02}$ as a function of pump-probe delay time, with linear fits to equation 3 (red lines) for the 1L-WS₂/Tc heterostructure.152
- Figure 7.1 Optical image of CVD grown WS₂-WSe₂ heterostructures with two twist angles (0° and 60°). Scale bar represents $10 \mu\text{m}$158

- Figure 7.2 (a) Fundamental light with a photon energy of 1.55 eV used in SHG measurements. (b) SHG signal (3.10 eV) from WS₂-WSe₂ heterostructures ($\theta = 0^\circ$ and 60°) and 1L-WS₂.....159
- Figure 7.3 (a) Schematic of band alignment in WS₂-WSe₂ heterostructures. (b) PL image of WS₂-WSe₂ heterostructures (0° and 60°) as shown in Figure 7.1. Scale bar represents 2 μm160
- Figure 7.4 (a) PL spectrum of 1L-WS₂ and WS₂-WSe₂ heterostructure (60°). (b) Raman spectrum of 1L-WS₂ and WS₂-WSe₂ heterostructures (0° and 60°).161
- Figure 7.5 PL spectrum of WS₂-WSe₂ heterostructures (0° and 60°), 1L-WS₂, and 1L-WSe₂ at 295 K (a) and 78 K (b).....162
- Figure 7.6 Temperature dependent PL spectrum for (a) 1L-WS₂, (b) 1L-WSe₂, (c) WS₂-WSe₂ (60°), and (d) WS₂-WSe₂ (0°).163
- Figure 7.7 (a) PL image of interlayer exciton emission in WS₂-WSe₂ (60°) at 78 K with a detection range between 1.30 and 1.55 eV. (b) PLE spectra of interlayer exciton emission in WS₂-WSe₂ (60°) at 78 K.....164
- Figure 7.8 (a) Temperature-dependent TRPL dynamics of interlayer excitons in WS₂-WSe₂ (60°). (Red lines are fits using a bi-exponential function convoluted with an IRF function). (b) A plot of fitted decay constant of TRPL dynamics shown in Figure 7.8 (a).164
- Figure 7.9 (a) Differential reflection spectrum of WS₂-WSe₂ heterostructures (0° and 60°) and 1L-WS₂. (b) Transient reflection spectrum of WS₂-WSe₂ heterostructures (0° and 60°) and 1L-WS₂.....165
- Figure 7.10 (a) Schematic of exciton broadening in WS₂-WSe₂ heterostructures. A exciton bleach of 1L-WS₂, WS₂-WSe₂ (0°), and WS₂-WSe₂ (60°). Red lines are fits using a Lorentzian function.....166
- Figure 7.11 (a) Schematic of electron transfer in WS₂/WSe₂ heterostructures when selectively exciting WSe₂ layer with a pump photon energy of 1.58 eV. (b) TAM imaging of WS₂-WSe₂ heterostructures (0° and 60°) at 0 ps. (pump photon energy is 1.58 eV; probe photon energy is 1.94 eV).....168
- Figure 7.12 (a) A representative result of charge transfer exciton dynamics of WS₂-WSe₂ heterostructures (0° and 60°). (pump photon energy is 1.58 eV; probe photon energy is 1.94 eV). Red lines are fits using a bi-exponential function convoluted with an IRF function. (b) Charge transfer exciton dynamics of different WS₂-WSe₂ heterostructures (0° and 60°).169
- Figure 7.13 Power dependent charge transfer exciton recombination dynamics of WS₂-WSe₂ (60°) and WS₂-WSe₂ (0°). (pump photon energy is 1.58 eV; probe photon energy is 1.94 eV).....170

- Figure 7.14 (a) Schematic of charge transfer in WS₂/WSe₂ heterostructures when exciting both WS₂ and WSe₂ layer with a pump photon energy of 3.14 eV. Here, electrons transfer from WSe₂ to WS₂ while holes transfer from WS₂ to WSe₂. (b) TAM imaging of WS₂-WSe₂ heterostructures (0° and 60°) at 0 ps. (pump photon energy is 3.14 eV; probe photon energy is 1.94 eV)170
- Figure 7.15 Charge transfer exciton dynamics of WS₂-WSe₂ heterostructures (0° and 60°). (pump photon energy is 3.14 eV; probe photon energy is 1.94 eV). Red lines are fits using a bi-exponential function convoluted with an IRF function.172
- Figure 7.16 Long-period Moiré superlattice and three representative interlayer atomic registries for (a) WS₂-WSe₂ (0°) and (b) WS₂-WSe₂ (60°).....173
- Figure 7.17 Schematic of Moiré potential landscape for WS₂-WSe₂ (0°).....175
- Figure 7.18 Temperature-dependent exciton dynamics of 1L-WS₂ (pump photon energy is 3.14 eV; probe photon energy is 1.94 eV). Solid lines are fits using a bi-exponential function convoluted with an IRF function.175
- Figure 7.19 Temperature dependent charge transfer exciton recombination dynamics of WS₂-WSe₂ (0°) and WS₂-WSe₂ (60°). (pump photon energy is 1.58 eV; probe photon energy is 1.94 eV). Solid lines are fits using a bi-exponential function convoluted with an IRF function.176
- Figure 7.20 Charge transfer exciton recombination constant extracted from Figure 7.16 as a function of temperature for WS₂-WSe₂ (0°) and WS₂-WSe₂ (60°).....176
- Figure 7.21 Exciton transport measurements of 1L-WS₂ and 1L-WSe₂. Spatial distribution of the exciton population at different delay time for 1L-WS₂ (a) and 1L-WSe₂ (c). Diffusion coefficient of 1L-WS₂ (b) and 1L-WSe₂ (d) is obtained from the linear fitting of the variance of Gaussian profile. Red lines are linear fits.178
- Figure 7.22 Exciton transport measurements of 2L-WS₂ and 2L-WSe₂. Spatial distribution of the exciton population at different delay time for 2L-WS₂ (a) and 2L-WSe₂ (c). Diffusion coefficient of 2L-WS₂ (b) and 2L-WSe₂ (d) is obtained from the linear fitting of the variance of Gaussian profile. Red lines are linear fits.180
- Figure 7.23 Exciton population profiles at different time delays with different interlayer exciton densities (a) $5.2 \times 10^{11} \text{ cm}^{-2}$ and (b) $1.7 \times 10^{12} \text{ cm}^{-2}$ for WS₂-WSe₂ (0°). The diffusion profiles are fitted with Gaussian functions at different delay times with the maximum ΔR signal normalized to unity.181
- Figure 7.24 Exciton population profiles at different time delays with different interlayer exciton densities (a) $5.2 \times 10^{11} \text{ cm}^{-2}$ and (b) $1.7 \times 10^{12} \text{ cm}^{-2}$ for WS₂-WSe₂ (60°). The diffusion profiles are fitted with Gaussian functions at different delay times with the maximum ΔR signal normalized to unity.181
- Figure 7.25 $\sigma t^2 - \sigma_0 t^2$ as a function of pump-probe delay time for both WS₂-WSe₂ (0°) and WS₂-WSe₂ (60°) at different interlayer exciton densities. Error bars of $\sigma t^2 - \sigma_0 t^2$ are the standard errors estimated from Gaussian fitting to the spatial intensity distributions. Solid lines are guides for eyes.182

Figure 7.26 Interlayer CT exciton transport in WS₂-WSe₂ heterostructures with a pump photon energy of 3.1 eV. (a) 2D image of transient reflection signal in WS₂-WSe₂ (60°) as it evolves with space and time. Exciton density is $1.6 \times 10^{11} \text{ cm}^{-2}$. Exciton population profiles at different delay time for (b) WS₂-WSe₂ (60°) and (c) WS₂-WSe₂ (0°). Exciton density is $1.6 \times 10^{11} \text{ cm}^{-2}$. The diffusion profiles are fitted with Gaussian functions at different delay times with the maximum ΔR signal normalized to unity. (d) $\sigma t^2 - \sigma_0^2$ as a function of pump-probe delay time for both WS₂-WSe₂ (0°) and WS₂-WSe₂ (60°). Error bars of $\sigma t^2 - \sigma_0^2$ are the standard errors estimated from Gaussian fitting to the spatial intensity distributions. Solid lines are linear fits.....183

ABSTRACT

Author: Yuan, Long. PhD

Institution: Purdue University

Degree Received: May 2019

Title: Spatial and Temporal Imaging of Exciton Dynamics and Transport in Two-Dimensional Semiconductors and Heterostructures by Ultrafast Transient Absorption Microscopy

Committee Chair: Libai Huang

Recently, atomically thin two-dimensional (2D) layered materials such as graphene and transition metal dichalcogenides (TMDCs) have emerged as a new class of materials due to their unique electronic structures and optical properties at the nanoscale limit. 2D materials also hold great promises as building blocks for creating new heterostructures for optoelectronic applications such as atomically thin photovoltaics, light emitting diodes, and photodetectors. Understanding the fundamental photo-physics process in 2D semiconductors and heterostructures is critical for above-mentioned applications.

In Chapter 1, we briefly describe photo-generated charge carriers in two-dimensional (2D) transition metal dichalcogenides (TMDCs) semiconductors and heterostructures. Due to the reduced dielectric screening in the single-layer or few-layer of TMDCs semiconductors, Columbo interaction between electron and hole in the exciton is greatly enhanced that leads to extraordinary large exciton binding energy compared with bulk semiconductors. The environmental robust 2D excitons provide an ideal platform to study exciton properties in TMDCs semiconductors. Since layers in 2D materials are holding by weak van de Waals interaction, different 2D layers could be assembled together to make 2D heterostructures. The successful preparation of 2D heterostructures paves a new path to explore intriguing optoelectronic properties.

In Chapter 2, we introduce various optical microscopy techniques used in our work for the optical characterization of 2D semiconductors and heterostructures. These optical imaging tools with high spatial and temporal resolution allow us to directly track charge and energy flow at 2D interfaces.

Exciton recombination is a critical factor in determining the efficiency for optoelectronic applications such as semiconductor lasers and light-emitting diodes. Although exciton dynamics have been investigated in different 2D semiconductor, large variations in sample qualities due to different preparation methods have prevented obtaining intrinsic exciton lifetimes from being conclusively established. In Chapter 3, we study exciton dynamics in 2D TMDCs semiconductors using ultrafast PL and transient absorption microscopy. Here we employ 2D WS₂ semiconductor as a model system to study exciton dynamics due to the low defect density and high quantum yield of WS₂. We mainly focus on how the exciton population affects exciton dynamics. At low exciton density regime, we demonstrate how the interlayer between the bright and dark exciton populations influence exciton recombination. At high exciton density regime, we exhibit significant exciton-exciton annihilation in monolayer WS₂. When comparing with the bilayer and trilayer WS₂, the exciton-exciton annihilation rate in monolayer WS₂ increases by two orders of magnitude due to enhanced many-body interactions at single layer limit.

Long-range transport of 2D excitons is desirable for optoelectronic applications based on TMDCs semiconductors. However, there still lacks a comprehensive understanding of the intrinsic limit for exciton transport in the TMDCs materials currently. In Chapter 4, we employ ultrafast transient absorption microscopy that is capable of imaging excitons transport with ~ 200 fs temporal resolution and ~ 50 nm spatial precision

to track exciton motion in 2D WS₂ with different thickness. Our results demonstrate that exciton mobility in single layer WS₂ is largely limited by extrinsic factors such as charge impurities and surface phonons of the substrate. The intrinsic phonon-limited exciton transport is achieved in WS₂ layers with a thickness greater than 20 layers.

Efficient photocarrier generation and separation at 2D interfaces remain a central challenge for many optoelectronic applications based on 2D heterostructures. The structural tunability of 2D nanostructures along with atomically thin and sharp 2D interfaces provides new opportunities for controlling charge transfer (CT) interactions at 2D interfaces. A largely unexplored question is how interlayer CT interactions contribute to interfacial photo-carrier generation and separation in 2D heterostructures. In Chapter 5, we present a joint experimental and theoretical study to address carrier generation from interlayer CT transitions in WS₂-graphene heterostructures. We use spatially resolved ultrafast transient absorption microscopy to elucidate the role of interlayer coupling on charge transfer and photo-carrier generation in WS₂-graphene heterostructures. These results demonstrate efficient broadband photo-carrier generation in WS₂-graphene heterostructures which is highly desirable for atomically thin photovoltaic and photodetector applications based on graphene and 2D semiconductors.

CT exciton transport at heterointerfaces plays a critical role in light to electricity conversion using 2D heterostructures. One of the challenges is that direct measurements of CT exciton transport require quantitative information in both spatial and temporal domains. In order to address this challenge, we employ transient absorption microscopy (TAM) with high temporal and spatial resolution to image both bright and dark CT excitons in WS₂-tetracene and CVD WS₂-WSe₂ heterostructure. In Chapter 6, we study the formation and

transport of interlayer CT excitons in 2D WS₂-Tetracene vdW heterostructures. TAM measurements of CT exciton transport at these 2D interfaces reveal coexistence of delocalized and localized CT excitons. The highly mobile delocalized CT excitons could be the key factor to overcome large CT exciton binding energy in achieving efficient charge separation. In Chapter 7, we study stacking orientational dependent interlayer exciton recombination and transport in CVD WS₂-WSe₂ heterostructures. Temperature-dependent interlayer exciton dynamics measurements suggest the existence of moiré potential that localizes interlayer excitons. TAM measurements of interlayer excitons transport reveal that CT excitons at WS₂-WSe₂ heterointerface are much more mobile than intralayer excitons of WS₂. We attributed this to the dipole-dipole repulsion from bipolar interlayer excitons that efficiently screen the moiré potential fluctuations and facilitate interlayer exciton transport. Our results provide fundamental insights in understanding the influence of moiré potential on interlayer exciton dynamics and transport in CVD WS₂-WSe₂ heterostructures which has important implications in optoelectronic applications such as atomically thin photovoltaics and light harvesting devices.

CHAPTER 1. INTRODUCTION

1.1 Two-dimensional van der Waals materials

1.1.1 Overview

Two dimensional (2D) van der Waals (vdW) materials including graphene, hexagonal-boron nitride, and transition-metal dichalcogenides (TMDCs) have recently emerged as a new class of materials due to unique optical and electronic properties¹⁻¹⁷ holding great promise for novel optoelectronic, spintronics, and plasmonic applications¹⁸⁻³².

Graphene is a single layer of carbon atoms arranged in a hexagonal lattice that is first isolated and studied by K.S. Novoselov and A.K. Geim¹. Due to its unique structure, graphene exhibits extraordinary electronic properties such as ultrahigh carrier mobility^{3,33-36}, superior thermal conductivity³⁷, and excellent mechanical properties³⁸. The rise of graphene also triggers explosive research interests on other 2D vdW materials. Transition metal dichalcogenides (TMDCs) such as MoS₂, MoSe₂, WS₂, and WSe₂ are analog of graphene with finite band gap. Atomically thin TMDCs exhibit unique electronic properties such as indirect to direct bandgap transition^{7, 10}, large spin-orbit coupling³⁹⁻⁴⁰, and strong light-matter interaction⁴¹. The atomically-thin nature of the monolayer TMDCs also gives rise to a strong enhancement of the Coulomb interaction between the electron and the hole⁴² which provides an exciting platform for both fundamental research and device applications.

1.1.2 Excitons in two-dimensional semiconductors

An exciton is a bounded electron and hole pair due to the Coulomb attraction⁴³. Excitons in solids are divided into two types which are Wannier (or Wannier-Mott) and Frenkel excitons depending on the strength of Coulomb interaction. In semiconductors, due to the large dielectric constant, Coulomb interaction is effectively screened by the dielectric environment, resulting in a delocalized exciton with a radius much larger than the lattice spacing. Such excitons are usually called Wannier excitons as shown in Figure 1.1 (a). The exciton binding energy of a typical Wannier exciton is on the order of 10 meV. On the other hand, in solids with small dielectric constant, such as ionic crystals and organic molecule semiconductors, electron and hole are tightly bounded with the exciton binding energy on the order of a few hundred meV. Such localized excitons are usually called Frenkel excitons. The size of a Frenkel exciton is usually the same order as the size of the unit cell. The illustration of Wannier and Frenkel exciton is shown in Figure 1.1.

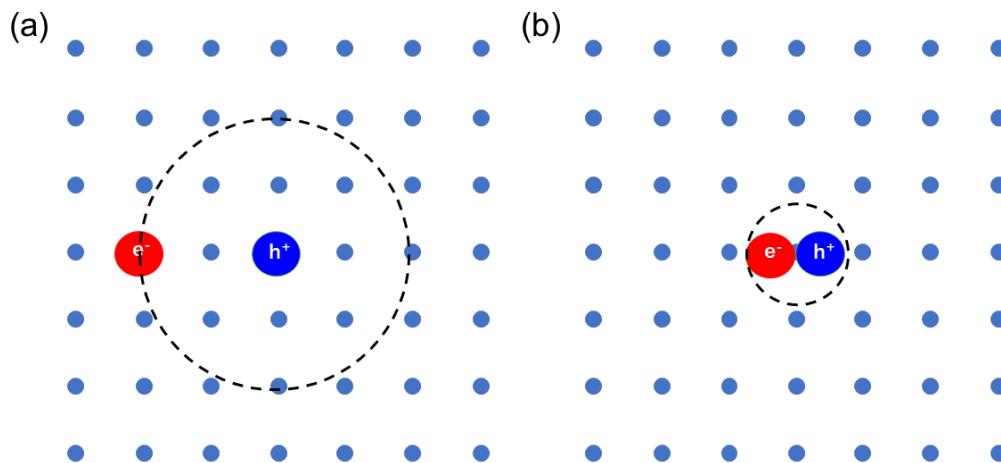


Figure 1.1 Schematic of two types of excitons: (a) Wannier exciton and (b) Frenkel exciton.

Besides the dielectric constant, exciton binding energy is also strongly dependent on the dimensionality as displayed in the following equation⁴⁴:

$$E_n = -\frac{E_0}{\left(n + \frac{\alpha-3}{2}\right)^2} \quad (1)$$

where n is the principle quantum number; α is the dimensionality; and E_0 is the exciton Rydberg.

Due to the reduced dimensionality, exciton binding energy is a factor of 4 larger in 2D excitons than 3D excitons without the effect of the dielectric environment. Since 2D exciton is strongly confined in the plane of single layer⁴², as shown in Figure 1.2, the dielectric screening is significantly reduced due to that the electric field between electrons and holes extend to the outside of the sample. The reduced dielectric screening further enhances exciton binding energy in 2D semiconductors⁴². Previous optical spectroscopy measurements have determined exciton binding energy in monolayer TMDCs to be on the order of several hundreds of meV^{42, 45-51}. The corresponding ground-state Bohr radii of excitons are on the order of nanometers and the wave function extends over several unit cells suggesting that 2D excitons lie in the marginal case in between typical Wannier excitons and Frenkel excitons^{47, 52}. The remarkable large exciton binding energy implies high thermal stability of 2D excitons even at room temperature that provides an ideal platform to study exciton dynamics and transport.

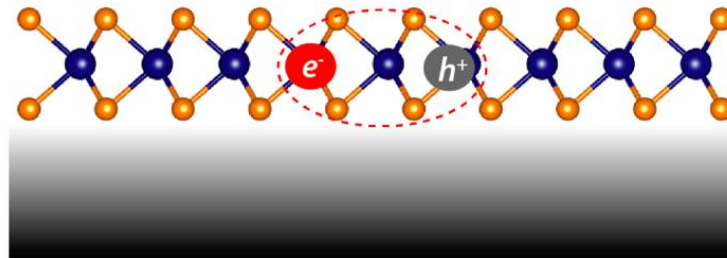


Figure 1.2 Schematic of excitons in the single layer WS₂ on a substrate.

1.2 2D van der Waals heterostructures

1.2.1 Assemble of 2D van der Waals heterostructures

Due to the weak van der Waals forces between layers in 2D materials, 2D heterostructures can be assembled by artificially stacking layers of different 2D materials without the restrict growth conditions in conventional bulk heterostructure such as lattice matching and atom interdiffusion⁵³⁻⁵⁶. Fabrication of 2D heterostructures with atomically sharp interfaces paves a new pathway for creating nanostructures with intriguing optoelectronic, spintronic, and plasmonic properties^{23, 25, 57-68}.

Typically, there are two protocols for preparing van der Waals heterostructures by mechanical transfer (top-down) and direct-growth (bottom-up) approaches. The mechanical transfer method is the most straightforward and widely used fabrication technique to create 2D heterostructures^{11, 69-73}. The initial technique is based on exfoliating a flake of 2D material on a sacrificial polymer, aligning and placing it on another flake, and then removing the polymer. Thermal annealing is typically used to remove the contaminants and improve the interfacial contact. Recently, a substitute dry transfer method is developed to use the membrane to lift a 2D flake up and transfer on another 2D flake. This technique leads to clean interfaces over large areas. Direct-growth technique such as chemical vapor deposition (CVD) is a promising way for scalable production of 2D heterostructures. The growth process usually involves the vapor-phase reactions in which the reactants are generated by thermal evaporation of specific source materials⁷⁴⁻⁷⁷.

1.2.2 Charge transfer in 2D heterostructures

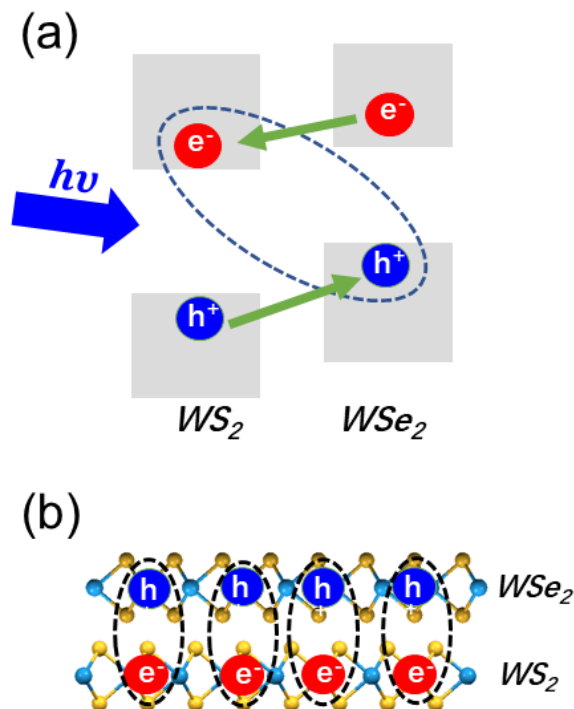


Figure 1.3 (a) Schematic of charge transfer in type II WS₂-WSe₂ heterostructures after photo-excitation; (b) Spatially indirect interlayer excitons in WS₂-WSe₂ heterostructures. After charge separation, electrons and holes are residing in WS₂ and WSe₂ layers respectively.

In TMDCs heterostructure with staggered type II band alignment⁷⁸⁻⁸⁰, photo-excited carriers could undergo efficient charge separation due to the built-in electric field at the interface. Take a 2D WS₂-WSe₂ heterostructure as a model system for illustration, after photo-excitation, electrons transfer from WSe₂ to WS₂ while holes transfer from WS₂ to WSe₂ as shown in Figure 1.3 (a). Previous studies demonstrated robust ultrafast charge transfer (≤ 50 fs) across the interface with arbitrary aligned hetero-bilayer⁸¹⁻⁹¹ independent of stacking orientation. In hetero-bilayers with large momentum mismatch, charge separation is expected to be accompanied by a significant momentum change. It is still a puzzle to understand how parallel momentum is conserved during the charge transfer. A

previous experiment suggests that excess electronic energy allows the sampling of a broader range of momentum space to overcome the momentum conservation⁹².

After charge separation, electrons and holes are spatially separated into different layers and result in the formation of a new bounded interlayer CT states as shown in Figure 1.3 (b). Due to the reduced dielectric screening, the interlayer exciton is tightly bounded with binding energy on the order of 100 meV^{52, 92}. The existence of interlayer CT exciton has been confirmed using PL spectroscopy^{58, 62, 73, 93-104}.

Understanding the interlayer exciton recombination and transport behavior provide fundamental insights to explore 2D heterostructures for optoelectronics and light harvesting applications. Time-resolved PL measurements present long-lived nature of interlayer exciton that is over two orders of magnitude longer than intralayer exciton lifetime at low temperature^{93, 96-97, 101, 105} due to the spatial separation of electrons and holes in different layers. Previous experimental evidence displays that interlayer excitons in MoS₂-WS₂ heterostructure decay mostly via non-radiative recombination such as defect-assisted recombination and exhibits no correlation with interfacial crystallographic alignment⁸². The large discrepancy in interlayer exciton lifetimes indicates that sample quality is critical to study intrinsic interlayer exciton recombination. Monolayer TMDCs semiconductors usually have short diffusion length due to fast exciton recombination and enhanced exciton-impurities and exciton-phonon scattering at the single layer limit¹⁰⁶⁻¹¹¹. The long-lived interlayer excitons in TMDCs heterostructures help overcome this limitation and enable long-range interlayer exciton transport^{62, 101}. A recent study by Unuchek et al demonstrates room temperature electrical control of interlayer exciton transport in MoSe₂-WSe₂ heterostructure⁶². The interlayer exciton diffusion is modulated

by applying a vertical electric field to create confining and repulsive potentials for the exciton flux⁶². Although interlayer exciton diffusion length is obtained through spatially-resolved PL imaging in the previous study⁶², it is a puzzle on how interlayer exciton motion evolves with time. Further investigation is necessary to elucidate this question by using time-resolved imaging technique.

1.2.3 Charge transfer in mixed-dimensional heterostructures

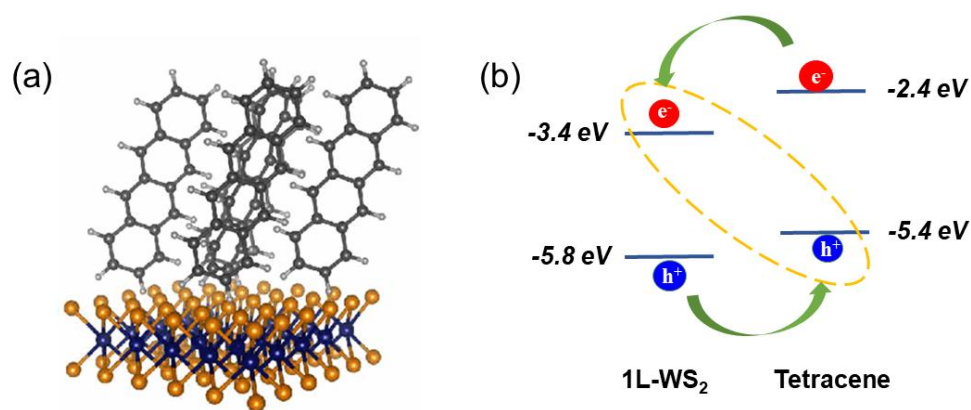


Figure 1.4 (a) Schematic of 2D WS₂-tetracene heterostructures. (b) Band alignment of the 1L-WS₂/tetracene heterostructure.

While the previous topic discusses the photo-physics process in 2D-2D heterostructures, the concept of van der Waals heterostructures can be extended to integrate any layered 2D materials with a class of materials with different dimensionality to form mixed-dimensional heterostructures. An interesting combination is to use TMDCs semiconductors and molecular semiconductors to build 2D-0D heterostructures^{68, 112-119}. Here, we use WS₂-tetracene (Tc) (Figure 1.4 (a)) as a model system to demonstrate charge transfer across hetero-interface. As shown in Figure 1.4 (b), 1L-WS₂ and Tc form a staggered type II band alignment. The conduction band minimum (CBM, -3.4 eV)¹²⁰ of

the 1L-WS₂ locates lower than the lowest unoccupied molecular orbital (LUMO, -2.4 eV)¹²¹ of Tc molecules allowing electron transfer from Tc to WS₂, whereas the valence band maximum (VBM, -5.8 eV)¹²⁰ of WS₂ lies lower than the highest occupied molecular orbital (HOMO, -5.4 eV)¹²¹ of Tc allowing hole transfer from WS₂ to Tc. Although a previous work presents ultrafast exciton dissociation in MoS₂-pentacene heterostructure on the time scale of 6.7 ps and the charge transfer states live as long as 5.1 ns¹¹², no direct experimental evidence of interlayer CT exciton has been provided. In photovoltaic devices based on 2D heterostructures, electrons and holes of CT excitons need to overcome large interlayer exciton binding energy to generate free electrons and holes leading to efficient photocurrent generation⁵². CT excitons diffusion is proposed to be essential for charge separation that requires further measurements to resolve this process.

CHAPTER 2. OPTICAL MICROSCOPY FOR TWO-DIMENSIONAL MATERIALS CHARACTERIZATION

This chapter is adapted with permission from Long Yuan, Ting-Fung Chung, Agnieszka Kuc, Yan Wan, Yang Xu, Yong P. Chen, Thomas Heine, and Libai Huang, *Science Advance*, 2018, 4, e1700324; Long Yuan and Libai Huang, *Nanoscale*, 2015, 7, 7402-7408; Tong Zhu, Long Yuan, Yan Zhao, Yan Wan, Jianguo Mei, Libai Huang, *Science Advance*, 2018, 4, eaao3104.

2.1 Ultrafast transient absorption microscopy

2.1.1 Description of ultrafast transient absorption microscopy

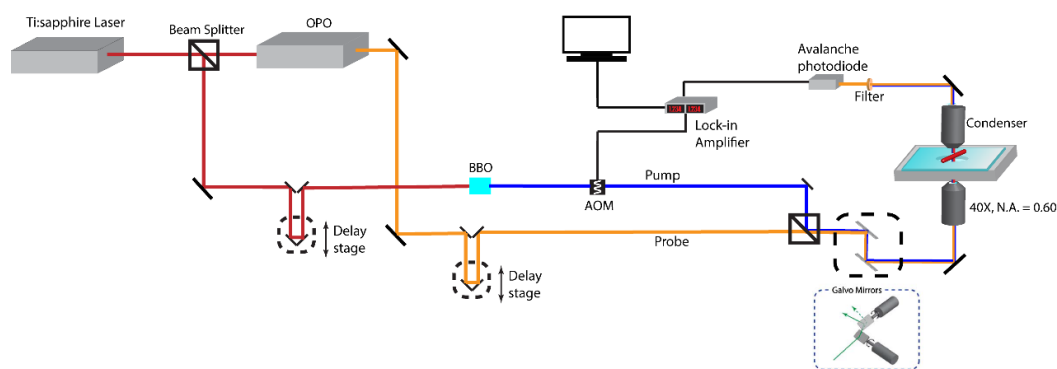


Figure 2.1 Schematics of TAM setup. OPO: optical parametric oscillator; AOM: acoustic optical modulator; BBO: beta barium borate.

Figure 2.1 displays a schematic diagram of home-built transient absorption microscopy (TAM) used in our work. Briefly, a Ti: Sapphire oscillator (Coherent Mira 900) pumped by a Verdi diode laser (Verdi V18) is used as the light source (output at 790 nm, 80 MHz repetition rate). 70% of the pulse energy is fed into the optical parametric oscillator (Coherent Mira OPO) to generate probe light between 610 and 640 nm, while the remaining 30% is doubled to 395 nm using a beta barium borate crystal. The pump beam is modulated at 1 MHz using an acoustic optical modulator (Model R21080-1DM, Gooch&Housego). An objective with high N.A. is used to focus both pump and probe beams onto the sample, and the reflection light is then collected by the same objective and detected by an avalanche

Si photodiode (Hamamatsu). The change in the probe reflection (ΔR) induced by the pump is detected by a lock-in amplifier (HF2LI, Zurich Instrument). For transient dynamics scans, pump beam and probe beam are overlapped spatially and a mechanical translation stage (Thorlabs, LTS300) is used to delay the probe with respect to the pump.

2.1.2 Transient absorption imaging

Typically, there are two common transient absorption imaging configurations: (1) morphological imaging; (2) exciton transport imaging. For morphological TAM imaging, pump beam and probe beam are overlapped spatially and a piezo-electric stage (P-527.3CI, Physik Instrumente) is used to scan the sample. For exciton transport imaging, the pump beam is fixed and a two-dimensional galvo mirror (GVS012, Thorlabs) is used to scan the probe beam relative to the pump beam in space to obtain the carrier propagation images.

2.1.3 Imaging exciton transport by transient absorption microscopy

To quantify exciton transport, exciton population as a function of space and time is described by a differential equation that includes both the transport out of the initial volume and population decay, which is given by,

$$\frac{\partial n(x,y,t)}{\partial t} = D \left[\frac{\partial^2 n(x,y,t)}{\partial x^2} + \frac{\partial^2 n(x,y,t)}{\partial y^2} \right] - \frac{n(x,y,t)}{\tau} \quad (1)$$

where $n(x, y, t)$ is the exciton population at time t , D is the exciton diffusion constant, and τ is the exciton lifetime. The initial population $n(x, y, 0)$ follows Gaussian distribution as created by a Gaussian pump beam at position (x_0, y_0) and is given by:

$$n(x, y, 0) = N \exp \left[-\frac{(x-x_0)^2}{2\sigma_{x,0}^2} - \frac{(y-x_0)^2}{2\sigma_{y,0}^2} \right] \quad (2)$$

Solution to Equation (1) indicates that exciton density at any later delay time (t) is also Gaussian and is described as:

$$n(x, y, t) = N \exp \left[-\frac{(x-x_0)^2}{2\sigma_{x,t}^2} - \frac{(y-y_0)^2}{2\sigma_{y,t}^2} \right] \quad (3)$$

The diffusion constant D is then given by:

$$D_{x(y)} = \frac{\sigma_{x(y),t}^2 - \sigma_{x(y),0}^2}{2t} \quad (4)$$

The exciton transport length, L , at delay time, t , is related to the variance of the exciton density profile and the exciton diffusion constant (D),

$$L_{x(y)}^2 = \sigma_{x(y),t}^2 - \sigma_{x(y),0}^2 = 2D_{x(y)}t \quad (5)$$

2.1.4 Factors that limit the spatial precision of exciton transport imaging

In the TAM imaging of exciton transport, the precision in determining the exciton propagation distance L is dictated by the smallest measurable change in the population profiles which is ~ 100 nm, and not directly by the diffraction limit. The measured carrier distribution is convoluted with profiles of both pump and probe beam so that the measured carrier distribution is written as:

$$\sigma_{(measurement)}^2 = \sigma_{(exciton)}^2 + \sigma_{(pump)}^2 + \sigma_{(probe)}^2 \quad (6)$$

The diffusion length of exciton propagation is written as:

$$L^2 = \sigma_{(t)}^2 - \sigma_{(0)}^2 \quad (7)$$

Since $\sigma_{(pump)}^2$ and $\sigma_{(probe)}^2$ don't change during pump-probe delay, the diffusion length is only determined by the change of carrier density profiles.

Here we perform a sensitivity analysis by differentiating equation 7 and obtain the error of measured diffusion length written as:

$$\Delta L = \sqrt{\frac{\sigma_{(t)}^2}{\sigma_{(t)}^2 - \sigma_{(0)}^2} (\Delta\sigma_{(t)}^2)^2 + \frac{\sigma_{(0)}^2}{\sigma_{(t)}^2 - \sigma_{(0)}^2} (\Delta\sigma_{(0)}^2)^2} = \sqrt{\Delta\sigma_{(t)}^2 + \left(\frac{\sigma_{(0)}}{L}\right)^2 (\Delta\sigma_{(0)}^2 - \Delta\sigma_{(t)}^2)} \quad (8)$$

From equation (8), we clearly see the error mainly comes from the uncertainty of Gaussian profiles obtained at different time delays, which is determined by the signal-to-noise of the TAM system.

2.1.5 Noise analysis

There are two main sources of noise contributing to TAM imaging: laser fluctuation noise and electronic noise from the detection system (for example, detector and lock-in amplifier). Noise due to laser intensity fluctuations can be effectively eliminated by using heterodyne lock-in detection with MHz modulation¹²² where the intensity of the excitation beam (or additional local oscillator) is modulated by an acoustic-optical modulator. Subsequently, a lock-in amplifier referenced to this modulation frequency can sensitively extract the induced signal. The fluctuation of laser intensity ($\frac{1}{f}$ noise) usually occurs at low frequency (< 10 kHz). When f is in the MHz range, the laser intensity noise becomes near the quantum shot noise limit, which is always present because of the Poissonian distribution of the photon counts at the detector. The pixel dwell time should be significantly longer than the modulation period to allow for reliable demodulation for each pixel. Such a modulation scheme has been successfully applied to transient absorption microscopy to achieve single-molecule sensitivity. In our experiments, we use a modulation frequency of 1 MHz. The TAM instrumentation described here is capable of detecting a differential transmission $\Delta T/T$ of 10^{-7} , three orders of magnitude higher sensitivity than conventional TA spectroscopy¹²³.

2.2 Transient absorption spectroscopy

The TA spectrum and dynamics are acquired by a home-built, femtosecond transient absorption spectroscopy setup as shown in Figure 2.2. The output of a high repetition rate amplifier (PHAROS Light Conversion Ltd., FWHM = 200 fs, 400 kHz repetition rate, pulse energy of 100 μ J, 1030 nm fundamentals) is split into two parts. One part is fed to an optical parametric amplifier (OPA, TOPAS-Twins, Light Conversion Ltd) to generate a 400 nm pump beam. The white light continuum (450 nm – 850 nm) is obtained by focusing the remaining part onto a Yttrium Aluminum Garnet (YAG) crystal. An optical chopper (MC2000B, Thorlabs) is employed to modulate the pump beam with a frequency of 195 Hz. Both pump and probe beams are focused on the sample and spatially overlapped. The probe light is then collected by a lens and focused on a CCD spectrometer (Exemplar LS, B&W Tek). For transient dynamics scans, the probe beam is delayed relative to the pump beam by a linear stepper motor stage (ILS100PP, Newport).

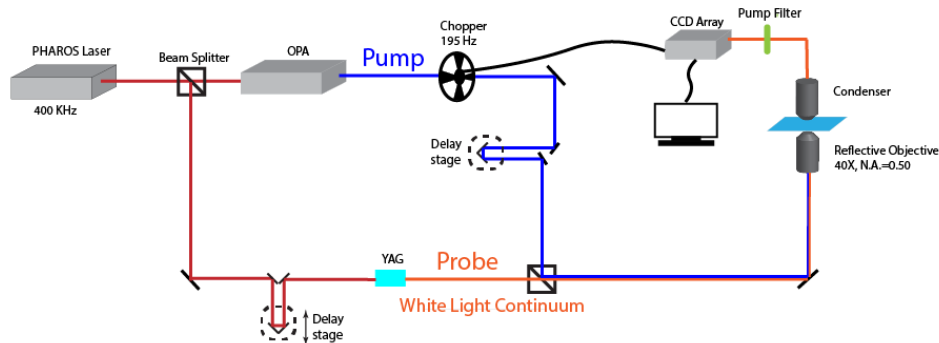


Figure 2.2 Schematics of transient absorption spectroscopy setup. OPA: optical parametric amplifier; YAG: Yttrium aluminum garnet; CCD: charge-coupled device.

2.3 Confocal photoluminescence microscopy

Steady-state photoluminescence (PL) and time-resolved PL measurements are performed by employing a home-built confocal micro-PL setup (Figure 2.3). A picosecond pulsed diode laser (PicoQuant, LDH-P-C-450B) with an excitation wavelength of 447 nm (Full width at half maxima (FWHM) = 50 ps) and a repetition rate of 40 MHz is used to excite the sample, which is focused by a 100 \times (NA = 0.95) objective. The beam size in PL measurements is less than 1 μm . The PL emission is collected with the same objective, dispersed with a monochromator (Andor Technology) and detected by a TE-cooled charge-coupled device (Andor Technology). To construct a PL image, a two-dimensional galvo mirror (GVS012, Thorlabs) is used to scan the beam. A single photon avalanche diode (PicoQuant, PDM series) is used to collect the PL emission signal, the dynamics of PL are measured using the single photon avalanche diode. The temporal resolution is about 100 ps.

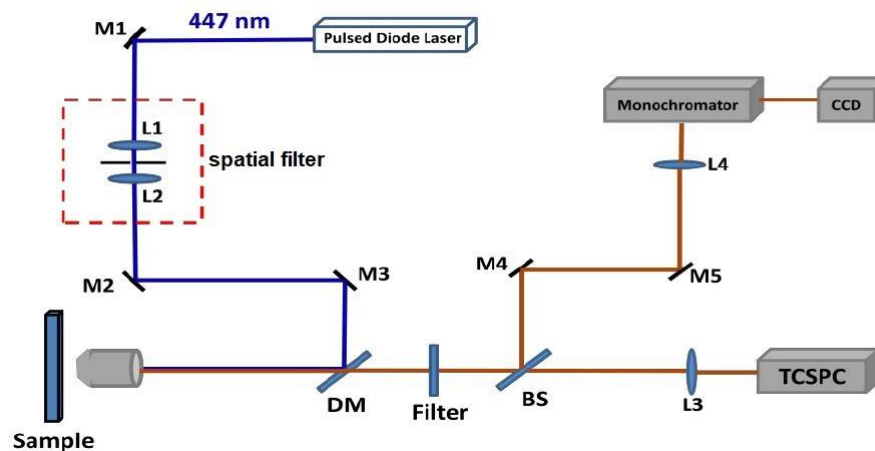


Figure 2.3 Schematic illustration of home-built confocal PL microscopy. DM: dichroic mirror; BS: beam splitter; TCSPC: time-correlated single photon counting; CCD: charge-coupled device.

2.4 Confocal Raman microscopy

Raman spectra are collected using a Renishaw Raman microscope (RM1000) equipped with an argon-ion laser at 514 nm as an excitation source. The excitation beam is focused using a 50 \times (NA = 0.75) objective, and the Raman scattered light is collected with the same objective. The beam size in Raman measurements is about 1 μm .

2.5 Differential reflection microscopy

Differential reflection spectrum is obtained by using a home-built micro-reflection setup (Figure 2.4). Briefly, the white light from a stabilized tungsten-halogen light source (Thorlabs) is focused into a pinhole with 10 μm diameter. It is then collimated and focused on the sample with a 50 \times /NA = 0.95 objective. The beam size is about 3 μm . The reflected light is collected with the same objective, dispersed with a monochromator (Andor Technology) and detected by a TE-cooled charge-coupled device (CCD) (Andor Technology).

The differential reflectance is defined as:

$$\delta R(\lambda) = \frac{R_{sample} - R_{substrate}}{R_{substrate}} \quad (9)$$

where R_{sample} is the reflectance intensity of sample the with substrate and $R_{substrate}$ is the reflectance intensity of bare substrate. For the ultrathin film on a transparent substrate, the differential reflection is directly related to the absorption by the following equation^{10, 124}:

$$\delta R(\lambda) = \frac{4}{n_{sub}^2 - 1} A(\lambda) \quad (10)$$

where n_{sub} is the refractive index of substrate and $A(\lambda)$ is the absorption coefficient.

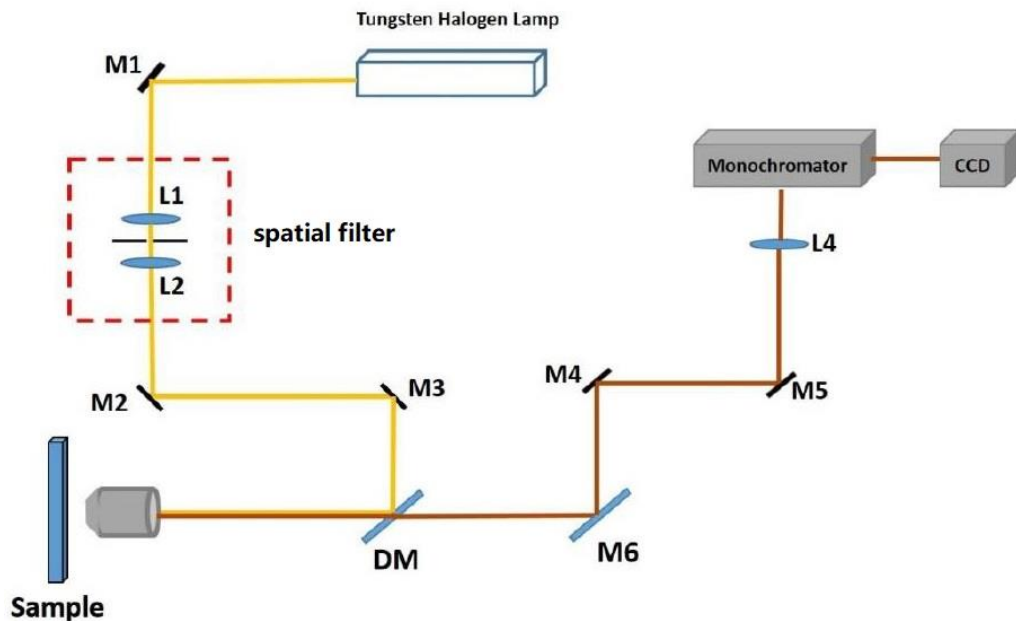


Figure 2.4 Schematic illustration of home-built differential reflection microscopy. DM: dichroic mirror; TCSPC: time-correlated single photon counting; CCD: charge-coupled device.

CHAPTER 3. EXCITON DYNAMICS AND ANNIHILATION IN TWO-DIMENSIONAL SEMICONDUCTORS

This chapter is adapted with permission from Long Yuan and Libai Huang, *Nanoscale*, 2015, 7, 7402-7408.

3.1 Abstract

In this chapter, we investigate exciton dynamics and many-body exciton interactions in exfoliated WS₂ monolayer, bilayer, and trilayer. We choose WS₂ as a model system because of the relatively low defect density in WS₂ as manifested by the higher photoluminescence (PL) quantum yield (QY) than other 2D semiconductors (~6% in WS₂, compared to ~0.1% of MoS₂). We measure exciton dynamics in both low and high exciton density regimes. At low exciton density regime, we discuss how the equilibrium between the bright and dark exciton populations affects exciton lifetimes. At high exciton density regime, we demonstrate that exciton-exciton annihilation in the monolayer is significantly enhanced compared with those in the bilayer and trilayer because of enhanced many-body interactions and different annihilation mechanisms for direct and indirect excitons.

3.2 Background

3.2.1 Exciton in two-dimensional transition metal dichalcogenides

Recently, semiconducting atomically thin layers of transition metal dichalcogenides (TMDs) such as MoS₂, MoSe₂, WS₂, and WSe₂ have attracted much research interest due to their unique electronic structures and optical properties.^{2, 12} These properties led to potential applications in optoelectronics and electronics^{15, 125}, including field-effect transistors^{20, 30, 126-128}, atomically thin photovoltaic devices^{59-60, 129} and ultrasensitive photodetectors.^{21, 130}

One of the unique properties of these atomically-thin 2D semiconductors is indirect to direct bandgap transition and the extraordinarily large exciton binding energy at the monolayer limit.⁷⁻⁸ The atomically-thin nature of the monolayer also leads to a strong enhancement of the Coulomb interaction between the electron and the hole. Recent theoretical calculations and experimental measurements showed that the exciton binding energy is around a few hundreds of meV for the TMD monolayers which is an order of magnitude larger than other previously investigated 2D excitonic structures, such as quantum wells.^{42, 45, 49, 131-133} As a result, excitons dominate the optical and electrical properties of these materials.

Exciton fine structure in monolayers of TMDCs results from strong spin-orbit coupling, broken inversion symmetry, and quantum confinement effects. As the number of layers reduces to Valance band edge splits into two spin-polarized bands at inequivalent valleys (K/K') in the Brillouin zone due to strong spin-orbit coupling effect¹³⁴, which has an energy difference of a few hundred meV.^{39, 131, 135-137} Spin-orbit coupling also leads to a splitting in the conduction band, albeit much smaller, from several meV to tens of meV, leading to close-lying spin-allowed bright and spin-forbidden dark exciton levels.¹³⁸⁻¹⁴³

3.2.2 Bright and dark exciton dynamics

Exciton dynamics in monolayers TMDCs have been extensively studied¹⁴⁴⁻¹⁵², however, the interpretation of these measurements varies with exciton lifetime ranging from a few picoseconds to nanoseconds.¹⁵⁰ Dark and bright exciton states are expected to play a key role in the dynamics of the 2D excitons^{140, 153}, however, how such exciton fine structure affects dynamics is not fully addressed in current literature. Because the dark states could lie either above or below the bright states depending on the materials^{139, 153},

the lack the understanding the dark states are likely one of the reasons for the wide-spread of exciton lifetimes measured. For instance, time-resolved PL spectroscopy and TA spectroscopy, the two most widely used tools to study exciton dynamics, are sensitive to different exciton populations. Both experimental and theoretical efforts to address the dynamics of dark and bright excitons will be necessary for realizing electronic and optoelectronic applications of TMDCs.

3.2.3 Many-body exciton interaction

Due to the reduced dimensionality in the two-dimensional electronic system, many-body interaction is greatly enhanced compared with the bulk phase. Upon the generation of a high density of electrons and holes, many-body scattering processes such as Auger recombination and exciton-exciton annihilation play an important role in nonradiative relaxation. Exciton-exciton annihilation and Auger recombination have been intensively investigated in quantum dots¹⁵⁴⁻¹⁵⁵, carbon nanotubes¹⁵⁶⁻¹⁵⁷, and semiconductor nanowires.¹⁵⁸⁻¹⁶⁰ While recent studies on MoS₂, MoSe₂, and WSe₂ monolayers have shown the existence of exciton-exciton annihilation at high excitation density, how quantum confinement of 2D excitons impacts the many-body exciton interaction is still elusive.^{106, 145, 161-165}

In this chapter, we investigate exciton dynamics and many-body exciton interactions in monolayered, bilayered, and trilayered exfoliated WS₂. We choose WS₂ as a model system because of the relatively low defect density as manifested by the higher photoluminescence (PL) quantum yield (QY) than other 2D semiconductors (~6% in WS₂, compared to ~0.1% of MoS₂). We discuss the intrinsic and extrinsic factors that control exciton dynamics in 2D TMDCs. First, we present how the equilibrium between the bright

and dark exciton populations affects exciton lifetimes. Second, we address how the environmental factors, such as defects and charged impurities, impact the dynamics of the excitons. Finally, we examine the exciton-exciton annihilation process at high exciton density regime that plays an important role in determining the non-radiative recombination rate in the high exciton density regime.

3.3 Experiential methods

3.3.1 Preparation of WS₂ monolayers and few-layer samples

We use a standard micromechanical cleavage method (commonly referred as “scotch-tape technique”) to exfoliate WS₂ monolayer and few-layer samples from bulk WS₂ crystals (2D semiconductors) onto Si wafer with 90 nm oxide thickness (Graphene Supermarket). The number of layers of WS₂ flakes is identified by optical contrast and further confirmed by Raman and steady-state PL spectroscopy.¹²⁰

3.3.2 Determination of quantum yield of WS₂ monolayers and few-layers

We measured the QY of WS₂ monolayer, bilayer, and trilayer following the method referring in a previous study.⁷ We used a calibrated reference consisting of a thin film of rhodamine-6G dye molecules. The films were prepared by spin coating a glass substrate with a concentrated methanol solution of rhodamine-6G. We firstly calibrated the absolute QY of our reference film using the methanol solution of rhodamine-6G, which has a quantum yield of 100%. With this reference, we then determined the QY of WS₂ flakes.

3.3.3 Determination of exciton density

In our PL experiments, excitons in WS₂ are generated by the absorption of the pump laser. The peak fluence of pump pulse (P_f) could be calculated as:

$$P_f = \frac{P}{A} \quad (1)$$

where P is the pump pulse energy, A is the pump excitation effective area. Since pump pulse is a Gaussian beam. To calculate the exciton density injected by the pump pulse, we assume that every absorbed pump photon could create one exciton. Then, the injected exciton density could be obtained as:

$$N = \frac{\alpha P_f}{\hbar\nu} \quad (2)$$

where α and $\hbar\nu$ are the absorption coefficient and photon energy of the pump pulse.

3.4 Results and discussion

3.4.1 Optical characterization of WS₂ with different thickness

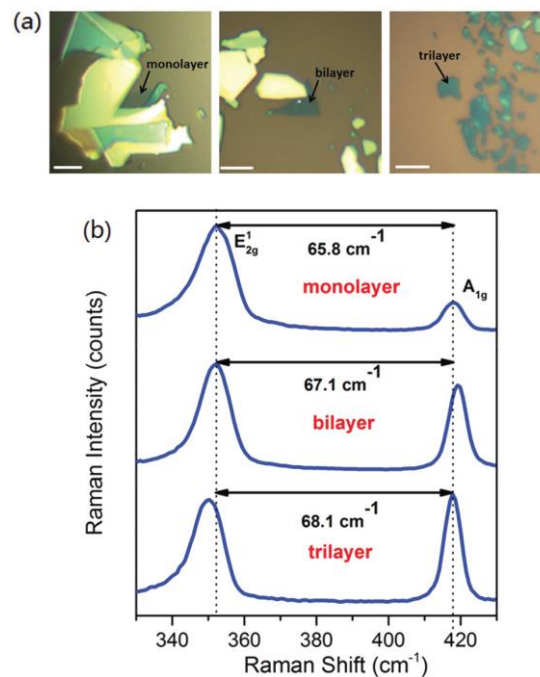


Figure 3.1 (a) Optical image of WS₂ monolayer, bilayer, and trilayer flakes on Si wafer with 90 nm oxide thickness; (b) Raman spectra of WS₂ monolayer, bilayer, and trilayer flakes. The scale bar represents 5 μm. The dashed lines mark the position of the E_{2g}¹ and A_{1g} positions for the monolayer.

We first identified the number of layers in exfoliated WS₂ samples by optical contrast and then confirmed by Raman and PL microscopy.¹²⁰ Figure 3.1 (a) displays optical images of WS₂ monolayer, bilayer, and trilayer samples. There are two characteristic Raman modes corresponding to the E_{2g}^1 (in-plane vibration) and A_{1g} (out-of-plane vibration) in WS₂ as shown in Figure 3.1 (b). The frequency of these two modes is around 352 cm⁻¹ and 418 cm⁻¹, respectively. The frequency difference between E_{2g}^1 and A_{1g} is dependent on the thickness and is used to identify the number of layers. Here, we obtain the frequency difference between E_{2g}^1 and A_{1g} modes of 65.8 cm⁻¹, 67.1 cm⁻¹, and 68.1 cm⁻¹ which are corresponding to the monolayer, bilayer, and trilayer, respectively.¹²⁰

Figure 3.2 (a) displays the reflective spectrum of 1L-WS₂ which clearly shows three excitonic transitions labeled as A, B, and C.¹⁰ A and B excitons are located around 615 nm and 515 nm that are originated from direct band transitions at the K -point as shown in Figure 3.2 (b). The energy difference (0.38 eV) between A and B excitonic transitions is originated from the large spin-orbit coupling in the valence band.¹⁰ C exciton emission is located around 437 nm that is attributed to the optical transitions between the density of states peaks in the valence and conduction bands also referred as band nesting effect.¹⁴⁵

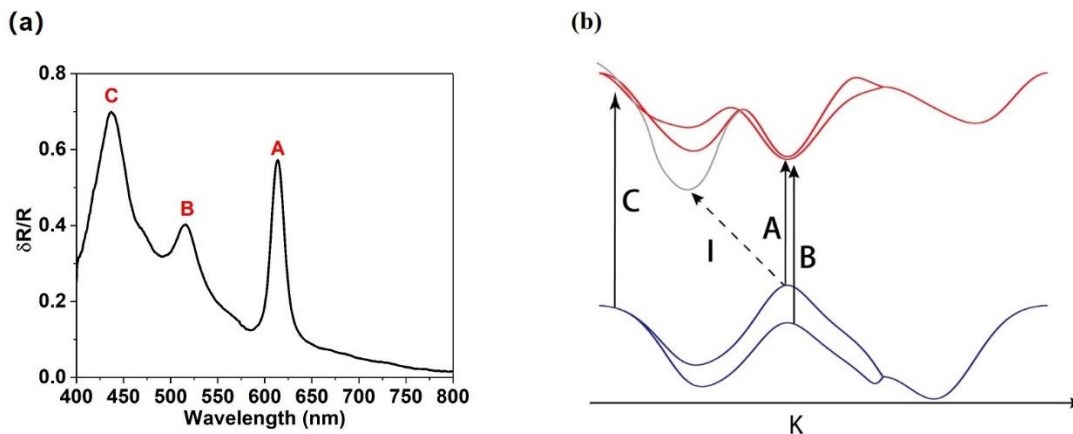


Figure 3.2 (a) Differential reflectance spectrum of 1L-WS₂. (b) Schematic drawing of the band structure of 1L-WS₂ and multilayer WS₂, with arrows indicating A, B, C, and I excitons.

The PL spectra of WS₂ monolayer, bilayer, and trilayer are shown in Fig. 3.3(a). In the WS₂ monolayer, we observed a single sharp peak locating around 615 nm which is attributed to direct band transition between conduction band minimum (CBM) and valence band maximum (VBM) at the *K*-point. We also performed PL measurements on different WS₂ monolayer flakes and didn't observe significant peak energy difference as shown in Figure 3.3 (b). In contrast, PL emission from WS₂ bilayer and trilayer display an additional broad with lower emission energies that are corresponding to the indirect exciton recombination where VBM remains at the *K*-point but the CBM is between the *K*- and Γ -points as shown in Figure 3.2 (b). The QY of WS₂ monolayer, bilayer, and trilayer are determined to be $\sim 6 \times 10^{-2}$, 1×10^{-3} , and 4×10^{-4} , respectively. The quantum yield of WS₂ bilayer and trilayer is over two orders of magnitude lower than the WS₂ monolayer which is consistent with the indirect to direct exciton transition at the monolayer limit.^{7-8, 10, 166}

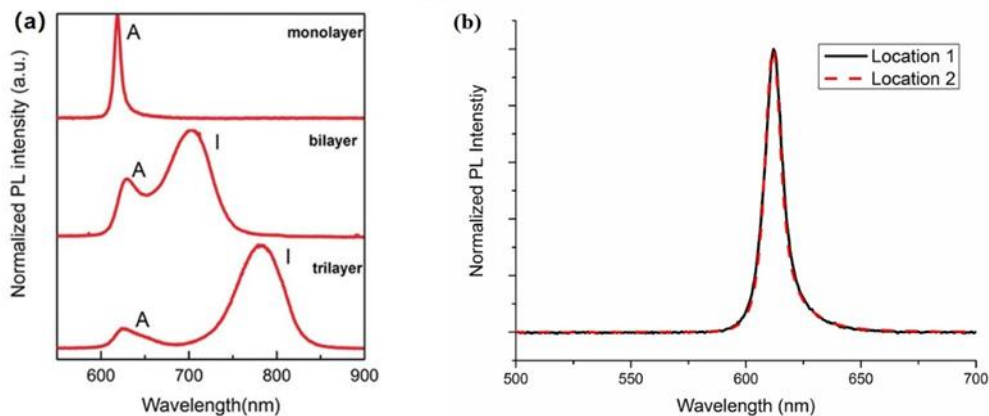


Figure 3.3 (a) PL spectra of WS₂ monolayer, bilayer, and trilayer. (b) PL spectrum at different locations for monolayer WS₂.

In WS₂ monolayer, due to the strong Coulomb interaction, neutral exciton could bound with excess electrons or holes to form a trion with binding energy around 20 meV.^{9, 167-168} The trion binding energy is comparable with $k_b T$ at room temperature which implies that trions can be dissociated by thermal energy. From the emission spectrum of WS₂ monolayer as shown in Figure 3.3 (a), we didn't observe a significant trion contribution indicating PL emission is dominated by the neutral exciton recombination.

3.4.2 Exciton dynamics of WS₂ without the effect of exciton-exciton annihilation

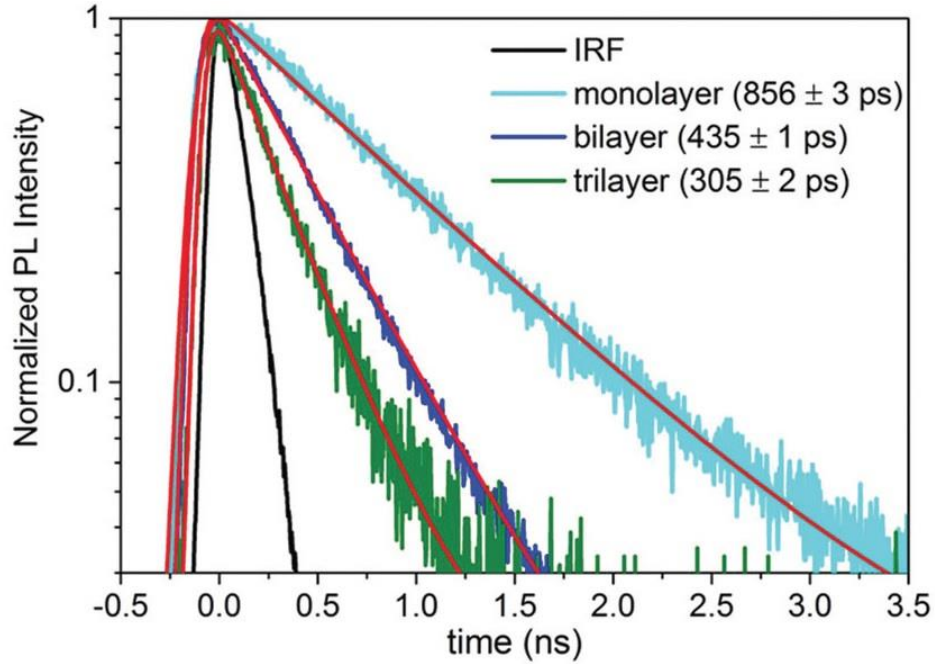


Figure 3.4 PL decay without exciton-exciton annihilation for WS₂ monolayer, bilayer, and trilayer at a pump intensity of 5 nJ cm^{-2} , $0.1 \text{ } \mu\text{J cm}^{-2}$, and $0.4 \text{ } \mu\text{J cm}^{-2}$, respectively. The photoluminescence lifetime measurements integrate the entire PL spectra from 500 nm to 850 nm. The black line is the instrument response function (IRF). The red lines are the fitting curves using a single exponential decay convoluted with a Gaussian response function.

To obtain the exciton dynamics without the effect of exciton-exciton annihilation, we first measured the PL dynamics at low exciton density by using a home-built confocal PL microscope with a time-resolved single-photon counting photodiode. The PL decay of monolayer, bilayer, and trilayer are shown in Figure 3.4. We employ a single exponential decay convoluted with a Gaussian instrument response function (IRF) to fit the PL dynamics. The equation is described as:

$$I(t) = \int_{-\infty}^t \text{IRF}(t') e^{-\frac{t-t'}{\tau}} dt \quad (3)$$

We obtained PL lifetimes of 856 ± 3 ps, 435 ± 1 ps, and 305 ± 2 ps for WS₂ monolayer, bilayer, and trilayer respectively. We also measured PL dynamics at different locations as shown in Figure 3.5. It displays a minor difference from position to position due to the variance in the local environments. The average PL lifetimes for monolayer, bilayer, and trilayer are measured to be 806 ± 37 ps, 401 ± 25 ps, and 332 ± 19 ps.

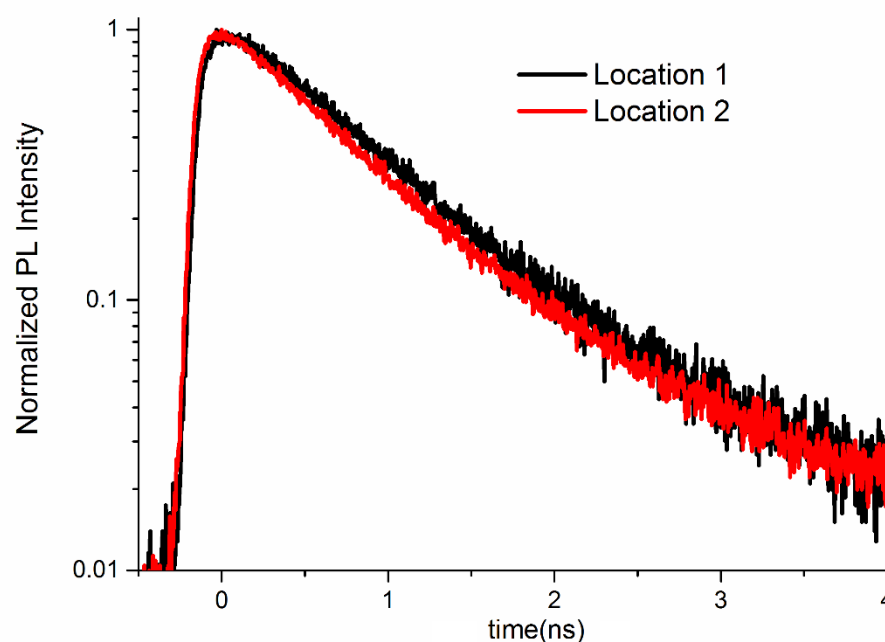


Figure 3.5 PL dynamics for WS₂ monolayer at different locations at the pump intensity of 5 nJ/cm^2 .

The single exponential of hundreds of ps PL decay is in direct contrast with the complex multi-exponential decay observed for MoS₂.^{144, 163, 169} Single exponential decay behavior implies that PL originates from a single state, indicative that other energy levels such as trap states induced by defects are not as significant in WS₂ in comparison with

MoS₂. Lower defect density is consistent with much higher PL quantum yield (~6%) of monolayered WS₂ than that of monolayered MoS₂ (~10⁻³).

We could relate the observed PL lifetime, τ_{ob} to the radiative and non-radiative lifetimes, τ_r and τ_{nr} , respectively, by the follow equation:

$$\frac{1}{\tau_{ob}} = \frac{1}{\tau_r} + \frac{1}{\tau_{nr}} \quad (4)$$

τ_r is related to τ_{ob} by the quantum yield (ϕ_{PL}):

$$\phi_{PL} = \frac{\tau_{ob}}{\tau_r} \quad (5)$$

For WS₂ monolayer, using the QY of $\sim 6 \times 10^{-2}$ and a τ_{ob} of ~ 806 ps, we could determine the radiative and non-radiative lifetimes to be ~ 13 ns and ~ 900 ps respectively. For WS₂ bilayer, the radiative and non-radiative lifetimes are determined to be ~ 400 ns and ~ 400 ps using the QY of $\sim 6 \times 10^{-2}$ and a τ_{ob} of ~ 401 ps. For WS₂ trilayer, the radiative and non-radiative lifetimes are determined to be ~ 830 ns and ~ 300 ps using the QY of $\sim 4 \times 10^{-4}$ and a τ_{ob} of ~ 332 ps. We observe much longer radiative lifetimes in bilayer and trilayer than monolayer due to the nature of indirect band transition. The low quantum yield of bilayer and trilayer indicates that non-radiative recombination dominates the exciton relaxation pathway. Interestingly, although the non-radiative lifetimes for both bilayer and trilayer are the same order as the monolayer, it decreases with the number of layers. One possible explanation is that nonradiative pathways are similar in nature for the monolayer, bilayer and trilayer related to electron–phonon scattering. The thickness dependence of the nonradiative lifetime is likely to be related to changes in dielectric environments.

3.4.3 Bright and dark exciton fine structure and dynamics

Recent evidences for the existence of the spin-forbidden dark excitons¹³⁹⁻¹⁴⁰ suggest that they will be critical in understanding exciton dynamics. For instance, the relaxation to the dark exciton levels has found to be important for systems such as single-walled carbon nanotubes.¹⁷⁰⁻¹⁷² In the following, we summarize current literatures on bright and dark exciton dynamics and discuss how the population equilibrium between the bright and dark states could affect exciton lifetime.

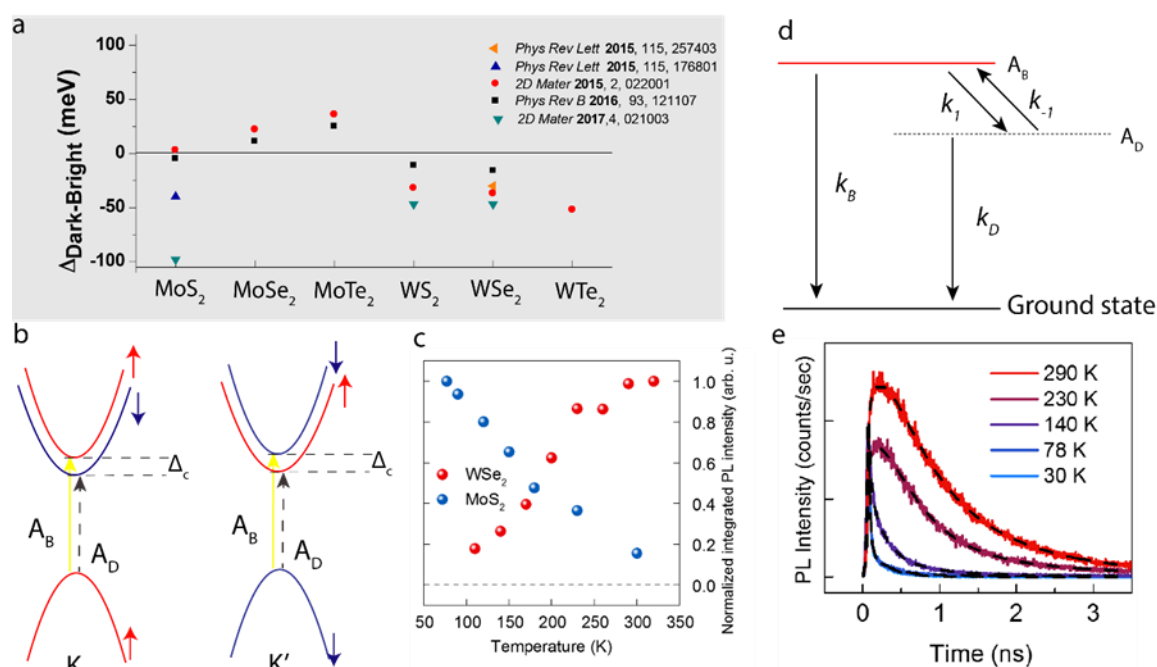


Figure 3.6 (a) Summary of literature reported bright-dark exciton energy splitting for TMDC monolayers, including both experimental and theoretical values. (b) Schematic illustration of the spin allowed bright exciton (A_B) and spin forbidden dark exciton (A_D) in W-based TMDCs at the K and K' valley. Δ_c is the bright-dark exciton energy splitting. (c) Comparison of the temperature dependence of the time-integrated PL intensity of WSe₂ and MoS₂. (d) A kinetic model for the dynamics of the bright and dark excitons. (e) Temperature-dependent PL lifetime from a suspended monolayer of WSe₂.

The conduction bands near the K and K' points are mainly from the d_{z^2} orbitals of metal atoms and no splitting is expected when considering only the d_{z^2} orbitals.¹³⁶

However, the chalcogen orbitals and higher order couplings to other orbitals of metal atoms also play a role, leading to a spin splitting of 10s meV in the conduction bands. Because the competition between these two effects, the sign of this conduction band splitting differs among the different TMDCs.¹³⁹⁻¹⁴⁰ For WX_2 ($X = S, Se, Te$), the lowest energy exciton is a dark state. For $MoSe_2$ and $MoTe_2$, on the other hand, electrons in the conduction band minimum (CBM) are expected to have the same sign polarization with holes in the valence band maximum (VBM), leading to a bright state as the lowest exciton energy level.^{142, 173} The case for MoS_2 is currently under debate: some concluded the bright exciton being the lowest level with a small splitting of a few meV,¹³⁹ while other inferred a dark exciton with energy as much as ~ 100 meV below the bright exciton.¹⁴¹ The conduction band splitting Δ_c for different TMDC materials is summarized in Figure 3.6 (a).^{136, 138, 140-141} Because of the splitting in the conduction band, there are two intravalley bright (singlet-like) excitons (A_B) and two intravalley spin-forbidden (triplet-like) “dark” excitons (A_D) as schematically depicted in Figure 3.6 (b), one of each at the K and K' valleys. There are also additional 4 intervalley dark excitons.¹⁴⁰

Zhang *et al.* first verified experimentally the existence of the dark exciton states in WSe_2 using temperature-dependent steady-state and time-resolved PL measurements.¹⁴⁰

The population of A_B and A_D (N_{A_B} and N_{A_D}) obey the Boltzmann distribution as given by

$$\frac{N_{A_B}}{N_{A_D}} = e^{-\frac{\Delta_c}{k_b T}}$$

PL intensity for WSe_2 decreases as temperature decreases, indicative of the

lowest exciton level being a dark state (Figure 3.6 (c)). On the contrary, PL intensity for MoS_2 increases as temperature decreases, implying the lowest exciton level being a bright state. The splitting in the conduction band Δ_c is ~ 30 meV for 1L- WSe_2 determined experimentally by Zhang *et al.*¹⁴⁰ More recently, Molas *et al.* demonstrated that the dark

excitons indeed could be brightened by an in-plane magnetic field, further validating the existence of spin-forbidden dark excitons.¹⁴¹

Bright excitons can relax to the dark state either by spin-conserving intervalley electron scattering between the K and K' valleys or by the spin-flip of the electron within the same valley.¹⁴⁰ Intervalley scattering on time scale of ps has been indicated by time-resolved spectroscopy measurements, suggesting the relaxation to the dark state *via* this pathway could be very rapid.¹⁷⁴ While spin-flip should be slow in a perfect monolayer, literature on carbon nanotube suggested that coupling to the environment, structural distortions, and defects could enhance this process.¹⁷⁰

Taking into account the scattering of populations between the two states (schematically shown in Figure 3.6 (d)), the dynamics of the bright and dark exciton states can be described by the following two coupled rate equations:

$$\frac{dN_{AB}}{dt} = -k_B N_{AB} - k_1 N_{AB} + k_{-1} N_{AD} \quad (6)$$

$$\frac{dN_{AD}}{dt} = -k_D N_{AD} - k_{-1} N_{AD} + k_1 N_{AB} \quad (7)$$

where k_B (k_D) is the relaxation rate of the bright (dark) state to the ground state, and $k_{1(-1)}$ is the rate for converting from the bright (dark) to the dark (bright) state. k_1 and k_{-1} are related by population equilibrium as given by $\frac{k_{-1}}{k_1} = \frac{N_{AB}}{N_{AD}} = e^{-\frac{\Delta_C}{k_b T}}$. When $k_1, k_{-1} \gg k_B \gg k_D$, the solution can be simplified to:

$$N_{AB} \sim e^{-(k_1+k_{-1})t} + \frac{k_{-1}}{k_1} e^{-(k_D+\frac{k_{-1}k_B}{k_1})t} \quad (8)$$

$$N_{AD} \sim -e^{-(k_1+k_{-1})t} + e^{-(k_D+\frac{k_{-1}k_B}{k_1})t} \quad (9)$$

Therefore, the population dynamics of the bright state should consist of two exponential decays, while there are an exponential rise and an exponential decay for the dynamics of the dark state. Recently, a similar rate equation model has been applied to explain the variation in the observed degree of circular polarization of the PL emission in different TMDCs monolayers, suggesting sub-picosecond relaxation from the bright to the dark state.¹⁴²

The fast relaxation from the bright to the dark exciton level in WSe₂ can also be inferred by the temperature-dependent PL lifetime measurements by Zhang *et al.*, which showed the fast decay component (< 10 ps) increased as temperature decreased (Figure 3.6 (e)) while the slow decay component (60 ps – 1 ns) decreased.¹⁴⁰ They attributed the fast decay to hot PL emission from the bright A excitons.¹⁴⁰ This observation is consistent with equation (8) because $\frac{k_{-1}}{k_1}$ approaches 0 at very low temperature (e.g. $\frac{k_{-1}}{k_1} \approx 10^{-16}$ at T = 10 K) and the bright exciton dynamics can be approximated by $e^{-k_1 t}$, suggesting picosecond relaxation to the dark state.

These recent measurements suggest that the relaxation of the bright excitons to the dark state could be very rapid, probably on the picosecond or faster time scale.^{140, 142} Because of the much longer lifetime, the dark exciton level could serve as a reservoir for exciton population for W-based TMDCs at room temperature.¹⁴² The population dynamics between the bright and dark states should be taken into account to correctly evaluate exciton radiative and non-radiative rates, similar to what has been done for single-walled carbon nanotubes.

3.4.4 Defect-assisted recombination in exciton dynamics

Besides the intrinsic relaxation to the dark exciton state discussed in the last section, extrinsic environmental factors such as defects also contribute significantly to the nonradiative pathways.¹⁷⁵ As indicated by the relatively low QY in monolayer TMDCs, nonradiative rather than radiative relaxation pathways dominate the dynamics. There are recent successes in improving the PL quantum yields by various surface passivation techniques¹⁷⁶⁻¹⁷⁹, however, the detailed mechanisms are still under debate, further pointing to the importance of the role of defects in exciton dynamics.

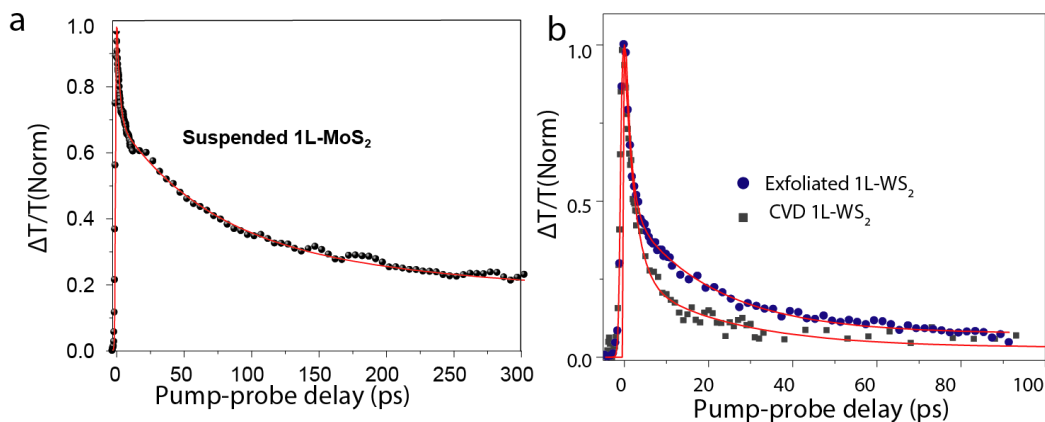


Figure 3.7 (a) TA dynamics of a suspended exfoliated 1L-MoS₂ flake. Redline is a fit using a triexponential function convoluted with an experimental response function. Pump fluence is 0.6 μJcm^{-2} . (b) TA dynamics of exfoliated 1L-WS₂ on SiO₂ substrate and CVD 1L-WS₂ on sapphire. Red lines are fits using a biexponential function convoluted with an experimental response function. Pump fluence is 1 μJcm^{-2} .

We have measured the transient absorption decay of A exciton in a suspended MoS₂ monolayer¹⁶⁹, which displays multi-exponential behavior implying more than one relaxation process is involved (Figure 3.7 (a)). Since the initial fast decay (2 – 4 ps) do not exhibit strong power dependence under pump fluences $<1.3 \mu\text{Jcm}^{-2}$ (pump wavelength = 400 nm) it is reasonable to rule out the effect of exciton-exciton annihilation in the results

presented here.¹⁶⁹ We attribute the fast ps decay to defect-assisted recombination.¹⁶⁹ For monolayer TMDCs, essentially all atoms are on the surface or at the interfaces, hence the number of surfaces and interfacial defects per atom is greatly enhanced compared to the thick crystal, thus increasing the probability of the defect scattering processes. More recently, the role of defect-assisted non-radiative recombination in MoS₂ is further investigated by Wang *et al.*¹⁴⁷ They have concluded that there are two stages of defect-assisted recombination; a fast pathway within 1–2 ps and slow recombination on a 60–70 ps time scale.¹⁴⁷

Defect-related relaxation pathways also lead to variations of exciton dynamics for samples fabricated by different methods. Figure 3.7 (b) shows the TA dynamics measured in a mechanical exfoliated and chemical vapor deposition (CVD) grown 1L-WS₂ flakes. Initial exciton decay (< 5 ps) is similar for the exfoliated and the CVD grown 1L-WS₂, indicating relaxation to the dark exciton level might dominate at this timescale. At timescale > 5 ps, faster exciton decay for the CVD grown is observed with an additional decay constant of ~ 10 ps, indicating that defect-related recombination pathways are more prevalent for the CVD grown samples. This is consistent with that defect density in CVD WS₂ ($\sim 3 \times 10^{13} \text{ cm}^{-2}$)¹⁸⁰ is four orders of magnitude higher than exfoliated WS₂ ($\sim 2 \times 10^9 \text{ cm}^{-2}$)¹⁸¹.

3.4.5 Exciton dynamics of WS₂ with the effect of exciton-exciton annihilation

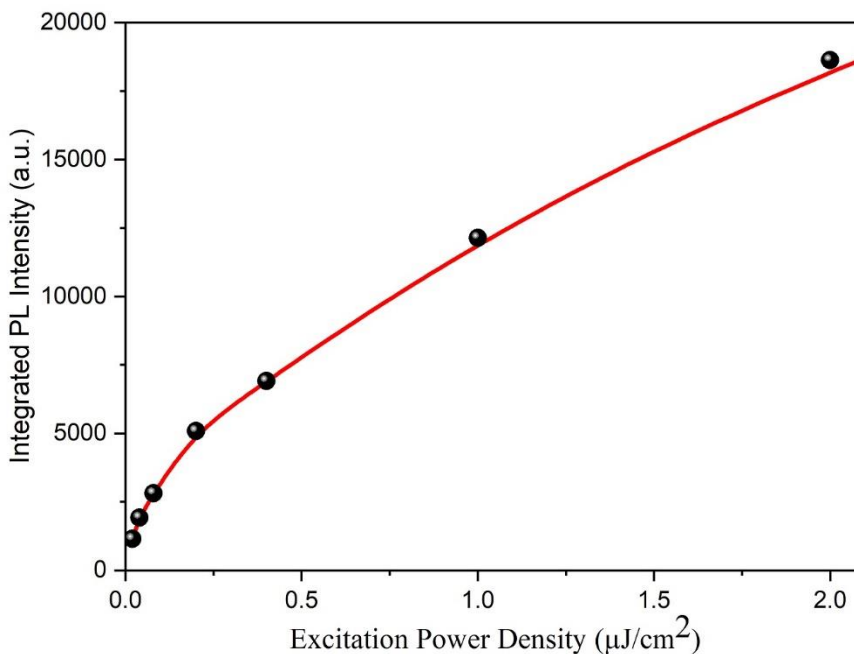


Figure 3.8 Integrated PL intensity for WS₂ monolayer as a function of pump intensity. The red line is a guide.

We first look at the PL emission intensity of 1L-WS₂ at high excitation density. It is obvious to see that the integrated PL intensity of 1L-WS₂ deviates from linear behavior at high pump intensities, as shown in Figure 3.8. We also study the exciton dynamics in the non-linear regime with high exciton density. As shown in Figure 3.9, in WS₂ monolayer, the PL dynamics is strongly dependent on exciton density. As the pump intensity increases, a faster decay component appears. In contrast, for WS₂ bilayer and trilayer, such an excitation density dependence is observed but not as significant as the monolayer. The fast dynamics along with the saturation of PL intensity at high exciton densities can be explained by Auger recombination or exciton-exciton annihilation. Typically, exciton-exciton annihilation is a scattering mechanism in which two excitons interact with each other, with one of them undergoing nonradiative recombination and transferring its energy

to another exciton that is then excited to a high-energy continuum state. Subsequently, the excited exciton undergoes thermal relaxation without emitting light. Another possible mechanism is the formation of biexciton that could occur at high exciton density and lead to fast dynamics. However, biexciton emission energy is typically lower than the exciton emission. As shown in Figure 3.10 (a), for the range of exciton density we used in the experiments, the spectral shape did not change as a function of exciton density. We only observed an obvious biexciton emission peak (~650 nm) at about 10 times higher intensity than the highest pump intensity used in the dynamics measurements shown in Figure 3.10 (b).

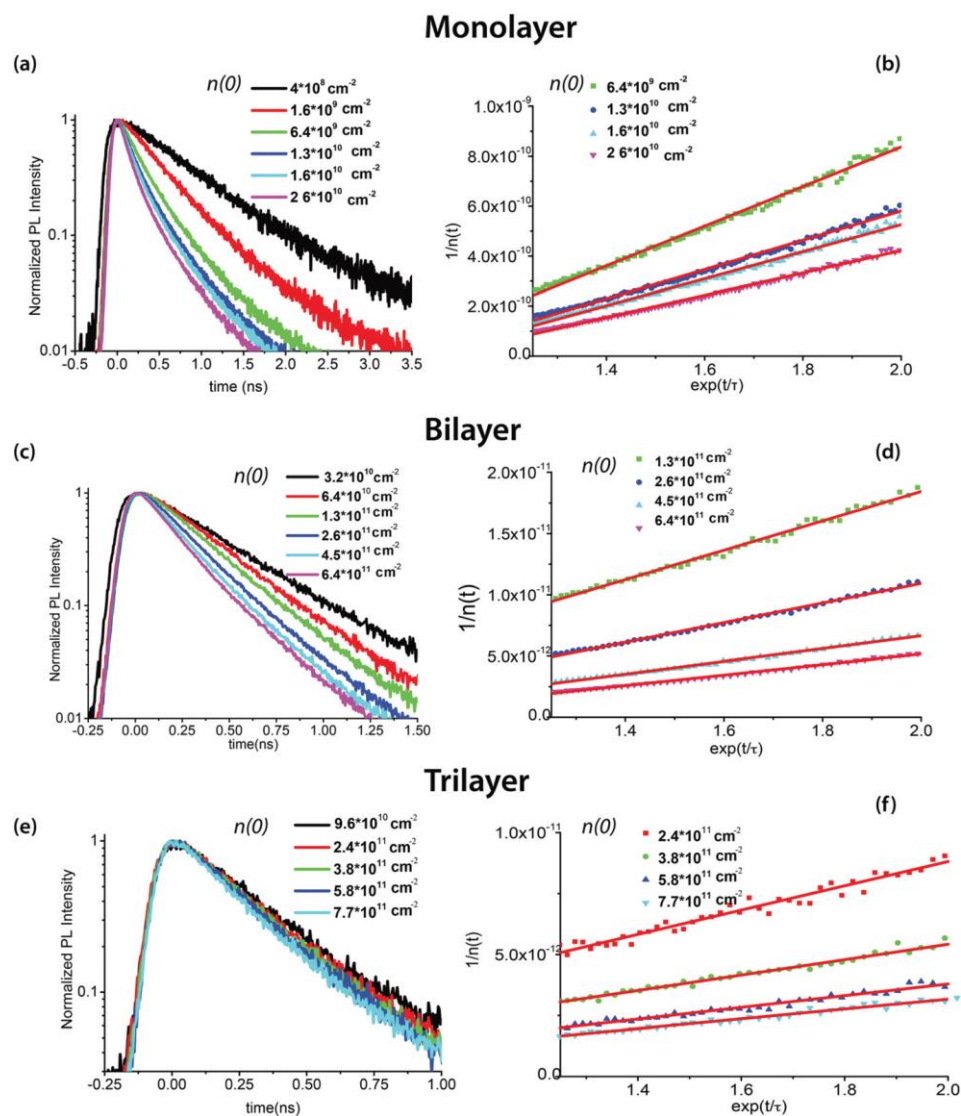


Figure 3.9 PL decay at different excitation densities for (a) monolayer, (c) bilayer, and (e) trilayer; linearized data using Equation (5) for the PL decay of (b) monolayer, (d) bilayer, and (f) trilayer. The red lines are linear fits to the data. $n(0)$ is the initial exciton density as described in the text.

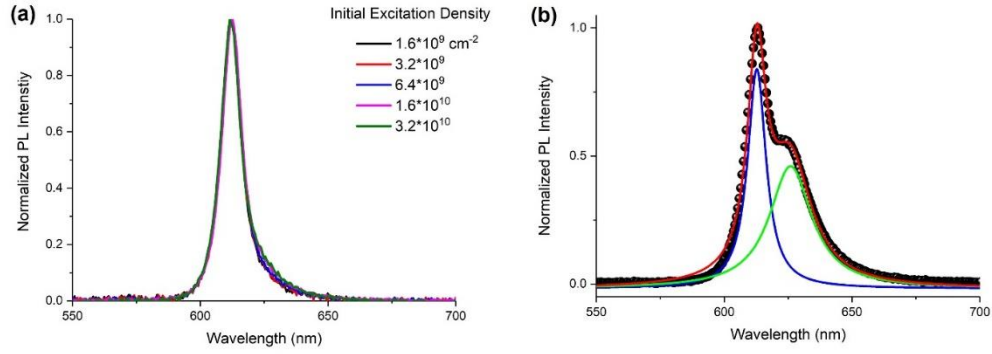


Figure 3.10 (a) Evolution of PL spectra in WS₂ monolayer with the pumping intensity. (b) PL spectrum of WS₂ monolayer at pump intensity great than $8.0 \times 10^{11} \text{ cm}^{-2}$. The black dot is experimental data. The red solid line is a fit using a sum of two Lorentz functions as shown in blue and green solid lines.

Due to the strongly enhanced Coulomb interaction in single layer WS₂ with a large exciton binding energy of $\sim 0.4 \text{ eV} \gg k_B T$ at room temperature, exciton–exciton annihilation is bimolecular process involves two excitons.^{156, 158} Note that biexciton formation could also lead to bi-molecular dynamics; however, as discussed above, biexciton formation is negligible for the exciton density used here. The rate equation of PL decay could be described by including both exciton–exciton annihilation term and exciton decay term¹⁸²:

$$\frac{dn}{dt} = -\frac{n}{\tau} - \gamma n^2 \quad (10)$$

where n is the exciton population, τ is the exciton lifetime without annihilation, and γ is the annihilation rate constant. Assuming that the γ is time-independent, the solution to the above equation is:

$$n(t) = \frac{n(0) \exp\left(-\frac{t}{\tau}\right)}{1 + \gamma \tau n(0) \left[1 - \exp\left(-\frac{t}{\tau}\right)\right]} \quad (11)$$

where $n(0)$ is the initial exciton density. The above equation can be rewritten as a linearized form:

$$\frac{1}{n(t)} = \left(\frac{1}{n(0)} + \gamma\tau \right) \exp\left(\frac{t}{\tau}\right) - \gamma\tau \quad (12)$$

The initial exciton density $n(0)$ is estimated using an absorption cross-section of $5 \times 10^5 \text{ cm}^{-1}$ per layer of WS_2 ¹⁸³ and assuming that every pump photon absorbed creates one exciton.

For the WS_2 monolayer, bilayer, and trilayer, exciton density-dependent PL dynamics are shown in Figure 3.9 (a), (c), and (e) which are replotted in the linear form as shown in 3.9 (b), (d), and (f), respectively. τ is given by the PL lifetime when free of exciton–exciton annihilation. We applied a global fit to the whole data set to equation (11) to determine the exciton–exciton annihilation rate γ . We obtain an exciton–exciton annihilation rate γ of 0.41 ± 0.02 , $(6.0 \pm 1.1) \times 10^{-3}$, and $(1.88 \pm 0.47) \times 10^{-3} \text{ cm}^2\text{s}^{-1}$ for the monolayer, bilayer, and trilayer, respectively.

3.4.6 Origin of thickness-dependent exciton-exciton annihilation

Surprisingly, the exciton-exciton annihilation rate is more than two orders magnitude larger in the monolayer than in the bilayer and trilayer. For the monolayer, exciton-exciton annihilation occurs at an exciton density as low as $10^9 \text{ excitons cm}^{-2}$ or 1 exciton per 10^5 nm^2 , corresponding to an average inter-exciton distance of $> 600 \text{ nm}$. The spatial extent of excitons for the monolayer has been estimated to be $\sim 3 \text{ nm}$.⁴² This large inter-exciton distance implies that exciton diffusion must precede exciton-exciton annihilation.¹⁶⁴ We could describe the kinetic process of exciton-exciton annihilation using two rate-determining steps as shown in Figure 3.11: (1) the diffusion of two excitons toward each other; (2) the annihilation of the two excitons when they are sufficiently close to each other.

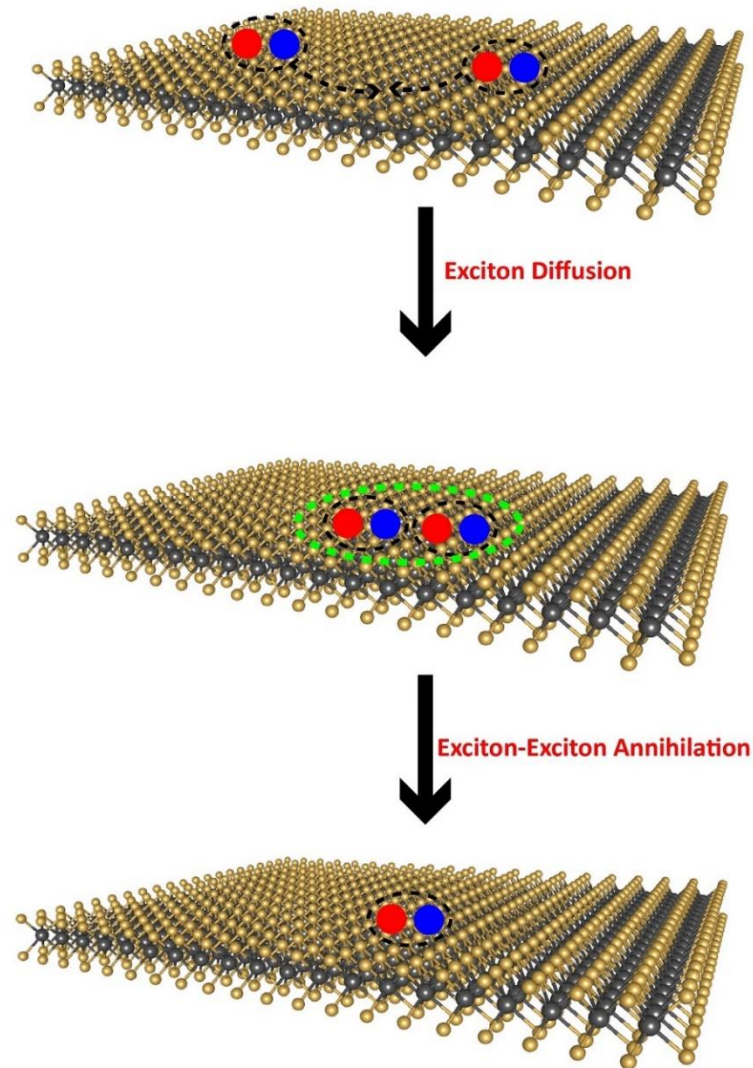
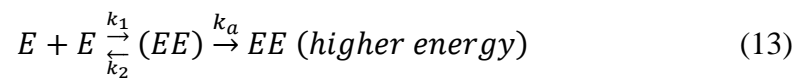


Figure 3.11 Schematic summary of the kinetic process of exciton-exciton annihilation.



where E is an isolated exciton, (EE) denotes an exciton pair sufficiently close that annihilation can take place, and k_a is the annihilation rate proceeding from (EE) . k_1 is defined as the rate of change of the number of close pairs per unit area and k_2 is the rate for the reverse process. The overall exciton-exciton annihilation rate becomes

$$\gamma = \frac{k_1 k_a}{k_2 + k_a} \quad (14)$$

The exciton diffusion rate is much higher in the bulk than the monolayer as demonstrated by recent transient absorption microscopy measurements of WS₂ monolayer and bulk with a diffusion constant D measured to be around 2.0 and 10.4 cm²s⁻¹ for the monolayer and bulk, respectively.¹⁰⁶ So, exciton diffusion is much faster than the exciton–exciton annihilation rate, which implies that $k_1, k_2 \gg k_a$, and the annihilation rate k_a is the rate-limited step. For the bilayer and trilayer, as the thickness increases, exciton binding energy decreases, which also results in more delocalized excitons. The more delocalized nature of the indirect exciton could lead to even faster exciton diffusion. Therefore, much reduced exciton–exciton annihilation rate constants measured in the bilayer and trilayer are most likely due to smaller values k_a rather than k_1 and k_2 .

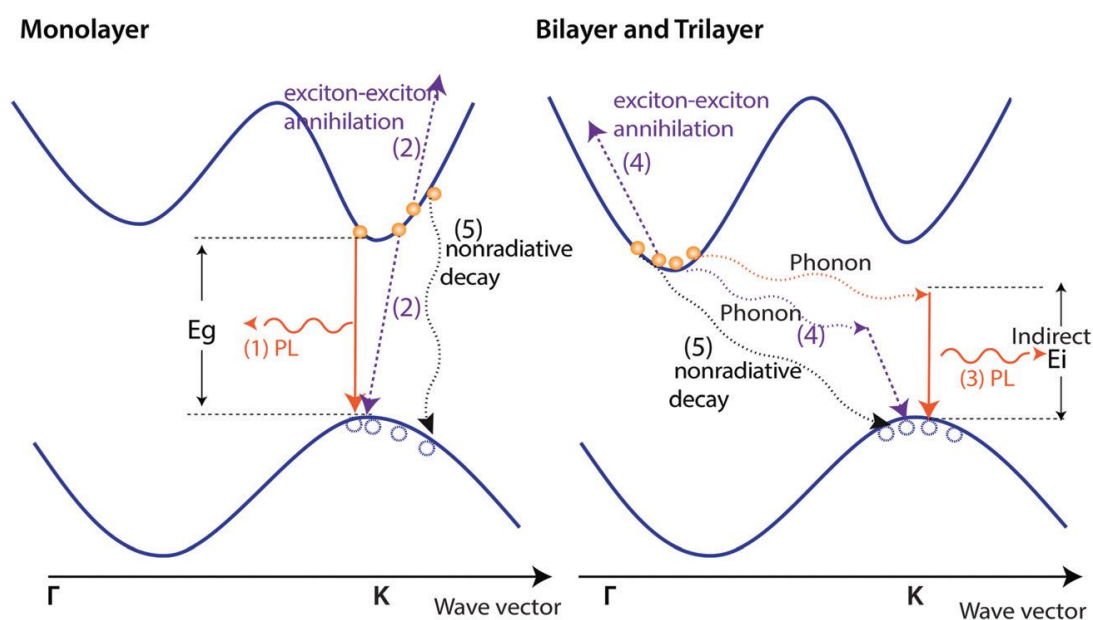


Figure 3.12 Schematic summary of relaxation pathways for WS₂ monolayer and few-layer. (1) Direct exciton recombination; (2) direct exciton-exciton annihilation; (3) indirect exciton recombination; and (4) indirect exciton-exciton annihilation; (5) other nonradiative pathways.

We explain the thickness dependence of k_a as follows. First, at the monolayer limit, stronger Coulomb interactions between the electrons and holes lead to stronger many-body interactions. Secondly, exciton–exciton annihilation requires conservation of both energy and momentum.¹⁸⁴ For WS₂ bilayer and trilayer, which are indirect semiconductors, momentum conservation requires assistance from phonons.¹⁸⁴⁻¹⁸⁵ In contrast, for the direct bandgap monolayer, the involvement of phonons is not necessary. This is schematically illustrated in Figure 3.12.

The additional requirement for phonon assistance makes exciton–exciton annihilation a much less probable event leading to γ at least two orders of magnitude smaller in the bilayer and trilayer than in the monolayer which indicates that only a fraction of exciton encounters results in annihilation in WS₂ bilayer and trilayer. The exciton–exciton annihilation is further reduced in the trilayer compared with the bilayer. Assuming that the PL in the bilayer and trilayer involves similar phonon-assisted processes as shown in Figure 3.10, the relative rate of k_a should be similar to that of the radiative rate. The radiative lifetimes for the bilayer and trilayer are ~ 400 ns and ~ 830 ns, respectively. The relative radiative rate of bilayer and trilayer is $\sim 2:1$. The annihilation rates of bilayer and trilayer are $(6.0 \pm 1.1) \times 10^{-3}$ and $(1.88 \pm 0.47) \times 10^{-3}$, leading to a ratio of exciton–exciton annihilation of $\sim 3:1$, which is similar to that of radiative rate.

The efficient exciton–exciton annihilation in WS₂ monolayer implies that the inverse process, impact ionization (multiple exciton generation)¹⁸⁶, could also be efficient. We could follow the method previously reported to obtain the Auger recombination time in quantum dots.¹⁵⁴ Briefly, we first normalize the decay curves at the low exciton density (without annihilation) and high exciton density (e.g., 1.6×10^9 cm⁻²) at a fixed delay time

(e.g., 2 ns) as shown in Figure 3.13(a). Then, we subtract the decay curve at the low exciton density from the high exciton density. Finally, we fit the subtracted curve with a single exponential decay and extract the exciton-exciton annihilation time to be ~ 400 ps in the monolayer at an initial exciton density of 1.6×10^9 excitons cm^{-2} as shown in Figure 3.13 (b). Such a slow exciton-exciton annihilation on the hundreds of ps time scale makes it quite possible to extract the additional exciton generated.

For monolayered WS_2 , the extraordinarily large exciton binding energy and significant correlation between electrons and holes compared to bulk semiconductors can explain the enhanced many-body interaction. Here, we measured the exciton-exciton annihilation rate of $0.41 \pm 0.02 \text{ cm}^2 \text{ s}^{-1}$ for the monolayer, comparable to that of $0.33 \pm 0.06 \text{ cm}^2 \text{ s}^{-1}$ measured for monolayered MoSe_2 ¹⁸⁷ and that of and that of $\sim 0.35 \text{ cm}^2 \text{ s}^{-1}$ for monolayered WSe_2 ¹⁶⁴. These values are about two orders of magnitude larger than that in 2D semiconducting quantum wells ($10^{-3} \text{ cm}^2 \text{ s}^{-1}$)¹⁸⁸ consistent with the increased correlation between electrons and holes in 2D TMDs. Previous theoretical calculations predicted that the Auger recombination rate could be enhanced by a factor of 50 for 2D systems when compared with the bulk.¹⁸⁹

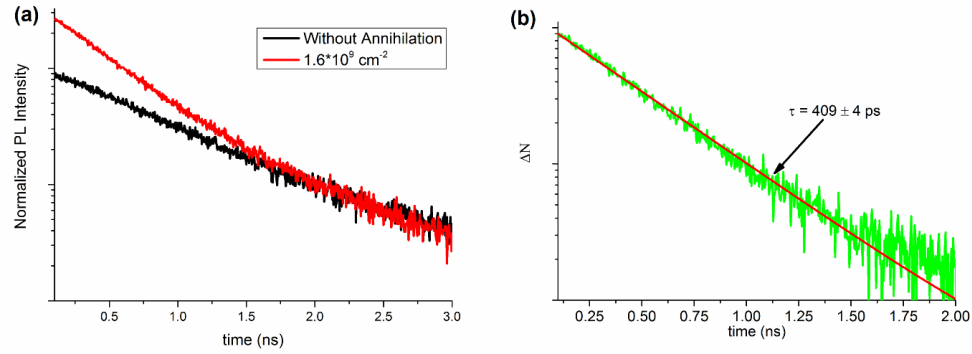


Figure 3.13 (a) Normalize the decay curves at the low pump intensity (without annihilation) and high exciton density ($1.6 \times 10^9 \text{ cm}^{-2}$) at the long delay time of 2 ns. (b) The subtracted decay curve (green) at the low pump intensity from the high pump intensity which is fitted with a single exponential decay (red).

3.5 Conclusion

We have investigated exciton dynamics in WS₂ monolayer, bilayer, and trilayer using time-resolved PL under conditions with and without exciton-exciton annihilation. Exciton decays of the monolayer, bilayer, and trilayer all exhibit mono-exponential decay behavior. The PL lifetime is measured to be 806 ± 37 ps, 401 ± 25 ps, and 332 ± 19 ps for WS₂ monolayer, bilayer, and trilayer, respectively, when free of exciton annihilation. The radiative lifetime of excitons was determined to be ~ 13 ns, ~ 400 ns, and ~ 830 ns for the monolayer, bilayer, and trilayer, respectively. Furthermore, two orders of magnitude enhancement of the exciton-exciton annihilation rate have been observed in the monolayer compared to the bilayer and trilayer. We attribute the strongly enhanced annihilation in monolayered WS₂ to enhanced electron-hole interactions and to the transition to the direct semiconductor, which eliminates the need for phonon assistance in exciton-exciton annihilation.

CHAPTER 4. EXCITON TRANSPORT IN TWO-DIMENSIONAL SEMICONDUCTORS

This chapter is adapted with permission from Long Yuan, Ti Wang, Tong Zhu, Mingwei Zhou, and Libai Huang, *Journal of Physical Chemistry Letters*, 2017, 8, 3371–3379.

4.1 Abstract

In this chapter, we present a systematic study of 2D exciton transport in WS₂ from the single layer to the bulk limit, employing spatially and temporally resolved transient absorption microscopy. Exciton diffusion is imaged directly in space and time with ~ 200 fs temporal resolution and ~ 50 nm spatial resolution. Our results demonstrate that the exciton diffusion coefficient of exfoliated single layer WS₂ is $2.8 \pm 0.2 \text{ cm}^2\text{s}^{-1}$. Exciton mobility for CVD grown single layer is more than an order of magnitude lower than the exfoliated sample, demonstrating that exciton diffusion at the single layer can be greatly influenced by extrinsic factors, such as impurities and surface optical phonon of the substrate. However, intrinsic phonon-limited exciton transport can be achieved in WS₂ layers thicker than 20 layers. Exciton diffusion coefficient as high as $10.4 \pm 0.4 \text{ cm}^2\text{s}^{-1}$ is measured for 100-layer thick WS₂, which agrees well with theoretical prediction.

4.2 Background

4.2.1 Strong Coulomb interaction in 2D TMDCs

Transition metal dichalcogenides (TMDCs), such as MoS₂, MoSe₂, WS₂, and WSe₂, are layered structures where adjacent layers are held by van der Waals force. Because the interlayer coupling is relatively weak, the electrons and holes are confined in the layer plane in TMDCs. One consequence of the Coulomb interaction between electrons and holes in TMDCs is the formation of 2D excitons with hydrogen-like bound states.^{42, 48}

Exciton binding energy is substantial in the bulk TMCDs, ~ 60 meV for WS_2 .¹⁹⁰ As thickness decreases, exciton binding energy increases further due to the reduced dielectric screening of the Coulomb interactions. For instance, exciton binding energy increases to ~ 400 meV in single layer WS_2 , more than an order of magnitude larger than other previously investigated 2D excitonic structures such as semiconducting quantum wells.^{42, 45, 190} In addition to extraordinary large exciton binding energy, some TMDCs, such as MoS_2 and WS_2 , undergo an indirect- to direct-gap transition at the single layer limit.^{7, 10} The strongly bound excitons at room temperature as well as unique excitonic properties make the TMDCs an ideal platform to study exciton behaviors in 2D systems.

4.2.2 2D exciton transport

Long-range transport of the direct and indirect 2D excitons is desirable for electronic and optoelectronic applications of TMDCs such as atomically thin photovoltaics.^{32, 60, 63, 125} Macroscopic motion of 2D excitons have been previously imaged in semiconducting quantum wells by photoluminescence (PL) microscopy, for instance in GaAs/AlGaAs coupled quantum wells.¹⁹¹⁻¹⁹³ However, the electron-hole interaction is rather weak in these quantum wells, with exciton binding energy only on the order of a few meV leading to very delocalized excitons and long-range transport on the order of 100s of μm . Much larger binding energy in TMDCs leads to more localized excitons with the size of < 2 nm and the range of exciton motion is expected to be shorter than previously investigated quantum wells.

There still currently lacks a comprehensive understanding of the intrinsic limit for exciton transport in the TMDCs materials. To address this challenge, quantitative information on exciton transport length scale length and dynamics are highly desirable.

Recently, temperature-dependent neutral exciton and trion diffusion in WS₂ on the μm range have been imaged by PL microscopy¹⁹⁴; however, no dynamics information was provided directly. Transient absorption imaging techniques have been applied to image exciton transport dynamics in WSe₂ and MoSe₂ for both single layers and bulk^{107, 109}, however, these previous reports showed somewhat inconsistent results: exciton diffusion coefficient is higher for single layer than for bulk WSe₂ but the opposite for MoSe₂.

In this chapter, we present a study of transport of spin-allowed bright and spin-forbidden dark A excitons in WS₂ employing spatially and temporally resolved transient absorption microscopy. The long-lived dark exciton is also quite mobile, with an exciton diffusion constant of $2.8 \pm 0.2 \text{ cm}^2\text{s}^{-1}$ for the exfoliated single layer. Exciton mobility for CVD grown single layer is more than an order of magnitude lower than the exfoliated sample, demonstrating that exciton diffusion at the single layer can be greatly influenced by extrinsic factors, such as impurities and surface optical phonon of the substrate. We evaluate intrinsic phonon-limited exciton transport in WS₂ layers thicker than 20 layers with exciton diffusion constant as high as $10.4 \pm 0.4 \text{ cm}^2\text{s}^{-1}$ is measured for 100 layers thick WS₂,

4.3 Experimental Methods

4.3.1 Preparation of WS₂ with different thickness

Single layer and multi-layers WS₂ with different thickness were mechanically exfoliated from commercial bulk WS₂ crystals (2D Semiconductor) onto fused silica substrate using a standard micromechanical cleavage method. We combined PL spectroscopy and atomic force microscopy (AFM) to identify the thickness of WS₂ layers.¹⁹⁵

4.3.2 Determination of pump fluence and exciton density

In our TAM experiments, excitons in WS₂ are generated by the absorption of the pump laser. The peak fluence of pump pulse (P_f) could be calculated as:

$$P_f = \frac{P}{A} \quad (1)$$

where P is the pump pulse energy, A is the pump excitation effective area. Since pump pulse is a Gaussian beam. To calculate the exciton density injected by the pump pulse, we assume that every absorbed pump photon could create one exciton. This assumption is widely used in previous optical measurements and gives reasonable explanations to experimental results. Then, the injected exciton density could be obtained as:

$$N = \frac{\alpha P_f}{\hbar\nu} \quad (2)$$

where α and $\hbar\nu$ are the absorption coefficient and photon energy of the pump pulse.

4.4 Results and discussion

4.4.1 Optical Characterization of WS₂ with different thickness on a quartz substrate

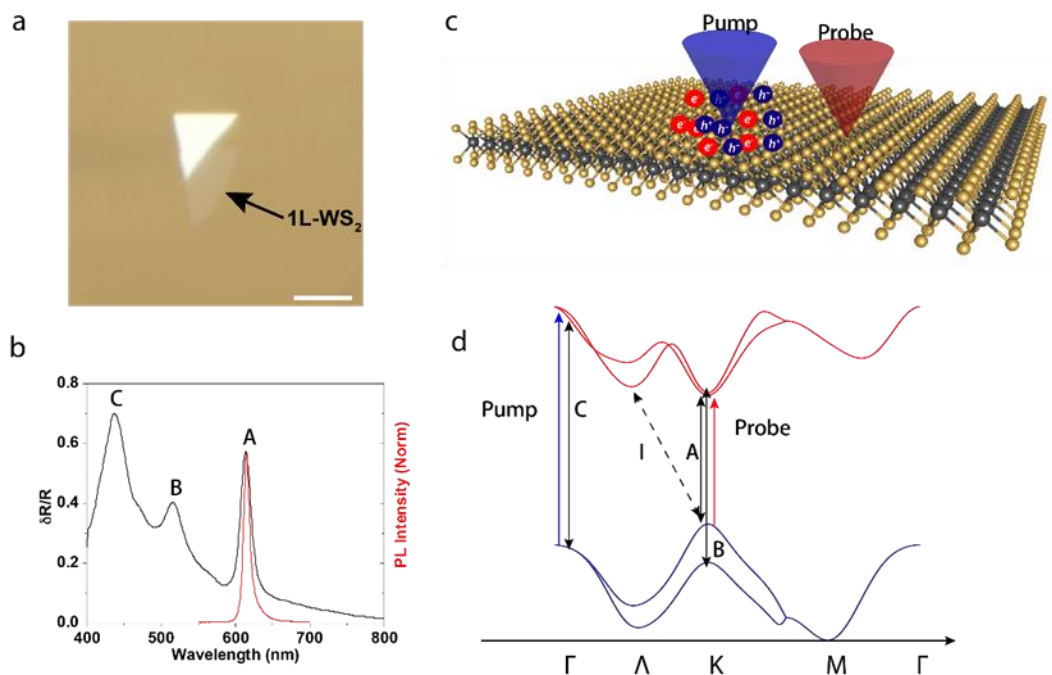


Figure 4.1 Experimental design and optical characterizations. (a) optical image of an exfoliated 1L-WS₂ on a fused silica substrate (scale bar represents 5 μm). (b) Differential reflection (black line) and PL spectra (red line) of 1L-WS₂. (c) Schematic description of exciton diffusion measurements. (d) Schematic drawing of band structure and excitonic transitions in 1L-WS₂ along with pump and probe energies for transient absorption measurements.

To systematically investigate exciton transport, WS₂ layers with the thickness ranging from 1 layer (1L) to 100 layers (100L) are exfoliated from bulk crystal onto a fused silica substrate. The thickness of the WS₂ layers is determined by the combination of Raman, PL, and atomic force microscopy. Figure 4.1(a) illustrates an optical image of a typical exfoliated 1L-WS₂ flake on a quartz substrate. Figure 4.1(b) shows the reflective spectrum exhibits three excitonic transitions (labeled as A, B, and C). Both A (613 nm) and B (516 nm) excitons originate from direct band transition at K point between the

valence band and the conduction band.¹⁰ The energy difference (380 meV) between A and B transition is due to the spin-orbit splitting of the valence band. The highest absorption peak (C, 437 nm) has been ascribed to band nesting effect.¹⁴⁵ The excitonic structure is schematically illustrated in Figure 4.1(c). 1L-WS₂ (Figure 4.1(b)) shows a single PL emission peak at 615 nm resulting from the direct interband recombination of A exciton.¹⁰ As thickness increases to more than 2L, the conduction band maximum moves to Λ point while the valence band maximum remaining at the K point, leading to the formation of indirect excitons (I).¹⁰ Raman spectrum of the 1L is shown in Figure 4.2 and PL spectra of the 2L and 3L are shown in Figure 4.3. For WS₂ flakes with the number of layers greater than 3, we employ AFM to identify the thickness of WS₂ samples.

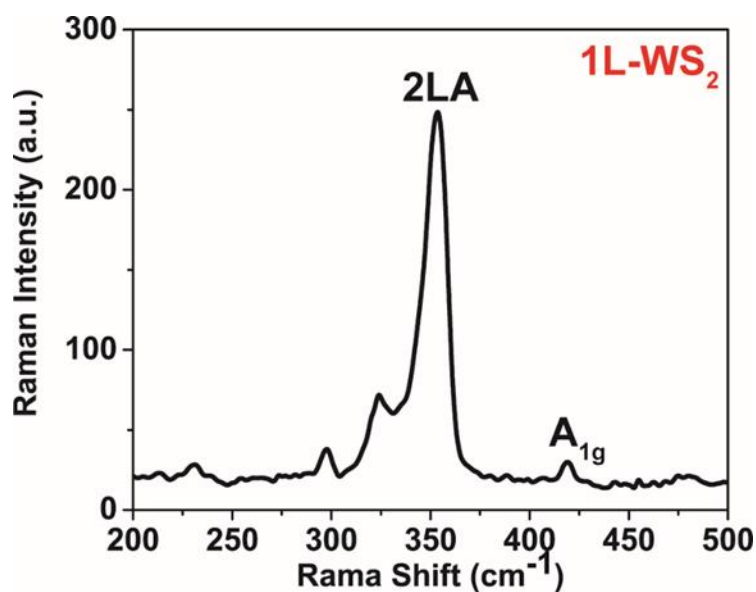


Figure 4.2 Raman spectra of 1L-WS₂ on a quartz substrate. The peak energy difference between 2LA and A_{1g} is 65 cm⁻¹ which indicates the number of layers to be the single layer.¹²⁰

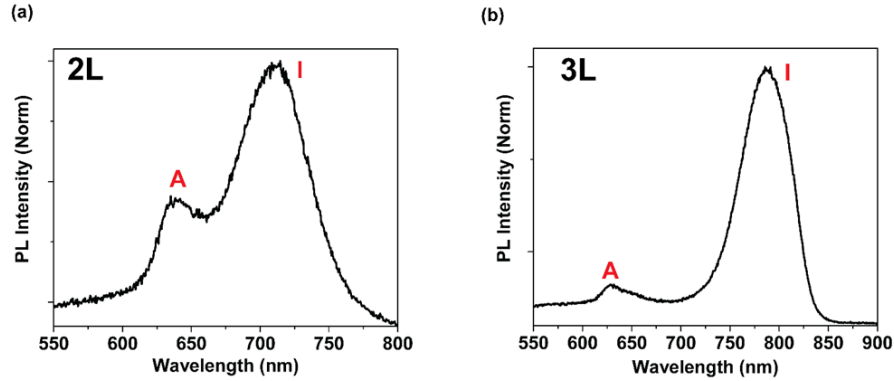


Figure 4.3 PL spectra of (a) 2L-WS₂ and (b) 3L-WS₂ on a quartz substrate are taken under excitation of 447 nm. We observed both A and I exciton emission. The emission energy of I exciton could be used to identify the number of the layer which is 712 nm (1.74 eV) and 788 nm (1.57 eV) for 2L- and 3L-WS₂ respectively.

4.4.2 Direct imaging of exciton transport using TAM

In order to investigate exciton diffusion directly, we employed pump-probe transient absorption microscopy (TAM) to directly image exciton population in both the spatial and temporal domains. The pump wavelength is at 395 nm exciting C excitons with a fluence of 1.1 $\mu\text{J}/\text{cm}^2$ while the probe near the A exciton resonance to monitor exciton dynamics as schematically shown in Figure 4.1(d). Using the absorption coefficient deduced from differential reflection spectra^{10, 163}, we calculate the corresponding injected exciton density to be $3.2 \times 10^{11} \text{ cm}^{-2}$ for the 1L-WS₂. Exciton dynamics with different pump fluence are measured for both 1L- and 32L-WS₂ and no significant exciton-exciton annihilation effects are observed in the transient absorption measurements (Figure 4.4) at this pump fluence. The magnitude of ΔT is proportional to pump intensity as shown in Figure 4.5.

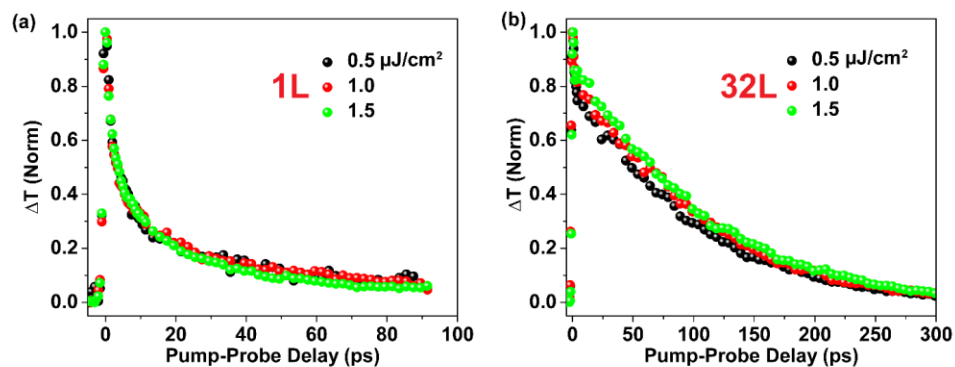


Figure 4.4 Transient dynamics of (a) 1L-WS₂ and (b) 32L-WS₂ with different pump fluence.

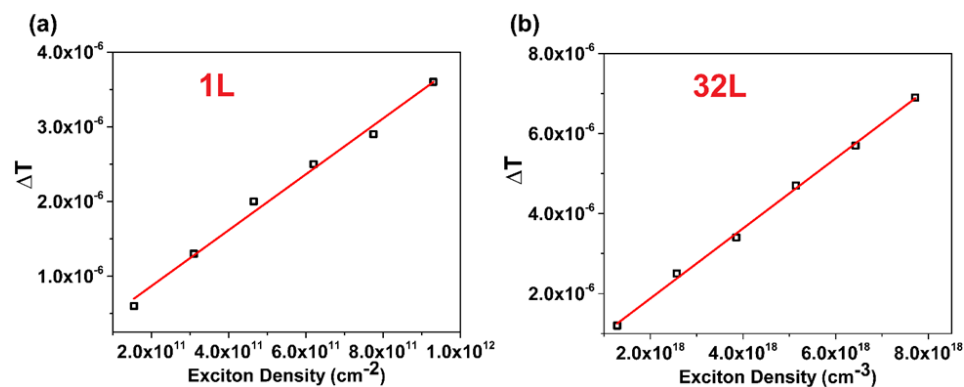


Figure 4.5 Transient absorption signal (ΔT) at 0 ps is plotted as a function of exciton density for (a) 1L-WS₂ and (b) 32L-WS₂. Red lines are linear fits.

The transient absorption spectra show the bleach of A exciton peak at 616 nm (Figure 4.6) for 1L-WS₂ due to the combination of Pauli blocking and bandgap renormalization effects.^{146, 148} For the multilayers, while photoexcitation creates indirect excitons, the A exciton transition is also modified by Pauli blocking of the holes. Therefore, bleaching at the A exciton resonance is also observed in multilayers (Figure 4.6). The A exciton bleach band redshifts as the thickness increases, which can be explained by quantum confinement effects.

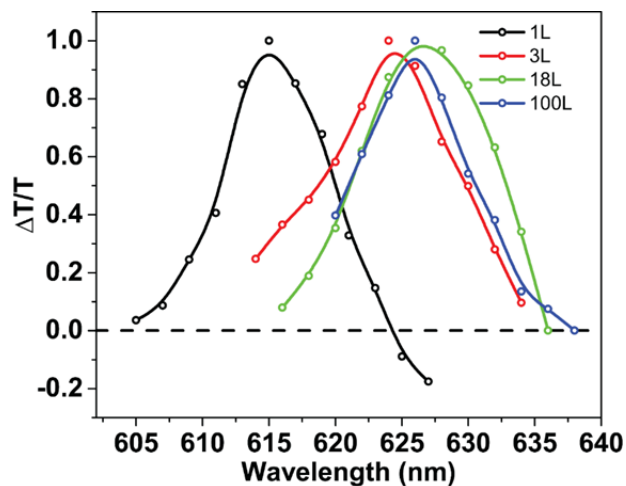


Figure 4.6 Normalized transient absorption spectra (395-nm pump) with different thickness.

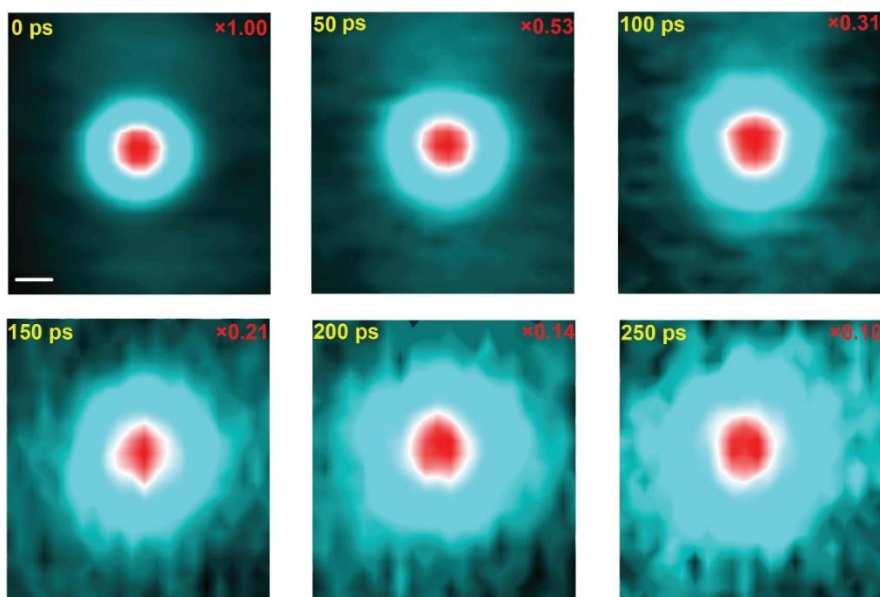


Figure 4.7 TAM imaging of exciton propagation in 48L-WS₂ (pump at 395 nm and probe at 626 nm) with an injected exciton density of $8.6 \times 10^{12} \text{ cm}^{-2}$ at different pump-probe time delays. The color scale is normalized at the maximum ΔT . The normalization factors are indicated on the images. The scale bar represents 1 μm .

To image exciton transport, the pump beam is held at a fixed position while the probe beam is scanned relatively to the pump with a pair of galvanometer scanners to form an image. The pump-induced change in probe transmission $\Delta T = T_{pump-on} - T_{pump-off}$ is collected. The amplitude of the transient absorption signal is proportional to exciton population. At zero delay time the TAM images reflect the initial population created by the pump beam, and at later delay time, the TAM images directly visualize how excitons transport out of the initial volume. As an example, the exciton population imaged at different pump-probe delay time for a 48L-WS₂ is illustrated in Figure 4.7. Clear exciton motion can be observed in the time window of 250 ps. Because no apparent anisotropy in 2D exciton propagation is observed as shown in Figure 4.7 (i.e. exciton diffusion along x and y directions is independent and with identical rates), exciton diffusion can be further reduced to a one-dimensional problem. The exciton distribution along one dimension at different delay times is obtained by taking the cross sections of the images (Figure 4.8).

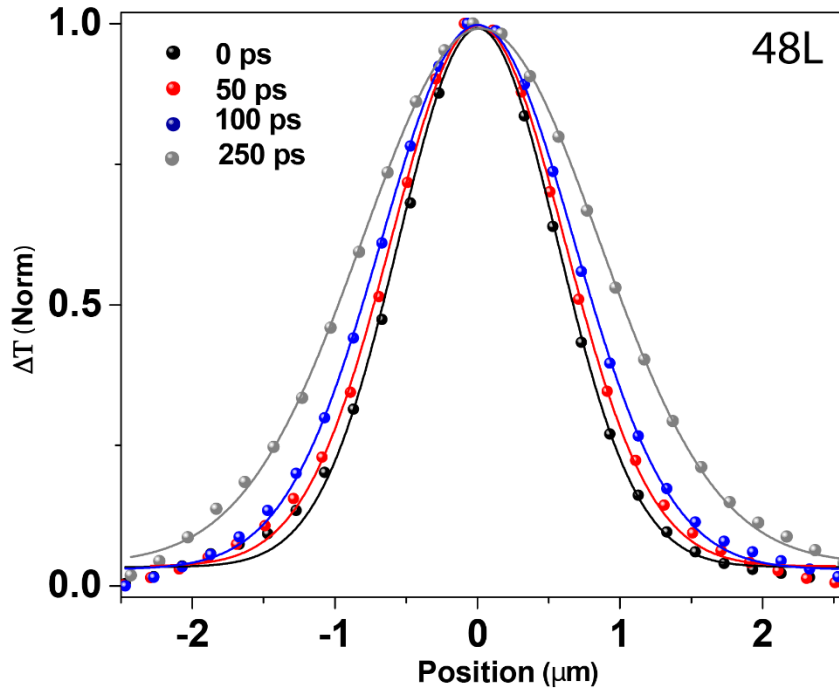


Figure 4.8 Spatial profiles of exciton distribution in 48L-WS₂ at different pump-probe delays. Solid lines are fits with Gaussian function.

Exciton motion is expected to be diffusive after carriers equilibrate with the lattice, which is on the order of ps.¹⁴⁵ Exciton population as a function of space and time can be described by a differential equation that includes both the diffusion out of the initial volume and population decay, which is given by,

$$\frac{\partial n(x,t)}{\partial t} = D \frac{\partial^2 n(x,t)}{\partial x^2} - \frac{n(x,t)}{\tau} \quad (3)$$

where D is the exciton diffusion constant and τ is the exciton lifetime. The initial population $n(x, 0)$ follows Gaussian distribution as created by a Gaussian pump beam at position (x_0) (the pump and beam profiles) and is given by:

$$n(x, 0) = N \exp \left[-\frac{(x-x_0)^2}{2\sigma_0^2} \right] \quad (4)$$

Solution to Equation (3) dictates that exciton density at any later delay time (t) is also Gaussian and can be described as:

$$n(x, t) = N \exp \left[-\frac{(x-x_0)^2}{2\sigma_t^2} \right] \quad (5)$$

The diffusion constant D is then given by:

$$D = \frac{\sigma_t^2 - \sigma_0^2}{2t} \quad (6)$$

To determine the exciton diffusion constants, we plot the variance square difference ($\sigma_t^2 - \sigma_0^2$) of 1L- and 100L-WS₂ from Gaussian function fitting as a function of time delays as shown in Figure 4.9(a) and (b). ($\sigma_t^2 - \sigma_0^2$) for all thicknesses can well be described by Equation (6), as shown in Figure 4.9(c), which indicates that the exciton motion in the WS₂ layers is indeed diffusive. The exciton diffusion constant of 1L-WS₂ and 100L-WS₂ is determined to be 2.8 ± 0.2 and 10.4 ± 0.4 cm²s⁻¹, respectively. The diffusion constant as a function of the number of layers is plotted in Figure 4.9(d) which increases monotonically with the number of layers.

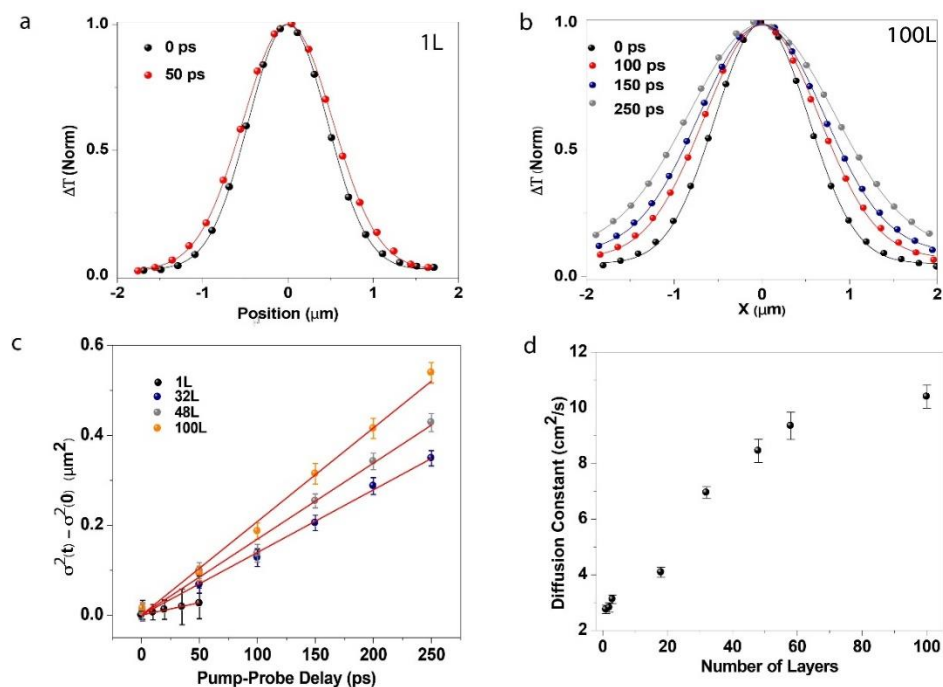


Figure 4.9 Exciton diffusion coefficient of WS₂ with different thickness extracted from time-dependent distribution profiles. Spatial profiles of exciton distribution in (a) 1L-WS₂ and (b) 100L-WS₂ with different pump-probe time delays. Solid lines are fits with Gaussian function. (c) The diffusion coefficient is obtained from the linear fitting of the variance of Gaussian profiles. Red lines are linear fits. (d) Extracted diffusion coefficients plotted as a function of the number of layers.

In order to elucidate that the diffusion measurement is not limited by the system resolution, we carried out a control experiment on 1L-MoS₂. The pump wavelength is at 395 nm while the probe wavelength is at 670 nm to probe A exciton resonance. In 1L-MoS₂, the transient dynamics shows excitons decay very fast within several ps as shown in Figure 4.10(a) which can be explained by the greater higher defect density. As shown in Figure 4.10(b), no detectable diffusion is observed in 1L-MoS₂.

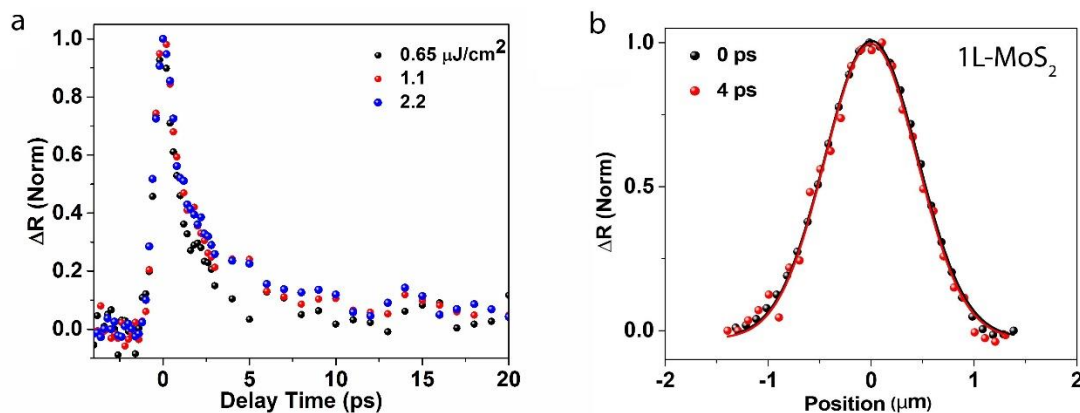


Figure 4.10 (a) Transient dynamics of 1L-MoS₂ with different pump fluence. (b) Spatial profiles of exciton distribution in control 1L-MoS₂.

4.4.3 Thickness-dependent exciton dynamics

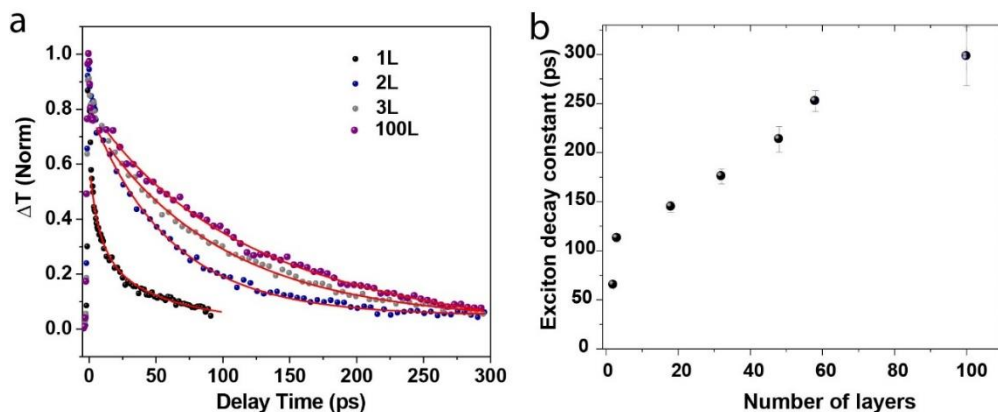


Figure 4.11 Thickness-dependent exciton lifetime. (a) Thickness-dependent transient dynamics are modeled by Equation (3). Fits are shown in red solid lines. (b) Extracted decay constant is plotted as a function of thickness.

TAM measurements also simultaneously provide information on exciton dynamics (Figure 4). All exciton decays show an initial fast relaxation of ~ 1 ps, which has been assigned to nonradiative relaxation of hot carriers at the Λ/K valleys prior to exciton formation.¹⁴⁵ Thus, we focus our discussion on exciton dynamics occurring on timescale greater than 2 ps. The dynamics are taken when both pump and probe beams are

overlapped in the center, and the exciton population decays are fitted to Equation (3) to extract exciton lifetime τ by using D deduced by Equation (6). Exciton dynamics differs significantly as thickness increases from 1L to 2L as expected for the transition from direct to indirect exciton and it gradually converges in the thicker sample ($N > 3$).¹⁰ The slower exciton decay in 2L than in 1L can be understood as the relaxation of indirect exciton that requires intervalley and interband phonon scattering. Further discussion on phonon scattering is presented in the next section. For the single layer, a bi-exponential decay is found with time constants of 4 ± 1 ps and 150 ± 20 ps, respectively. The fast decay component agrees well with the lifetime for the bright A exciton, and the short exciton lifetime reflects the direct nature of the exciton.¹⁴⁰ The slow decay component is assigned to the spin-forbidden “dark” exciton level lying ~ 30 meV below the bright A exciton in the 1L.¹⁴⁰ Exciton dynamics for the 2L and thicker can be well fitted with single-exponential decay as shown in Figure 4b and Figure S8. The exciton lifetimes of 2L- and 100L-WS₂ are determined to be 65 ± 2 ps and 300 ± 30 ps, respectively. The extracted exciton lifetimes for the 2L and thicker are plotted in Figure 4b as a function of the number of layers.

4.4.4 Extrinsic factors in 2D exciton transport

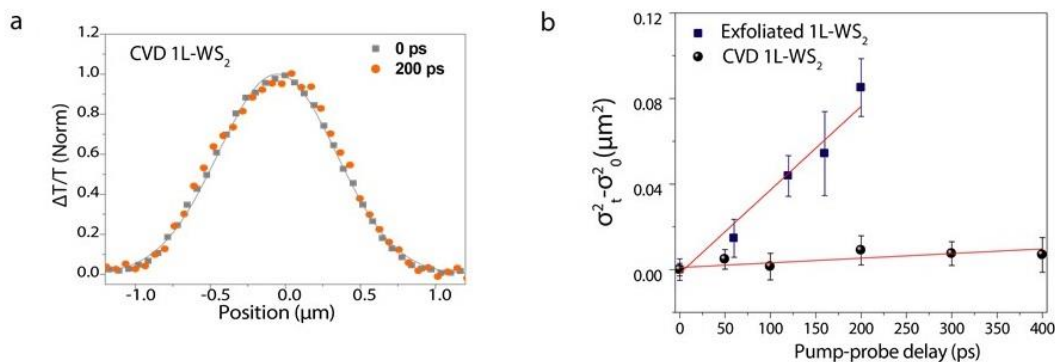


Figure 4.12 (a) Spatial profiles of excitons in a CVD 1L-WS₂ at different pump-probe delay times. (b) Diffusion constants of both exfoliated 1L-WS₂ and CVD 1L-WS₂ are obtained from the linear fitting of the variance of Gaussian profiles using equation (6). Red lines are the linear fits.

Exciton motion in the CVD grown 1L-WS₂ is more than one order of magnitude slower than exfoliated 1L-WS₂, with a diffusion constant of $0.1 \pm 0.04 \text{ cm}^2 \text{ s}^{-1}$ and no discernable exciton transport within the 400 ps experimental window, as shown in Figure 4.12. Since defect density in CVD WS₂ ($\sim 3 \times 10^{13} \text{ cm}^{-2}$)¹⁸⁰ is greatly higher than exfoliated WS₂ ($\sim 2 \times 10^9 \text{ cm}^{-2}$)¹⁸¹, this drastically difference can be explained by the more prevalent defect and/or impurity scattering for the CVD grown sample compared to the exfoliated sample.

4.4.5 Intrinsic factors than control 2D exciton transport

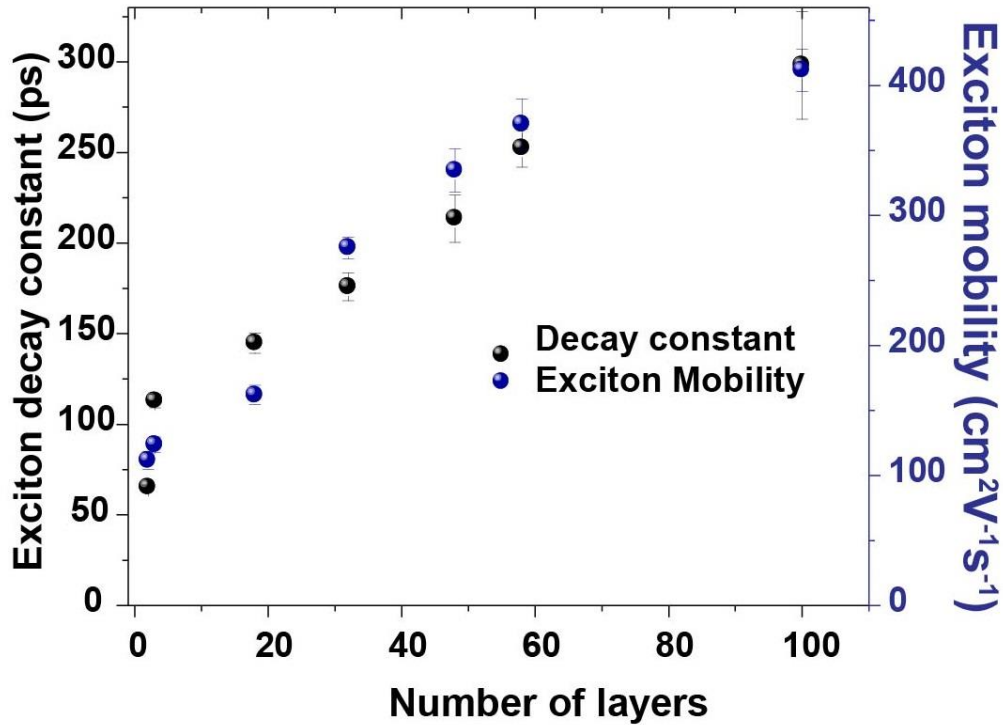


Figure 4.13 Extracted decay constant and exciton mobility is plotted as a function of thickness.

To compare our experimental results to previous measurements and theoretical calculations on carrier mobility, we relate exciton diffusion constant D to mobility (μ) by Einstein relation, $\mu = \frac{eD}{k_B T}$, where e , k_B , and T is the elementary charge, Boltzmann constant, and temperature, respectively. For 1L-WS₂, exciton mobility is determined to be 109 ± 6 cm²V⁻¹s⁻¹, which is on the same order as electron mobility of 50 cm²V⁻¹s⁻¹ from electrical measurements.¹⁹⁶ Exciton mobility for 2L and thick is plotted in Figure 4.13.

We relate exciton motion to electron and hole motions using the center of mass coordination, $R = \frac{m_e^* r_e + m_h^* r_h}{M}$, where $m_{e(h)}^*$ is electron (hole) effective mass, M is exciton effective mass as given by $M = (m_e^* + m_h^*)$, and R , r_e , and r_h are exciton, electron, and

hole coordinates, respectively.¹⁹⁷ Because diffusion constant and mobility is related to mean squared displacement, as expressed by $\langle R - R_0 \rangle^2 = 2Dt = \frac{2\mu k_B T t}{e}$. Therefore, exciton mobility can be expressed as

$$\mu = \frac{m_e^{*2} \mu_e + m_h^{*2} \mu_h + m_e^* m_h^* \sqrt{\mu_e \mu_h}}{M^2} \quad (5)$$

Intrinsic phonon-limited room temperature electron and hole mobility has been calculated to be $320 \text{ cm}^2 \text{V}^{-1} \text{s}^{-1}$ and $540 \text{ cm}^2 \text{V}^{-1} \text{s}^{-1}$, respectively for single layer WS_2 .¹⁹⁸ By using $m_e^* = 0.31 m_0$ and $m_h^* = 0.42 m_0$ at the K point, intrinsic exciton mobility is found to be $370 \text{ cm}^2 \text{V}^{-1} \text{s}^{-1}$ for 1L- WS_2 ¹⁹⁸, which is more than 3 folds higher than the experimental exciton mobility of $109 \pm 6 \text{ cm}^2 \text{V}^{-1} \text{s}^{-1}$ measured here.

Significantly lower exciton mobility in the 1L- WS_2 than the predicted intrinsic phonon scattering limit indicates extrinsic factors dominate. For 2D layered semiconductors, three types of lattice phonons contribute to the intrinsic scattering of carriers and excitons: (1) in-plane polar optical phonons through Frölich interaction; (2) out-of-plane homopolar (nonpolar) phonons *via* deformation potential; and (3) acoustic phonons *via* deformation potential.¹⁹⁹⁻²⁰¹ For the single layer and few layers, charge carriers and excitons are subjected to interfacial Coulomb scattering by charge impurities and remote scattering from surface phonons of the substrate in addition to intrinsic phonon scattering²⁰²⁻²⁰³. Charge impurities and surface optical phonons have found to dominate the electron mobility in the single layer and few layers cases and become less significant for the thicker layers.²⁰²⁻²⁰³ Previous electron mobility measurements showed a maximum of $240 \text{ cm}^2 \text{V}^{-1} \text{s}^{-1}$ at a thickness around 10 nm .^{181, 203} However, electrical measurements in the field effect transistor (FET) geometry cannot fully evaluate thickness dependent mobility because, for large layer thickness, FET mobility drops dramatically due to a resistor network model.²⁰⁴⁻

²⁰⁵ For back gating in FETs, metal contacts only directly connect to the bottom layers. The connection to the top layers requires additional interlayer resistors. Thus, the carrier mobility decreases with layer thickness artificially because of the increased interlayer resistance.²⁰⁴⁻²⁰⁵

The TAM measurements presented here, on the other hands, do not depend on any contact and should reflect the true limit of exciton and carrier transport. As shown in Figure 4b, exciton mobility tracks exciton lifetime almost perfectly for thickness greater than 20L. Because the indirect exciton lifetime for thickness greater than 2L directly reflects exciton-phonon scattering time, Figure 4.13 implies that phonon-limited exciton transport is achieved in layers thicker than 20L. For 20L or thinner, exciton mobility increases at a slower rate than exciton decay constant, indicating that charge impurities and remote phonon scattering still play a role. Interestingly, exciton mobility and decay constant continue to increase until a thickness of $\sim 100L$ and mobility of $411 \pm 16 \text{ cm}^2\text{V}^{-1}\text{s}^{-1}$, implying that intrinsic exciton-phonon scattering is thickness dependent even for thickness greater than 20L. One possible mechanism is that out-of-plane homopolar phonons scattering perpendicular to the layers reduces as thickness increases. This is consistent with quenching of the homopolar mode in monolayer MoS₂ when 30 nm thick top gate with a high dielectric constant is deposited.^{201, 206}

The results shown in Figure 4.13 show that phonon-limited intrinsic exciton mobility is $\sim 400 \text{ cm}^2\text{V}^{-1}\text{s}^{-1}$ for multilayer WS₂, which is similar to the value of phonon-limited $370 \text{ cm}^2\text{V}^{-1}\text{s}^{-1}$ deduced for 1L WS₂. We interpret the mobility using scattering theory $\mu = \frac{e^*\langle\tau_s\rangle}{M}$ where $\langle\tau_s\rangle$ is the average scattering time of the excitons. A $\langle\tau_s\rangle$ of $\sim 500 \text{ fs}$ is calculated for 100 L-WS₂ by using an effective mass of the indirect exciton of

$1.02 m_0$ (electron effective mass at Λ valley is $0.6 m_0$)¹⁹⁸, which agrees well with the theoretical prediction of intrinsic phonon scattering.

4.5 Conclusion

In summary, we employed ultrafast microscopy to evaluate intrinsic and extrinsic factors that control 2D exciton transport in WS₂. We successfully image the exciton population and dynamics in space and in time. The exciton mobility in single layer WS₂ is determined to be $(109 \pm 6 \text{ cm}^2\text{V}^{-1}\text{s}^{-1})$ and is largely limited by extrinsic factors such as charge impurities and surface phonons of the substrate. Therefore, one needs to effectively screen the scattering by charge impurities and surface optical phonons *via* interface engineering in order to achieve the phonon-limited exciton transport in single layers. Our results demonstrated that the intrinsic phonon-limited exciton transport with mobility as high as $411 \pm 16 \text{ cm}^2\text{V}^{-1}\text{s}^{-1}$ is achievable for samples with the thickness greater than 20 layers. These results show that both direct and indirect excitons in TMDCs are intrinsically quite mobile, with mobility on par with the 2D excitons in coupled GaAs quantum wells, making them attractive for optoelectronic applications.

CHAPTER 5. ULTRAFAST CHARGE TRANSFER AND ENHANCED PHOTO-CARRIER GENERATION IN TWO-DIMENSIONAL WS₂/GRAPHENE HETEROSTRUCTURES

This chapter is adapted with permission from Long Yuan, Ting-Fung Chung, Agnieszka Kuc, Yan Wan, Yang Xu, Yong P. Chen, Thomas Heine, and Libai Huang, *Science Advance*, 2018, 4, e1700324.

5.1 Abstract

Efficient interfacial carrier generation in van der Waals heterostructures is critical for their electronic and optoelectronic applications. In this chapter, we present a joint experimental and theoretical study to address charge generation from interlayer charge-transfer (CT) transitions in WS₂/graphene heterostructures by imaging interlayer-coupling dependent charge generation using ultrafast transient absorption microscopy. CT transitions allow for carrier generation by excitation well below the WS₂ bandgap, and the experimentally determined transition energies agree with those predicted from the first-principles band-structure calculations. Excitation of the CT transitions also leads to additional carrier generation in the visible spectral range in the heterostructures compared to that in single layer WS₂ alone. The lifetime of the charge-separated states is measured to be ~ 1 ps. These results suggest that interlayer interactions make graphene/2D semiconductor heterostructures very attractive for photovoltaic and photodetector applications, because of the combined benefits of enhanced broadband photocarrier generation due to the CT states and high carrier mobility.

5.2 Background

5.2.1 Two-dimensional Van der Waals heterostructures

Nanostructured materials hold great promises as building blocks for creating new architectures for electronic and optoelectronic devices. Atomically thin van der Waals layers^{2, 53} represent a new two-dimensional (2D) material class with unusual optical and electronic properties emerging at the single layer or few-layer limit^{3, 5-8, 12, 28, 42, 207}, which provide opportunities to design new functionalities. Specifically, heterostructures can be formed by artificially stacking layers of different 2D materials, because traditional restrictions in heterostructure-growth such as lattice matching conditions and atom interdiffusion are no longer required.⁵³⁻⁵⁶ In the past few years, heterostructures constructed from graphene, boron nitride, and semiconducting transition metal dichalcogenides (TMDCs) have established a remarkable platform for photoactive applications, including photodetectors, light-emitting diodes, and atomically thin photovoltaics.^{25, 63, 208-216}

5.2.2 Charge transfer transitions

The structural tunability of 2D nanostructures along with atomically thin and sharp 2D interfaces provides new opportunities in controlling charge transfer interactions at the interfaces.^{52, 90} Charge transfer at 2D interfaces has been demonstrated to be very rapid occurring on timescales ranging from 50 fs to a few ps and interlayer charge-transfer (CT) exciton transitions have been observed.^{81-82, 88-89, 93-95, 217-221} It is still elusive that how interlayer charge transfer interactions contribute to interfacial charge generation and separation in 2D heterostructures. Charge separation could take place directly by exciting CT transitions at the interface. Because the interlayer distance between the graphene and the 2D semiconductor layer could be as small as 3 Å, interlayer interactions beyond London

dispersion are apparent, leading to modification of optical absorption and band structure.^{88, 222-225} In addition, since practically every atom is on the surface, interfacial charge transfer is expected to play a much more important role in 2D heterostructures than those formed by bulk materials. Despite emission from interlayer CT excitons have been observed in 2D heterostructures^{57, 93-95, 101-102, 221}, no direct excitation of such CT states has been reported, partly due to relatively weak oscillator strengths.¹⁰⁴

In this chapter, we present a joint experimental and theoretical investigation to address charge generation from interlayer CT transitions in TMDC/graphene heterostructures. We use spatial ultrafast transient absorption microscopy (TAM) to directly compare charge generation at different interlayer coupling strengths to elucidate the role of CT transitions in WS₂-graphene heterostructures. These results demonstrate effective broadband carrier generation by excitations below the bandgap in TMDC/graphene heterostructures.

5.3 Experiential Methods

5.3.1 WS₂/Graphene heterostructures fabrication

Single layer and bilayer WS₂ were mechanically exfoliated from bulk WS₂ crystals (2D Semiconductors, Inc) onto Si wafer with a 90 nm-thick oxide. The number of layers was confirmed by using a combination of photoluminescence and Raman spectroscopy.¹⁹⁵ Monolayer graphene film was grown on copper (Cu) foils at atmospheric pressure using chemical vapor deposition (CVD).²²⁶⁻²²⁸ The CVD graphene used in this work is polycrystalline with an average grain size of ~15 μm . The heterostructures were assembled by depositing CVD-grown graphene on top of single layer and bilayer WS₂ using an

alternative poly (methyl methacrylate) (PMMA) transfer process to minimize aqueous solution at the WS₂/graphene interface.^{71, 229} The CVD-grown graphene on Cu foil was spin-coated (3000 r.p.m.) with 950PMMA-A4 (MicroChem). PMMA-coated graphene was adhered to a polymer frame with a hole at the center and suspended by Cu etching. The residual etchant was diluted with DI water. The PMMA/graphene membrane was gently blown dry with nitrogen and then brought into contact with WS₂ layers followed by baking at around 350 K for 5 minutes to promote adhesion between graphene and WS₂. Finally, the heterostructure was annealed at 420 K in the vacuum of 10⁻⁵ Torr for 2 hours followed by natural cooling. Figure 1 displays the optical image of a 2L-WS₂/graphene heterostructure. The orientation of WS₂ and graphene layers are not aligned in any particular way in the momentum space.

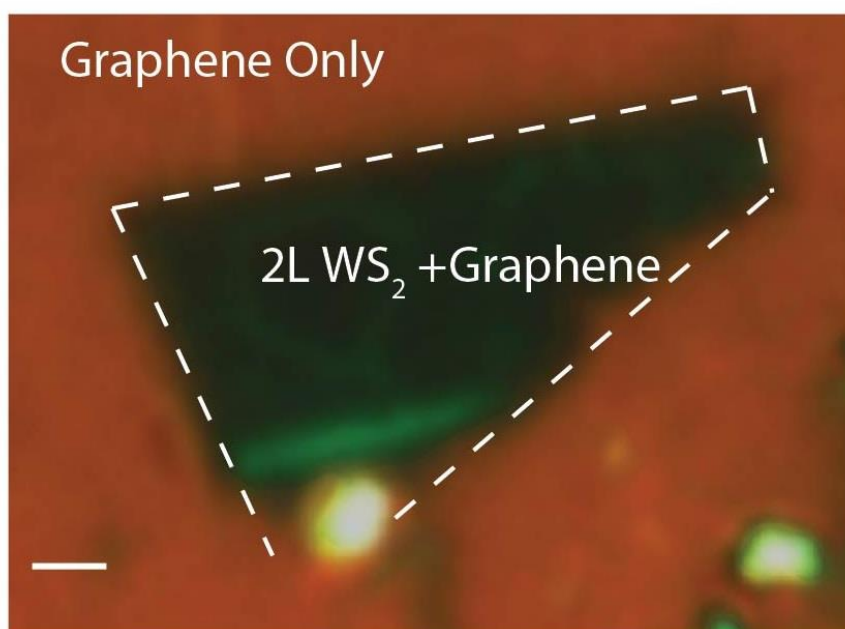


Figure 5.1 Optical image of a 2L-WS₂/graphene heterostructure.

5.3.2 Linear absorption microscopy

We doubled the fundamental light (1.57 eV) from a Ti: Sapphire oscillator (Coherent Mira 900) to measure the linear absorption at 3.14 eV of a CVD-WS₂/graphene on a transparent sapphire substrate. A 40 × /NA = 0.60 objective was used to focus light onto the sample. Both the transmission and reflection light were then collected and detected by avalanche Si photodiodes (Hamamatsu). The absorption of WS₂/graphene is calculated by using the graphene only region on the same substrate as the reference and solving the following two equations together:

$$I = T_g + CR_g + A_g \times I \text{ (on the reference graphene only region)} \quad (1)$$

$$I = T_{\frac{WS_2}{G}} + CR_{\frac{WS_2}{G}} + A_{\frac{WS_2}{G}} \times I \text{ (on the heterostructure region)} \quad (2)$$

where I is the total incident light intensity; T_g is the transmitted light intensity of graphene; R_g is the reflection light intensity of graphene; A_g is the absorption of graphene; $T_{\frac{WS_2}{G}}$ is the transmitted light intensity of WS₂/graphene; $R_{\frac{WS_2}{G}}$ is the reflection light intensity of WS₂/graphene; $A_{\frac{WS_2}{G}}$ is the absorption of WS₂/graphene; C is the collection efficiency of the reflection arm. We use a A_g value of 0.0424 for graphene at 3.14 eV from a previous report.¹²⁴

230

5.3.3 First-principles calculations

All systems were fully optimized (atomic positions and lattice vectors) within the density-functional theory (DFT). In the commensurate model, we have averaged the lattice vectors of graphene and WS₂ using 5×5 and 4×4 unit cells, respectively. This results in the lattice parameter $a = 12.433 \text{ \AA}$, corresponding to 0.6% stretch of graphene and 1.7% compression of WS₂. In the incommensurate model, we superposed the band structure of

perfect monolayers of graphene and WS₂ for the presentation of the band structure and the mismatch of the Brillouin zones of both materials. The models were fully optimized using CRYSTAL09 with the following basis sets: C 6-21G*²³¹, S 86-311G*²³², W large-core ECP²³³, and the PBE functional²³⁴ with the D3 dispersion correction proposed by Grimme²³⁵. Band structures were obtained from the VASP code²³⁶⁻²³⁸ using projector-augmented waves (PAW) with the energy cutoff of 500 eV for the commensurate model and 600 eV for the unit cells. We have used the HSE06 functional²³⁹ together with the spin-orbit coupling for the incommensurate band structure representation, while the commensurate system was treated using PBE. The layered models were calculated with a 20 Å vacuum, to ensure negligible interactions with the neighboring cells in the 3D periodic boundary condition representation. The dispersion corrections were treated at the D3 level. 3×3×1 and 6×6×1 k-point mesh were used for the larger and smaller models, respectively.

5.3.4 Spatial resolution of TAM

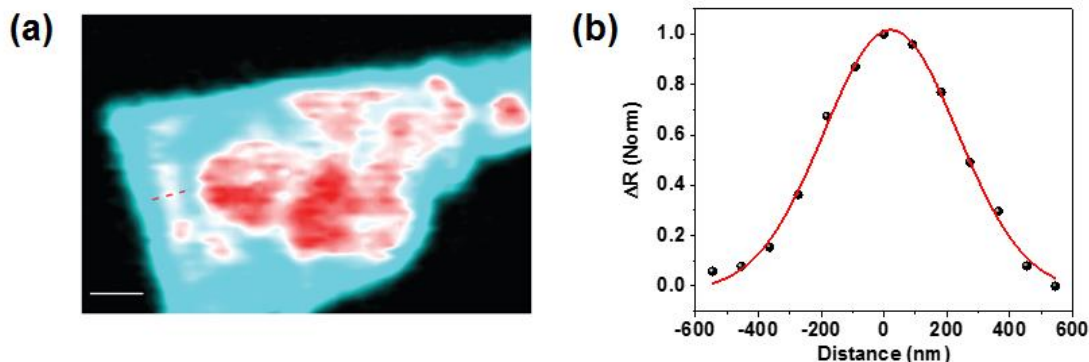


Figure. 5.2 Determination of spatial resolution of TAM. (a) TAM image of a 2L-WS₂/graphene heterostructure. (b) Gaussian function fit of line profile shown in Figure 5.2 (a).

We determine the spatial resolution of TAM to be ~ 400 nm by fitting a very small feature (red dash line in a) in the TAM imaging with a Gaussian function (b).

5.3.5 Determination of pump fluence and exciton density in the TAM measurements

In TAM experiments, excitons in WS_2 are generated by the absorption of the pump laser. The peak fluence of pump pulse (P_f) could be calculated as:

$$P_f = \frac{P}{A} \quad (3)$$

where P is the pump pulse energy, A is the pump excitation effective area. Since pump pulse is a Gaussian beam. To calculate the exciton density injected by the pump, we assume that every absorbed pump photon could create one exciton. This assumption is widely used in previous optical measurements and gives reasonable explanations to experimental results.^{107, 163, 176, 187} Then, the injected exciton density could be obtained as:

$$N = \frac{\alpha P_f}{\hbar\nu} \quad (4)$$

where α and $\hbar\nu$ are the absorption coefficient and photon energy of the pump pulse.

5.4 Results and discussion

5.4.1 Spatial heterogeneity in WS_2 /graphene heterostructure

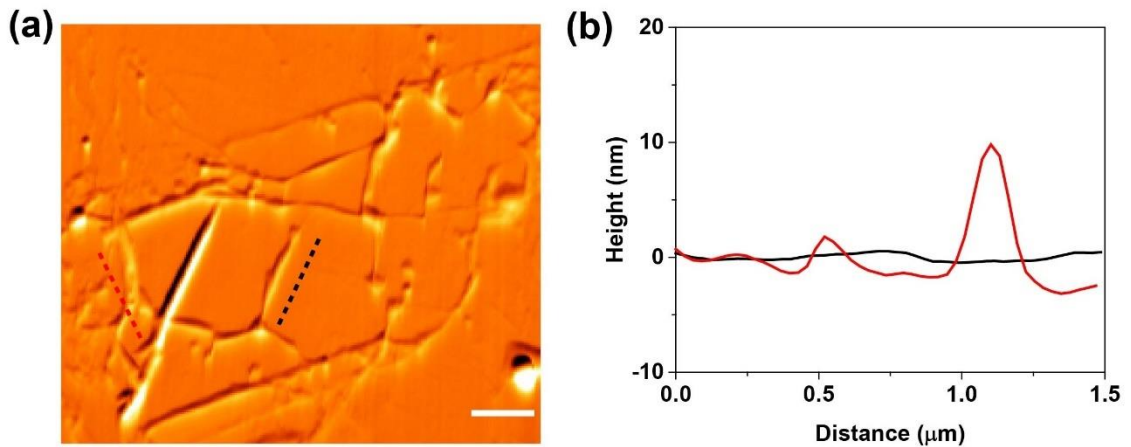


Figure 5.3 AFM measurement of the 2L- WS_2 /graphene heterostructure. (a) AFM image of the 2L- WS_2 /graphene heterostructure. (b) Line profiles taken along the black and red dashed lines indicated in (a). Scale bar represents 1 μm .

From the AFM image (Figure 5.3 (a)), significant spatial heterogeneity in the contact between the 2L-WS₂ and the graphene layer can be observed, which is common for heterostructures fabricated by transfer methods. Specifically, there is an area 1 with very flat morphology while another area 2 has a lot of ripples, which indicates good contact between the graphene and the WS₂ layers in area 1 and poor contact in area 2. The difference in contact can also be clearly seen by the AFM line scans from areas 1 and 2 shown in Figure 5.3 (b).

5.4.2 Interlayer coupling dependent charge transfer

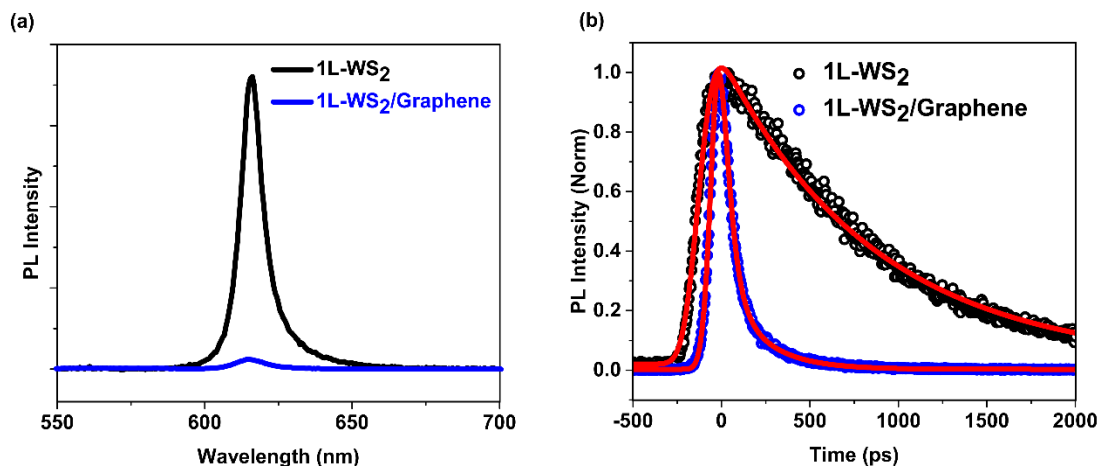


Figure 5.4 PL spectra (a) and normalized time-resolved PL dynamics (c) of individual 1L-WS₂ and 1L-WS₂/graphene, red lines are exponential fittings.

We applied photoluminescence microscopy to study charge transfer in 1L-WS₂/graphene. The integrated PL intensity of 1L-WS₂/graphene is about 70 times weaker than the individual 1L-WS₂ as shown in Figure 5.4 (a). The strong PL quenching in 1L-WS₂/graphene was also observed in previous optical measurements.^{217, 240-241} In Figure 5.4 (b), we demonstrated how charge transfer affects the PL dynamics of 1L-WS₂/graphene. In the individual 1L-WS₂, a single-exponential function convoluted with instrument

response function (IRF) was used to fit the PL dynamics. We obtained a decay constant of 675 ps, which agrees well with previous time-resolved measurement.¹⁹⁵ In the heterostructure, The PL decay is much faster and shows a two-component decay behavior with a fast decay of 44 ps (76%) and slow decay of 229 ps (24 %). We attributed the fast decay in 1L-WS₂/graphene to the charge transfer between graphene and WS₂. We noticed the heterogeneity could strongly affect the measurements results. We measured the PL signal at different locations. The data displayed here is a position where charge transfer quenching dominates.

The inherent spatial heterogeneity as imaged in Figure 5.3 (a) presents a major difficulty in elucidating interfacial charge transfer dynamics in relation to interlayer coupling.¹⁰³ To circumvent this difficulty, we employ TAM with high spatial and temporal resolutions to image how interlayer-coupling affects the dynamics of charge transfer from WS₂ to graphene. We first excite WS₂ at 3.14 eV and probing the A exciton bleach at 1.99 eV to investigate charge transfer from WS₂ to graphene. The pump fluence of $\sim 2 \mu\text{Jcm}^{-2}$ corresponds to an exciton density of $\sim 3.6 \times 10^{11} \text{ cm}^{-2}$ in 1L-WS₂ ($\sim 7.2 \times 10^{11} \text{ cm}^{-2}$ in 2L-WS₂). To construct an image, pump-induced change in probe reflection ΔR is plotted as a function of the sample position. Note that the graphene-only regions of the samples have no detectable signal under the experimental conditions due to a lower absorption coefficient compared to WS₂.

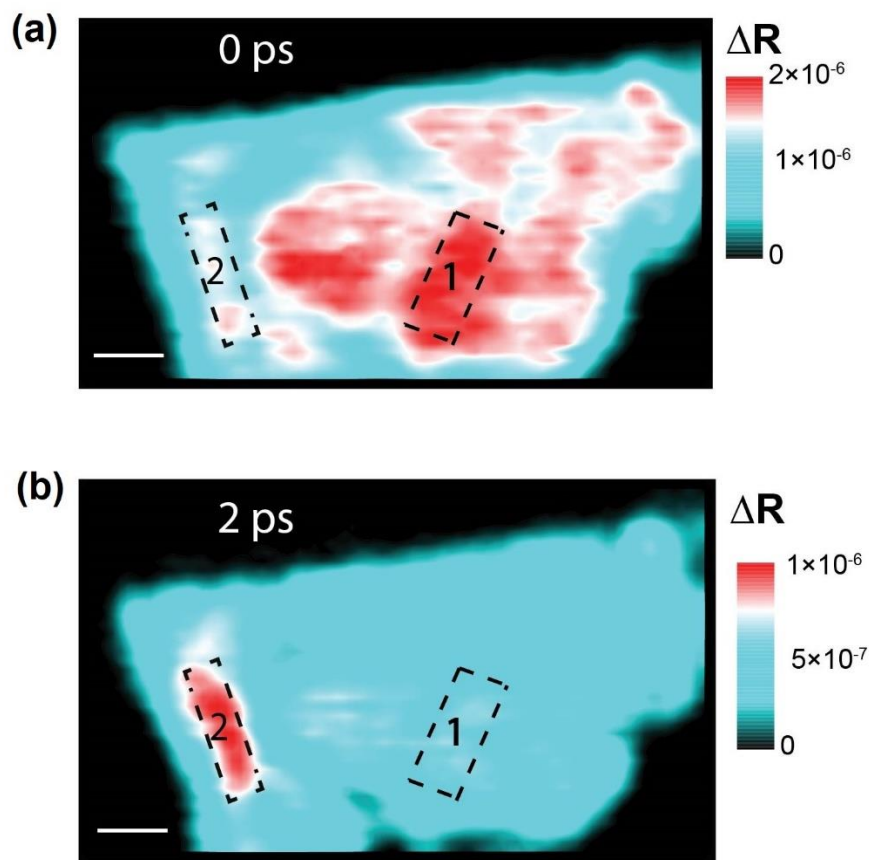


Figure 5.5 TAM image of the 2L-WS₂/graphene measured at 0 ps (pump at 395 nm and probe at 624 nm, pump fluence ~ 2 uJ/cm²). (e) TAM image measured at 2 ps.

The TAM images at 0 ps and 2 ps pump-probe delay are shown in Figures 5.5 (a) and (b), respectively. Most interestingly, TAM image at 0 ps exhibits significant heterogeneity in transient absorption (TA) signal level that correlates with morphology mapped by AFM (Figure 5.3 (a)), with higher TA signal observed for the stronger coupling area 1. The graphene only region of the sample has no detectable signal under the same pump intensity. In contrast, TAM image at 2 ps shows that area 2 has a higher signal than area 1. The result indicates that area 1 has a much faster charge transfer from WS₂ to graphene than area 2. As expected, better interlayer contact leads to faster charge transfer.

A control 2L-WS₂ is also imaged as shown in Figure 5.6 (a) and (b). No spatial heterogeneity is observed which also proves that the spatial heterogeneity in the TA signal resulted from interlayer coupling between WS₂ and graphene.

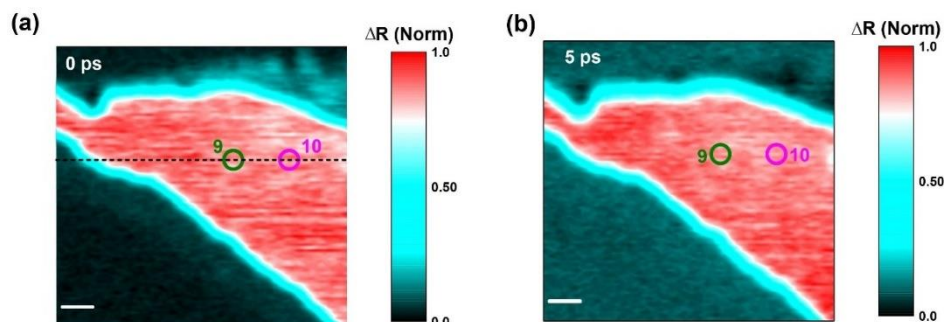


Figure 5.6 TAM images of a control 2L-WS₂ flake at time delays of 0 ps (a) and 5 ps (b) with 3.14 eV pump and 1.99 eV probe.

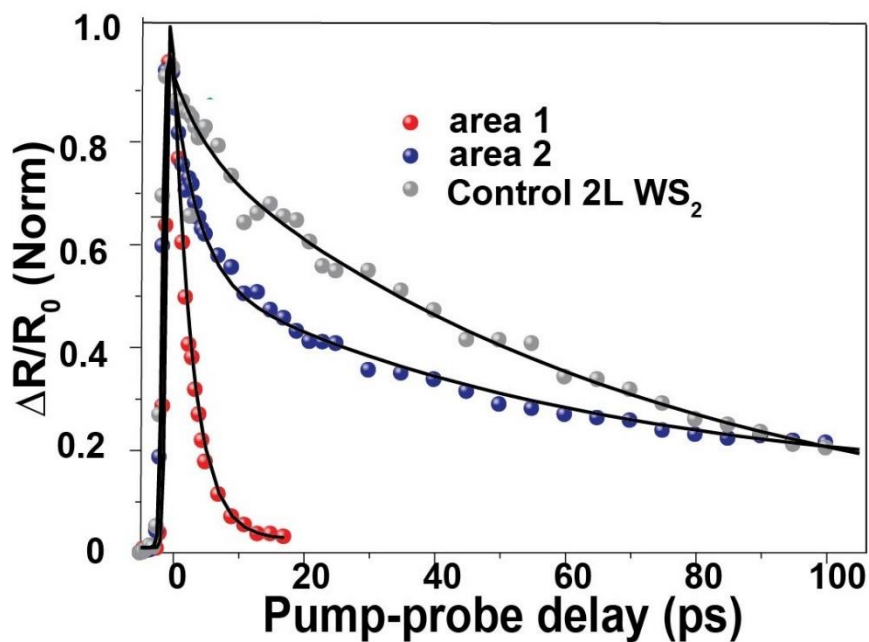


Figure 5.7 Normalized transient dynamics of the heterostructure at area 1, 2 as marked, and a control 2L-WS₂. Solid lines are the fitting curves with exponential decays convoluted with experimental response function. All scale bars represent 1 μm .

The exciton decay at the strong-coupling area 1 can be fitted with a single exponential function with a decay constant of 3.0 ± 0.1 ps (Figure. 5.7), similar to what has been reported previously.²¹⁷ On the other hand, the weak-coupling area 2 shows a much slower bi-exponential exciton decay, with a fast component of 3.8 ± 0.3 ps (55%) and a slow component of 71.3 ± 3.0 ps (45%) (Figure. 5.7). The slow decay component observed for area 2 is very similar to that from a control 2L-WS₂ flake, consistent with poor contact hampering charge transfer from WS₂ to graphene. The transient dynamics of control 2L-WS₂ is also measured as shown in Figure.5.8 and no spatial heterogeneity is observed in exciton dynamics.

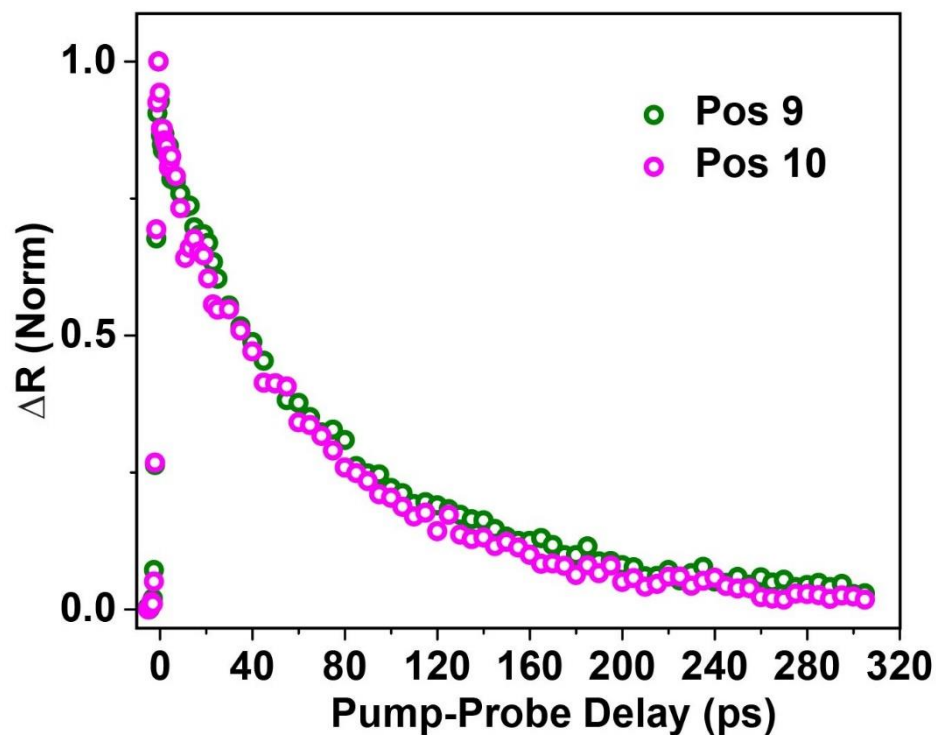


Figure 5.8 Normalized transient dynamics of position 9 and 10 in 2L-WS₂ indicated in Figure 5.5 with a pump fluence of $8.4 \mu\text{J cm}^{-2}$.

Similar spatial heterogeneity in TAM image is also observed in the 1L-WS₂/graphene heterostructure as shown in Figure 5.9 (a). Charge transfer at a strong-coupling location of the 1L-WS₂/graphene heterostructure has a characteristic time of 1.4 ± 0.1 ps (Figure 5.9 (b)), demonstrating even stronger coupling between graphene and the 1L-WS₂ layer than in the 2L-WS₂/graphene heterostructure.

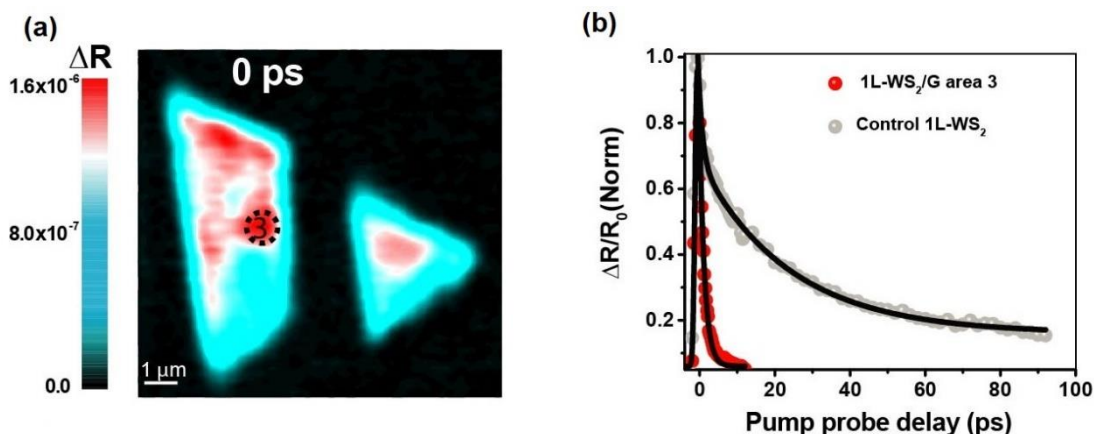


Figure 5.9 (a) Correlated TAM image of the 1L-WS₂/G heterostructure measured at 0 ps probing the A exciton resonance. Pump photon energy = 3.14 eV and probe photon energy = 1.99 eV (b) Normalized transient dynamics of the heterostructure at areas 1 and 2 as marked, and the control 2L-WS₂ layer. Solid lines are the fitting curves with exponential decays convoluted with the experimental response function. All scale bars represent 1 μm .

5.4.3 Signature of charge transfer in Raman imaging

Here we employed Raman spectroscopy to characterize the quality of interfacial contact and charge transfer doping between graphene and WS₂ layer. We found largely increase of the position of G mode (ω_G),²⁴² at which directly associates with charge carrier doping (n), in graphene in the heterostructures compared to another area without WS₂ layer shown in Figure 5.10 (a). On the other hand, the 2D mode of graphene stiffens in the heterostructure, suggesting that graphene is further p-doped (estimated $n \sim 5 \times 10^{12} \text{ cm}^{-2}$

from $\omega_G \sim 1591 \text{ cm}^{-1}$ at region A) by the underneath 2L-WS₂ via surface charge transfer (Figure 5.10 (b)). The background hole doping in graphene adjacent to the heterostructure is estimated to be $n \sim 2.5 \times 10^{12} \text{ cm}^{-2}$ ($\omega_G \sim 1585 \text{ cm}^{-1}$). In the heterostructure,

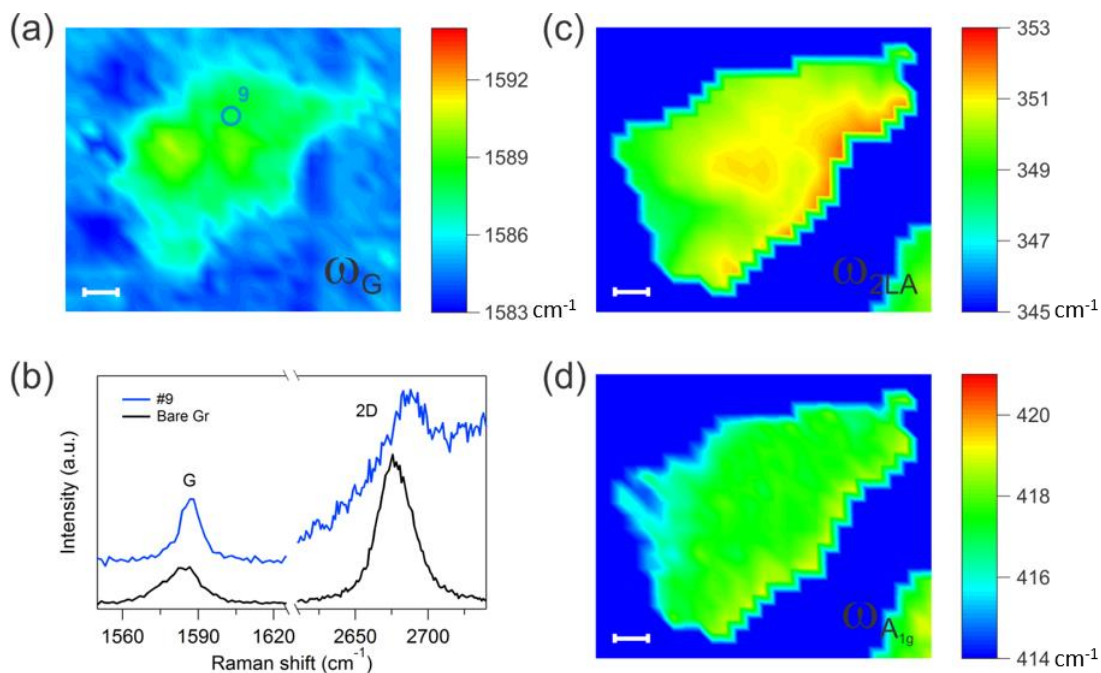


Figure 5.10 (a) Raman mapping of the G band of graphene in 2L-WS₂/graphene. Obvious shift of the G band is due to surface charge transfer doping from underneath WS₂; (b) Comparison of the Raman spectrum of graphene while sitting on a 2L-WS₂ (position 9) and a bare Si substrate (90 nm thick SiO₂). Curves are vertically shifted for clarity. The rising background for the wavenumber above 2600 cm⁻¹ originates from the photoluminescence of WS₂; Raman mapping of the position of (c) the strong peak (2LA and E¹_{2g}) and (d) the A_{1g} peak in 2L-WS₂/graphene heterostructure. All scale bars represent 1 μm.

the main peak (2LA and E¹_{2g}) shifts to a higher wavenumber while the A_{1g} remains almost unchanged (Figure 5.10 (c) and (d)). Furthermore, the full width at half-maximum (FWHM) of these peaks broadens compared to normal individual 2L-WS₂. These results can be understood by a combination of mechanical strain and charge transfer doping. We ignore the factor of temperature owing to the same measurement condition. It has been shown that

the two Raman-active phonon modes E_{12g}^1 and A_{1g} in the case of a MoS₂/graphene heterostructure downshifts (due to in-plane tensile strain) and upshifts (due to van der Waals interaction with adjacent layers), respectively.²⁴³ Since there are lattice mismatch and different thermal expansion coefficient (TEC = $6.4 \times 10^{-6} \text{ K}^{-1}$ for WS₂²⁴⁴ and $\sim -8 \times 10^{-6} \text{ K}^{-1}$ for graphene²⁴⁵), lattices of WS₂ and graphene are expected to suffer tensile and compressive strains respectively when forming a heterostructure. We indeed observe a compressive strain of $\sim -0.3 \%$ in graphene of the heterostructure by analyzing the correlation between the two Raman modes (G and 2D) of graphene²⁴⁶, but do not find tensile strain (downshift of the E_{12g}^1) in the 2L-WS₂ layer which is inconsistent with the expectation due solely to lattice and TEC mismatch. Since notable p-doping is found in the graphene of 2L-WS₂/graphene, comparable effect of charge transfer (electron) doping must be accounted for the interpretation of the Raman data measured in WS₂. It has been reported that chemical doping of WS₂ on typical Si substrate with lithium fluoride (n-type dopant) yields downshifting and broadening of A_{1g} peak²⁴⁷, which could compensate the upshift (no position change of A_{1g}) caused by van der Waals interaction at the interface of WS₂ and graphene. On the other hand, the pre-dominant 2LA mode in the strongest peak at $\sim 350 \text{ cm}^{-1}$ slightly upshifts upon electron doping, which could overcompensate the effect of tensile strain, resulting in an upshift of the peak (Figure 5.11). Hence, our Raman result in the WS₂ is qualitatively consistent with the synergistic effect arising from interfacial charge doping and mechanical strain.

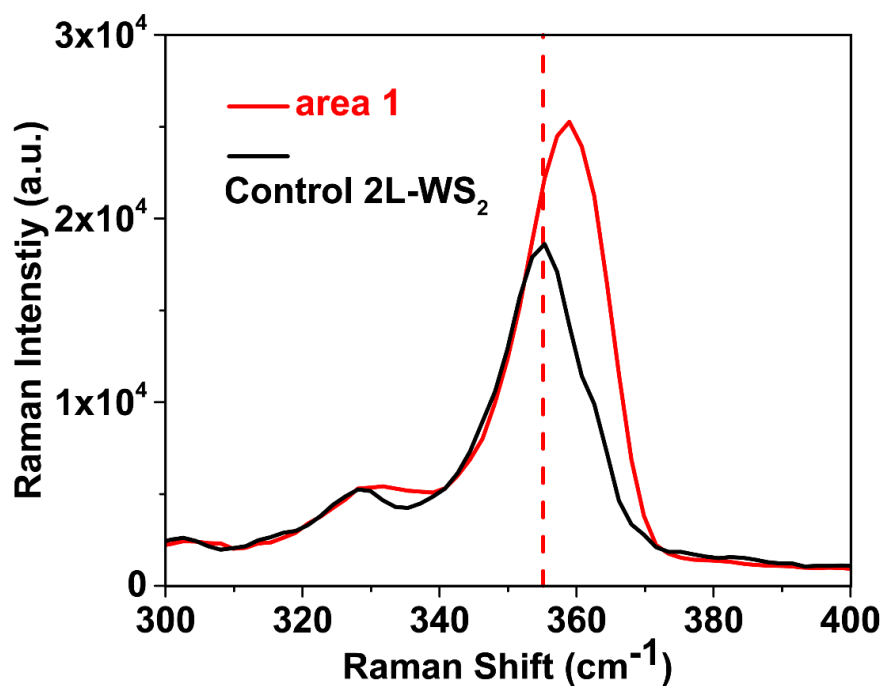


Figure 5.11 Raman spectra of 2L-WS₂/G heterostructure (area 1 as shown in Figure 1 (d)) (red line) and control 2L-WS₂ (black line). The enhancement ratio of Raman intensity is about 1.4 times in 2L-WS₂/graphene than control 2L-WS₂.

5.4.4 Transient bandgap renormalization

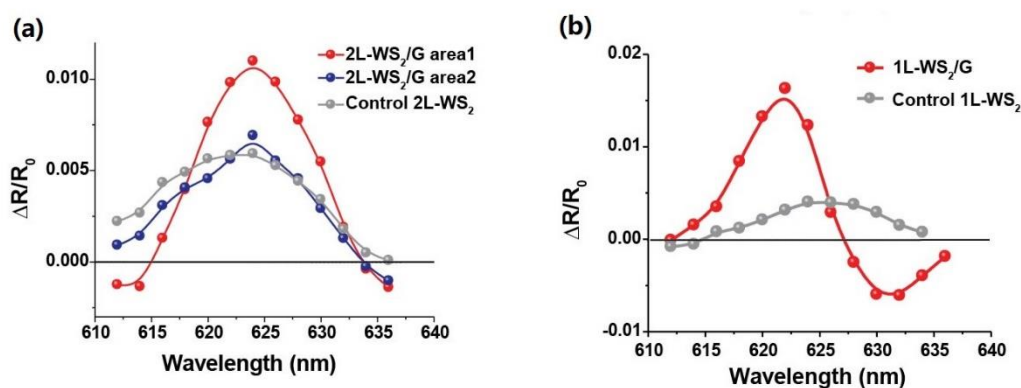


Figure 5.12 (a) TA spectrum of A exciton resonance in 2L-WS₂/graphene (0 ps delay) at different positions as well as for a control 2L-WS₂. Pump photon energy is 3.14 eV and pump fluence of 2 μJ / cm². (b) TA spectrum of A exciton resonance in 1L-WS₂/graphene and a control 1L-WS₂ at 0 ps delay.

Figure 5.12 (a) plots transient absorption spectra of 2L-WS₂/graphene at areas 1 and 2 along with the control 2L-WS₂ taken with pump excitation energy of 3.14 eV pump. The three spectra are taken under identical experimental conditions. Photoinduced bleaching of the A exciton band (also known as saturation of absorption) ~ 2.0 eV is observed for both the heterostructure and the control 2L-WS₂ flake, similar to previously reported. The magnitude of the TA signal at strong-coupling position 1 is ~ 2 times higher than the control 2L-WS₂ while the weak-coupling area 2 has similar TA amplitude as the control. The enhanced TA signal at strong-coupling area 1 is greater than the simple addition of signals from graphene and WS₂ because graphene only has no detectable signal under the experimental condition. TA spectrum from a strong-coupling location of a 1L-WS₂/graphene heterostructure is shown in Figure 5.12 (b), along with a control 1L-WS₂. Notably, the TA signal is enhanced even more in 1L-WS₂/graphene heterostructure, ~ 4 times over the control 1L-WS₂ flake, consistent with stronger graphene-WS₂ coupling. The TA spectrum of the 1L-WS₂/graphene heterostructure is very different from the control: it has a derivative shape with a new redshifted photoinduced absorption band.

The derivative shaped TA spectrum with the redshifted photoinduced band observed for 1L-WS₂/G heterostructure (Figure 5.12 (b)) is a signature of bandgap renormalization due to the screening of photogenerated free carriers.^{146, 148, 248} The transient reduction of E_{opt} is estimated to be ~ 30 meV at 0 ps from Figure 5.12 (b). Bandgap renormalization occurs when the screening of Coulomb interaction by free electrons and holes becomes more significant, which usually caused by exciton dissociation at high density.¹⁴⁶ One consequence of screening by free carriers is the shrinkage of the single-particle band gap (bandgap renormalization); the other consequence is the reduction of

exciton binding energy E_b . The final E_{opt} reflects the balance of the two energy shifts. In 2D semiconductors the shrinking of the single particle bandgap is more significant than the reduction of E_b and the combined effect is a redshifted E_{opt} at high free carrier concentration.^{133, 146, 148, 249-250} The observation of bandgap renormalization effects in 1L- WS_2 /graphene heterostructure is very surprising because the pump intensity we use here is about an order of magnitude lower than the previous studies that reported bandgap renormalization. The exciton density here corresponding to an inter-exciton distance of ~ 6 nm, much greater than the radius of the A exciton of ~ 1.5 nm¹⁹⁰, thus many body excitonic effects such as bandgap renormalization should be negligible. At such low exciton density, Pauli blocking by excitons dominates, which could broaden absorption but should not shift optical bandgap energy E_{opt} .²⁵¹ Similar transient bandgap renormalization has also been observed for another 1L- WS_2 /graphene heterostructure on a sapphire substrate (Figure 5.13).

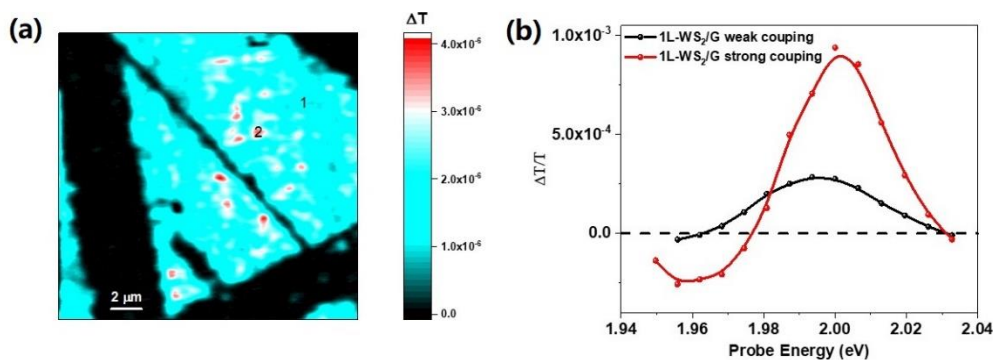


Figure 5.13 TA image (a) and spectrum of A exciton resonance for a strong and a weak coupling location of a 1L - WS_2 /graphene heterostructure on a sapphire substrate at 0 ps. Pumped at 3.14 eV.

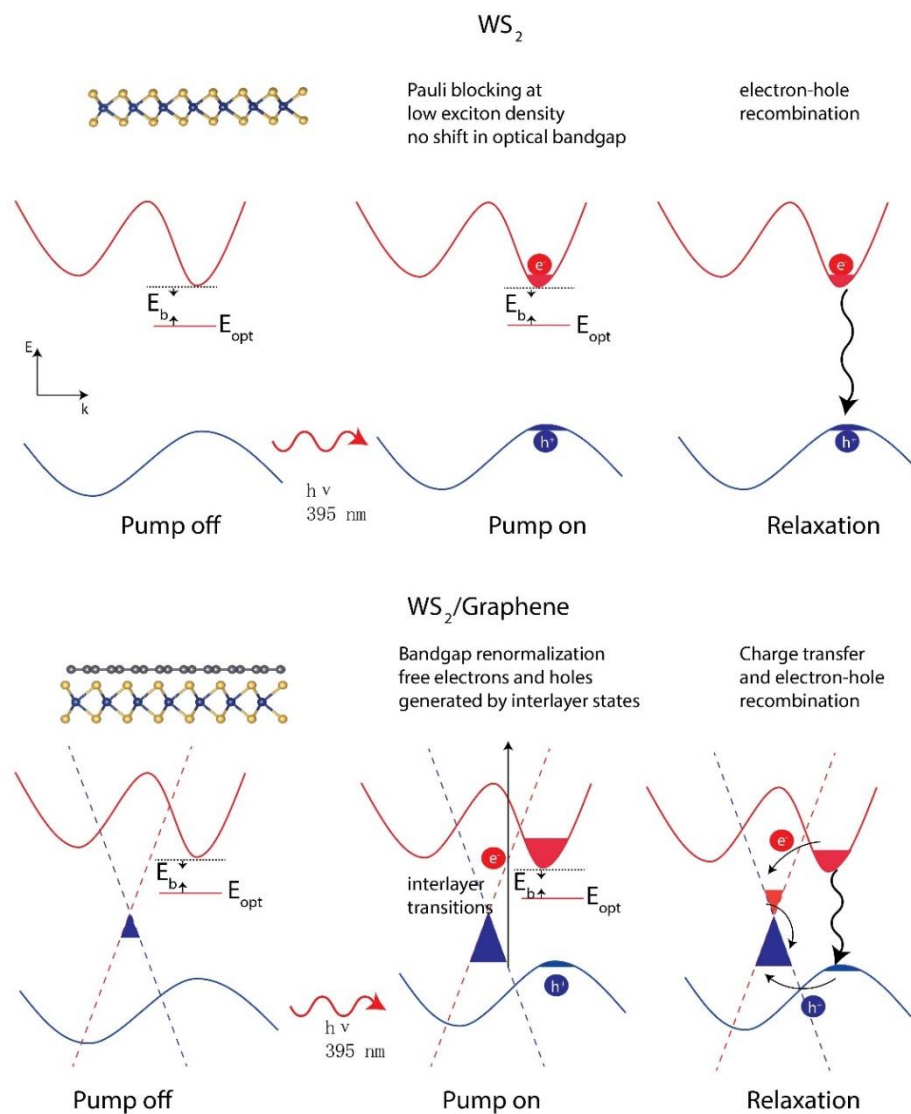


Figure 5.14 Summary of different processes following photoexcitation in WS_2 layers (a) and in 1L- WS_2 /graphene heterostructure (b).

Figure 5.14 schematically summarizes different processes following 395 nm photoexcitation in the heterostructures and corresponding controls. As illustrated in Figure 5.12 (a), photoexcitation of the WS_2 layers forms excitons that decay by electron-hole recombination and other nonradiative pathways (not shown). Photoexcitation of the heterostructures creates two types of excited states: excitons through intralayer excitonic transitions and free electron and holes (electrons in the WS_2 layer and the holes in the

graphene) through interlayer transitions. The relaxation processes in the heterostructures are more complex involving rapid electron and hole transfer from WS₂ to graphene. Screening from the free carriers leads to transient bandgap renormalization in the 1L-WS₂/graphene heterostructure. Note that the density of free carriers is not quite high enough for the 2L-WS₂/graphene heterostructure to observe bandgap renormalization effects because the interlayer transitions are weaker than those in 1L-WS₂/graphene heterostructure (Figure 5.12).

The larger transient bandgap renormalization effects at the strong coupling locations could be explained by the lower binding energy of the interfacial CT states than that for the A excitons in WS₂ (~200 meV when it is covered by graphene). Because of the spatially separated nature and the efficient screening of Coulomb interaction by graphene, electrons and holes generated at the interface from the CT states are more “free” and can potentially screen the Coulomb interaction more effectively than the A excitons, which result in a larger shift in the exciton resonance.

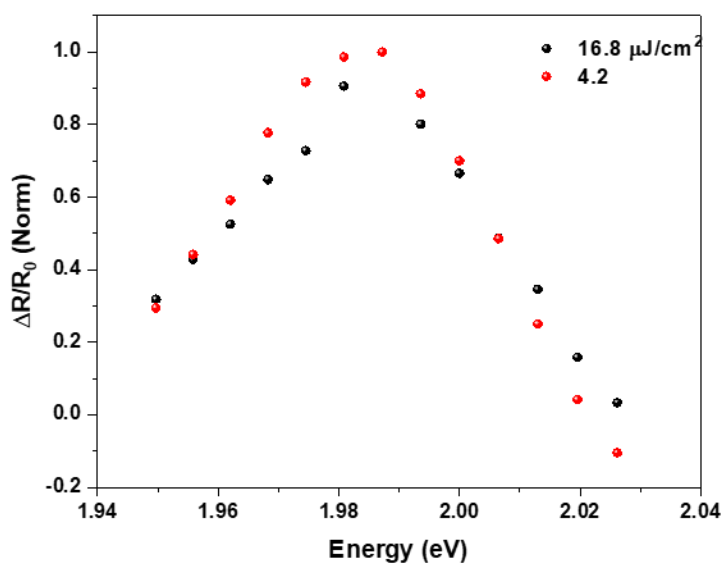


Figure 5.15 Pump intensity dependent TA spectra of a control 1L-WS₂ flake. Pump photon energy = 3.14 eV.

To verify the transient bandgap renormalization effects observed is not just due to higher exciton density, we have measured TA spectrum of 1L-WS₂ at exciton density from $7.2 \times 10^{11} \text{ cm}^{-2}$ to $2.9 \times 10^{12} \text{ cm}^{-2}$ (see Figure 5.15) Even at 8 times higher exciton density than that in the measurements of Fig. 4A, no obvious transient bandgap renormalization has been observed. We note that a previous study²⁵² reported the exciton redshift at exciton density of as low as 10^{11} cm^{-2} under similar non-resonant excitation condition, which is somewhat inconsistent with our results.

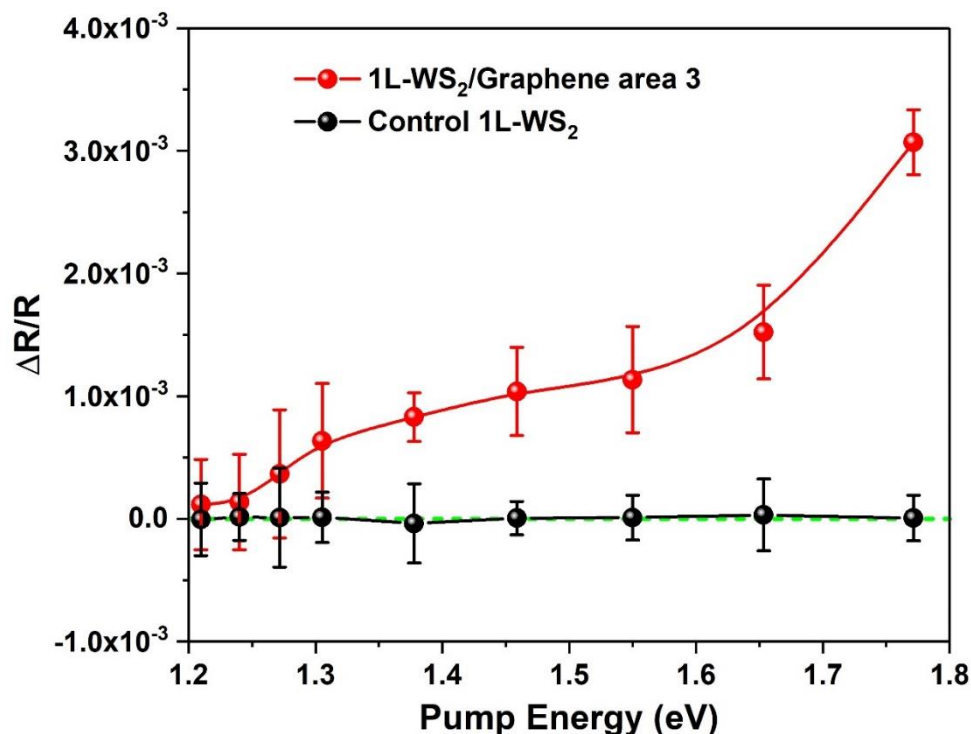
5.4.5 Carrier generation by excitations below the WS₂ bandgap

Figure 5.16 TA signal at 0 ps probed at 1.99 eV (A exciton resonance) for the 1L-WS₂/graphene heterostructure when varying the pump photon energy from 1.2 eV to 1.8 eV, pump fluence $\sim 2 \mu\text{J cm}^{-2}$.

We perform measurements with pump photon energies below the WS₂ bandgap where only the interlayer CT transitions and graphene can be excited. Figure 5.16 plots the TA signal intensity at 0 ps probed at the A exciton resonance (1.99 eV) in the 1L-WS₂/graphene heterostructure and a control 1L-WS₂ when varying the pump photon energy from 1.2 eV to 1.8 eV (bandgap of WS₂ is ~ 2 eV) with a pulse spectral width of ~ 20 meV. No detectable TA signal above the noise level is observed for the control 1L-WS₂ layer with pump energy lower than 1.8 eV.

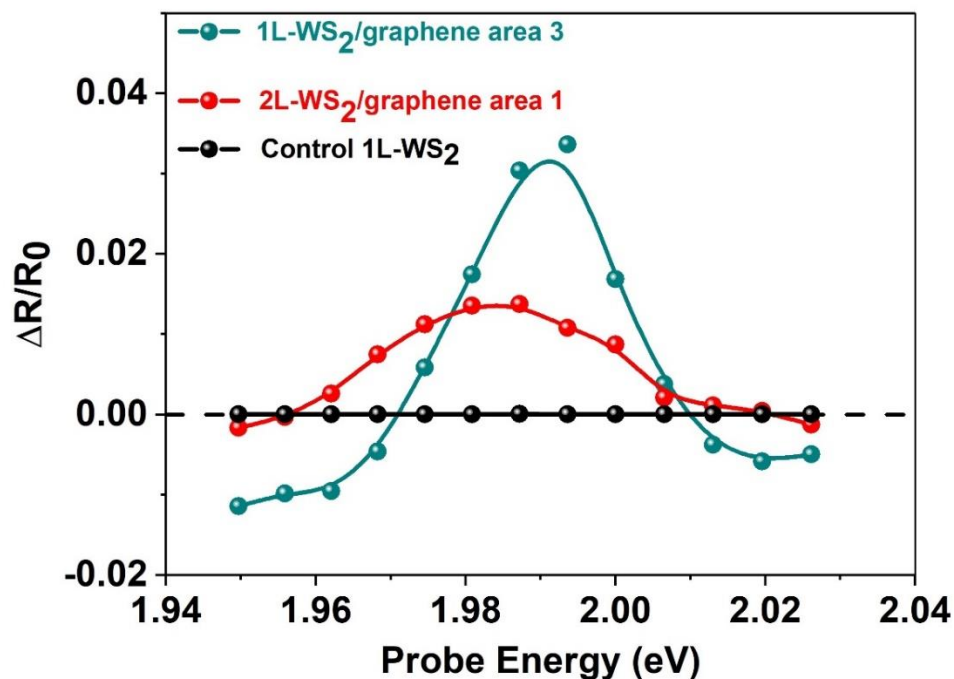


Figure 5.17 TA spectrum of A exciton resonance in the 1L-WS₂/graphene, 2L-WS₂/graphene heterostructures, and the control 1L-WS₂ at 0 delay time with 1.57 eV pump photon energy, pump fluence $\sim 17 \mu\text{J cm}^{-2}$.

In contrast, both heterostructures show TA spectra that track the WS₂ A exciton resonance with pump energy of 1.57 eV (Figure 5.17). The TA signal intensity is strongly dependent on the interlayer coupling. Figure 5.18 illustrates TAM images at 0 ps delay with 1.57 eV pump photon energy for the same 2L-WS₂/graphene heterostructure as shown in Figure 5.1. TA signal intensity is higher at the strong-coupling area 1 than the weak-coupling area 2. The overall patterns observed by TAM imaging with the 1.57 eV pump (Figure 5.18) are similar to those with the 3.14 eV pump as shown in Figure 5.5 (a).

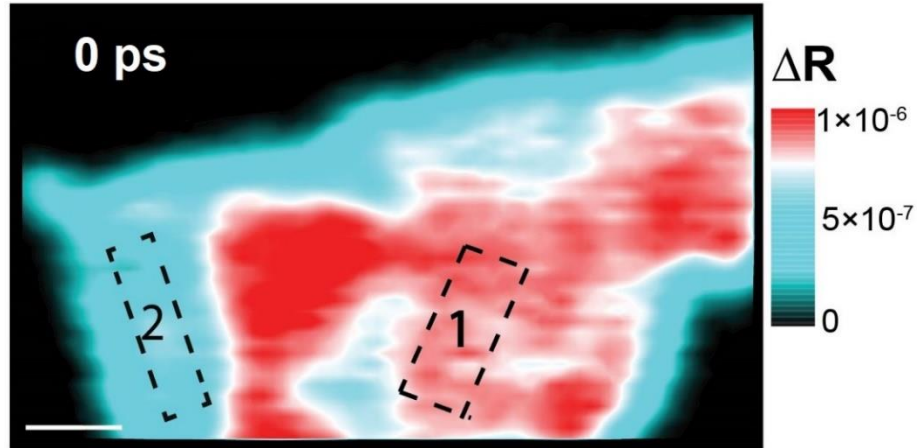


Figure 5.18 TAM imaging of 2L-WS₂/graphene at 0 ps, scale bar represents 1 μm . 1.57 eV pump and 1.99 eV probe, pump fluence $\sim 17 \mu\text{J cm}^{-2}$.

There are two possible mechanisms (illustrated in Figure 5.19) that could lead to the bleaching of A exciton by excitation below the WS₂ bandgap. One possibility is that the photon is absorbed by the graphene layer and hot carriers are subsequently transferred from graphene to WS₂ (mechanism 1, only electron pathway is shown).²⁵³ Similar mechanism has led to the generation of photocurrent with excitations below the bandgap in graphene/WSe₂ heterostructures, as reported by Massicotte et al.²⁵³ The absorption by graphene is due to interband transitions, creating photoexcited electrons and holes with energy $E = \frac{E_{\text{photon}}}{2}$. Carrier-carrier scattering establishes a quasi-equilibrium distribution in ~ 30 fs with an elevated effective electron temperature T_e (41). For hot electron injection, the Schottky barrier is equal $\Phi_B = (E_{\text{CBM}} - E_D)$ where E_{CBM} is the conduction band minimum (CBM) of WS₂²⁵⁴⁻²⁵⁵ and E_D is the Dirac point of the graphene layer. Φ_B can vary depending on the doping level of the two layers and the substrate. The hot electrons with energy larger than the barrier height Φ_B can be injected into the WS₂ layer. The number of electrons with sufficient energy is given by Boltzmann distribution and scales

with $e^{-\frac{\Phi_B}{k_b T_e}}$, where k_b is the Boltzmann constant.²⁵³ Similar process also exists for the holes. The other possible mechanism is through direct excitation of interlayer CT transitions (mechanism 2 in Figure 5.19), where electrons can be promoted from graphene to WS₂ (shown in Figure 5.19) or holes promoted from WS₂ to graphene (not shown). For mechanism 2, the momentum of graphene and WS₂ needs to be taken into account and the transition energies will be discussed in the following section.

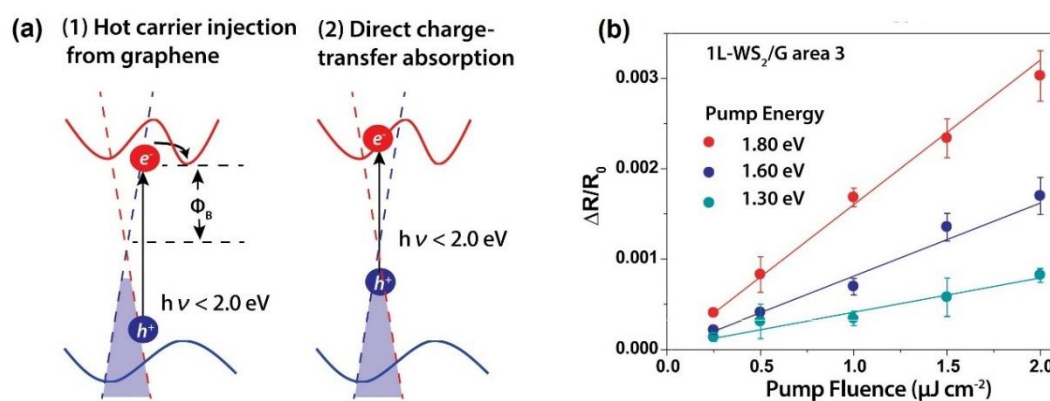


Figure 5.19 (a) Schematic showing two possible mechanisms. One possibility is that the graphene layer is excited and hot carrier is subsequently transferred from graphene to WS₂ (mechanism 1), and the other possibility is the direct excitation of interlayer CT transitions (mechanism 2). (b) The amplitude of the TA signal at a 0-ps time delay versus pump fluence for the 1L-WS₂/graphene heterostructure at area 3 showing a linear dependence at three different pump photon energies (probe, 1.99 eV).

Both mechanisms illustrated in Figure 5.19 could contribute to the TA signal; however, it is highly challenging to separate these two contributions. In principle, although linear absorption could directly measure the CT transitions from mechanism 2, this is a difficult task because of the weak oscillator strengths.²⁵⁶ For instance, the interlayer exciton oscillator strength in MoSe₂/WSe₂ heterostructures is at least 20 times weaker than that of the intralayer exciton.¹⁰⁴ To separate the contribution from the two mechanisms, we

examined the pump fluence dependence when excited below the WS₂ bandgap. As demonstrated by Massicotte et al²⁵³, the photocurrent exhibits a P^α ($\alpha > 1$) dependence on the pump fluence due to the hot carrier injection contribution when excited below the bandgap of WSe₂, which can be explained by the fact that the number of electrons with sufficient energy scales with $e^{-\frac{\Phi_B}{k_b T e}}$. In contrast, direct absorption by WSe₂ above the bandgap leads to a linear power dependence ($\alpha = 1$). As shown in Figure 5.19 (b), a linear dependence (that is, $\Delta R \propto P$, $\alpha = 1$) is observed for excitations at 1.30, 1.60, and 1.80 eV in the 1L-WS₂/graphene heterostructure, which could not be explained by hot carrier injection from graphene. A linear pump fluence dependence is also observed for the 2L-WS₂/graphene heterostructure when excited at 1.57 eV as shown in Figure 5.20.

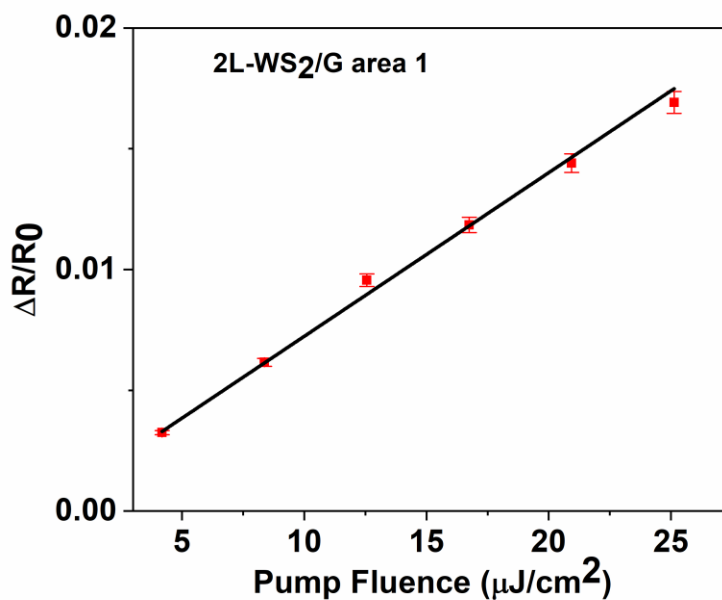


Figure 5.20 The amplitude of the TA signal at 0 ps time delay versus pump fluence for the 2L-WS₂/graphene heterostructure at area 1. Pump = 1.57 eV, probe = 1.99 eV.

On the other hand, direct CT absorption (mechanism 2) should lead to the linear power dependence similar to the absorption by WS₂ above the bandgap. Therefore, we conclude that direct CT absorption also contributes to the observed TA signal in the 1L-WS₂/graphene and 2L-WS₂/graphene heterostructures when excited below the bandgap. We note that the WSe₂ structures in the graphene/WSe₂ heterostructures studied by Massicotte et al²⁵⁵ are multilayer (3 to more than 100 layers), and the contribution from interlayer CT absorption to the photocurrent should be much weaker than in the heterostructures based on the single-layer WS₂ investigated here. This is because the oscillator strength of the CT transitions decreases as the thickness of the TMDC increases, as the additional layers screen the electron-hole interaction in the CT states.²⁵⁷⁻²⁵⁸ The decreased exciton oscillator strength as the dielectric constant increases has been observed in single-walled carbon nanotubes.²⁵⁷

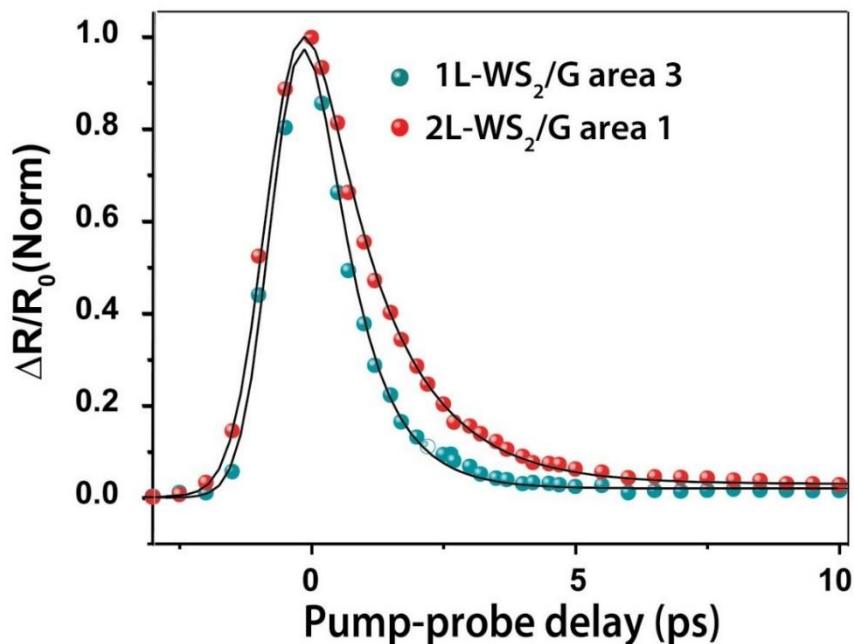


Figure 5.21 Normalized transient dynamics of the 1L-WS₂/graphene heterostructure at area 3 and the 2L-WS₂/graphene heterostructure at area 1. Pump photon energy is 1.57 eV and probe photon energy is 1.99 eV. Solid lines are fits with a single exponential decay function convoluted with the experimental response function.

Both hot carrier injection and direct CT absorption mechanisms can lead to a charge-separated state, where the electron (hole) resides in the WS₂ and the hole (electron) remains on the graphene layer. Consequently, the bleaching of A-exciton transition results from Pauli blocking and/or bandgap renormalization in WS₂.¹⁴⁸ The dynamics of charge generation and recombination has been measured following the 1.57-eV pump excitation (Figure 5.21). For mechanism 1, a rise time is expected corresponding to hot carrier transfer from graphene. In contrast, direct excitation of the CT transitions should lead to an instantaneous rise of the TA signal. The TA signal rise is instantaneous within a pulse width of ~300 fs for both the 1L-WS₂/graphene and 2L-WS₂/graphene heterostructures (Figure 5.21), probably due to the fact that the time resolution of our experiments is not sufficient to resolve hot carrier injection from graphene. In the 1L-WS₂/graphene

heterostructure, the recombination of the electrons and holes at the interface is 0.78 ± 0.04 ps, which is shorter than that of 1.30 ± 0.03 ps in the 2L-WS₂/graphene heterostructure. The faster recombination in the 1L-WS₂/graphene heterostructure suggests that the interfacial charge-separated states are dependent on the detailed electronic coupling at interfaces.⁵² The interfacial electron-hole interaction strength decreases as the thickness of TMDC increases because the additional layers screen the interaction.²⁵⁷⁻²⁵⁸ For the charge-separated states, the spatial indirect nature (that is, electrons and holes reside in different layers) should dictate the recombination process. The indirect intralayer exciton band structure of 2L-WS₂ probably does not play an important role in determining the lifetime of interfacial charge recombination.

5.4.6 First-principles calculation of interlayer charge transfer transitions

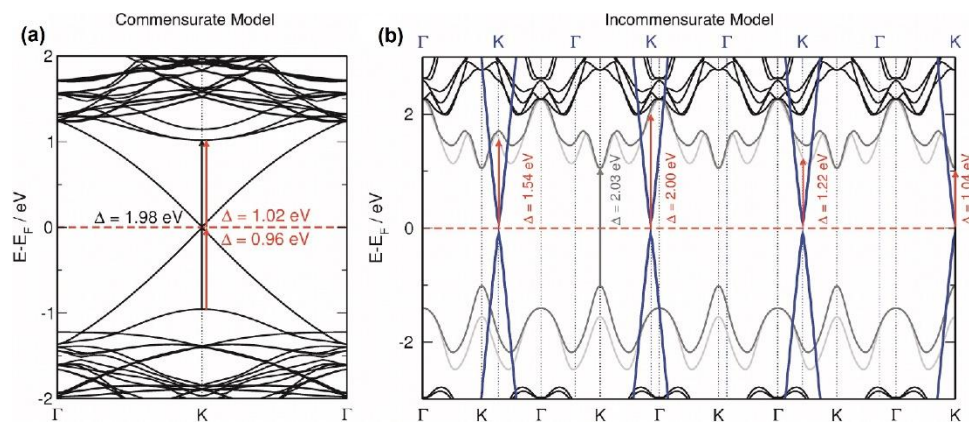


Figure 5.22 Band structure of the heterostructure. (A) Commensurate model of a 5×5 graphene/ 4×4 WS₂ supercell (at the PBE level) and (B) incommensurate model of corresponding perfect unit cells (as in a single layer) of each component (at the HSE06/SOC level) along the Γ -K direction. The red arrows indicate interlayer transitions.

To identify possible interlayer CT transitions, we performed band structure calculation for the 1L-WS₂/graphene heterostructure from first principles using density functional theory (DFT). We considered two models, the commensurate and

incommensurate. In the first model, we take a 4×4 WS₂ and a 5×5 graphene supercell, because the lattice vectors of these two cells have a mismatch of only 2.3%. We then average both lattice vectors so that 4×4 WS₂ and 5×5 graphene supercell sizes match exactly. This results in small stretching of the WS₂ monolayer and compression of the graphene layer. The corresponding band structure (Figure 5.22(a)) is an almost perfect superposition of the two individual band structures of graphene and WS₂, that is, the band edges of both systems are kept almost unaffected by one another, and we can determine the band shift of the WS₂ with respect to graphene: Conduction band of WS₂ is situated at about 1 eV above the Dirac point of graphene. Note that the Dirac point might not be the most precise in the present context, because there is a small band gap (~ 11 meV) opening in the heterostructure.

Because the lattices in the actual heterostructures are not aligned, we next consider an incommensurate model to account for a large lattice mismatch of $\sim 22\%$ (lattice constant of graphene is 2.46 \AA and that of WS₂ is 3.15 \AA). Although this first-principles calculation is not computationally feasible at present, we calculated the separate perfect monolayers and plotted their band structure as an overlap, with the shift of the band edges calculated in the previous step. The result for the Γ -K direction is shown in Figure 5.22(b). Because of the lattice mismatch, the Brillouin zones are also shifted with respect to each other. Therefore, the K points do not overlap in every cell, in contrast to the commensurate model. As shown in Figure 5.22(b), additional interlayer excitations exist in the incommensurate lattices, which allow the excited electrons from graphene to WS₂ or holes from WS₂ to graphene that could enhance carrier generation. However, the interlayer excitations are not observed for the other direction along the Γ -M path (see Figure 5.23).

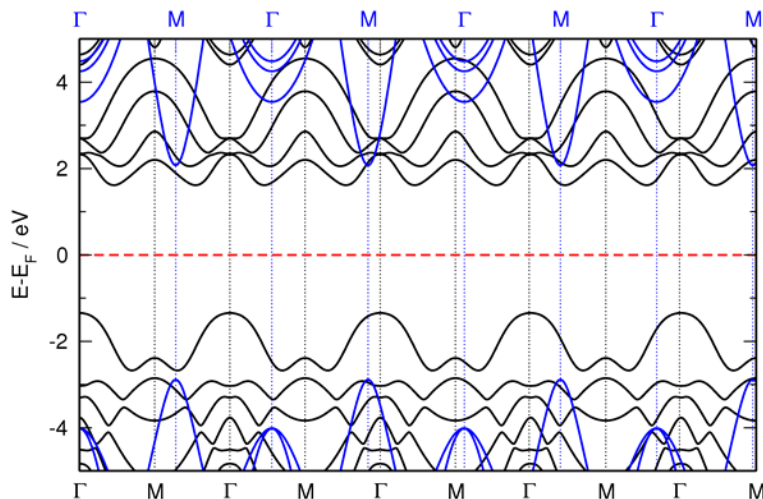


Figure 5.23 Band structure of the incommensurate model of the perfect unit cells calculated along the Γ -M directions (at the HSE06/SOC level). No additional transitions between graphene and WS₂ are expected in comparison with the Γ -K directions shown in Figure 5.22.

The interlayer CT transitions below the bandgap of WS₂ are identified in Figure 5.22(b). There is a transition of electron from the K point of graphene to the K point of WS₂ at 1.04 eV, a transition from the K point of graphene to the conduction band of WS₂ near the Γ point with an energy of 1.22 eV, and a transition at 1.54 eV from the K point of graphene to between the Γ and K point of WS₂. Note that inherent errors of DFT neglect exciton binding energy and may introduce a constant energy shift of the conduction band. According to high-level calculations on a single-layer WS₂, the error in predicting the transition energies should be no more than 0.5 eV.²⁵⁹ In addition, the graphene layer is p-doped with a Fermi level shifted by ~ 0.17 eV, as determined by Raman spectroscopy (Figure. 5.24). Taking these two effects into account, the predicted transition energies are consistent with the absorption band of 1.2 to 1.8 eV, as shown in Figure 5.16. On the basis of the agreement, we assign the interlayer transitions observed to electrons from the valence bands of graphene that are promoted to the conduction bands of WS₂. We cannot

entirely rule out the transitions prompting holes from WS₂ to graphene, and they probably also contribute. Note that our model in Figure 5.22(b) is incomplete, and it reflects only one WS₂/graphene rotation angle (with matching lattice orientations). Therefore, the intensities of the interlayer excitations may be dependent on the mutual rotation of the layers. However, the CT transition energies should still fall within the same range of 1 to 2 eV regardless of the rotation angle, because the band structure of the heterostructure is almost perfectly the superposition of that of graphene and WS₂. Further, because of a large lattice mismatch of ~22% and the polycrystalline nature of the CVD graphene, many rotation angles likely coexist in the heterostructures measured experimentally. Therefore, the measured CT transition energies are probably the average of many rotation angles.

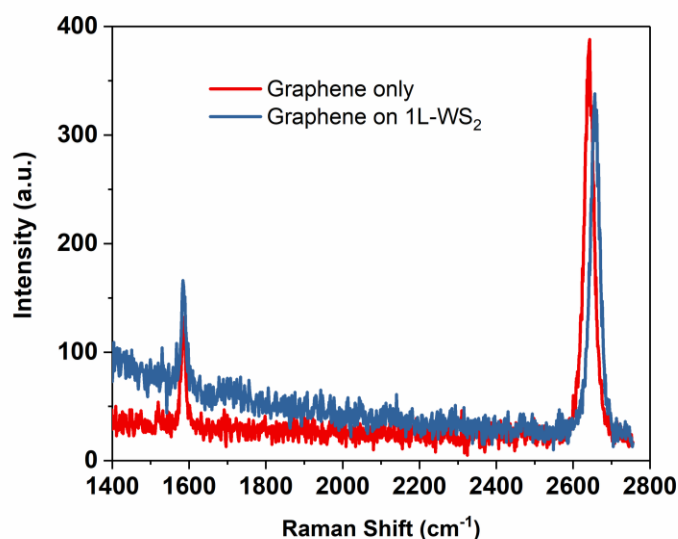


Figure. 5.24 Raman spectra of the 1L-WS₂/graphene heterostructure and the Fermi level shift of graphene. No obvious change in the position of G peak ($\sim 1586 \text{ cm}^{-1}$) in the two regions, whereas there is a blue shift of the 2D peak ($\sim 15 \text{ cm}^{-1}$) for the graphene layer on WS₂. By analyzing the correlation of the two peaks, we estimate a p-doping density of $2 \times 10^{12} \text{ cm}^{-2}$ in graphene on 1L-WS₂ corresponding to a Fermi level shift of 0.17 eV. Spectra are shifted vertically for clarity.

5.4.7 Enhanced carrier generation by excitation above the bandgap

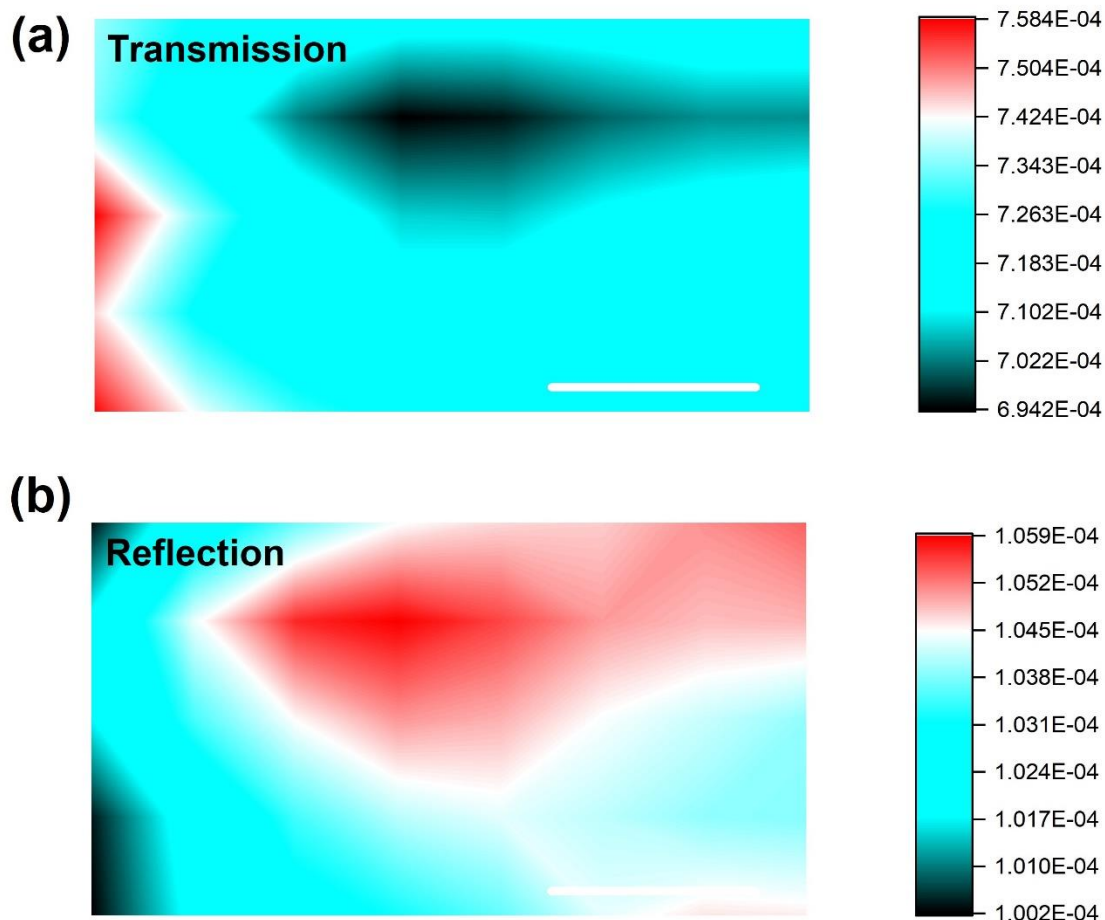


Figure 5.25 Correlated (a) transmission and (b) reflection images of the same 1L-WS₂/graphene heterostructure on a transparent sapphire substrate. Scale bars: 200 nm.

To directly measure the interlayer coupling–dependent absorption at 3.14 eV, we imaged correlated transmission and reflection of 1L-WS₂/graphene on a transparent sapphire substrate as shown in Figure 5.25. The linear absorption is deduced using approaches described in Experiential Methods. The linear absorption and correlated TAM image are shown in Figure 5.26. Both linear absorption and transient absorption are increased at a strong-coupling location. Having graphene on top leads to static bandgap renormalization of WS₂ and reduces the exciton binding energy^{133, 250}. It is possible that

the increased linear absorption is due to static screening from graphene that modifies the absorption of WS₂ instead of the absorption by the CT transitions. However, the absorption at 3.14 eV is not near any exciton resonances, and therefore, the change in the absorption due to static screening from graphene should not be significant. Although linear absorption increased by ~25% at a strong-coupling location compared to a weak-coupling location (Figure 5.26 (a)), the TA signal intensity at the same location is increased by ~70% (Figure 5.26 (b)), indicating that the increased absorption accounts partially for the increased TA intensity. The linear absorption and the TA images do not look exactly the same, probably due to the higher spatial resolution of TAM being a two-photon technique²⁶⁰ or interlayer (WS₂ and graphene) orientation.

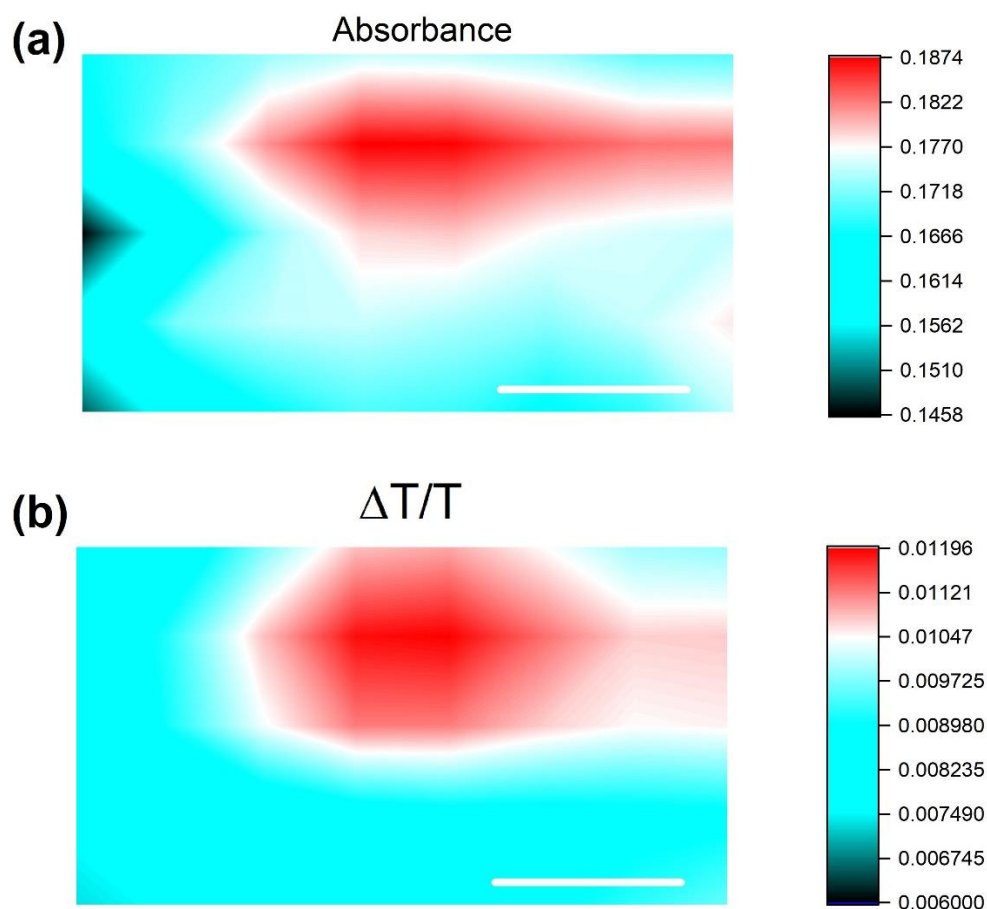


Figure 5.26 Zoomed-in linear absorption (a) and correlated TAM image (D) of the 1L-WS₂/G heterostructure on a transparent sapphire substrate. The TAM image is measured at 0 ps (pump, 3.14 eV; probe, 1.99 eV). Scale bars, 200 nm.

5.4.8 Potential to extract carriers generated by the charge transfer states

The lifetime of the charge-separated states at the graphene-WS₂ interface has been measured to be ~ 1 ps (Figure 5.21). Although the charge-separated states live relatively short, the high carrier mobility of graphene on WS₂ makes it very promising to harvest these charge carriers. For instance, electron mobility of $38,000 \text{ cm}^2\text{V}^{-1} \text{ s}^{-1}$ at room temperature has been measured for graphene on the WS₂ substrate²⁶¹, similar to that of graphene on hexagonal boron nitride. Ultrafast carrier extraction from graphene in as short

as 50 fs has been demonstrated²⁶²; therefore, the 1-ps lifetime should be sufficiently long. Although our measurements do not directly measure the electron-hole binding energy at the interface, successful charge extraction has been confirmed in graphene/WS₂ photodetector devices^{209,253}, which is probably facilitated by a built-in field at the interface. Therefore, the binding energy of these interlayer states can be overcome to achieve extraction.

5.5 Conclusion

In summary, ultrafast microscopy in combination with first-principles calculation provides a comprehensive picture of carrier generation resulting from interlayer coupling in WS₂-graphene heterostructures. Interlayer CT transitions and hot carrier injection promote electrons from graphene to WS₂, allowing carrier generation by excitation of CT transitions below the WS₂ bandgap and leading to enhancement in photocarrier generation by visible optical excitation. The CT transition energies predicted by first-principles calculations have been verified by experimental measurements. Broadband enhancement in carrier generation is highly attractive for photovoltaic applications of heterostructures based on graphene and 2D semiconductors.

CHAPTER 6. CHARGE TRANSFER EXCITON FORMATION AND TRANSPORT IN TWO-DIMENSIONAL WS₂-TETRACENE HETEROSTRUCTURES

This chapter is adapted with permission from Tong Zhu, Long Yuan, Yan Zhao, Yan Wan, Jianguo Mei, Libai Huang, *Science Advance*, 2018, 4, eaao3104.

6.1 Abstract

Charge-transfer (CT) excitons at hetero-interfaces play a critical role in light to electricity conversion using organic and nanostructured materials. However, how CT excitons migrate at these interfaces is poorly understood. Here we investigate the formation and transport of CT excitons in two-dimensional (2D) WS₂-tetracene van der Waals (vdW) heterostructures employing ultrafast spectroscopy and microscopy. Electron and hole transfer occur on the timescale of a few picoseconds and emission of interlayer CT excitons with a binding energy of ~ 0.3 eV has been observed. Transport of the CT excitons is directly measured by transient absorption microscopy (TAM), revealing coexistence of delocalized and localized states. Trapping-detrapping dynamics between the delocalized and localized states leads to stretched-exponential PL decay with an average lifetime of ~ 2 ns. The delocalized CT excitons are remarkably mobile with a diffusion constant of ~ 1 cm²s⁻¹. These highly mobile CT excitons could have important implications in overcoming large interfacial binding energy to achieve charge separation.

6.2 Background

6.2.1 Charge transfer in van der Waals heterostructures

Charge transfer and separation at hetero-interfaces play a key role in determining the efficiency of light to electricity conversion using organic and nanostructured materials⁵².

²⁶³⁻²⁶⁶. In these systems, charge separation occurs as an exciton created in one material is dissociated into a spatially separated electron-hole (e-h) pair across the material interface. Semiconducting transition metal dichalcogenides (TMDCs) are versatile building blocks for fabricating two-dimensional (2D) van der Waals (vdW) heterostructures with atomically thin and sharp interfaces, allowing for applications such as photovoltaics and photodetectors^{13-14, 53, 59-60, 67, 125, 210, 267-268}. Molecular and polymeric semiconductors can also be integrated with 2D TMDCs to form vdW heterostructures^{68, 112-113, 116-117, 269-272}, and charge generation at organic-TMDC interfaces has been recently demonstrated¹¹⁶.

Charge transfer at the interface of TMDC heterostructures has been found to be extremely rapid, as short as 50 fs^{73, 81-84, 87, 112}. However, due to the inefficient screening of the interfacial Coulomb potential, the spatially separated e-h pair are not free but bound with energy on the order of 200 meV⁸⁰, leading to the formation of charge-transfer (CT) excitons also known as interlayer excitons in TMDC heterostructures (such as MoS₂/WS₂)^{73, 93, 99, 101, 221}. When incorporated with molecular semiconductors, the nature of the interfacial CT states following charge transfer events remains elusive at the 2D organic-TMDC interfaces. While CT excitons have been inferred in recent studies^{112, 116}, no direct experimental evidence has been provided.

6.2.2 Charge transfer exciton transport

CT exciton diffusion has been proposed as a mechanism for the electrons and holes to escape the large interfacial Coulomb potential (on the order of hundreds of meV) to achieve charge separation²⁷³. However, the CT states so far have been mostly studied in largely disordered systems such as organic solar cells^{263, 273-275}, where measurements are averaged over many different kinds of interfaces making it difficult to obtain the upper

limit of CT exciton transport. To overcome this difficulty, we use heterostructures that integrate exfoliated WS₂ layers with tetracene thin film as a model system with 2D crystalline organic-inorganic interfaces²⁷³. Another challenge is that direct measurements of CT exciton transport require quantitative information in both spatial and temporal domains. Recent photoluminescence (PL) microscopy measurements have revealed that CT excitons move 5–10 nm in space at disordered organic-organic interfaces²⁷³. However, a drawback for PL based techniques is that only emissive species are investigated while many of the CT states are optically dark.

To address this challenge, we employ transient absorption microscopy (TAM) that is capable of imaging both bright and dark excitons with ~ 200 fs temporal resolution and ~ 50 nm spatial precision²⁷⁶⁻²⁷⁷. The measurements on WS₂/tetracene heterostructures presented here reveal highly mobile CT excitons at 2D organic-TMDC interfaces with a diffusion constant of ~ 1 cm²s⁻¹, which could be an important factor in achieving efficient charge separation

6.3 Experimental Methods

6.3.1 Sample preparation

WS₂ flakes of different thickness are obtained by mechanically exfoliating from bulk WS₂ onto Si/SiO₂ substrate. Numbers of WS₂ layers are identified by photoluminescence microscopy^{10, 195}. Tetracene (Tc) thin film is deposited onto WS₂ flakes by the physical vapor deposition method. Briefly, Tetracene thin film was deposited by thermal evaporation in the glove box at a deposition rate of 2 nm/s under high vacuum (< 7 × 10⁻⁴ Pa). The substrate temperature was kept at 290 K. The Tc film thickness of ~20 nm is identified by Atomic Force Microscopy (AFM) measurements WS₂ flakes from 1 to

7 layers have been exfoliated and integrated with Tc thin film to fabricate the heterostructures.

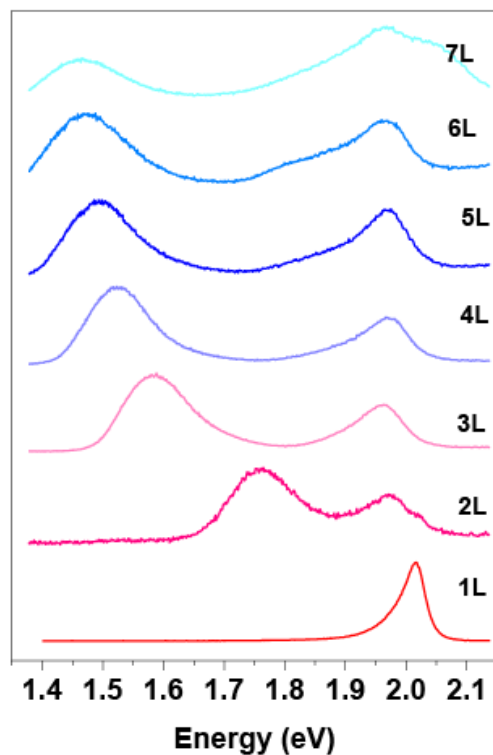


Figure 6.1 Identification of numbers of WS₂ layers using photoluminescence spectroscopy. PL spectrum of WS₂ from 1L to 7L is shown from bottom to top.

6.3.2 Atomic force microscopy

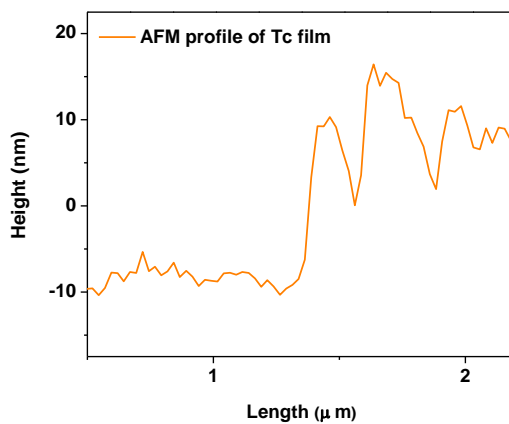


Figure 6.2 AFM line profile of the Tc film thickness.

AFM measurements were performed under ambient conditions using a Veeco Dimension 3100 AFM instrument in the tapping mode

6.4 Results and discussion

6.4.1 Charge transfer excitons emission and dynamics

Figure 6.3 shows the construction of a heterostructure from a single-layer WS₂ (1L-WS₂) and a tetracene (Tc) thin film. The optical image of the exfoliated 1L-WS₂ flake before the Tc deposition is shown in Figure 6.3 (a). Polycrystalline Tc thin film is deposited onto the WS₂ flakes by physical vapor deposition, as detailed in the Experimental Methods. A film thickness of ~20 nm is determined using atomic force microscopy (AFM) (Figure 6.3 (b) and Figure 6.2). The Tc molecules are likely to pack edge-on in the herringbone structure on WS₂²⁷⁸, as schematically shown in Figure 6.3 (c) (29). The absorption and PL spectrum of Tc film and 1L-WS₂ are shown in Figure 6.4.

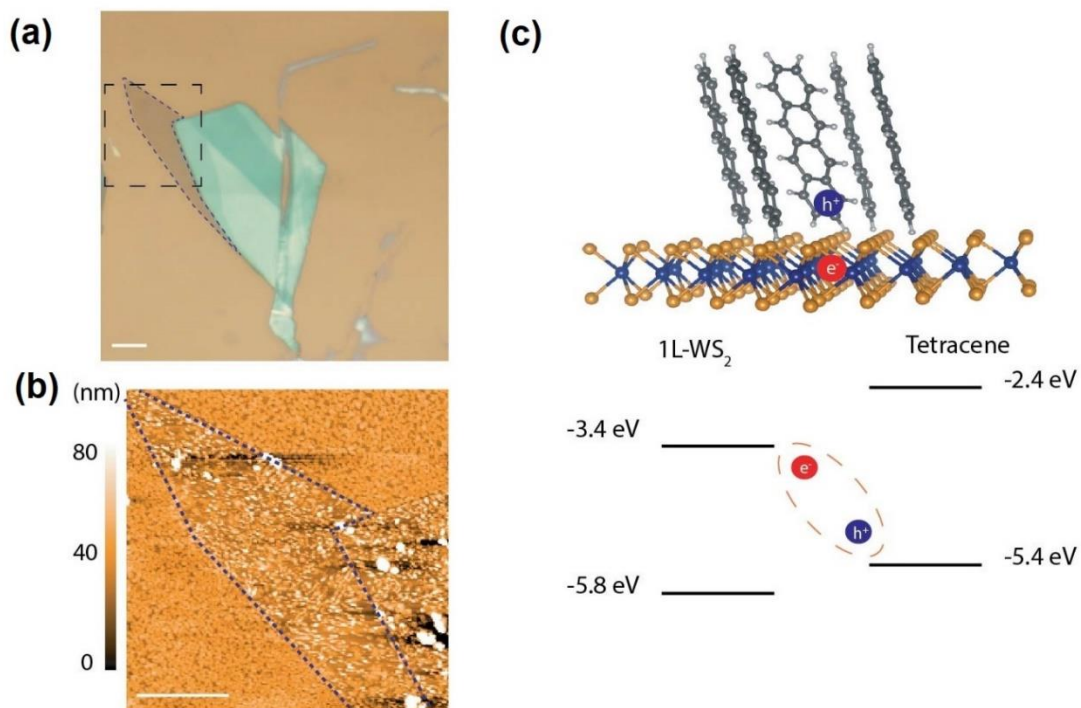


Figure 6.3 (a) Optical image of WS₂ flakes exfoliated on Si/SiO₂ substrate. The 1L-WS₂ is indicated by the dashed line. The dashed square shows the area imaged by AFM in (b). Scale bar represents 10 μm . (b) AFM image of the same 1L-WS₂ flake in (a) with a Tc thin film deposited on top. Scale bar represents 5 μm . (c) Schematic of the formation of CT excitons and the band alignment of the 1L-WS₂/Tc heterostructure, showing the formation of a type II heterojunction.

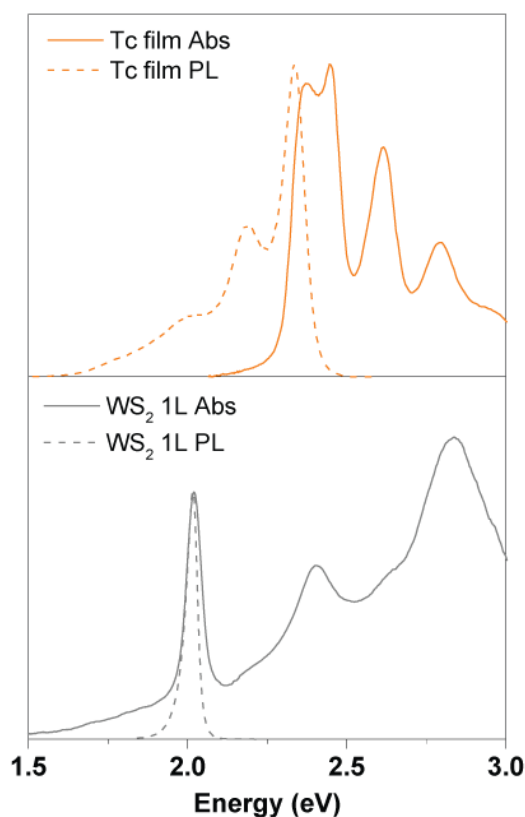


Figure 6.4 Absorption and PL spectrum of Tc film and 1L-WS₂.

Figure 6.5 compares the steady-state PL spectra from the 1L-WS₂/Tc heterostructure, a Tc-only region of the film, and the 1L-WS₂ before deposition of Tc, with photoexcitation at 2.8 eV exciting both the 1LWS₂ and the Tc film. The 1L-WS₂ shows an emission peak near 2.0 eV corresponding to the direct interband recombination of the A exciton¹⁰. An additional low-energy emission peak at 1.7 eV from the heterostructure is observed in addition to the emission of the A exciton of WS₂ and the singlet exciton of Tc. We have confirmed this low-energy emission peak in all the 1L-WS₂/Tc heterostructures fabricated. The intensity of the low-energy emission could vary significantly from sample to sample, probably due to the variations in morphology of different samples.

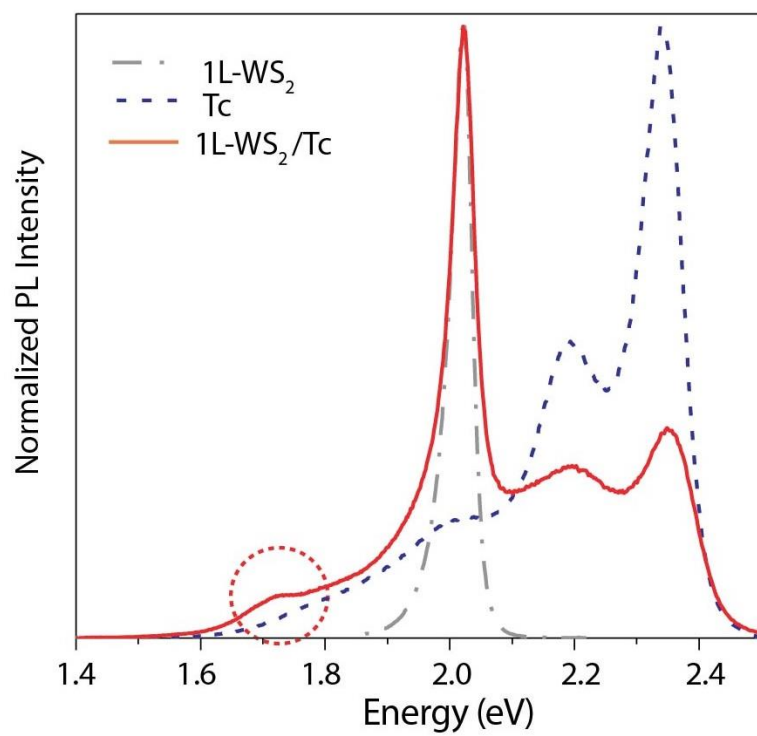


Figure 6.5 Steady-state PL spectra of a 1L-WS₂, Tc thin film, and a 1L WS₂/Tc heterostructure. The new emission band at 1.7 eV indicates the formation of interlayer CT excitons.

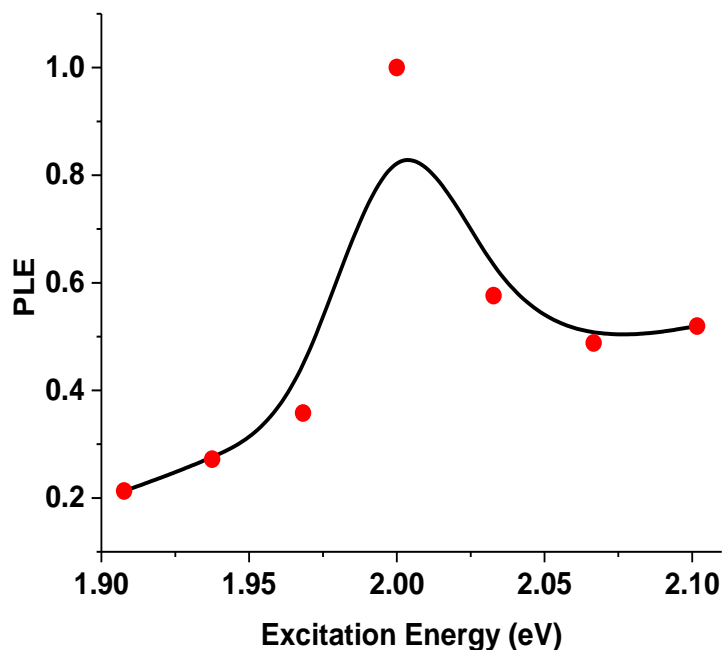


Figure 6.6 Photoluminescence excitation (PLE) measurements monitoring CT exciton emission at 1.7 eV.

The 1L-WS₂ and the Tc molecules form a type II heterojunction, as schematically shown in Figure 6.3 (c). The conduction band minimum (-3.4 eV)¹²⁰ of the 1L-WS₂ lies lower than the lowest unoccupied molecular orbital level (-2.4 eV)¹²¹ of Tc molecules allowing electron transfer from Tc to WS₂, whereas the valence band maximum (VBM; -5.8 eV)¹²⁰ of WS₂ is located lower than the highest occupied molecular orbital (HOMO) level of Tc (-5.4 eV)¹²¹, facilitating hole transfer from WS₂ to Tc. On the basis of the band alignment, we attribute the emission band at 1.7 eV to interlayer CT excitons where the electrons and the holes reside on the 1L-WS₂ and the Tc film, respectively (Figure 6.3 (c)). We have also carried out PL excitation (PLE) measurements confirming the excitation of the A exciton in WS₂ leads to CT exciton emission (Figure 6.6). From the energy level

alignment and 1.7-eV emission energy, the binding energy for the CT excitons is estimated to be ~ 0.3 eV, assuming that the energy levels do not change significantly at the interfaces. This binding energy is slightly larger than that of ~ 0.2 eV for the CT excitons in MoSe₂/WSe₂ heterostructures^{80,82}, which can be explained by the lower dielectric constant of the Tc thin film ($\epsilon \sim 5$) in comparison to that for MoSe₂ ($\epsilon \sim 15$) and WSe₂⁵², leading to less efficient screening of the Coulomb potential.

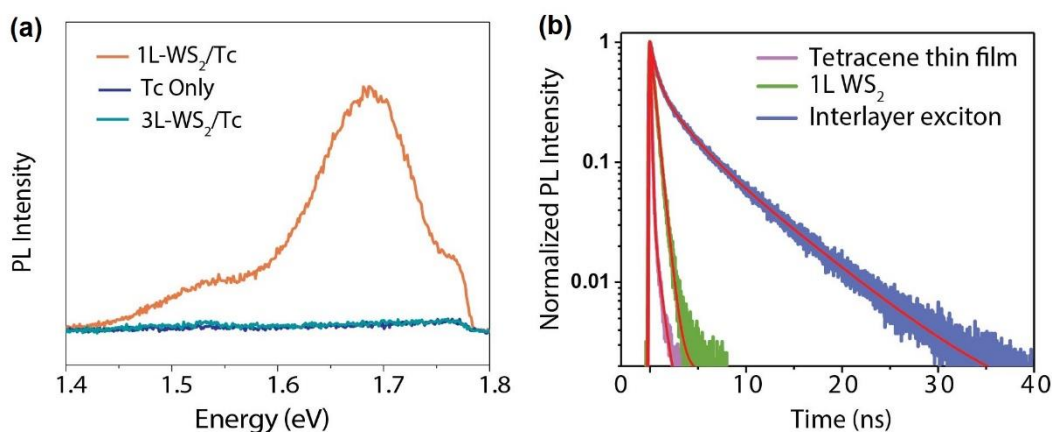


Figure 6.7 (a) PL spectra of a 1L-WS₂/Tc heterostructure, a 3L-WS₂/Tc heterostructure, and a Tc thin film with excitation energy of 2.1 eV and 700-nm long-pass filter selectively exciting WS₂ in the heterostructures and detecting only interlayer CT exciton emission. (b) Time-resolved PL measurements on the interlayer CT exciton in a 1L-WS₂/Tc heterostructure, a Tc film, and a 1L-WS₂ flake. The CT exciton PL decay is fitted with a stretched exponential function, as described in the main text.

We monitor the CT exciton emission with photoexcitation energy below the Tc bandgap at 2.1 eV exciting only WS₂ to eliminate the background emission from Tc at energy similar to the CT excitons. As shown in Figure 6.7 (a), the emission from the interlayer CT excitons is broad, indicative of a distribution in CT exciton energy levels. The CT excitons exhibit overall much longer PL lifetime than the singlet exciton of the Tc

(~100 ps) and the A exciton of WS₂ (~500 ps), as expected from the spatial indirect nature of the CT excitons (Figure 6.7 (b)).

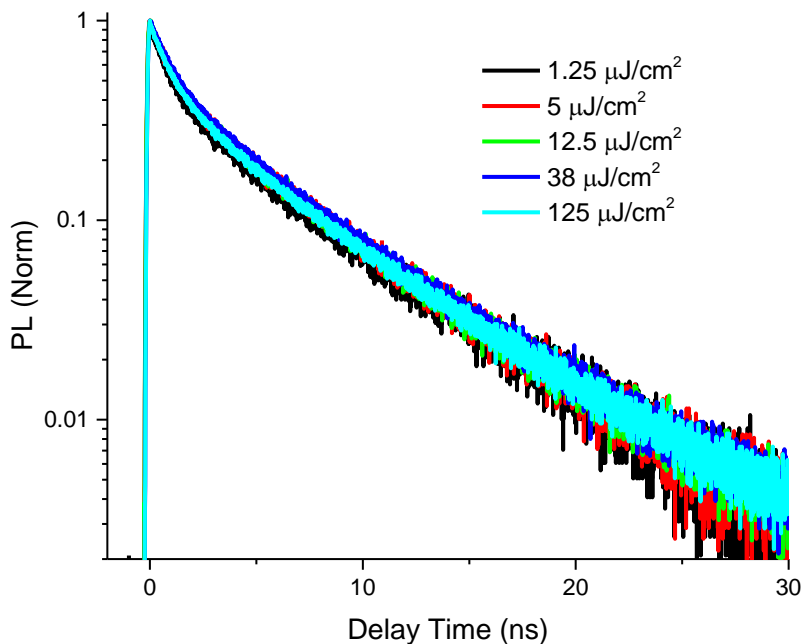


Figure 6.8 Excitation intensity dependent measurements of PL dynamics of CT exciton emission. Excitation photon energy: 2.1 eV.

The PL decay of the CT excitons is not a single exponential but only can be fitted with a stretched-exponential function:

$$I(t) = I_0 e^{-\left(\frac{t}{\tau}\right)^\beta} \quad (1)$$

where $\tau = 0.97 \pm 0.1$ ns and $\beta = 0.48 \pm 0.01$ is the stretching exponent. The need for a stretched-exponential fit is due to a superposition of many exponentials with different decay time constants τ_j that probably arises from multiple configurations of the CT excitons²⁷⁹⁻²⁸⁰. The dispersion of the decay time constant is described by β ($0 < \beta < 1$), where the smaller the β value, the broader the distribution of τ_j . The average exciton

lifetimes $\langle \tau_j \rangle$ given as $\left(\frac{\tau}{\beta}\right) \Gamma\left(\frac{1}{\beta}\right) = 2.1$ ns, where Γ represents Gamma function. We have carried out excitation intensity-dependent measurements that show negligible variations in dynamics with fluences ranging from 1.25 to 125 μJcm^{-2} (Figure 6.8), indicating that exciton-exciton annihilation processes do not play an important role here.

6.4.2 Hole transfer from WS₂ to Tc

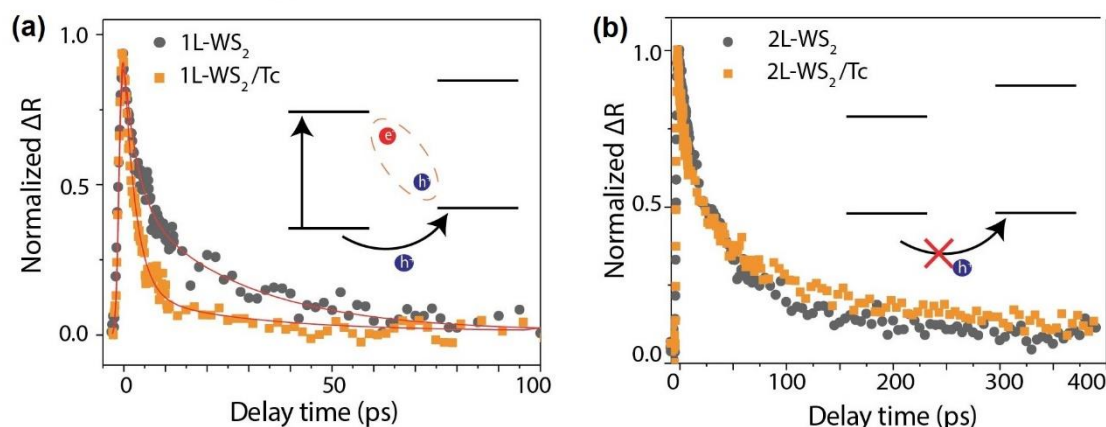


Figure 6.9 (a) Transient absorption dynamics probed at the A exciton bleach of the 1L-WS₂ before and after Tc deposition with pump energy of 2.1 eV (pump fluence: 50 $\mu\text{J}/\text{cm}^2$). Red solid lines are fittings with a bi-exponential function convoluted with an experimental response function. Inset of band alignment shows the hole transfer process in the 1L-WS₂/Tc heterostructure. (b) Transient absorption dynamics probed at the A exciton bleach of 2L-WS₂ before and after Tc deposition with pump energy of 2.1 eV, showing no hole transfer in the 2L-WS₂/Tc heterostructure.

We excite the 1L-WS₂/Tc heterostructure with a pump photon energy of 2.1 eV that is below the absorption edge of Tc (Figure 6.4) to selectively investigate hole transfer from WS₂ to Tc. The dynamics of the same 1L-WS₂ flake is probed at the A exciton bleach (2.0 eV) before and after Tc deposition (Figure 6.9 (a)). On the time scale of a few picoseconds, the dynamics become faster after the deposition of Tc, which can be explained by the additional hole-transfer pathway from WS₂ to Tc in the heterostructure. The dynamics

before Tc deposition can be fitted with a biexponential decay function (Figure 6.9 (a)), and hole transfer is competing with the fast decay component on the picosecond time scale. We can extract the hole-transfer rate by subtracting the fast decay rate before Tc deposition from that of after Tc deposition and obtain a hole transfer time constant of 3.2 ± 0.5 ps. This hole-transfer time is consistent with recent measurements at pentacene/MoS₂ interfaces¹¹².

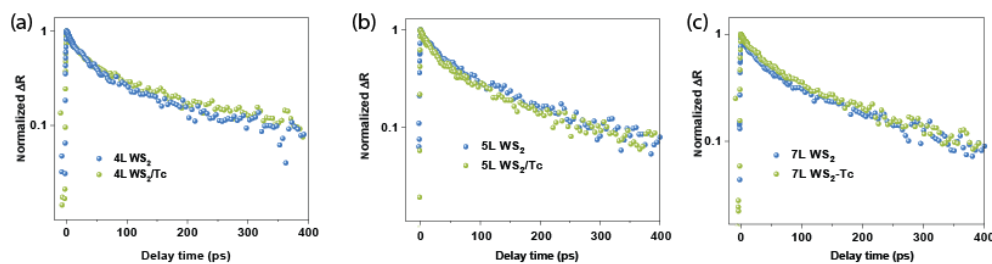


Figure 6.10 TAM Dynamics of 4L, 5L, and 7L-WS₂ before and after Tc deposition. TAM dynamics of 4L (a), 5L (b) and 7L-WS₂ (c) before (blue) and after (green) Tc deposition showing no hole transfer in the heterostructures built by thick WS₂ flakes and Tc film. (2.1 eV pump and 2.0 eV probe).

To investigate driving force for dissociating the A exciton in WS₂, we perform measurements on WS₂/Tc heterostructures constructed with a different thickness ranging from 1 layer to 7 layers (7L-WS₂). The interlayer CT exciton emission disappears as the thickness of the WS₂ increases to two layers or thicker (Fig.2A). There is also no obvious difference in the WS₂ transient absorption dynamics after Tc deposition (Figure 6.9 (b) for 2L-WS₂ and Figure 6.10 for 4L-WS₂, 5L-WS₂, and 7L-WS₂), implying that hole transfer does not occur, which explains the absence of the CT exciton in these heterostructures. This thickness dependence confirms that the below-bandgap emission is from CT excitons and not from defects or other origins.

In order for hole transfer to occur, the offset between the VBM of WS₂ and the HOMO of the Tc molecules that provides the driving force²⁸¹ for A exciton dissociation has to be greater or similar to the A exciton binding energy of ~ 0.4 eV⁴². This requirement is satisfied in 1L-WS₂/Tc heterostructures. However, as thickness increases to 2L-WS₂, the VBM energy level increases¹²⁰, and energy offset decreases to ~ 0.2 eV. The fact that hole transfer is not observed in the heterostructures constructed with 2L-WS₂ or thicker indicates that the energy offset between the VBM of WS₂ and the HOMO of Tc is not large enough to drive the dissociation of the A exciton in WS₂, and hence, the CT excitons do not form.

6.4.3 Electron versus energy transfer from Tc to WS₂

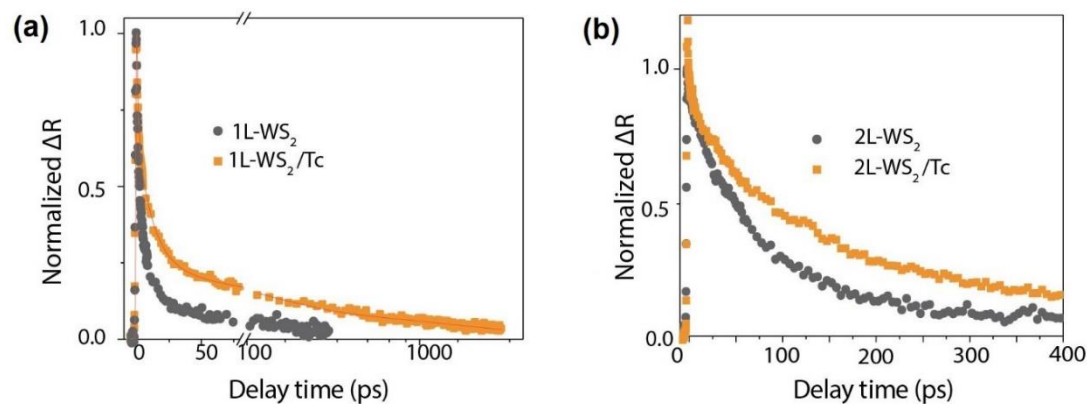


Figure 6.11 (a) 1L-WS₂ dynamics before and after Tc deposition. (b) 2L-WS₂ dynamics before and after Tc deposition. Pump = 3.1 eV (pump fluence: $2.2 \mu\text{Jcm}^{-2}$), probe = 2.0 eV.

Next, we use a pump photon energy of 3.1 eV to investigate electron and energy transfer dynamics from Tc to WS₂. Under this condition, excitons are generated in both WS₂ and Tc. Because the singlet exciton emission of Tc overlaps with the absorption spectrum of WS₂ (Figure 6.4), Förster-type resonance energy transfer from Tc to WS₂ is

also possible. Dynamics probed at the A exciton resonance (2.0 eV) in WS₂ before and after Tc deposition are shown in Figure 6.11. (a and b) for the 1L-WS₂/Tc and 2L-WS₂/Tc heterostructures, respectively. Note that measurements on Tc-only regions under the same experimental conditions show no detectable transient absorption signal when probing at 2.0 eV. Dynamics probed at the A exciton resonance become slower in the 1L-WS₂/Tc heterostructure than in the control 1L-WS₂ (Figure 6.11. (a)), which is the opposite from when only 1L-WS₂ is excited (Figure 6.9 (a)). The slower decay in the heterostructure could be due to either energy transfer or electron transfer from Tc to WS₂. We follow the procedure of Rowland et al.²⁸² to subtract the dynamics of the control 1L-WS₂ from that of the 1L-WS₂/Tc heterostructure (Figure 6.12), and a rise time of 2.1 ± 0.2 ps is obtained, which might contain contributions from both electron and energy transfer.

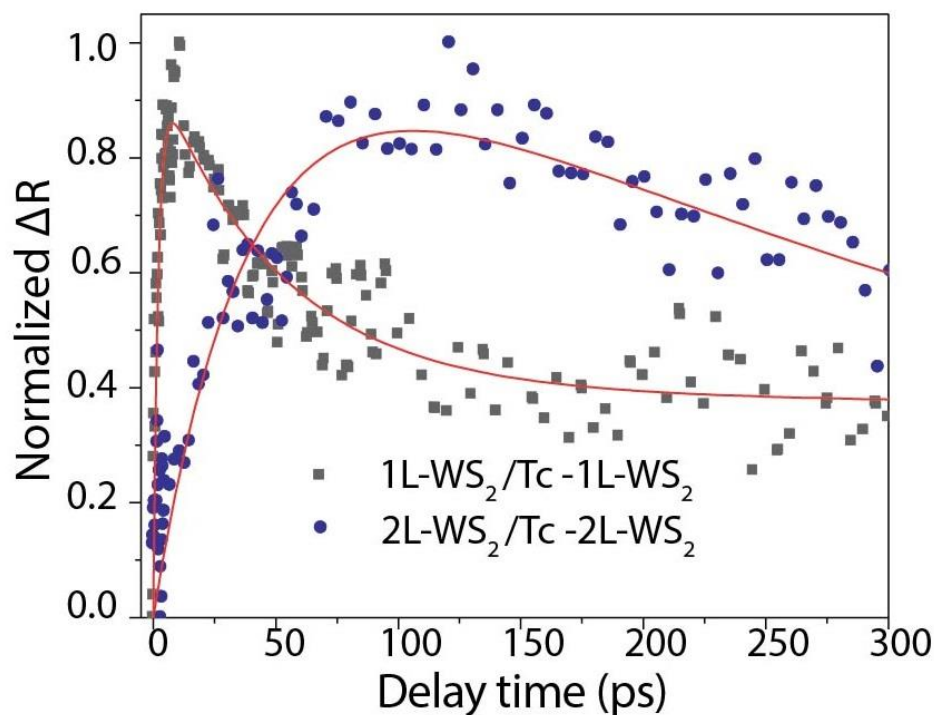


Figure 6.12 Subtraction of 1L-WS₂ dynamics from 1L-WS₂/Tc dynamics fitted with an exponential growth function with a time constant of 2.1 ± 0.2 ps and subtraction of 2L-WS₂ dynamics from 2L-WS₂/Tc dynamics yielding a rise time constant of 44 ± 5 ps.

To separate the contribution from energy transfer, we examine dynamics in heterostructures constructed with 2L-WS₂ (Figure 6.12) and thicker (Figure 6.13). In these heterostructures, type I instead of type II heterojunctions are formed because hole transfer from WS₂ is blocked, and only exciton energy transfer is possible. After the deposition of Tc, the dynamics probed at the A exciton resonance become slower in these heterostructures when the Tc molecules are excited because of energy transfer. By subtracting the dynamics of the control 2L-WS₂ from that of the 2L-WS₂/Tc heterostructure, we obtain a rise time constant of 44 ± 5 ps corresponding to the energy transfer time from Tc to 2L-WS₂ (Figure 6.12). Energy transfer rates have been measured

as a function of the thickness of WS₂, ranging from 2L to 7L, as plotted in Figure 6.14. Energy transfer rate decreases as the thickness of WS₂ increases, which is consistent with the recent reports on energy transfer between quantum dots and MoS₂^{258, 283-284}. This thickness dependence arises from the decreased electric field strength of the top layer WS₂ as thickness increases due to enhanced dielectric screening^{258, 283}.

We fit the WS₂ thickness–dependent energy transfer rate by using the electromagnetic model developed by Raja et al²⁵⁸. Briefly, the energy transfer rate Γ_{ET} as a function of the number of layers of WS₂ (d) is written as:

$$\Gamma_{ET} \approx A\eta'' \frac{1+|\eta|^2 e^{-2Cd}}{1-2\text{Re}|\eta|^2 e^{-2Cd}+|\eta|^4 e^{-4Cd}} \quad (2)$$

where A and C are constants and are obtained from fitting, η , η' and η'' are related to dielectric constant of WS₂ (ϵ), and are given as, $\eta = \eta' + i\eta''$, $\eta = \frac{|\epsilon|^2 - 1 + 2i\epsilon''}{|\epsilon|^2 + 2\epsilon' + 1}$, and $\epsilon = \epsilon' + i\epsilon''$. By using values of the real part ($\epsilon' = 16.2$) and the imaginary part ($\epsilon'' = 6.4$) of WS₂ dielectric constant²⁸⁵, the dependence of energy transfer rate on WS₂ thickness from 2L to 7L was fitted to extrapolate energy transfer rate from Tc to 1L-WS₂.

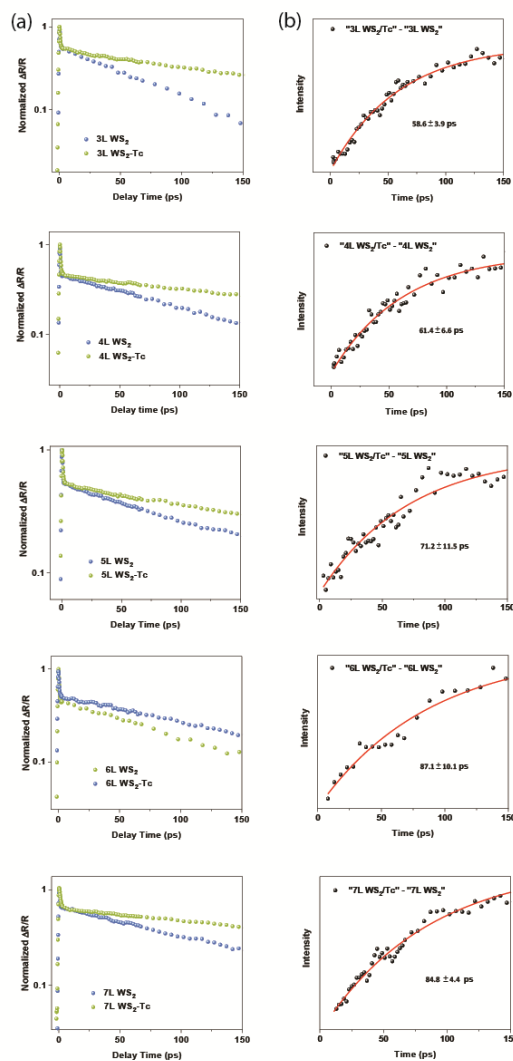


Figure 6.13 Energy transfer from Tc to WS_2 measured with TAM (3.1 eV pump and 2.0 eV probe). (a) Transient dynamics of 3L-7L WS_2 before (blue) and after (green) Tc deposition. (b) Subtraction of WS_2 dynamics from WS_2/Tc dynamics yielding rising curves fitted with an exponential function for each WS_2 thickness, indicating energy transfer time constants.

Using this model, a time constant of 37 ps is extrapolated for energy transfer from Tc to 1L- WS_2 . Because this energy transfer time is more than one order of magnitude slower than the 2.1 ± 0.2 ps rise-time, we conclude that electron transfer instead of energy transfer dominates the dynamics in the 1L- WS_2/Tc heterostructure. The electron transfer

time can be obtained by subtracting the energy transfer contribution from the rise-time,

$$\frac{1}{\frac{1}{2.1ps} - \frac{1}{37ps}} = 2.2 ps.$$

Transient absorption dynamics of the 1L-WS₂/Tc heterostructure probed at the A exciton resonance show an additional slow decay with a characteristic time > 1 ns (limited by the time window of the measurements) as shown in Figure 6.11 (a), which is attributed to the recombination of the interlayer CT excitons.

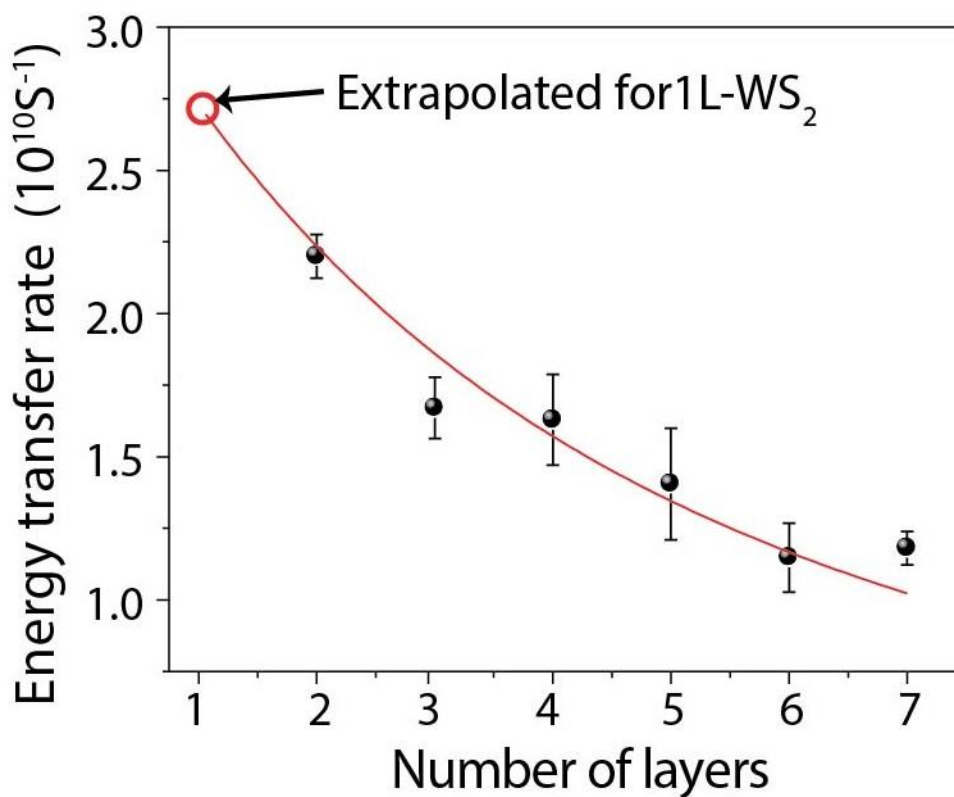
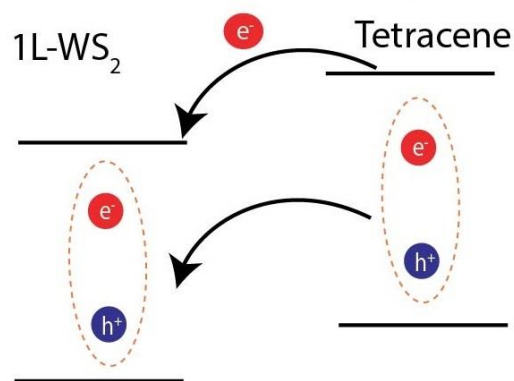


Figure 6.14 Energy transfer rate dependence on numbers of WS₂ layers fitted to the electromagnetic model as described in the main text.

Figure 6.15 summarizes the charge and energy transfer in WS₂/Tc heterostructures. For 1L-WS₂/Tc, due to type II band alignment, both electron and energy transfer are allowed after photo-excitation. In heterostructures constructed with 2L and thicker WS₂,

only exciton energy transfer is possible due to the type I band alignment. The energy transfer rate is reduced as thickness increases.

Electron transfer + Energy Transfer



Energy transfer only

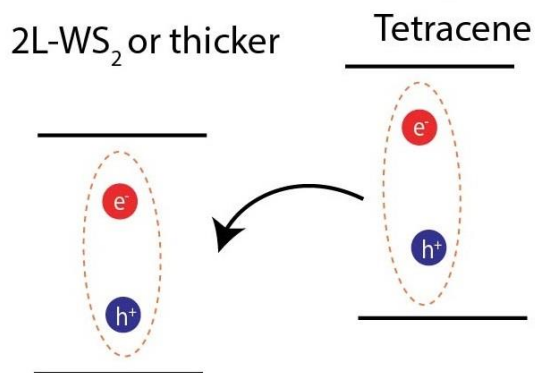


Figure 6.15 Schematic illustration of electron and energy transfer processes. In the heterostructures constructed from 2L-WS₂ or thicker, type I heterojunctions are formed and only exciton energy transfer is possible.

6.4.4 Transport of the delocalized and localized CT excitons

A possible mechanism leading to the stretched-exponential behavior of the CT exciton PL decay as shown in Figure 6.7 (b) is trapping and detrapping dynamics between delocalized and localized states²⁷⁹. This mechanism known as multiple trapping-detrapping has successfully explained the stretched-exponential PL decay observed in porous

silicon²⁸⁶. In WS₂/tetracene heterostructure, since CT exciton binding energy E_B is inversely proportional to the e-h distance, delocalized CT excitons with large e-h distance have smaller E_B and higher energy. When the e-h distance is reduced, the more localized CT excitons with lower energies can serve as traps²⁸⁷. There could be certain sites to accommodate the lower-energy and more localized states where emission is more likely to occur²⁷³. PL dynamics of the CT excitons are controlled by the competition between the diffusion to these sites and the detrapping of the exciton from these sites²⁸⁶. The density and spatial distribution of the low-energy sites determine the dispersion of CT exciton lifetime and hence the value of β in Equation. 1²⁸⁷.

To validate the mechanism proposed, we image the transport of CT excitons directly with TAM by mapping population in both the spatial and temporal domains²⁷⁶. The pump beam is held at a fixed position, whereas the probe beam is scanned relative to the pump with a pair of galvanometer scanners to obtain the exciton distribution at a given pump-probe delay time. The pump-induced change in probe reflectance $\Delta R = R_{pump-on} - R_{pump-off}$ is collected. The pump energy is 3.1 eV exciting both WS₂ and Tc, and the probe energy is 2.0 eV probing WS₂. At zero delay time, the TAM results reflect the initial population created by the pump beam, and at later delay time, the TAM images directly visualize how excitons transport out of the initial volume. We have also carried out exciton transport experiments on a control 1L-WS₂ flake.

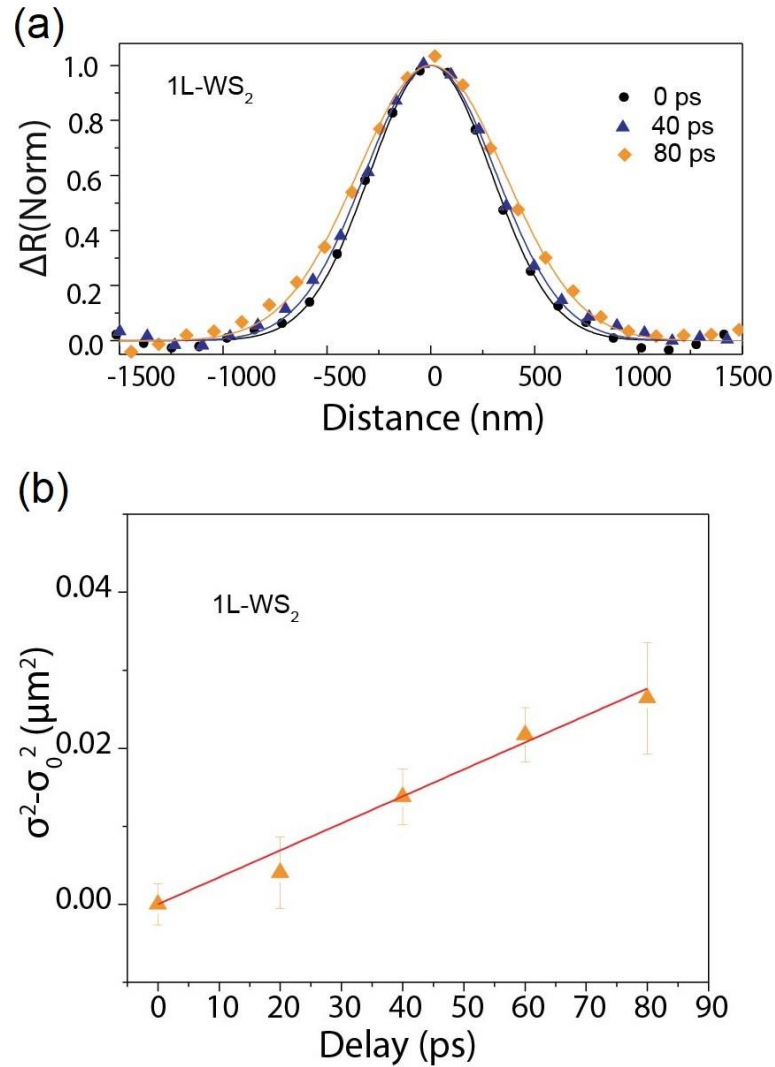


Figure 6.16 (a) Exciton population profiles fitted with Gaussian functions at different delay times with the maximum ΔT signal normalized to unity for the control 1L-WS₂. The pump photon energy is 3.1 eV (pump fluence: 4.4 $\mu\text{J}/\text{cm}^2$) and the probe energy is 2.0 eV. (b) $\sigma_t^2 - \sigma_0^2$ as a function of pump-probe delay time, with a linear fit to equation 3 (line) for the control 1L-WS₂. Error bars of $\sigma_t^2 - \sigma_0^2$ are the standard errors estimated from Gaussian fitting to the spatial intensity distributions.

In one dimension (1D), the initial population $n(x, 0)$ follows Gaussian distribution as created by a Gaussian pump beam of 3.1 eV at position (x_0) with a variance of σ_0^2 and is given by, $n(x, 0) = N \exp\left[-\frac{(x-x_0)^2}{2\sigma_0^2}\right]$. Population as a function of space and time can be

described by a differential equation that includes both the diffusion out of the initial volume and population decay, which is given by:

$$\frac{\partial n(x,t)}{\partial t} = D \frac{\partial^2 n(x,t)}{\partial x^2} - \frac{n(x,t)}{\tau} \quad (3)$$

where D is the exciton diffusion constant and τ is the exciton lifetime. Solution to equation (3) dictates that exciton distribution at any later delay time (t) is also Gaussian and can be described as $n(x,t) = N \exp\left[-\frac{(x-x_0)^2}{2\sigma_t^2}\right]$ with a variance of σ_t^2 . The solution also gives the diffusion constant D as,

$$D = \frac{\sigma_t^2 - \sigma_0^2}{2t} \quad (4)$$

Using this analysis, the population of the A excitons in the control 1L-WS₂ flake at different delay times are fitted to Gaussian functions and the diffusion constant is determined to be $1.7 \pm 0.1 \text{ cm}^2\text{s}^{-1}$ (Figures 6.16 (a) and 6.16 (b)).

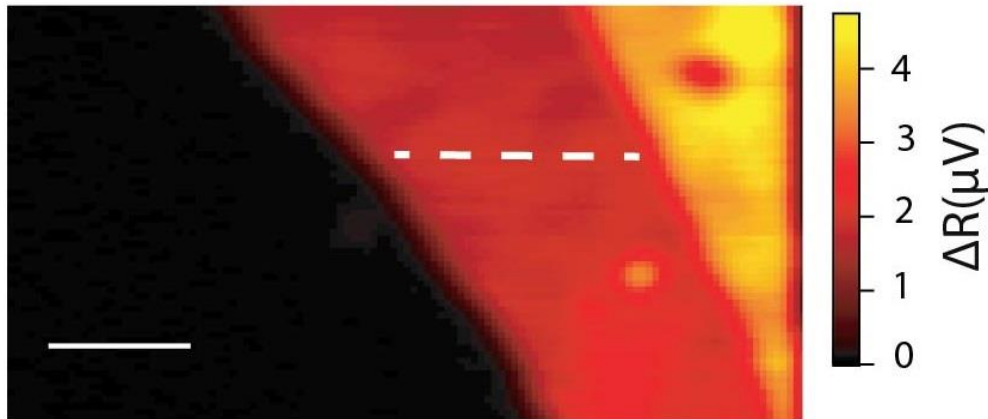


Figure 6.17 TAM image of the same 1L-WS₂/Tc heterostructure shown in Figure 1 taken with spatially overlapped pump and probe beams at 0 ps. Scale bar represents 2 μm . The pump energy is 3.1 eV (pump fluence: $4.4 \mu\text{J}/\text{cm}^2$) and the probe energy is 2.0 eV.

For the 1L-WS₂/Tc heterostructure, population profiles at different delay times have been taken along the line indicated in Figure 6.17 with a pump fluence 4.4 μJ/cm². Sums of at least two Gaussian functions are required to fit the population profile at a given pump-probe delay time (Figures 6.18 and 6.19), as given by $n(x, t) = N_1 \exp\left[-\frac{(x-x_0)^2}{2\sigma_{1,t}^2}\right] + N_2 \exp\left[-\frac{(x-x_0)^2}{2\sigma_{2,t}^2}\right]$, implying there are at least two populations migrating with different diffusion constants. The extracted $\sigma_{1,t}^2$ and $\sigma_{2,t}^2$ are plotted as a function of pump-probe delay time in Fig. 4E. Very rapid diffusion is observed before 100 ps, possibly due to the transport of the free electrons in the 1L-WS₂ dissociated from the hot CT exciton states created by the 3.1 eV pump that has 1.4 eV excess energy²⁶³.

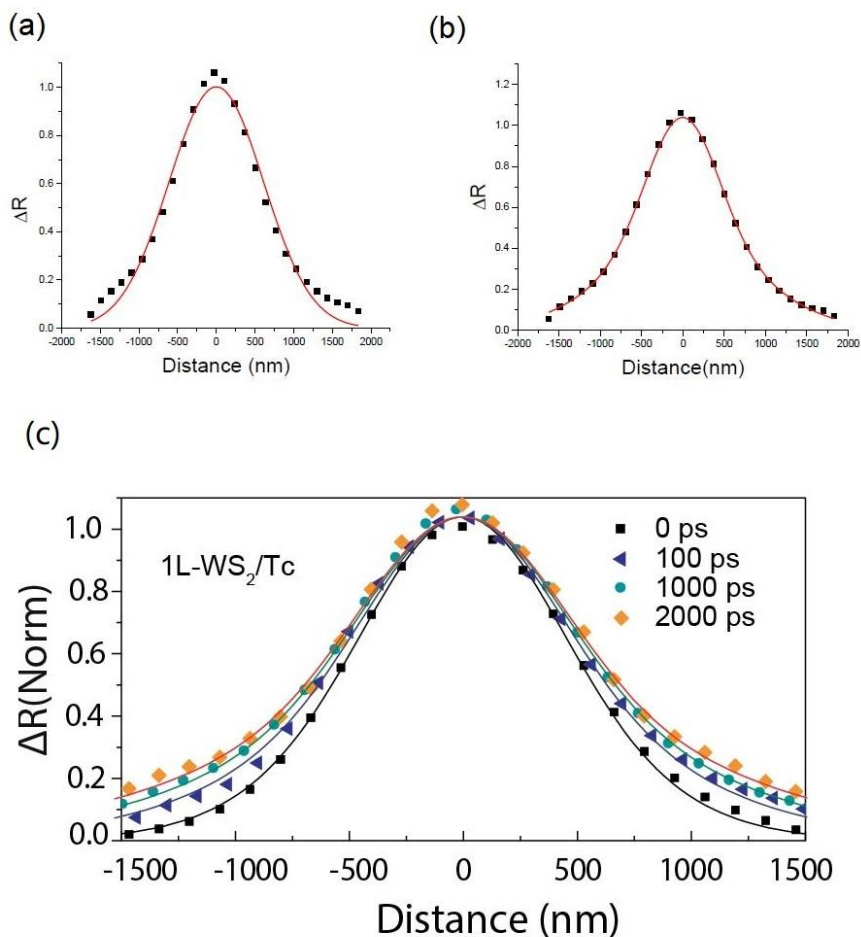


Figure 6.18 Exciton population profile at 1 ns delay fitted with a single Gaussian function (a) and a sum of two Gaussian functions (b) as described in the main text for the 1L-WS₂/Tc heterostructure. The pump photon energy is 3.1 eV (pump fluence: 4.4 $\mu\text{J}/\text{cm}^2$) and the probe energy is 2.0 eV. (c) Exciton population profiles fitted with a sum of two Gaussian functions as described in the text at different delay times with the maximum ΔR signal normalized to unity for the 1L-WS₂/Tc heterostructure along the line indicated in Figure 6.17.

We focus on timescale > 100 ps where the intralayer A excitons in the 1L-WS₂ have mostly decayed (Figure. 6.11 (a)). The long-lived transient absorption signal in the heterostructures reflects the CT exciton population because the formation of CT excitons leaves the electronic states occupied in WS₂ and results in the long-lived bleaching of A exciton transition. A diffusion constant $D_1 = 1.0 \pm 0.1 \text{ cm}^2\text{s}^{-1}$ is obtained in the heterostructure for delay

time > 100 ps by fitting the time dependence of σ_1^2 , corresponding to the fast moving population with $N_1 = 0.4$. The diffusion constant for the slow moving population ($N_2 = 0.6$) is more than one order of magnitude slower, $D_2 = 0.04 \pm 0.01$ cm²s⁻¹.

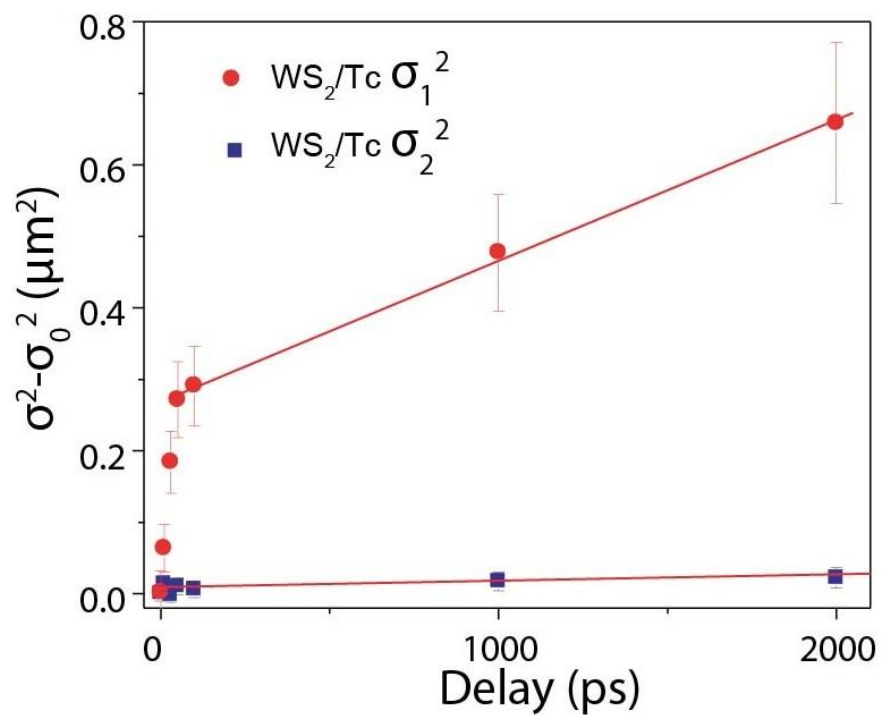


Figure 6.19 $\sigma_{1,t}^2 - \sigma_0^2$ and $\sigma_{2,t}^2 - \sigma_0^2$ as a function of pump-probe delay time, with a linear fit to equation 3 (line) for the 1L-WS₂/Tc heterostructure.

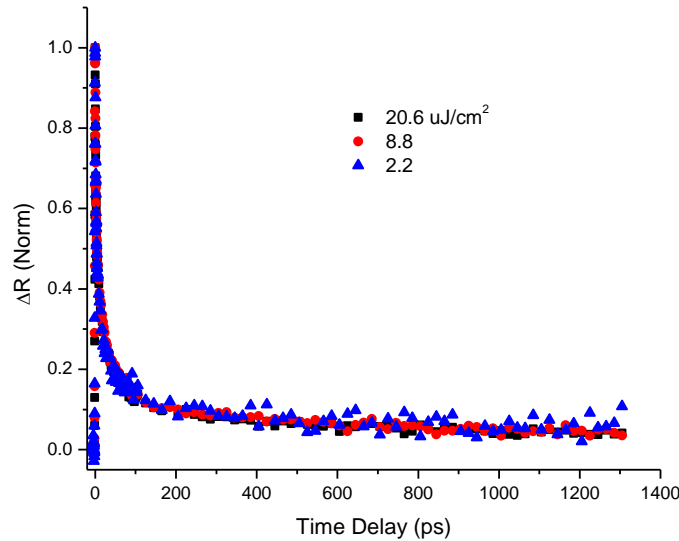


Figure 6.20 Transient absorption dynamics of a 1L-WS₂/Tc heterostructure measured at different pump fluences. Pump = 3.1 eV, probe = 2.0 eV.

To correctly measure exciton transport, it is important to account for exciton-exciton annihilation processes. Because the exciton density at the center of the spot is higher than the edge, exciton-exciton annihilation could lead to artificially broadening of σ . We have carried out pump intensity dependent dynamics and transport measurements to rule out the interference from exciton-exciton annihilation. Transient absorption dynamics measured at pump fluences from 2.2 to 20.6 μJcm^{-2} exhibit essentially the same decay (Figure 6.20). TAM measurements at two higher pump fluences of 10.0 μJcm^{-2} and 20.6 μJcm^{-2} show similar bi-population diffusion behavior (Figure 6.21). These measurements yield almost identical diffusion constants as those measured at 4.4 μJcm^{-2} , with $D_1 = 1.0 \pm 0.1 \text{ cm}^2\text{s}^{-1}$ and $D_2 = 0.04 \pm 0.01 \text{ cm}^2\text{s}^{-1}$ for pump fluence at 10.0 μJcm^{-2} (Figure 6.20 (a)) and $D_1 = 0.9 \pm 0.1 \text{ cm}^2\text{s}^{-1}$ and $D_2 = 0.03 \pm 0.02 \text{ cm}^2\text{s}^{-1}$ for pump fluence at 20.6 μJcm^{-2} (Figure 6.20 (b)), respectively. The lack of pump intensity dependence implies that exciton-

exciton annihilation processes do not contribute to the two diffusion constants measured. It has been established that exciton-exciton annihilation^{176, 195} threshold in single layer TMDCs is as low as nJ cm^{-2} . However, the key difference in the 1L-WS₂/Tc heterostructures is that charge transfer processes occur at 2-3 ps timescale, much shorter than exciton-exciton annihilation time of hundreds of ps in monolayer WS₂¹⁹⁵. Therefore, the formation of CT excitons outcompetes exciton-exciton annihilation, leading to much less pronounced annihilation.

The fact that there exist at least two CT exciton populations with different diffusion constants directly supports the delocalized and localized states proposed to explain the stretched exponential PL decay behavior. We attribute the fast-moving population to the CT excitons with a large e-h distance. It is likely that the fast-moving population also leads to the dissociated free electrons. The slow-moving population is the more localized CT excitons trapped at low-energy sites. The energy difference D between the delocalized and localized states can be estimated by $\frac{N_1}{N_2} = e^{-\frac{\Delta}{k_B T}}$, where k_B is the Boltzmann constant and T is temperature. Δ has a value of $\sim 10 \text{ meV} < k_B T$ at room temperature, allowing for detrapping of exciton from the localized states and resulting in the stretched-exponential decay behavior.

A diffusion constant as high as $1 \text{ cm}^2\text{s}^{-1}$ for CT excitons is remarkable, which indicates that the diffusion length, $L = \sqrt{D\tau}$, is up to $\sim 450 \text{ nm}$ when using an average lifetime of 2 ns. A possible explanation for the extremely mobile CT excitons is that the electron mobility in WS₂¹⁹⁶ of $\sim 50 \text{ cm}^2\text{s}^{-1}\text{V}^{-1}$ is more than one order of magnitude higher than and hole mobility in Tc ($\sim 1 \text{ cm}^2\text{s}^{-1}\text{V}^{-1}$)²⁸⁸. CT exciton transport has been proposed to occur *via* asynchronous electron and hole motion. Because the mobile electrons in the WS₂ layer can sample a much

larger distance than the holes in Tc, large e-h distances can be achieved. Dimensionality could also play an important role in increasing e-h distances as suggested by recent theoretical simulations where 2D electron transport increases the dissociation yield of CT excitons by an order of magnitude over 1D case²⁷⁵. CT exciton mobility of $\sim 10 \text{ cm}^2\text{s}^{-1}$ has also been reported in $\text{MoSe}_2/\text{WSe}_2$ interfaces⁸³.

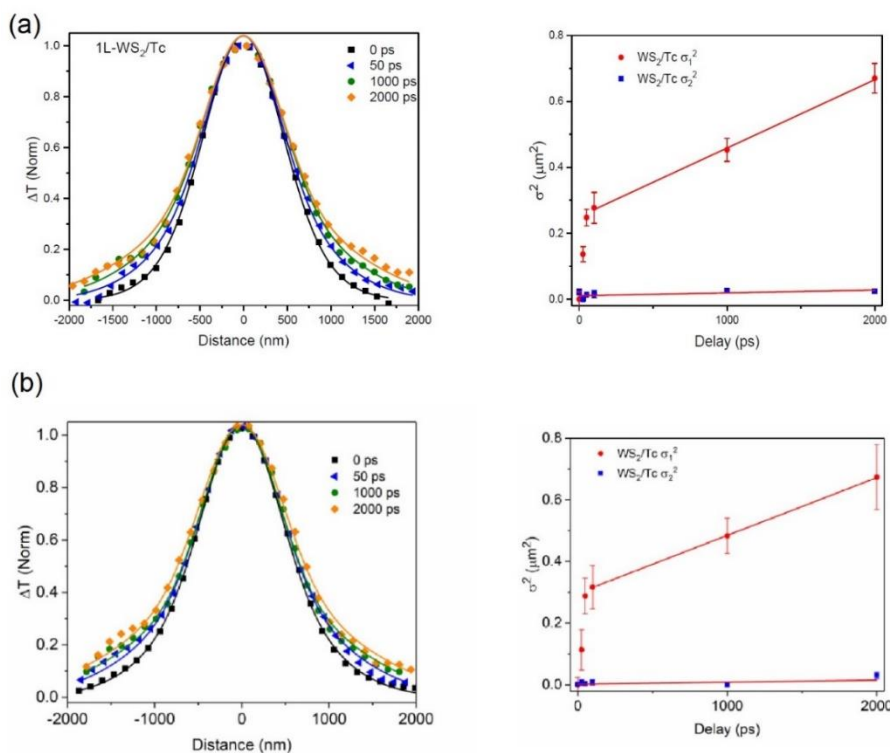


Figure 6.21 Power-dependence exciton population profiles (a) pump fluence: $10.0 \mu\text{J}/\text{cm}^2$. (b) pump fluence: $10.0 \mu\text{J}/\text{cm}^2$. $\sigma_{1,t}^2 - \sigma_0^2$ and $\sigma_{2,t}^2 - \sigma_0^2$ as a function of pump-probe delay time, with linear fits to equation 3 (red lines) for the 1L- WS_2/Tc heterostructure.

The highly mobile CT excitons at the crystalline 2D organic-inorganic interfaces can lead to large e-h distances and facilitate exciton dissociation at interfaces, which could have important implications for charge separation in excitonic solar cells. For instance, the interfaces between conjugated polymer donors and fullerene acceptors are highly

crystalline at the length scale of a few nanometers in organic solar cells, despite overall the system is highly disordered²⁶⁶. The mobile CT excitons at the crystalline nanoscale interfaces could sample large distance in short time (10 nm in 1 ps assuming $D = 1 \text{ cm}^2\text{s}^{-1}$), which could be the key factor for overcoming large CT exciton binding energy to achieve efficient charge separation.

6.5 Conclusion

In summary, the formation and transport of interlayer CT excitons have been elucidated in 2D organic-inorganic vdW heterostructures constructed from WS₂ layers and tetracene thin films. PL measurements confirm the formation of interlayer excitons with a binding energy of $\sim 0.3 \text{ eV}$. Electron and hole transfer processes at the interface between monolayer WS₂ and tetracene thin film are very rapid, with time constants of $\sim 2 \text{ ps}$ and $\sim 3 \text{ ps}$, respectively. TAM measurements of exciton transport at these 2D interfaces reveal coexistence of delocalized and localized CT excitons, with diffusion constant of $\sim 1 \text{ cm}^2\text{s}^{-1}$ and $\sim 0.04 \text{ cm}^2\text{s}^{-1}$, respectively. The trapping-detrapping dynamics of the delocalized and localized states leads to stretch-exponential PL decay. The high mobility of the delocalized CT excitons could be the key factor to overcome large CT exciton binding energy in achieving efficient charge separation.

CHAPTER 7. CHARGE TRANSFER EXCITON DYNAMICS AND TRANSPORT IN TWO-DIMENSIONAL WS₂-WSe₂ HETEROSTRUCTURES

7.1 Abstract

Interlayer charge-transfer (CT) excitons at hetero-interfaces play a critical role in light to electricity conversion using two-dimensional heterostructures. However, how CT excitons recombine and migrate at these interfaces is poorly understood. Here we investigate the formation, dynamics, and transport of interlayer excitons in CVD grown two-dimensional (2D) WS₂-WSe₂ van der Waals (vdW) heterostructures with different stacking orientation (0° and 60°) by combining PL microscopy, ultrafast transient absorption microscopy, and first-principle calculations. Our results present that interlayer exciton dynamics and transport exhibit stacking orientation dependent behavior. Temperature-dependent interlayer exciton dynamics suggests the existence of moiré potential which localizes interlayer excitons. Interlayer exciton transport in WS₂-WSe₂ heterostructures is much more mobile than intralayer excitons in 1L-WS₂ or WSe₂. The dipole repulsion from interlayer excitons could efficiently screen moiré potential fluctuations and facilitates CT exciton transport. We also demonstrate that excess excitation energy promotes charge transfer exciton transport by overcoming the moiré potential. Our results provide fundamental insights in understanding charge transfer exciton dynamics and transport in CVD WS₂-WSe₂ heterostructures which has important implications in optoelectronic applications at the nanoscale limit.

7.2 Background

7.2.1 Charge transfer in two-dimensional van der Waals heterostructures

Transition metal dichalcogenides (TMDCs) are two-dimensional layered semiconductors which hold unique optoelectronic and spintronic properties at the nanoscale limit such as indirect to direct band transition^{7-8, 289-292}, extraordinary large exciton binding energy^{42, 45, 80, 132, 270, 293-294}, and strong spin-orbit interaction^{40, 120, 134, 173, 295-297}. Due to the weak van der Waals interactions, different TMDCs semiconductors could be assembled into two-dimensional heterostructures in which lattice matching and atom inter-diffusion conditions are longer required^{53-54, 56}. 2D Van der Waals heterostructures with type II band alignment^{78-80, 259}, particularly bilayers of TMDCs (MX_2 , where $\text{M} = \text{Mo}, \text{W}$; $\text{X} = \text{S}, \text{Se}, \text{Te}$) have open new avenue in exploring emerging exciton physics properties and optoelectronic^{4, 14, 26, 60-61, 63, 298-299}, valleytronic^{23, 101, 105, 300-304}, and spintronic applications³⁰⁵⁻³⁰⁷ at the nanoscale limit.

In a type II van der Waals heterostructure, photo-excited carriers could undergo efficient charge separation due to the built-in electric field at the interface. Previous studies demonstrated ultrafast charge transfer (≤ 50 fs) across the interface with arbitrary aligned orientation^{81-82, 84-87, 91}. After charge separation, electrons and holes are residing into different layers to form interlayer charge transfer excitons^{52, 93, 98-99, 221, 308}. Owing to the spatially indirect nature, interlayer excitons hold a much longer lifetime than intralayer excitons in monolayer TMDCs^{93-97, 100, 309-311}.

7.2.2 Moiré superlattice

In 2D van der Waals heterostructures, lattice mismatch or rotational misalignment lead to the formation of in-plane moiré superlattice³¹²⁻³¹³. The moiré pattern has been

displayed to have a remarkable effect on the impact on the electronic, optical, and magnetic properties of van der Waals heterostructures³¹⁴⁻³²⁰. According to a recent theoretical study, interlayer excitons are modulated by periodically potential in the moiré superlattice and form perfect arrays of nanodots that act as uniform quantum emitters³¹⁴. The predicted moiré potential is about 100 meV which can be tuned by applying electrical field and strain^{314, 321-322}. Such a deep potential is expected to localize interlayer excitons even at room temperature. Although recent studies demonstrated that multiple exciton states are confined within the moiré potential by detecting interlayer exciton emission^{58, 323-325}, it is still elusive on how moiré potential modifies interlayer exciton recombination and transport.

7.2.3 Interlayer charge transfer excitons dynamics and transport

Understanding the interlayer exciton dynamics and transport of moiré excitons in van der Waals heterostructures is critical for fundamental research and optoelectronic applications. Recent optical measurements on moiré excitons are mostly studying how moiré potential affects interlayer exciton emission in van der Waals heterostructures⁵⁸. However, a drawback for PL based techniques is that only emissive species are investigated while many of the interlayer CT states are optically dark. To address this challenge, we employ transient absorption microscopy (TAM) that is capable of imaging both bright and dark interlayer excitons and track the interlayer excitons recombination and transport modulated by moiré potential.

7.3 Experiential Methods

7.3.1 Second-harmonic generation (SHG) microscopy

SHG measurements were taken using the confocal PL microscope as described previously. Briefly, the fundamental light from an optical parametric amplifier (OPA, TOPAS-Twins, Light Conversion Ltd) with a photon energy of 1.55 eV was focused on the sample using a 50X (N.A. = 0.95) objective. The reflected SHG light with a photon energy of 3.10 eV was collected using the same objective, dispersed with a monochromator (Andor Technology) and detected by a TE-cooled charge-coupled device (Andor Technology). The reflected fundamental light was removed using a short-pass filter.

7.3.2 Determination of exciton density

In our PL experiments, excitons in WS₂ are generated by the absorption of the pump laser. The peak fluence of pump pulse (P_f) could be calculated as:

$$P_f = \frac{P}{A} \quad (1)$$

where P is the pump pulse energy, A is the pump excitation effective area. Since pump pulse is a Gaussian beam. To calculate the exciton density injected by the pump, we assume that every absorbed pump photon could create one exciton. Then, the injected exciton density could be obtained as:

$$N = \frac{\alpha P_f}{\hbar\nu} \quad (2)$$

where α and $\hbar\nu$ are the absorption coefficient and photon energy of the pump pulse.

7.4 Result and discussions

7.4.1 Charge transfer exciton emission in CVD WS_2 - WSe_2 heterostructures

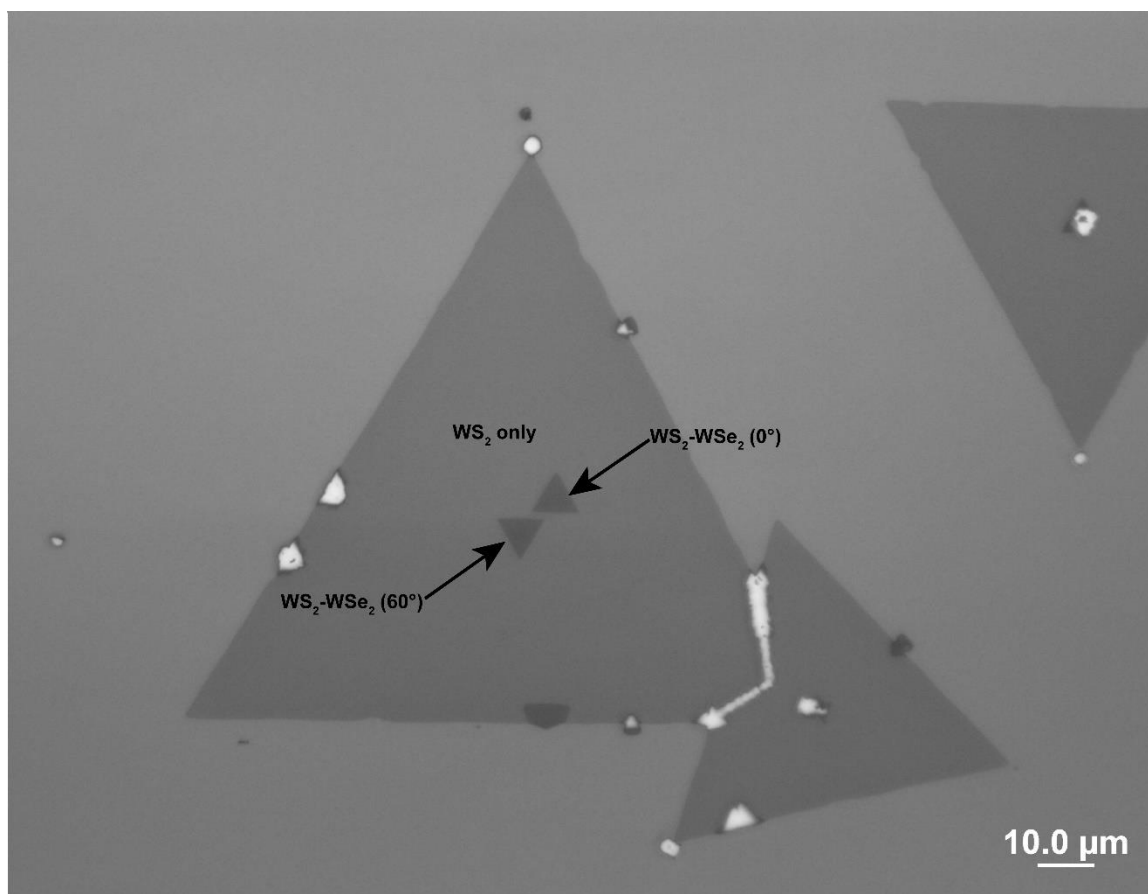


Figure 7.1 Optical image of CVD grown WS_2 - WSe_2 heterostructures with two twist angles (0° and 60°). Scale bar represents 10 μm .

In our experiment, we grow WS_2 - WSe_2 heterostructures with different stacking orientation by chemical vapor deposition (CVD)^{74, 326-327}. Figure 7.1 shows an optical reflection image of WS_2 - WSe_2 heterostructures with twist angles of $\theta = 0^\circ$ and 60° . We first grow single layer WS_2 on the SiO_2/Si substrate shown as a single crystalline triangular with lateral size around 100 micrometers. Then, we directly grow single layer WSe_2 on top of WS_2 with a lateral size around 10 micrometers.

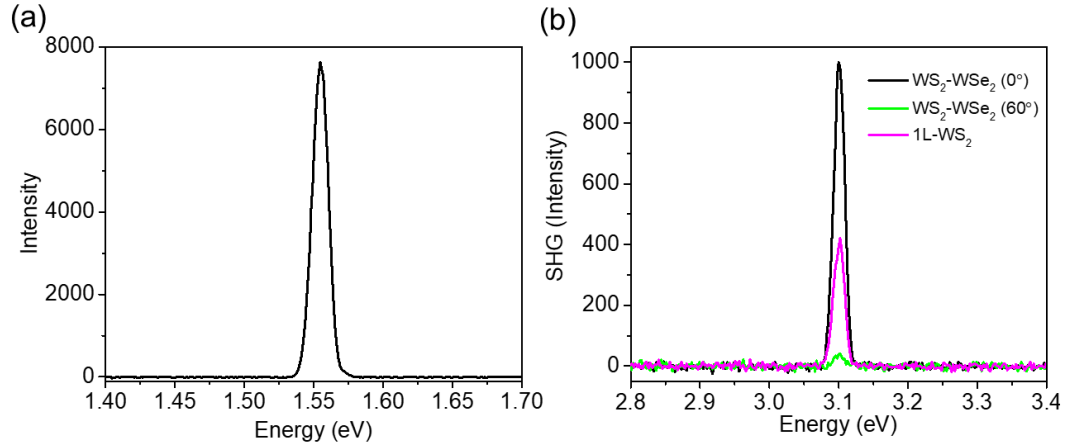


Figure 7.2 (a) Fundamental light with a photon energy of 1.55 eV used in SHG measurements. (b) SHG signal (3.10 eV) from WS₂-WSe₂ heterostructures ($\theta = 0^\circ$ and 60°) and 1L-WS₂.

CVD grown WS₂-WSe₂ heterostructures typically have two twist angles (0° and 60°) which can be readily determined by the relative stacking orientation of top and bottom triangular shapes due to that the orientation of each triangle is directly correlated with its microscopic crystal orientation^{84, 328}. We further confirm the stacking orientation using SHG microscopy. Previous studies have displayed that the SHG signal is very sensitive to the crystalline symmetry and orientation^{84, 328-330}. The SHG from the twisted bilayers is a coherent superposition of the SH fields from the individual layers, with a phase difference depending on the stacking angle. A full description of the model for SHG in twisted bilayer with an arbitrary stacking angle was reported before³²⁹. Briefly, if the laser electric field $\vec{E}_1(\omega)$ has an angle of φ_1 (φ_2) with armchair direction of monolayer flake 1 (flake 2), the generated SH electric field $\vec{E}_1(2\omega)$ [$\vec{E}_2(2\omega)$] from flake 1 (flake 2) is then $3\varphi_1$ ($3\varphi_2$) away from the laser polarization. The total SH electric field $\vec{E}_{total}(2\omega)$ in the stacking bilayer is equal to the vector superposition of SH field in monolayer flakes 1 and 2:

$\vec{E}_{total}(2\omega) = \vec{E}_1(2\omega) + \vec{E}_2(2\omega)$. The total SHG intensity in the stacking region is proportional to $|\vec{E}_{total}(2\omega)|^2$ which can be described as

$$I_{total}(\theta) = I_1 + I_2 + 2\sqrt{I_1 I_2} \cos 3\theta \quad (1)$$

where I_{total} , I_1 , and I_2 represent SH intensity of stacking bilayer, flake 1, and flake 2, respectively, and $\theta = \varphi_1 - \varphi_2$ is the stacking angle which is defined as the angle between two nearest perpendicular bisectors of the two triangular flakes. In WS₂-WSe₂ heterostructures, $\theta = 0^\circ$ yields a completely constructive interference while $\theta = 60^\circ$ yields a completely destructive interference of SH fields. This model is well agreed with SHG measurement results shown in Figure 7.2. The SHG intensity of WS₂-WSe₂ ($\theta = 0^\circ$) is strongly enhanced compared with single-layer WS₂ while it is greatly suppressed in WS₂-WSe₂ ($\theta = 60^\circ$).

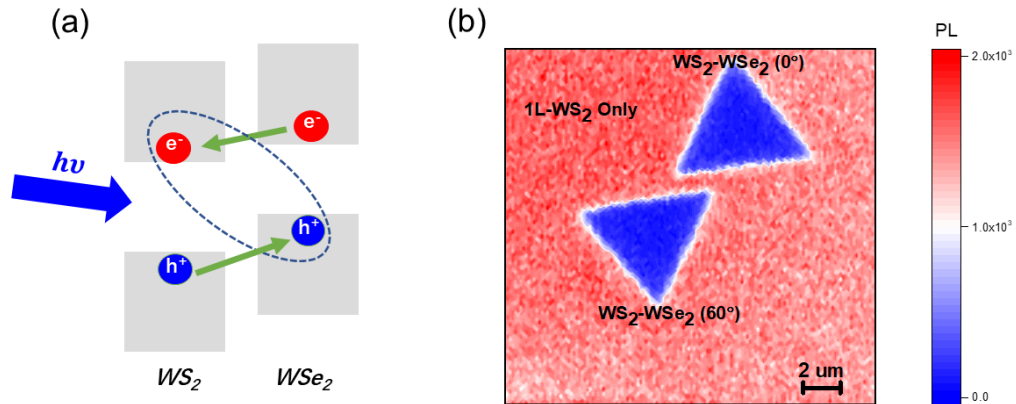


Figure 7.3 (a) Schematic of band alignment in WS₂-WSe₂ heterostructures. (b) PL image of WS₂-WSe₂ heterostructures (0° and 60°) as shown in Figure 7.1. Scale bar represents 2 μm.

Previous DFT band structure calculations⁷⁸ have displayed that WS₂-WSe₂ bilayer has a type II band alignment as shown schematically in Figure 7.3 (a). After photoexcitation, electrons transfer from WSe₂ to WS₂ while holes transfer from WS₂ to WSe₂.

Previous reports display that charge transfer occurs in tens of femtosecond which is much faster than the exciton recombination of single-layer WS₂ or WSe₂. As a result, the ultrafast charge separation would greatly reduce the radiative recombination for both WS₂ and WSe₂ in the heterostructure region. Figure 7.3 (b) displays a PL image of WS₂-WSe₂ heterostructures (0° and 60°) which clearly shows significant PL quench on the heterostructures region. Figure 7.4 (a) displays that PL intensity decreased by a factor of 30 in WS₂-WSe₂ (60°) bilayer which indicates efficient charge separation^{81, 88}. Raman measurement (Figure 7.4 (b)) shows two characteristic Raman peaks (E_{2g}^1 and A_{1g}) which are corresponding to in-plane and out-of-plane vibration modes.

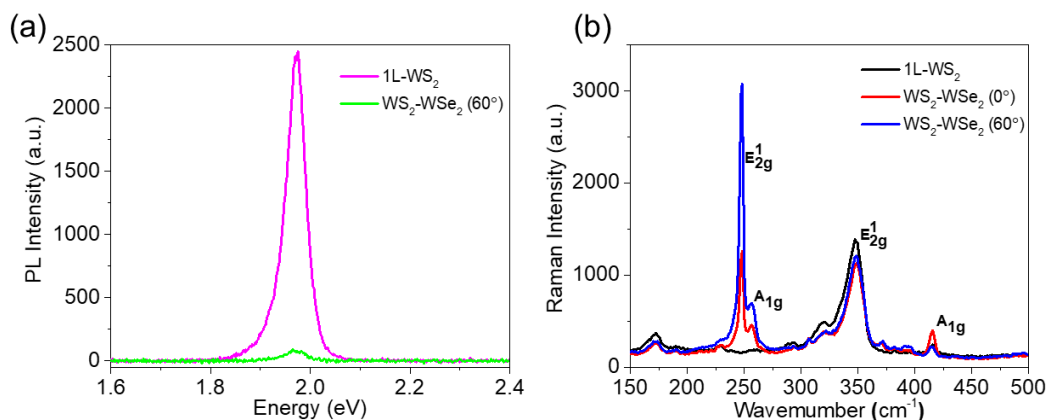


Figure 7.4 (a) PL spectrum of 1L-WS₂ and WS₂-WSe₂ heterostructure (60°). (b) Raman spectrum of 1L-WS₂ and WS₂-WSe₂ heterostructures (0° and 60°).

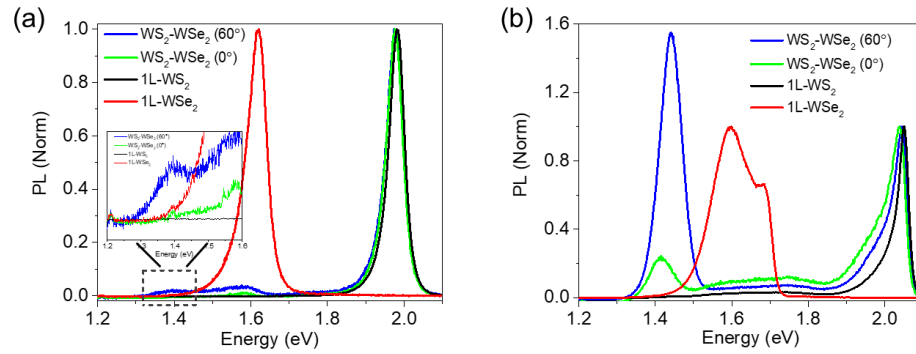


Figure 7.5 PL spectrum of WS₂-WSe₂ heterostructures (0° and 60°), 1L-WS₂, and 1L-WSe₂ at 295 K (a) and 78 K (b).

The efficient charge separation in WS₂-WSe₂ bilayer leads to the formation of spatially indirect interlayer exciton which is likely emitting photons by radiative recombination with lower energy than the band gap of WS₂ or WSe₂. Here, we observe a new emission peak at ~1.4 eV (Figure 7.5 (a)) in WS₂-WSe₂ (60°) which doesn't exist in either 1L-WS₂ or WSe₂ layers. We attribute this new emission to the radiative recombination of interlayer excitons. PL emission from interlayer excitons is greatly enhanced at 78 K for both WS₂-WSe₂ heterostructures (0° and 60°) as shown in Figure 7.5 (b) which is due to the suppressed non-radiative recombination at low temperature. It is also interesting to see that interlayer exciton emission displays stacking orientation dependence behavior. The interlayer exciton emission in WS₂-WSe₂ (60°) is about one order magnitude higher than WS₂-WSe₂ (0°) at 78 K. We also carried out temperature-dependent PL measurements for 1L-WS₂, 1L-WSe₂, WS₂-WSe₂ (0°), and WS₂-WSe₂ (60°) as shown in Figure 7.6. Interlayer exciton emission intensity in both WS₂-WSe₂ (0°) and WS₂-WSe₂ (60°) increases with temperature decreases.

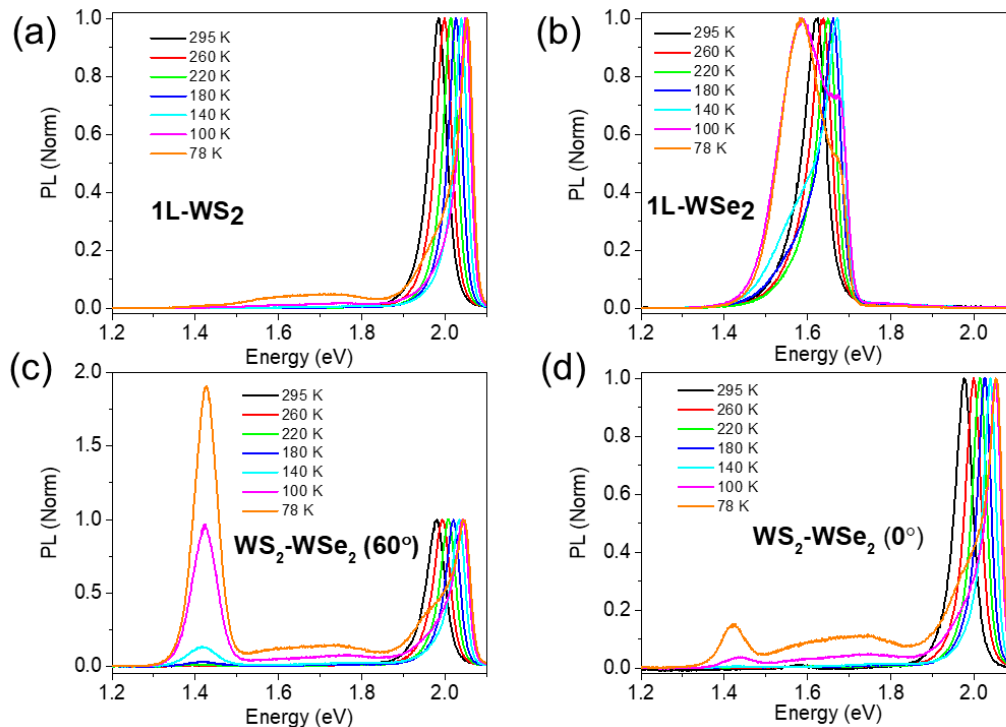


Figure 7.6 Temperature dependent PL spectrum for (a) 1L-WS₂, (b) 1L-WSe₂, (c) WS₂-WSe₂ (60°), and (d) WS₂-WSe₂ (0°).

Figure 7.7 (a) displays a PL image of interlayer exciton emission from a WS₂-WSe₂ (60°) bilayer by detecting the emitting photon energy between 1.30 and 1.55 eV. It clearly shows that interlayer exciton emission only exists in the heterostructure region. The existence of interlayer exciton emission is further confirmed by the photoluminescence excitation (PLE) spectroscopy presented in Figure 7.6 (b). Briefly, we monitor the interlayer emission intensity by scanning the excitation energies at 78 K. It displays that interlayer emission could track A exciton resonance (~2.03 eV) of 1L-WS₂, which vanishes when excitation energies are below the optical band gap of 1L-WS₂.

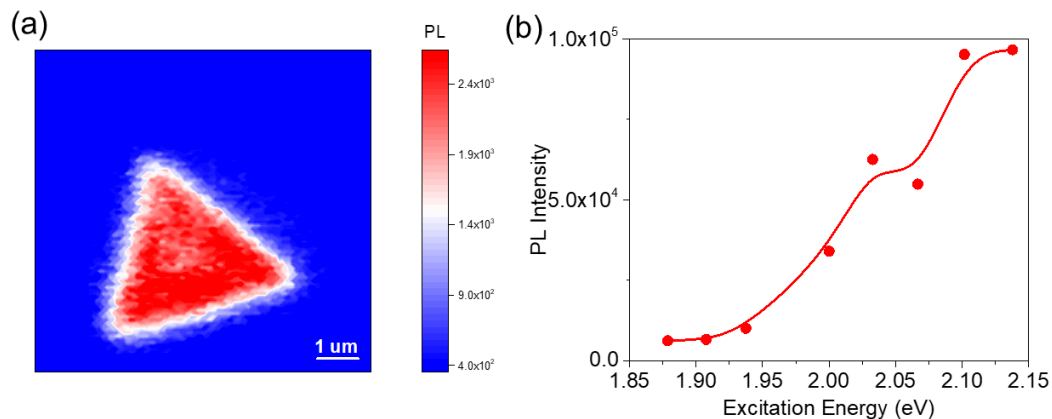


Figure 7.7 (a) PL image of interlayer exciton emission in $\text{WS}_2\text{-WSe}_2$ (60°) at 78 K with a detection range between 1.30 and 1.55 eV. (b) PLE spectra of interlayer exciton emission in $\text{WS}_2\text{-WSe}_2$ (60°) at 78 K.

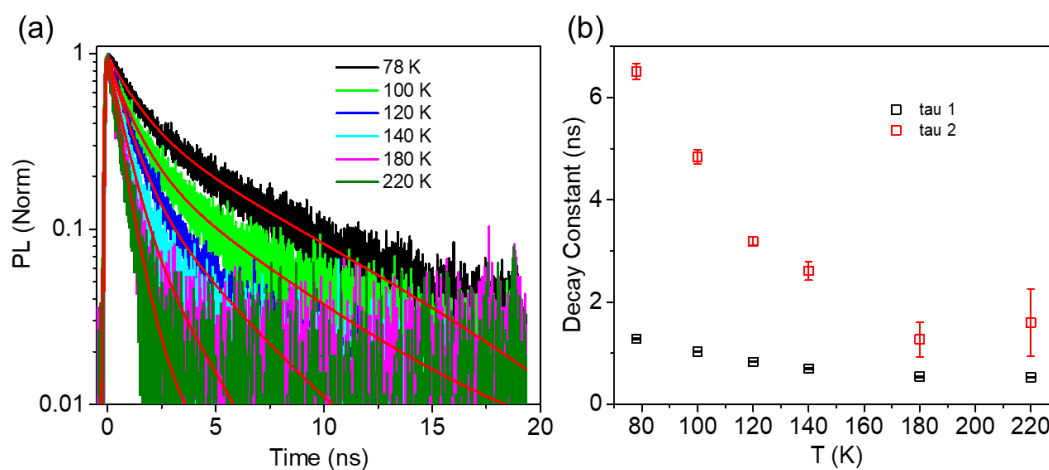


Figure 7.8 (a) Temperature-dependent TRPL dynamics of interlayer excitons in $\text{WS}_2\text{-WSe}_2$ (60°). (Red lines are fits using a bi-exponential function convoluted with an IRF function). (b) A plot of fitted decay constant of TRPL dynamics shown in Figure 7.8 (a).

Figure 7.8 (a) presents temperature dependent interlayer exciton PL dynamics of $\text{WS}_2\text{-WSe}_2$ (60°). Interlayer exciton recombination rate decreases as temperature decreases. Here we employ a bi-exponential function convoluted with an IRF function to fit the PL dynamics shown in Figure 7.8 (b). We observe two decay components in the nanosecond

range which increases with temperature decreases. The longer interlayer exciton recombination lifetime at low temperature is probably due to the suppressed non-radiative recombination.⁹⁶

7.4.2 Stacking orientation dependent charge transfer exciton formation in CVD WS₂-WSe₂ heterostructures

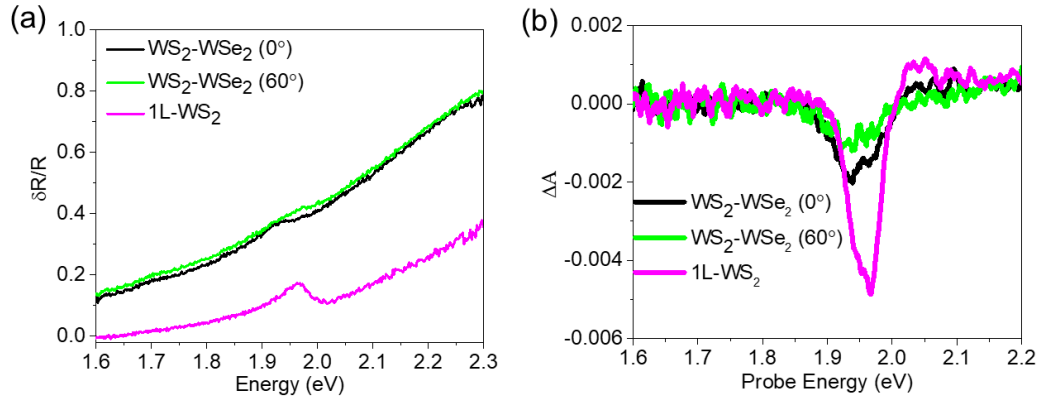


Figure 7.9 (a) Differential reflection spectrum of WS₂-WSe₂ heterostructures (0° and 60°) and 1L-WS₂. (b) Transient reflection spectrum of WS₂-WSe₂ heterostructures (0° and 60°) and 1L-WS₂.

Figure 7.9 (a) displays the differential reflectance spectrum ($\frac{\delta R}{R}$) of WS₂-WSe₂ heterostructures (0° and 60°) and 1L-WS₂ at room temperature. Here, $\frac{\delta R}{R} = \frac{R_{sample} - R_{substrate}}{R_{substrate}}$, where R_{sample} is the reflectance of the sample on the SiO₂/Si substrate and $R_{substrate}$ is the reflectance of bare SiO₂/Si substrate. In 1L-WS₂, A exciton resonance associated with band edge absorption has a notable absorption peak around 1.96 eV. However, in WS₂-WSe₂ heterostructures (0° and 60°), A exciton absorption peak displays a significant red shift (~20 meV) compared with 1L-WS₂. Since the optical band gap (E_{opt}) of WS₂ is related to single-particle band gap (E_{single}) and exciton binding energy ($E_{exciton}$), $E_{opt} = E_{single} - E_{exciton}$, the reduction of E_{op} in WS₂ is attributed to the reduction of

both E_{single} and $E_{exciton}$ by the enhanced dielectric screening due the presence of WSe_2 and weakly bounded interlayer excitons. $E_{exciton}$ is further reduced than E_{single} to cause the downshift of E_{opt} . Similar behavior is also observed in the downshift of A exciton bleach energies in the transient reflection spectrum shown in Figure 7.9 (b).

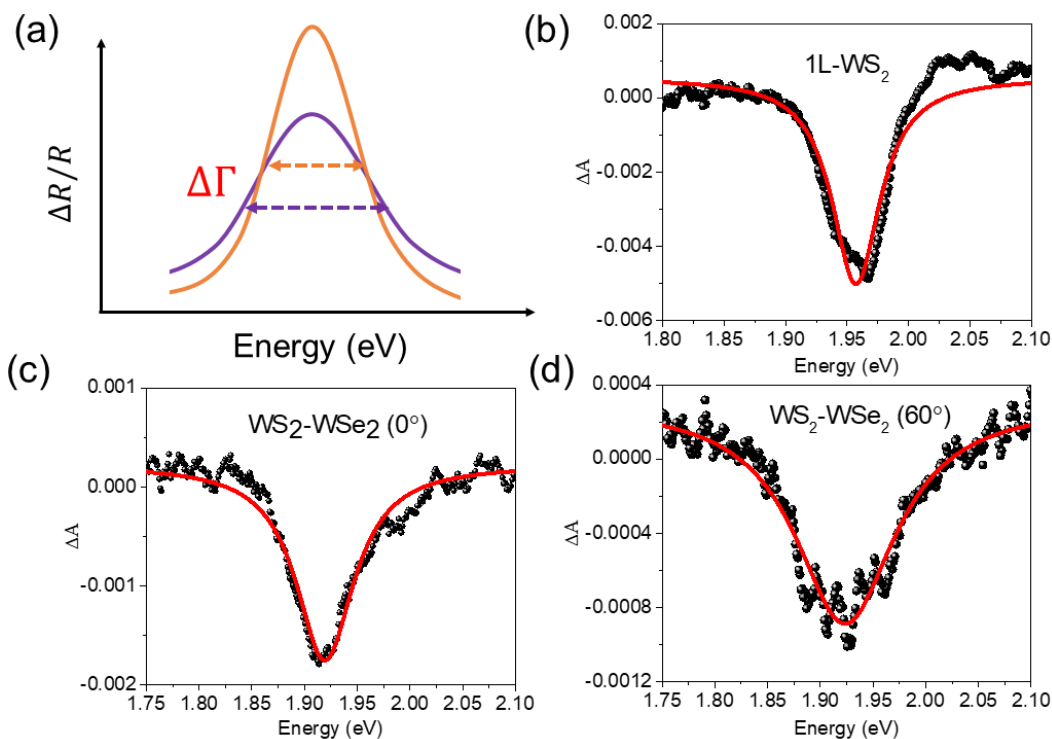


Figure 7.10 (a) Schematic of exciton broadening in WS_2 - WSe_2 heterostructures. A exciton bleach of 1L- WS_2 , WS_2 - WSe_2 (0°), and WS_2 - WSe_2 (60°). Red lines are fits using a Lorentzian function.

The broadening of A exciton resonance in WS_2 - WSe_2 heterostructures is also shown in the transient reflection spectrum (Figure 7.9 (b)). By fitting the exciton bleach with a Lorentzian function, A exciton linewidth of 1L- WS_2 , WS_2 - WSe_2 (0°), and WS_2 - WSe_2 (60°) are determined to be 47.6, 67.4, and 116.6 meV, respectively. By using the uncertain principle, $\tau = \frac{\hbar}{\Delta\Gamma}$, the timescale of population time (τ) is determined to be 34.6 and 9.1 fs for WS_2 - WSe_2 (0°) and WS_2 - WSe_2 (60°). Here, we consider three typical physical

processes underlying the observed line width increase: enhanced phonon scattering in the heterostructure, energy transfer, and charge transfer between layers⁸⁹.

In 1L-WS₂, the measured exciton line width of A exciton resonance is about 50 meV. Previous temperature dependent measurements determined the contribution to the line width from thermal phonon is about 20-30 meV. However, enhancement of photon scattering rate by a factor of 2 and 3 for WS₂-WSe₂ (0°) and WS₂-WSe₂ (60°) is very unlikely due to the scattering of carriers in one layer with the phonons in the adjacent layer should be much less efficient than in the same layer. In addition, this mechanism could not explain the difference in the exciton broadening between WS₂-WSe₂ (0°) and WS₂-WSe₂ (60°).

Next, we consider the effect of energy transfer. If energy transfer dominates, we could expect it causes the quench of PL intensity in WS₂ and enhancement of PL intensity in WSe₂. However, PL measurements present a significant reduction of PL intensity of both WS₂ and WSe₂ in the heterostructure. Furtherly, a recent experiment has determined the low bound of the energy transfer rate in WS₂/MoSe₂ heterostructure to be in picosecond to subpicosecond time scales which is much slower than tens of femtosecond inferred from the measured peak broadening. We conclude that energy transfer is not dominated in the exciton broadening.

Finally, we consider charge transfer as the dominated factor. PL measurements have indicated extremely efficient charge transfer between WS₂ and WSe₂. Due to the temporary limitation of femtosecond pump-probe spectroscopy (~ 300 fs) used in this measurement, it is very difficult to directly resolve charge transfer time scales with different twist angle. We could only provide an upper bound limit of charge transfer which has a lower bound

limit for charge transfer (9-35 fs) in WS₂-WSe₂ heterostructures. The stacking orientation dependent charge transfer is surprising because a recent study displays ultrafast (< 40 fs) charge transfer in MoS₂/WSe₂ heterostructures which is independent of twist angle. A recent ab initio time-dependent density functional theory (TDDFT) molecular dynamics simulation on MoS₂/WS₂ heterostructures revealed that the minor change of interlayer geometry can significantly modulate the charge transfer time from 100 fs to 1 ps scale which is governed by the electronic coupling between specific interlayer states⁸⁶.

7.4.3 Stacking orientation dependent interlayer exciton recombination in CVD WS₂-WSe₂ heterostructures

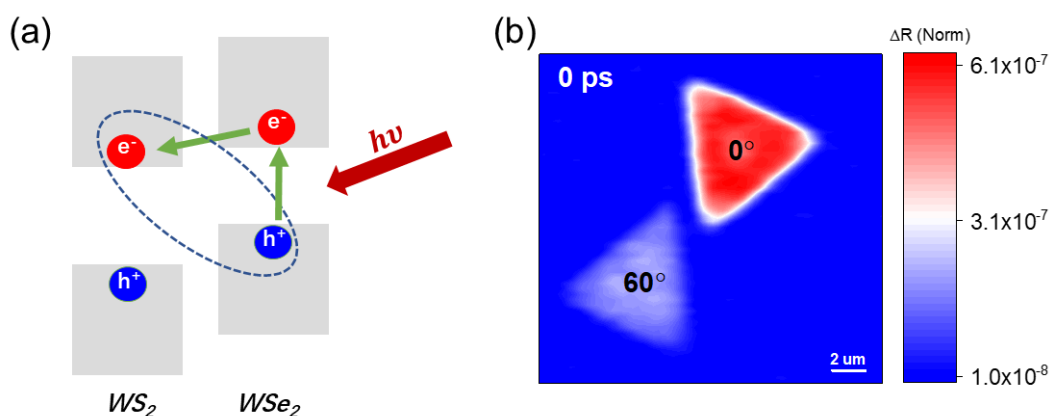


Figure 7.11 (a) Schematic of electron transfer in WS₂/WSe₂ heterostructures when selectively exciting WSe₂ layer with a pump photon energy of 1.58 eV. (b) TAM imaging of WS₂-WSe₂ heterostructures (0° and 60°) at 0 ps. (pump photon energy is 1.58 eV; probe photon energy is 1.94 eV)

In order to study interlayer exciton recombination dynamics, we selectively excite the WSe₂ layer in the WS₂-WSe₂ heterostructure using a photon energy of 1.58 eV shown in Figure 7.11 (a). After photo-excitation, electrons could transfer from WSe₂ layers to WS₂ layers and induce bleach signal of WS₂ due to Pauli blocking principle. By probing at the A exciton resonance of WS₂ (1.94 eV), we could directly measure interlayer exciton

dynamics. Figure 7.11 (b) displays a TAM image of WS₂-WSe₂ heterostructures (0° and 60°) with pump photon energy of 1.58 eV and probe photon energy of 1.94 eV. Here we only observe bleach signal from the heterostructure region with no detectable signal from the WS₂ only area.

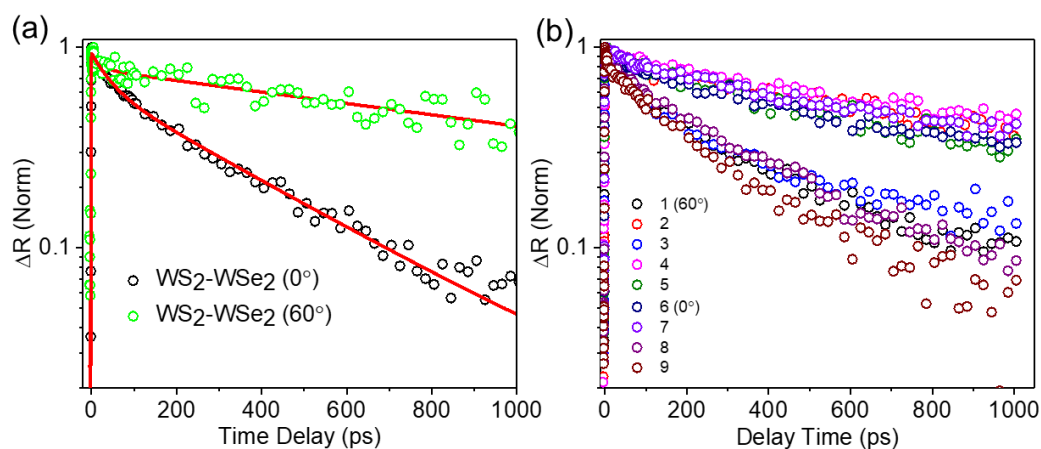


Figure 7.12 (a) A representative result of charge transfer exciton dynamics of WS₂-WSe₂ heterostructures (0° and 60°). (pump photon energy is 1.58 eV; probe photon energy is 1.94 eV). Red lines are fits using a bi-exponential function convoluted with an IRF function. (b) Charge transfer exciton dynamics of different WS₂-WSe₂ heterostructures (0° and 60°).

Table 7.1 Fitted decay constants of TA dynamics traces shown in Figure 7.11 (a).

	τ_1 (ps)	τ_2 (ps)
0°	25.3	358.6
60°	45.0	1456.0

Figure 7.12 (a) presents charge transfer exciton dynamics of WS₂-WSe₂ heterostructures (0° and 60°) at room temperature which displays significant stacking configuration dependent recombination dynamics. WS₂-WSe₂ heterostructures (0°) lives much longer than WS₂-WSe₂ heterostructures 60°. By fitting the dynamics with a bi-

exponential function convoluted with an IRF function, we obtain recombination constant of WS₂-WSe₂ heterostructures (0° and 60°) shown in table 1. The decay constant of WS₂-WSe₂ heterostructure (60°) lives four times longer than WS₂-WSe₂ heterostructure (0°). The stacking dependent recombination dynamics display insignificant power dependence shown in Figure 7.13.

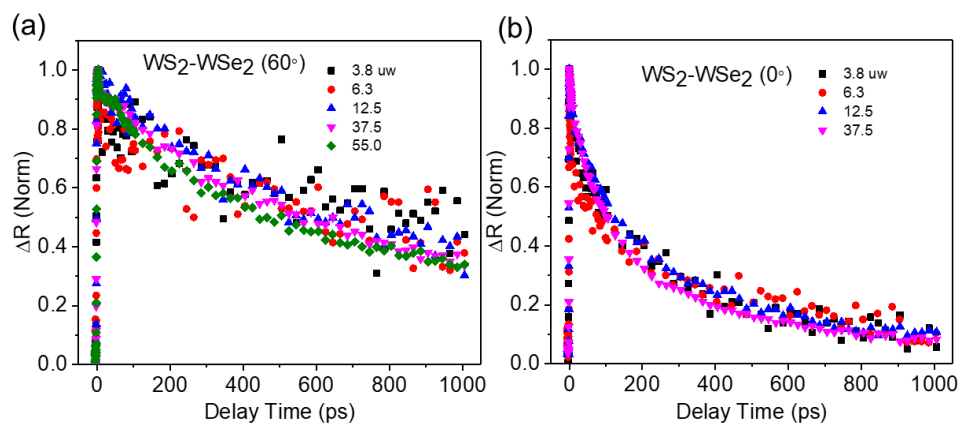


Figure 7.13 Power dependent charge transfer exciton recombination dynamics of WS₂-WSe₂ (60°) and WS₂-WSe₂ (0°). (pump photon energy is 1.58 eV; probe photon energy is 1.94 eV).

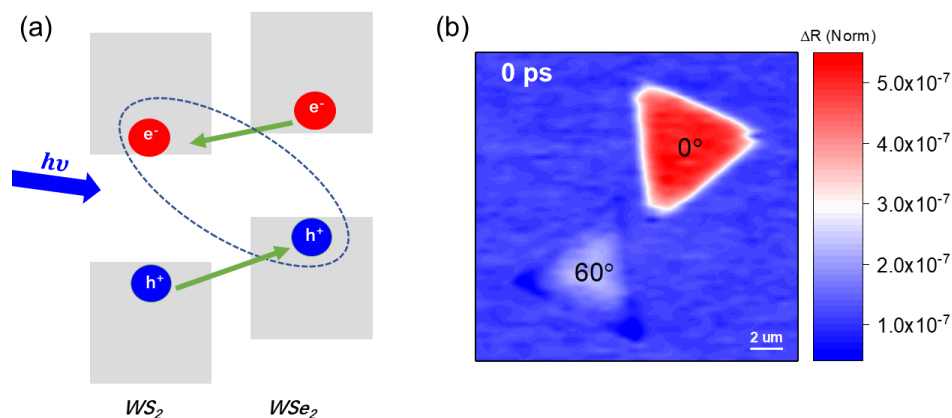


Figure 7.14 (a) Schematic of charge transfer in WS₂/WSe₂ heterostructures when exciting both WS₂ and WSe₂ layer with a pump photon energy of 3.14 eV. Here, electrons transfer from WSe₂ to WS₂ while holes transfer from WS₂ to WSe₂. (b) TAM imaging of WS₂-WSe₂ heterostructures (0° and 60°) at 0 ps. (pump photon energy is 3.14 eV; probe photon energy is 1.94 eV)

We also carried out transient absorption measurements at a pump photon energy of 3.14 eV which could excite both WS₂ and WSe₂. Under this experiment condition, we expect electrons and holes transfer could occur simultaneously. Electrons could transfer from WSe₂ to WS₂ while holes could transfer from WS₂ to WSe₂ as shown in Figure 7.14 (a). Figure 7.14 (b) displays a TAM image at 0 ps with a probe photon energy of 1.94 eV. Here, we observe TA signal in WS₂-WSe₂ (0°) is around 2 times of magnitude higher than WS₂-WSe₂ (60°) which agrees well with the transient absorption spectroscopy measurements in Figure 7.10.

Figure 7.15 compares transient absorption dynamics of WS₂-WSe₂ (0°), WS₂-WSe₂ (60°), 1L-WS₂, and 2L-WS₂. By fitting the dynamics traces using a bi-exponential function convoluted with an IRF function (Table 2), It clearly displays the contrast of lifetime between charge transfer exciton in WS₂-WSe₂ heterostructures and intralayer exciton in 1L-WS₂ or 2L-WS₂. Charge transfer exciton in the heterostructures could live up to hundreds of picoseconds to several nanoseconds depending on stacking orientation while intralayer exciton in either 1L-WS₂ or 2L-WS₂ could only display short lifetimes up to tens of picosecond.

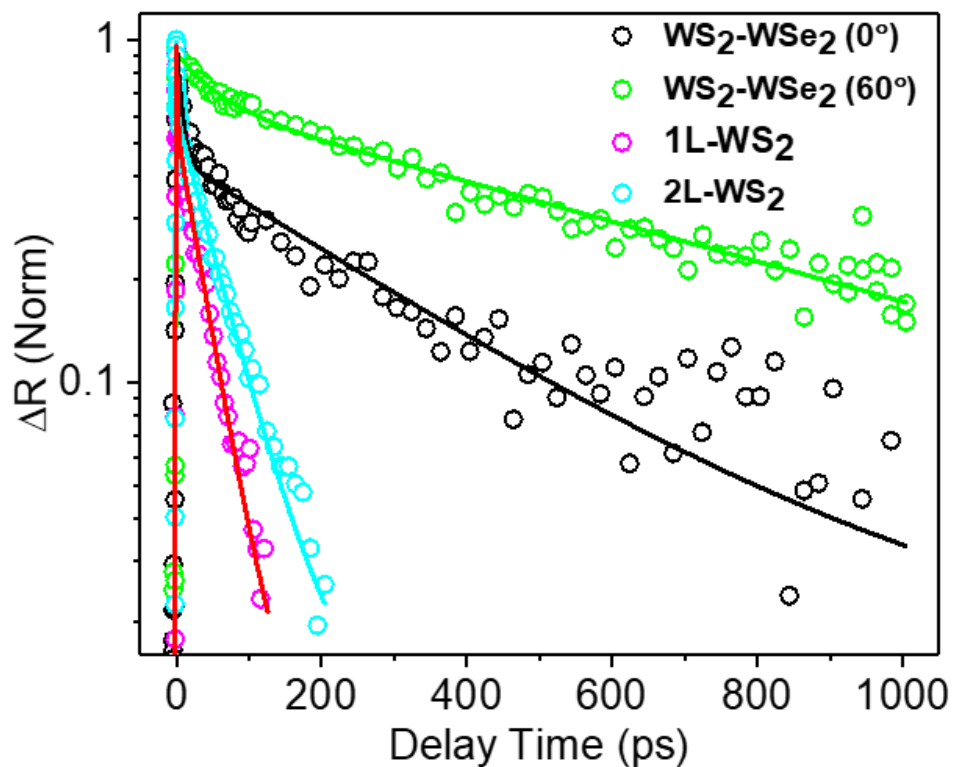


Figure 7.15 Charge transfer exciton dynamics of WS₂-WSe₂ heterostructures (0° and 60°). (pump photon energy is 3.14 eV; probe photon energy is 1.94 eV). Red lines are fits using a bi-exponential function convoluted with an IRF function.

Table 7.2 Fitted decay constants of TA dynamics traces shown in Figure 7.15.

	τ_1 (ps)	τ_2 (ps)
0°	7.4	316.6
60°	53.1	744.7
1L-WS ₂	1.3	35.0
2L-WS ₂	1.0	53.3

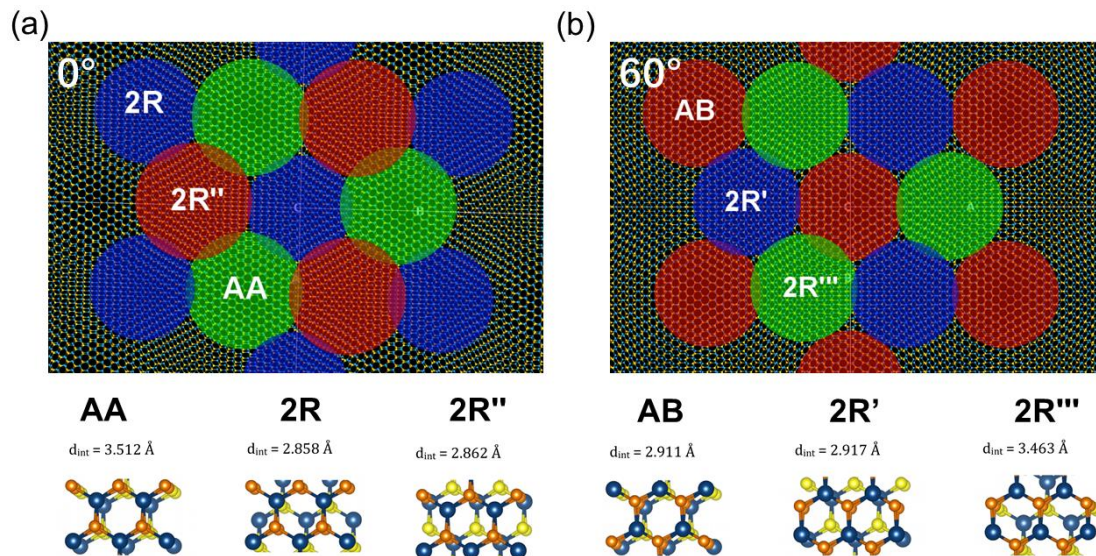
7.4.4 Moiré trapped interlayer exciton dynamics of CVD WS₂-WSe₂ heterostructures

Figure 7.16 Long-period Moiré superlattice and three representative interlayer atomic registries for (a) WS₂-WSe₂ (0°) and (b) WS₂-WSe₂ (60°).

Due to lattice constants of WS₂ ($a = 0.315 \text{ nm}$) and WSe₂ ($a = 0.328 \text{ nm}$) is slight different, lattice mismatch (4%) leads to the formation of Moiré superlattice in WS₂-WSe₂ heterostructures. The Moiré superlattice constant (b) is calculated as³¹⁴:

$$b \approx \frac{a}{\sqrt{\delta\theta^2 + \left(\frac{a'}{a} - 1\right)^2}} \quad (2)$$

where a (a') is the lattice constant of WS₂ (WSe₂) and $\delta\theta$ is the small deviation angle between the zigzag crystalline axes of the two layers. The Moiré superlattice constants for both WS₂-WSe₂ (0°) and WS₂-WSe₂ (60°) are about 6.7 nm. From first-principle calculation, we obtain three representative interlayer atomic registries and the corresponding interlayer distance in the Moiré superlattices for WS₂-WSe₂ (0°) and WS₂-WSe₂ (60°) shown in Figure 7.16.

Table 7.3 First-principle calculations of the band gap, total energy, and interlayer distance for different bilayer stacking registries shown in Figure 7.16.

System	Gap@K [eV]	DE [meV]	d_{int} [Å]	System	Gap@K [eV]	DE [meV]	d_{int} [Å]
AB	0.681	0.0	2.911	AA	0.597	109.3	3.512
2R'	0.648	27.8	2.917	2R	0.755	0.0	2.858
2R'''	0.587	103.5	3.463	2R''	0.542	14.9	2.862

. Since interlayer distance varies in different interlayer atomic registries in the Moiré superlattices, the band gap should also vary with different atomic registries as shown in Table 3. For example, 2R'' in WS₂-WSe₂ (0°) has the smallest bandgap which indicates the lowest potential energy in all three stacking geometries. DFT calculations indicate that the Moiré potential in WS₂-WSe₂ (0°) is about 213 meV which is over two times magnitude higher than in WS₂-WSe₂ (60°) (94 meV). Although it is still challenging to obtain accurate bandgap through DFT calculations, it suggests that Moiré potential in WS₂-WSe₂ (0°) is significantly larger than in WS₂-WSe₂ (60°). We plot a schematic of potential energies in different atomic registries in Figure 7.17. The large Moiré potential is expected to trap and promote the recombination of interlayer excitons. Particularly, at low temperature, due to the reduction of thermal energy for thermal activation, interlayer excitons are localized in these potential wells and recombine through radiative and non-radiative pathways.

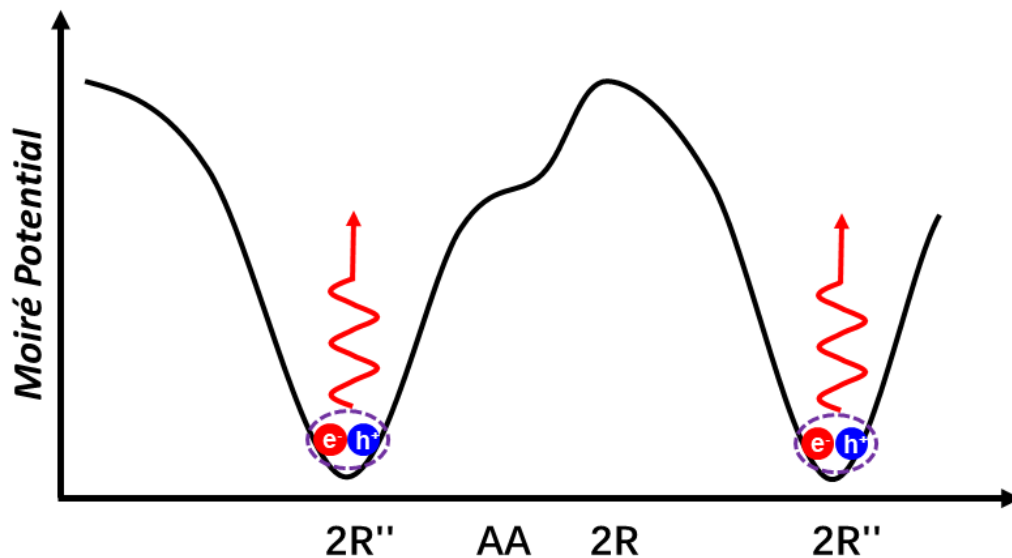


Figure 7.17 Schematic of Moiré potential landscape for WS₂-WSe₂ (0°).

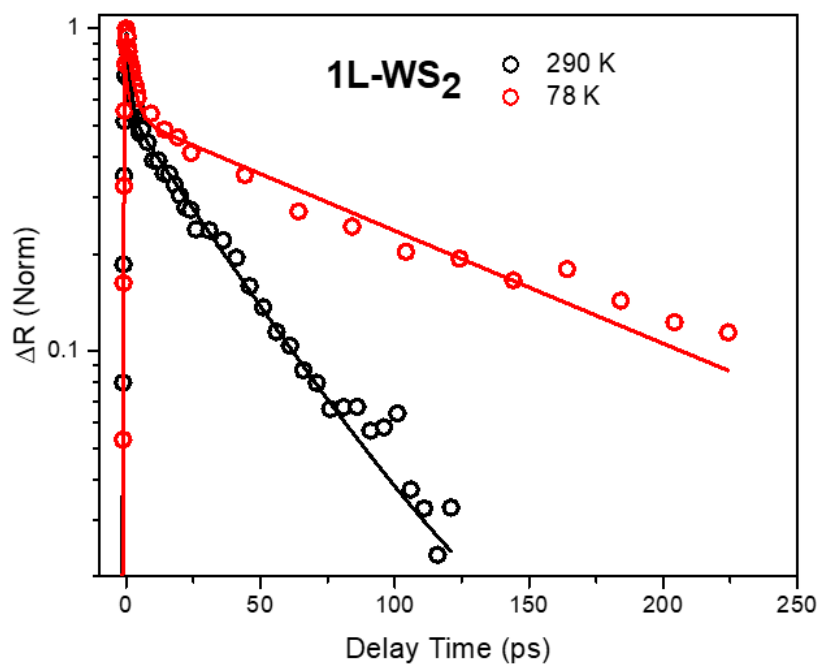


Figure 7.18 Temperature-dependent exciton dynamics of 1L-WS₂ (pump photon energy is 3.14 eV; probe photon energy is 1.94 eV). Solid lines are fits using a bi-exponential function convoluted with an IRF function.

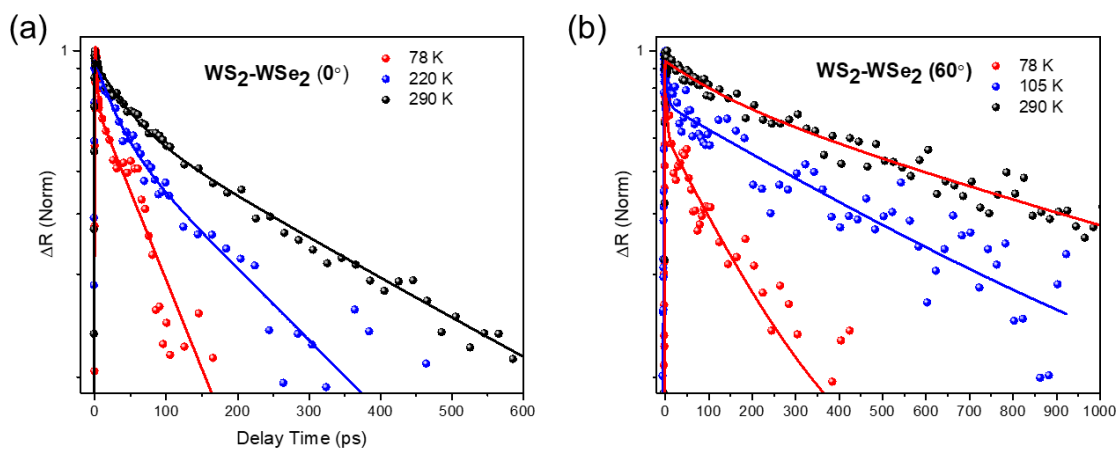


Figure 7.19 Temperature dependent charge transfer exciton recombination dynamics of WS_2-WSe_2 (0°) and WS_2-WSe_2 (60°). (pump photon energy is 1.58 eV; probe photon energy is 1.94 eV). Solid lines are fits using a bi-exponential function convoluted with an IRF function.

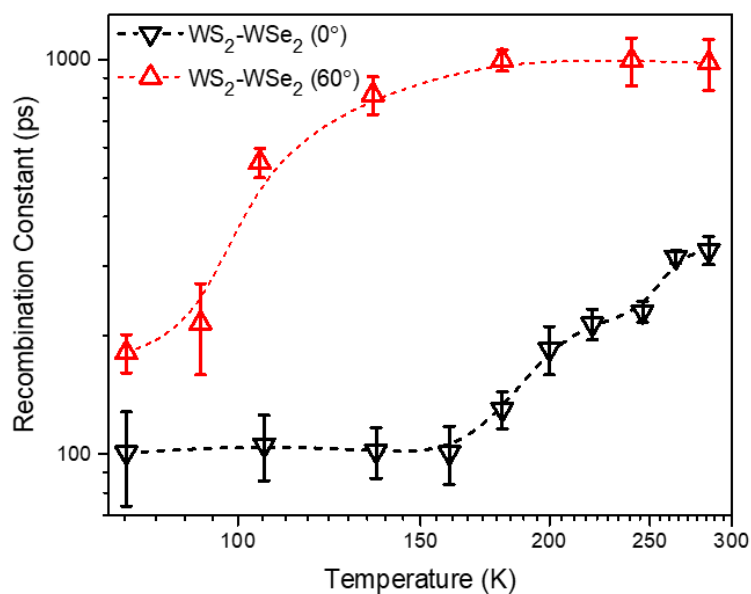


Figure 7.20 Charge transfer exciton recombination constant extracted from Figure 7.16 as a function of temperature for WS_2-WSe_2 (0°) and WS_2-WSe_2 (60°).

To study how Moiré potential modifies interlayer exciton recombination, we measure transient absorption dynamics by varying lattice temperature for WS_2-WSe_2 (0°), WS_2-WSe_2 (60°), and control 1L- WS_2 samples. Figure 7.18 exhibits temperature-dependent

exciton dynamics of 1L-WS₂. The recombination constants are increased from 35 ps at 290 K to 122 ps at 78 K. The increase of lifetime in 1L-WS₂ at 78 K is attributed to the reduced exciton-photon scattering due to the reduced phonon population at low temperature. However, for both WS₂-WSe₂ (0°) and WS₂-WSe₂ (60°), interlayer exciton dynamics show a contrasting behavior with 1L-WS₂ which becomes significantly faster with the decrease of lattice temperature as shown in Figure 7.19. This behavior can't be explained by the reduced exciton-phonon scattering. The fitted recombination constants for both WS₂-WSe₂ (0°) and WS₂-WSe₂ (60°) are plotted in Figure 7.20. Here, we also observe a significantly different behavior for different stacking orientation. For WS₂-WSe₂ (60°), the increase of charge transfer exciton recombination is very rapid compared in WS₂-WSe₂ (60°) than WS₂-WSe₂ (0°) as increasing lattice temperature. The recombination constant starts to increase at 160 K in WS₂-WSe₂ (0°) while it already becomes steady in WS₂-WSe₂ (60°). A reasonable explanation is that the amplitude of Moiré potential is much smaller in WS₂-WSe₂ (60°) than WS₂-WSe₂ (0°). We estimate the Moiré potential depth to be on the order of tenth meV WS₂-WSe₂ (60°) which is much smaller than the value from DFT calculation. The deviation may arise from the strain in CVD grown WS₂-WSe₂ heterostructures which originate from strain induced from the mismatch of the thermal expansion coefficient (TEC) between that of TMDs layers and substrate. During the thermal annealing, a large tensile strain is expected to form in the heterostructures^{103, 331}. By comparing the emission energies between exfoliated¹⁹⁵ and CVD grown WS₂ samples, we observe a redshift of emission energy (~ 50 meV) in CVD WS₂ with exfoliated 1L-WS₂, which is corresponding to ~ 0.6% tensile strain according to a previous report. Such large tensile strain significantly modifies Moiré potential amplitude.

7.4.5 Stacking orientation dependent charge transfer exciton transport in CVD WS₂-WSe₂ heterostructures

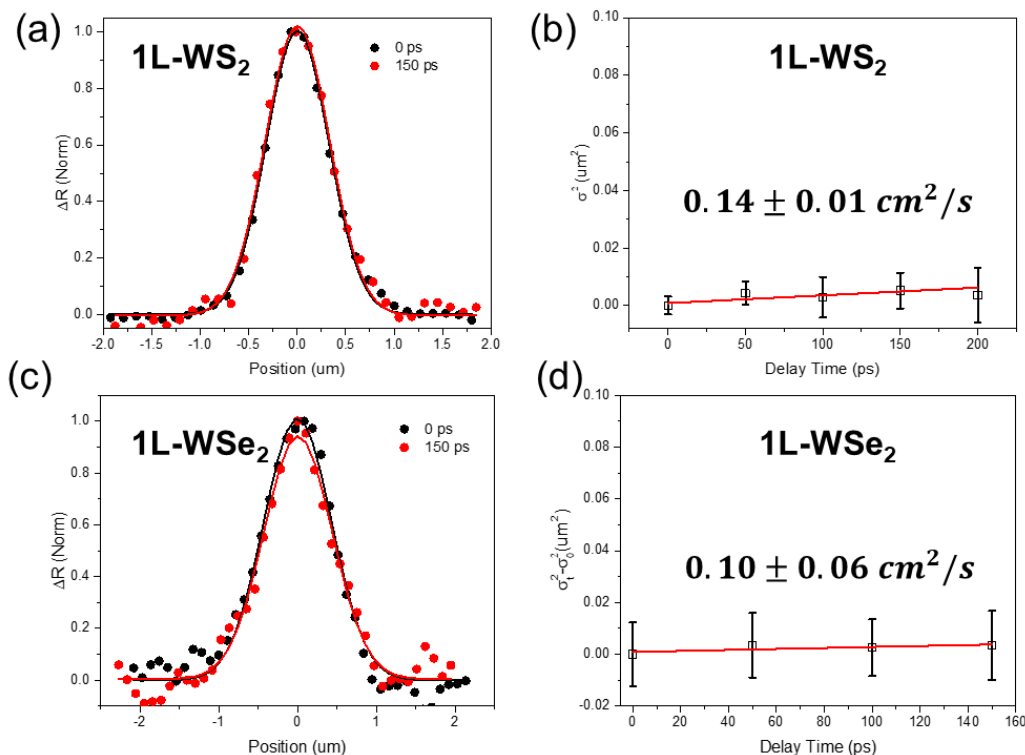


Figure 7.21 Exciton transport measurements of 1L-WS₂ and 1L-WSe₂. Spatial distribution of the exciton population at different delay time for 1L-WS₂ (a) and 1L-WSe₂ (c). Diffusion coefficient of 1L-WS₂ (b) and 1L-WSe₂ (d) is obtained from the linear fitting of the variance of Gaussian profile. Red lines are linear fits.

Here, we study the transport properties of intralayer and CT exciton using TAM. We fix the pump beam on the sample and scan the probe beam relative to the pump beam with a pair of galvanometer scanners to obtain exciton propagation information at different time delays. The pump-induced change in probe reflectance $\Delta R = R_{pump-on} - R_{pump-off}$ is collected. The pump energy is 3.1 eV to excite 1L-WS₂ and 1L-WSe₂, and the probe energies are 2.0 eV and 1.6 eV probing WS₂ and WSe₂. At zero delay time, the TAM results reflect the initial population created by the pump beam, and at later delay time, the TAM images directly visualize how excitons transport out of the initial volume. In one dimension

(1D), the initial population $n(x, 0)$ follows Gaussian distribution as created by a Gaussian pump beam of 3.1 eV at position (x_0) with a variance of σ_0^2 and is given by, $n(x, 0) = N \exp\left[-\frac{(x-x_0)^2}{2\sigma_0^2}\right]$. Population as a function of space and time can be described by a differential equation that includes both the diffusion out of the initial volume and population decay, which is given by:

$$\frac{\partial n(x,t)}{\partial t} = D \frac{\partial^2 n(x,t)}{\partial x^2} - \frac{n(x,t)}{\tau} \quad (3)$$

where D is the exciton diffusion constant and τ is the exciton lifetime. Solution to equation (3) dictates that exciton distribution at any later delay time (t) is also Gaussian and can be described as $n(x, t) = N \exp\left[-\frac{(x-x_0)^2}{2\sigma_t^2}\right]$ with a variance of σ_t^2 . The solution also gives the diffusion constant D as,

$$D = \frac{\sigma_t^2 - \sigma_0^2}{2t} \quad (4)$$

Using this analysis, the population of the A excitons in the 1L-WS₂ and 1L-WSe₂ at different delay times are fitted to Gaussian functions and the diffusion constants are determined to be 0.14 ± 0.01 and 0.10 ± 0.06 cm²s⁻¹, respectively (Figures 7.21). By using the same method, we also carry out diffusion measurement on 2L-WS₂ and 2L-WSe₂. The diffusion constants are slightly larger than single layers shown in Figure 7.22. Excitons diffusion in CVD WS₂ are about one order magnitude lower than exfoliated 1L- and 2L-WS₂, which is attributed to the much higher defect and impurities density in CVD WS₂. It could significantly scatter excitons and impede exciton transport.

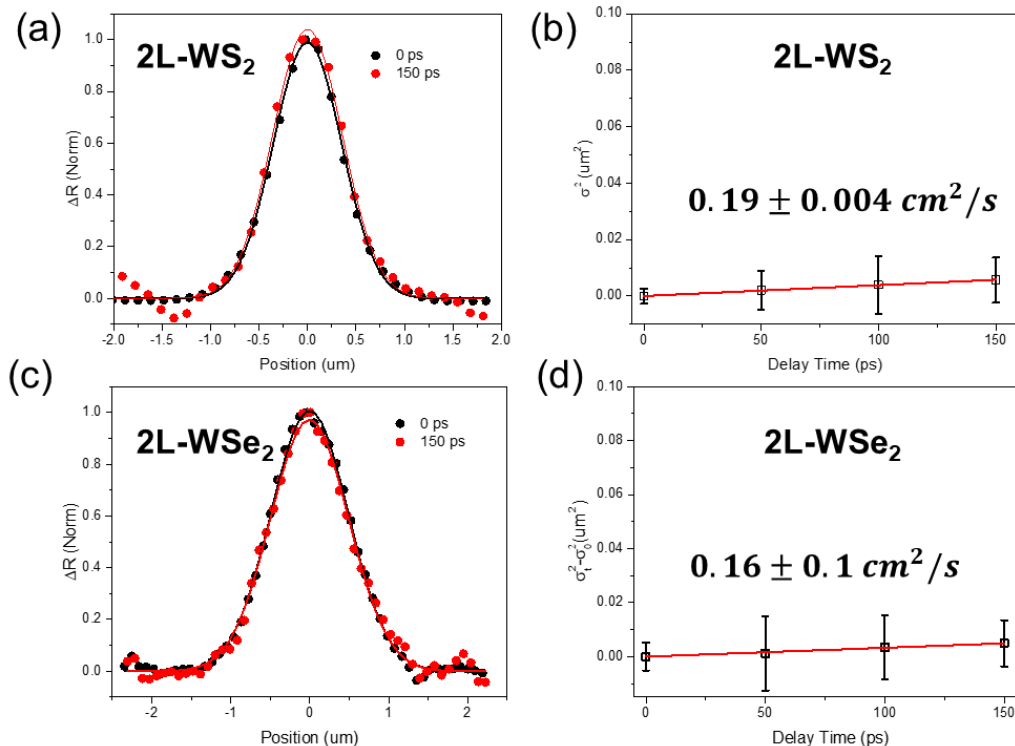


Figure 7.22 Exciton transport measurements of 2L-WS₂ and 2L-WSe₂. Spatial distribution of the exciton population at different delay time for 2L-WS₂ (a) and 2L-WSe₂ (c). Diffusion coefficients of 2L-WS₂ (b) and 2L-WSe₂ (d) are obtained from the linear fitting of the variance of Gaussian profile. Red lines are linear fits.

Next, we look at the CT exciton transport in WS₂-WSe₂ heterostructures. The pump photon energy is 1.57 eV exciting 1L-WSe₂ and probe energy is 1.95 eV probing A exciton bleach of 1L-WS₂. We carry out diffusion measurements at various exciton densities ($5.2 \times 10^{11} \text{ cm}^{-2}$ and $1.7 \times 10^{12} \text{ cm}^{-2}$) for both WS₂-WSe₂ (0°) and WS₂-WSe₂ (60°) shown in Figure 7.23 and 7.24 respectively. The CT exciton transport displays exciton density and stacking orientation dependent behavior which is clearly shown in Figure 7.25 by plotting $\sigma_t^2 - \sigma_0^2$ as a function of time delays. CT exciton transport in both WS₂-WSe₂ (0°) and WS₂-WSe₂ (60°) is much more mobile than intralayer excitons in 1L and 2L-WS₂ or WSe₂. Unlike the time-independent exciton diffusion in 1L and 2L-WS₂ or WSe₂, CT exciton

diffusion exhibits time dependent behavior. Initially, CT exciton diffusion expands very fast in 100 ps and then reduces significantly at longer time delay. We also observe stacking-dependent CT exciton transport in which WS₂- WSe₂ (60°) always moves a longer distance than in WS₂- WSe₂ (0°) at various exciton densities.

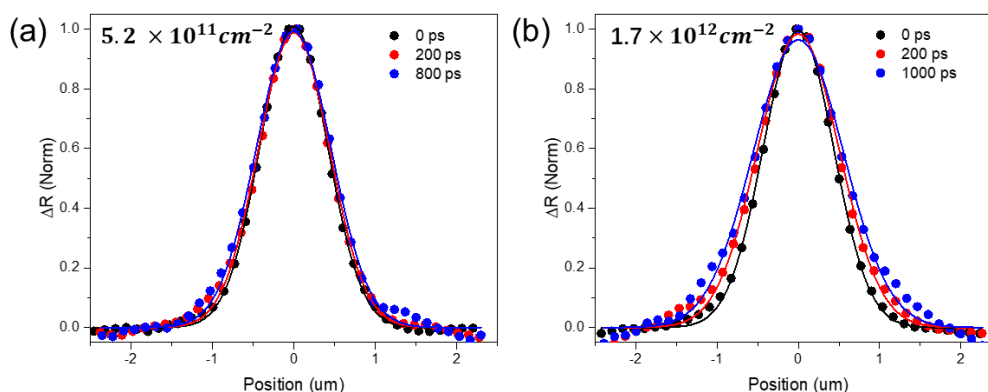


Figure 7.23 Exciton population profiles at different time delays with different interlayer exciton densities (a) $5.2 \times 10^{11} \text{ cm}^{-2}$ and (b) $1.7 \times 10^{12} \text{ cm}^{-2}$ for WS₂-WSe₂ (0°). The diffusion profiles are fitted with Gaussian functions at different delay times with the maximum ΔR signal normalized to unity.

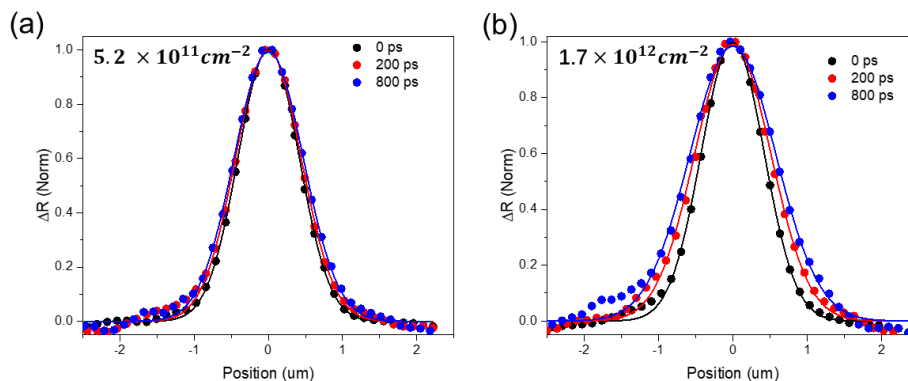


Figure 7.24 Exciton population profiles at different time delays with different interlayer exciton densities (a) $5.2 \times 10^{11} \text{ cm}^{-2}$ and (b) $1.7 \times 10^{12} \text{ cm}^{-2}$ for WS₂-WSe₂ (60°). The diffusion profiles are fitted with Gaussian functions at different delay times with the maximum ΔR signal normalized to unity.

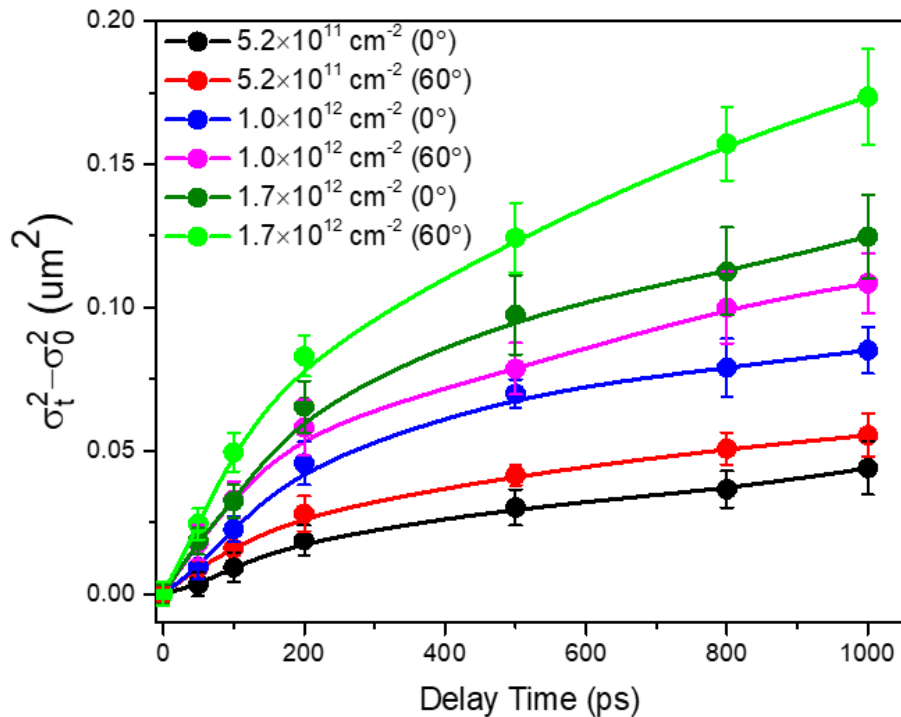


Figure 7.25 $\sigma_t^2 - \sigma_0^2$ as a function of pump-probe delay time for both WS₂-WSe₂ (0°) and WS₂-WSe₂ (60°) at different interlayer exciton densities. Error bars of $\sigma_t^2 - \sigma_0^2$ are the standard errors estimated from Gaussian fitting to the spatial intensity distributions. Solid lines are guides for eyes.

Typically, interlayer exciton diffusion coefficients are dominated by scattering at potential fluctuations caused by defects or impurities. Due to the presence of large Moiré potential ($\sim 100 \text{ meV}$) in WS₂-WSe₂ heterostructure, interlayer excitons are localized at such potential fluctuations. Because the dipolar interlayer excitons repel each other, at high exciton density, such potential fluctuations are effectively screened by the excitons at the energy bottom of the dipolar exciton gas³³²⁻³³³.

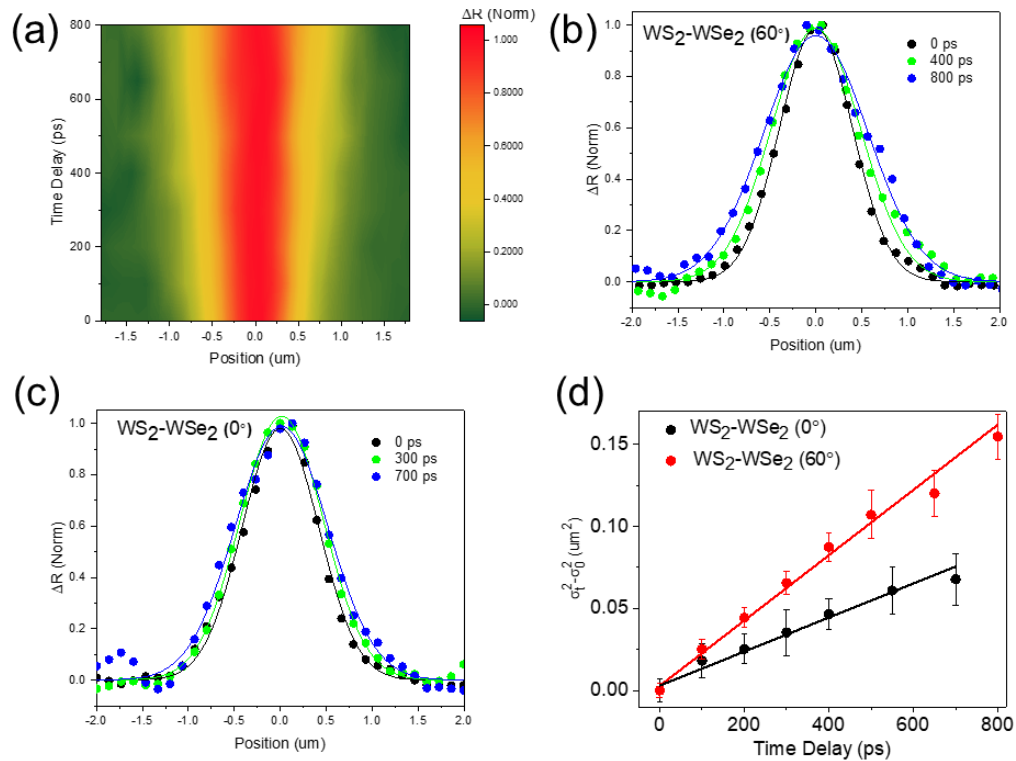


Figure 7.26 Interlayer CT exciton transport in $\text{WS}_2\text{-WSe}_2$ heterostructures with a pump photon energy of 3.1 eV. (a) 2D image of transient reflection signal in $\text{WS}_2\text{-WSe}_2$ (60°) as it evolves with space and time. Exciton density is $1.6 \times 10^{11} \text{ cm}^{-2}$. Exciton population profiles at different delay time for (b) $\text{WS}_2\text{-WSe}_2$ (60°) and (c) $\text{WS}_2\text{-WSe}_2$ (0°). Exciton density is $1.6 \times 10^{11} \text{ cm}^{-2}$. The diffusion profiles are fitted with Gaussian functions at different delay times with the maximum ΔR signal normalized to unity. (d) $\sigma_t^2 - \sigma_0^2$ as a function of pump-probe delay time for both $\text{WS}_2\text{-WSe}_2$ (0°) and $\text{WS}_2\text{-WSe}_2$ (60°). Error bars of $\sigma_t^2 - \sigma_0^2$ are the standard errors estimated from Gaussian fitting to the spatial intensity distributions. Solid lines are linear fits.

We also carry out interlayer exciton transport measurements at a pump photon energy of 3.1 eV which is 1.7 eV higher than the band gap of the interlayer exciton (~ 1.4 eV). The probe energy is 2.0 eV to probe A exciton bleach of 1L- WS_2 . The photo-excited exciton density is $1.6 \times 10^{11} \text{ cm}^{-2}$. Figure 7.26 (a) presents a 2D image of the transient reflection signal in $\text{WS}_2\text{-WSe}_2$ (60°) evolving with space and time. It clearly displays broadening of exciton population profiles which indicates interlayer exciton diffusion. We fit exciton population profiles at different delay time for both $\text{WS}_2\text{-WSe}_2$ (60°) and $\text{WS}_2\text{-WSe}_2$ (0°)

using Gaussian functions shown in Figure 7.26 (b) and (c). By plotting $\sigma_t^2 - \sigma_0^2$ as a function of pump-probe delay time shown in Figure 7.26 (d), it is surprising to see a time-independent diffusion behavior which is directly contrast with the results measured at 1.57 eV-pump. By fitting with linear functions, we obtain the diffusion constants of 1.0 ± 0.04 and $0.52 \pm 0.03 \frac{cm^2}{s}$ for WS₂-WSe₂ (60°) and WS₂-WSe₂ (0°), respectively. The interlayer exciton diffusion constant of WS₂-WSe₂ (60°) is nearly two times higher than in WS₂-WSe₂ (60°) which is consistent with the results measured at 1.57 eV-pump. Since the interlayer exciton density at 3.14 eV-pump is much lower than that in the measurements with 1.57 eV-pump, dipole-dipole repulsion from dipolar interlayer excitons can't explain such behavior. A possible reason is that the excess excitation energy promotes interlayer excitons to escape the Moiré potential and leads to long range CT excitons transport⁵².

7.5 Conclusion

In summary, we study interlayer exciton formation, recombination, and transport in CVD WS₂-WSe₂ heterostructures by combining PL microscopy, transient absorption microscopy, and DFT calculations. Temperature-dependent interlayer exciton dynamics suggests the existence of moiré potential that localizes interlayer excitons. The potential depth is strongly dependent on the stacking orientation. The dipole-dipole repulsion from bipolar interlayer excitons efficiently screen the moiré potential fluctuations and facilitates interlayer exciton transport. Our results provide fundamental insights in understanding the influence of moiré potential on interlayer exciton dynamics and transport in CVD WS₂-WSe₂ heterostructures which has important implications in optoelectronic applications at the nanoscale limit.

REFERENCES

1. Novoselov, K. S.; Geim, A. K.; Morozov, S. V.; Jiang, D.; Zhang, Y.; Dubonos, S. V.; Grigorieva, I. V.; Firsov, A. A., Electric Field Effect in Atomically Thin Carbon Films. *Science* **2004**, *306* (5696), 666.
2. Novoselov, K. S.; Jiang, D.; Schedin, F.; Booth, T. J.; Khotkevich, V. V.; Morozov, S. V.; Geim, A. K., Two-dimensional atomic crystals. *Proceedings of the National Academy of Sciences of the United States of America* **2005**, *102* (30), 10451.
3. Novoselov, K. S.; Geim, A. K.; Morozov, S. V.; Jiang, D.; Katsnelson, M. I.; Grigorieva, I. V.; Dubonos, S. V.; Firsov, A. A., Two-dimensional gas of massless Dirac fermions in graphene. *Nature* **2005**, *438*, 197.
4. Das, S.; Robinson, J. A.; Dubey, M.; Terrones, H.; Terrones, M., Beyond Graphene: Progress in Novel Two-Dimensional Materials and van der Waals Solids. *Annual Review of Materials Research* **2015**, *45* (1), 1-27.
5. Geim, A. K., Graphene: Status and Prospects. *Science* **2009**, *324* (5934), 1530.
6. Bonaccorso, F.; Sun, Z.; Hasan, T.; Ferrari, A. C., Graphene photonics and optoelectronics. *Nature Photonics* **2010**, *4*, 611.
7. Mak, K. F.; Lee, C.; Hone, J.; Shan, J.; Heinz, T. F., Atomically Thin MoS₂: A New Direct-Gap Semiconductor. *Physical Review Letters* **2010**, *105* (13), 136805.
8. Splendiani, A.; Sun, L.; Zhang, Y.; Li, T.; Kim, J.; Chim, C.-Y.; Galli, G.; Wang, F., Emerging Photoluminescence in Monolayer MoS₂. *Nano Letters* **2010**, *10* (4), 1271-1275.
9. Mak, K. F.; He, K.; Lee, C.; Lee, G. H.; Hone, J.; Heinz, T. F.; Shan, J., Tightly bound trions in monolayer MoS₂. *Nature Materials* **2012**, *12*, 207.
10. Zhao, W.; Ghorannevis, Z.; Chu, L.; Toh, M.; Kloc, C.; Tan, P.-H.; Eda, G., Evolution of Electronic Structure in Atomically Thin Sheets of WS₂ and WSe₂. *ACS Nano* **2013**, *7* (1), 791-797.
11. Dean, C. R.; Young, A. F.; Meric, I.; Lee, C.; Wang, L.; Sorgenfrei, S.; Watanabe, K.; Taniguchi, T.; Kim, P.; Shepard, K. L.; Hone, J., Boron nitride substrates for high-quality graphene electronics. *Nature Nanotechnology* **2010**, *5*, 722.
12. Wang, Q. H.; Kalantar-Zadeh, K.; Kis, A.; Coleman, J. N.; Strano, M. S., Electronics and optoelectronics of two-dimensional transition metal dichalcogenides. *Nature Nanotechnology* **2012**, *7*, 699.

13. Fiori, G.; Bonaccorso, F.; Iannaccone, G.; Palacios, T.; Neumaier, D.; Seabaugh, A.; Banerjee, S. K.; Colombo, L., Electronics based on two-dimensional materials. *Nature Nanotechnology* **2014**, *9*, 768.
14. Mak, K. F.; Shan, J., Photonics and optoelectronics of 2D semiconductor transition metal dichalcogenides. *Nature Photonics* **2016**, *10*, 216.
15. Eda, G.; Maier, S. A., Two-Dimensional Crystals: Managing Light for Optoelectronics. *ACS Nano* **2013**, *7* (7), 5660-5665.
16. Castro Neto, A. H.; Guinea, F.; Peres, N. M. R.; Novoselov, K. S.; Geim, A. K., The electronic properties of graphene. *Reviews of Modern Physics* **2009**, *81* (1), 109-162.
17. Chhowalla, M.; Shin, H. S.; Eda, G.; Li, L.-J.; Loh, K. P.; Zhang, H., The chemistry of two-dimensional layered transition metal dichalcogenide nanosheets. *Nature Chemistry* **2013**, *5*, 263.
18. Grigorenko, A. N.; Polini, M.; Novoselov, K. S., Graphene plasmonics. *Nature Photonics* **2012**, *6*, 749.
19. Schwierz, F., Graphene transistors. *Nature Nanotechnology* **2010**, *5*, 487.
20. Radisavljevic, B.; Radenovic, A.; Brivio, J.; Giacometti, V.; Kis, A., Single-layer MoS₂ transistors. *Nature Nanotechnology* **2011**, *6*, 147.
21. Lopez-Sanchez, O.; Lembke, D.; Kayci, M.; Radenovic, A.; Kis, A., Ultrasensitive photodetectors based on monolayer MoS₂. *Nature Nanotechnology* **2013**, *8*, 497.
22. Mak, K. F.; He, K.; Shan, J.; Heinz, T. F., Control of valley polarization in monolayer MoS₂ by optical helicity. *Nature Nanotechnology* **2012**, *7*, 494.
23. Schaibley, J. R.; Yu, H.; Clark, G.; Rivera, P.; Ross, J. S.; Seyler, K. L.; Yao, W.; Xu, X., Valleytronics in 2D materials. *Nature Reviews Materials* **2016**, *1*, 16055.
24. Zeng, H.; Dai, J.; Yao, W.; Xiao, D.; Cui, X., Valley polarization in MoS₂ monolayers by optical pumping. *Nature Nanotechnology* **2012**, *7*, 490.
25. Koppens, F. H. L.; Mueller, T.; Avouris, P.; Ferrari, A. C.; Vitiello, M. S.; Polini, M., Photodetectors based on graphene, other two-dimensional materials and hybrid systems. *Nature Nanotechnology* **2014**, *9*, 780.
26. Buscema, M.; Island, J. O.; Groenendijk, D. J.; Blanter, S. I.; Steele, G. A.; van der Zant, H. S. J.; Castellanos-Gomez, A., Photocurrent generation with two-dimensional van der Waals semiconductors. *Chemical Society Reviews* **2015**, *44* (11), 3691-3718.
27. Xu, X.; Yao, W.; Xiao, D.; Heinz, T. F., Spin and pseudospins in layered transition metal dichalcogenides. *Nature Physics* **2014**, *10*, 343.

28. Xia, F.; Wang, H.; Xiao, D.; Dubey, M.; Ramasubramaniam, A., Two-dimensional material nanophotonics. *Nature Photonics* **2014**, *8*, 899.
29. Mak, K. F.; McGill, K. L.; Park, J.; McEuen, P. L., The valley Hall effect in MoS₂ transistors. *Science* **2014**, *344* (6191), 1489.
30. Ross, J. S.; Klement, P.; Jones, A. M.; Ghimire, N. J.; Yan, J.; Mandrus, D. G.; Taniguchi, T.; Watanabe, K.; Kitamura, K.; Yao, W.; Cobden, D. H.; Xu, X., Electrically tunable excitonic light-emitting diodes based on monolayer WSe₂ p–n junctions. *Nature Nanotechnology* **2014**, *9*, 268.
31. Bernardi, M.; Palumbo, M.; Grossman, J. C., Extraordinary Sunlight Absorption and One Nanometer Thick Photovoltaics Using Two-Dimensional Monolayer Materials. *Nano Letters* **2013**, *13* (8), 3664-3670.
32. Pospischil, A.; Furchi, M. M.; Mueller, T., Solar-energy conversion and light emission in an atomic monolayer p–n diode. *Nature Nanotechnology* **2014**, *9*, 257.
33. Geim, A. K.; Novoselov, K. S., The rise of graphene. *Nature Materials* **2007**, *6*, 183.
34. Morozov, S. V.; Novoselov, K. S.; Katsnelson, M. I.; Schedin, F.; Elias, D. C.; Jaszczak, J. A.; Geim, A. K., Giant Intrinsic Carrier Mobilities in Graphene and Its Bilayer. *Physical Review Letters* **2008**, *100* (1), 016602.
35. Chen, J.-H.; Jang, C.; Xiao, S.; Ishigami, M.; Fuhrer, M. S., Intrinsic and extrinsic performance limits of graphene devices on SiO₂. *Nature Nanotechnology* **2008**, *3*, 206.
36. Bolotin, K. I.; Sikes, K. J.; Jiang, Z.; Klima, M.; Fudenberg, G.; Hone, J.; Kim, P.; Stormer, H. L., Ultrahigh electron mobility in suspended graphene. *Solid State Communications* **2008**, *146* (9), 351-355.
37. Balandin, A. A.; Ghosh, S.; Bao, W.; Calizo, I.; Teweldebrhan, D.; Miao, F.; Lau, C. N., Superior Thermal Conductivity of Single-Layer Graphene. *Nano Letters* **2008**, *8* (3), 902-907.
38. Lee, C.; Wei, X.; Kysar, J. W.; Hone, J., Measurement of the Elastic Properties and Intrinsic Strength of Monolayer Graphene. *Science* **2008**, *321* (5887), 385.
39. Kormányos, A.; Zólyomi, V.; Drummond, N. D.; Burkard, G., Spin-Orbit Coupling, Quantum Dots, and Qubits in Monolayer Transition Metal Dichalcogenides. *Physical Review X* **2014**, *4* (1), 011034.
40. Zhu, Z. Y.; Cheng, Y. C.; Schwingenschlögl, U., Giant spin-orbit-induced spin splitting in two-dimensional transition-metal dichalcogenide semiconductors. *Physical Review B* **2011**, *84* (15), 153402.

41. Liu, X.; Galfsky, T.; Sun, Z.; Xia, F.; Lin, E.-c.; Lee, Y.-H.; Kéna-Cohen, S.; Menon, V. M., Strong light–matter coupling in two-dimensional atomic crystals. *Nature Photonics* **2014**, *9*, 30.
42. Chernikov, A.; Berkelbach, T. C.; Hill, H. M.; Rigosi, A.; Li, Y.; Aslan, O. B.; Reichman, D. R.; Hybertsen, M. S.; Heinz, T. F., Exciton Binding Energy and Nonhydrogenic Rydberg Series in Monolayer WS₂. *Physical Review Letters* **2014**, *113* (7), 076802.
43. Knox, R. S., *Theory of excitons*. Academic Press: 1963.
44. He, X.-F., Excitons in anisotropic solids: The model of fractional-dimensional space. *Physical Review B* **1991**, *43* (3), 2063-2069.
45. Zhu, B.; Chen, X.; Cui, X., Exciton Binding Energy of Monolayer WS₂. *Scientific Reports* **2015**, *5*, 9218.
46. Chernikov, A.; van der Zande, A. M.; Hill, H. M.; Rigosi, A. F.; Velauthapillai, A.; Hone, J.; Heinz, T. F., Electrical Tuning of Exciton Binding Energies in Monolayer WS₂. *Physical Review Letters* **2015**, *115* (12), 126802.
47. Ye, Z.; Cao, T.; O'Brien, K.; Zhu, H.; Yin, X.; Wang, Y.; Louie, S. G.; Zhang, X., Probing excitonic dark states in single-layer tungsten disulphide. *Nature* **2014**, *513*, 214.
48. Hill, H. M.; Rigosi, A. F.; Roquelet, C.; Chernikov, A.; Berkelbach, T. C.; Reichman, D. R.; Hybertsen, M. S.; Brus, L. E.; Heinz, T. F., Observation of Excitonic Rydberg States in Monolayer MoS₂ and WS₂ by Photoluminescence Excitation Spectroscopy. *Nano Letters* **2015**, *15* (5), 2992-2997.
49. He, K.; Kumar, N.; Zhao, L.; Wang, Z.; Mak, K. F.; Zhao, H.; Shan, J., Tightly Bound Excitons in Monolayer WS₂. *Physical Review Letters* **2014**, *113* (2), 026803.
50. Hanbicki, A. T.; Currie, M.; Kioseoglou, G.; Friedman, A. L.; Jonker, B. T., Measurement of high exciton binding energy in the monolayer transition-metal dichalcogenides WS₂ and WSe₂. *Solid State Communications* **2015**, *203*, 16-20.
51. Wang, G.; Chernikov, A.; Glazov, M. M.; Heinz, T. F.; Marie, X.; Amand, T.; Urbaszek, B., Colloquium: Excitons in atomically thin transition metal dichalcogenides. *Reviews of Modern Physics* **2018**, *90* (2), 021001.
52. Zhu, X.; Monahan, N. R.; Gong, Z.; Zhu, H.; Williams, K. W.; Nelson, C. A., Charge Transfer Excitons at van der Waals Interfaces. *Journal of the American Chemical Society* **2015**, *137* (26), 8313-8320.
53. Geim, A. K.; Grigorieva, I. V., Van der Waals Heterostructures. *Nature* **2013**, *499*, 419.

54. Lotsch, B. V., Vertical 2D Heterostructures. *Annual Review of Materials Research* **2015**, *45* (1), 85-109.
55. Novoselov, K. S.; Castro Neto, A. H., Two-dimensional crystals-based heterostructures: materials with tailored properties. *Physica Scripta* **2012**, *T146*, 014006.
56. Duesberg, G. S., A perfect match. *Nature Materials* **2014**, *13*, 1075.
57. Rivera, P.; Yu, H.; Seyler, K. L.; Wilson, N. P.; Yao, W.; Xu, X., Interlayer valley excitons in heterobilayers of transition metal dichalcogenides. *Nature Nanotechnology* **2018**, *13* (11), 1004-1015.
58. Ciarrocchi, A.; Unuchek, D.; Avsar, A.; Watanabe, K.; Taniguchi, T.; Kis, A., Polarization switching and electrical control of interlayer excitons in two-dimensional van der Waals heterostructures. *Nature Photonics* **2019**, *13* (2), 131-136.
59. Furchi, M. M.; Pospischil, A.; Libisch, F.; Burgdörfer, J.; Mueller, T., Photovoltaic Effect in an Electrically Tunable van der Waals Heterojunction. *Nano Letters* **2014**, *14* (8), 4785-4791.
60. Lee, C.-H.; Lee, G.-H.; van der Zande, A. M.; Chen, W.; Li, Y.; Han, M.; Cui, X.; Arefe, G.; Nuckolls, C.; Heinz, T. F.; Guo, J.; Hone, J.; Kim, P., Atomically thin p-n junctions with van der Waals heterointerfaces. *Nature Nanotechnology* **2014**, *9*, 676.
61. Liu, Y.; Weiss, N. O.; Duan, X.; Cheng, H.-C.; Huang, Y.; Duan, X., Van der Waals heterostructures and devices. *Nature Reviews Materials* **2016**, *1*, 16042.
62. Unuchek, D.; Ciarrocchi, A.; Avsar, A.; Watanabe, K.; Taniguchi, T.; Kis, A., Room-temperature electrical control of exciton flux in a van der Waals heterostructure. *Nature* **2018**, *560* (7718), 340-344.
63. Withers, F.; Del Pozo-Zamudio, O.; Mishchenko, A.; Rooney, A. P.; Gholinia, A.; Watanabe, K.; Taniguchi, T.; Haigh, S. J.; Geim, A. K.; Tartakovskii, A. I.; Novoselov, K. S., Light-emitting diodes by band-structure engineering in van der Waals heterostructures. *Nature Materials* **2015**, *14*, 301.
64. Woessner, A.; Lundeberg, M. B.; Gao, Y.; Principi, A.; Alonso-González, P.; Carrega, M.; Watanabe, K.; Taniguchi, T.; Vignale, G.; Polini, M.; Hone, J.; Hillenbrand, R.; Koppens, F. H. L., Highly confined low-loss plasmons in graphene-boron nitride heterostructures. *Nature Materials* **2014**, *14*, 421.
65. Dai, S.; Ma, Q.; Liu, M. K.; Andersen, T.; Fei, Z.; Goldflam, M. D.; Wagner, M.; Watanabe, K.; Taniguchi, T.; Thieme, M.; Keilmann, F.; Janssen, G. C. A. M.; Zhu, S. E.; Jarillo-Herrero, P.; Fogler, M. M.; Basov, D. N., Graphene on hexagonal boron nitride as a tunable hyperbolic metamaterial. *Nature Nanotechnology* **2015**, *10*, 682.

66. Roy, K.; Padmanabhan, M.; Goswami, S.; Sai, T. P.; Ramalingam, G.; Raghavan, S.; Ghosh, A., Graphene–MoS₂ hybrid structures for multifunctional photoresponsive memory devices. *Nature Nanotechnology* **2013**, *8*, 826.
67. Georgiou, T.; Jalil, R.; Belle, B. D.; Britnell, L.; Gorbachev, R. V.; Morozov, S. V.; Kim, Y.-J.; Gholinia, A.; Haigh, S. J.; Makarovskiy, O.; Eaves, L.; Ponomarenko, L. A.; Geim, A. K.; Novoselov, K. S.; Mishchenko, A., Vertical field-effect transistor based on graphene–WS₂ heterostructures for flexible and transparent electronics. *Nature Nanotechnology* **2012**, *8*, 100.
68. Jariwala, D.; Marks, T. J.; Hersam, M. C., Mixed-dimensional van der Waals heterostructures. *Nature Materials* **2016**, *16*, 170.
69. Song, J.; Kam, F.-Y.; Png, R.-Q.; Seah, W.-L.; Zhuo, J.-M.; Lim, G.-K.; Ho, P. K. H.; Chua, L.-L., A general method for transferring graphene onto soft surfaces. *Nature Nanotechnology* **2013**, *8*, 356.
70. Castellanos-Gomez, A.; Buscema, M.; Molenaar, R.; Singh, V.; Janssen, L.; van der Zant, H. S. J.; Steele, G. A., Deterministic transfer of two-dimensional materials by all-dry viscoelastic stamping. *2D Materials* **2014**, *1* (1), 011002.
71. Petrone, N.; Dean, C. R.; Meric, I.; van der Zande, A. M.; Huang, P. Y.; Wang, L.; Muller, D.; Shepard, K. L.; Hone, J., Chemical Vapor Deposition-Derived Graphene with Electrical Performance of Exfoliated Graphene. *Nano Letters* **2012**, *12* (6), 2751-2756.
72. Wang, L.; Meric, I.; Huang, P. Y.; Gao, Q.; Gao, Y.; Tran, H.; Taniguchi, T.; Watanabe, K.; Campos, L. M.; Muller, D. A.; Guo, J.; Kim, P.; Hone, J.; Shepard, K. L.; Dean, C. R., One-Dimensional Electrical Contact to a Two-Dimensional Material. *Science* **2013**, *342* (6158), 614.
73. Fang, H.; Battaglia, C.; Carraro, C.; Nemsak, S.; Ozdol, B.; Kang, J. S.; Bechtel, H. A.; Desai, S. B.; Kronast, F.; Unal, A. A.; Conti, G.; Conlon, C.; Palsson, G. K.; Martin, M. C.; Minor, A. M.; Fadley, C. S.; Yablonovitch, E.; Maboudian, R.; Javey, A., Strong interlayer coupling in van der Waals heterostructures built from single-layer chalcogenides. *Proceedings of the National Academy of Sciences* **2014**, *111* (17), 6198.
74. Gong, Y.; Lin, J.; Wang, X.; Shi, G.; Lei, S.; Lin, Z.; Zou, X.; Ye, G.; Vajtai, R.; Yakobson, B. I.; Terrones, H.; Terrones, M.; Tay, Beng K.; Lou, J.; Pantelides, S. T.; Liu, Z.; Zhou, W.; Ajayan, P. M., Vertical and in-plane heterostructures from WS₂/MoS₂ monolayers. *Nature Materials* **2014**, *13*, 1135.
75. Liu, Z.; Song, L.; Zhao, S.; Huang, J.; Ma, L.; Zhang, J.; Lou, J.; Ajayan, P. M., Direct Growth of Graphene/Hexagonal Boron Nitride Stacked Layers. *Nano Letters* **2011**, *11* (5), 2032-2037.

76. Wang, S.; Wang, X.; Warner, J. H., All Chemical Vapor Deposition Growth of MoS₂:h-BN Vertical van der Waals Heterostructures. *ACS Nano* **2015**, *9* (5), 5246-5254.
77. Huang, C.; Wu, S.; Sanchez, A. M.; Peters, J. J. P.; Beanland, R.; Ross, J. S.; Rivera, P.; Yao, W.; Cobden, D. H.; Xu, X., Lateral heterojunctions within monolayer MoSe₂-WSe₂ semiconductors. *Nature Materials* **2014**, *13*, 1096.
78. Kang, J.; Tongay, S.; Zhou, J.; Li, J.; Wu, J., Band offsets and heterostructures of two-dimensional semiconductors. *Applied Physics Letters* **2013**, *102* (1), 012111.
79. Özçelik, V. O.; Azadani, J. G.; Yang, C.; Koester, S. J.; Low, T., Band alignment of two-dimensional semiconductors for designing heterostructures with momentum space matching. *Physical Review B* **2016**, *94* (3), 035125.
80. Wilson, N. R.; Nguyen, P. V.; Seyler, K.; Rivera, P.; Marsden, A. J.; Laker, Z. P. L.; Constantinescu, G. C.; Kandyba, V.; Barinov, A.; Hine, N. D. M.; Xu, X.; Cobden, D. H., Determination of band offsets, hybridization, and exciton binding in 2D semiconductor heterostructures. *Science Advances* **2017**, *3* (2), e1601832.
81. Hong, X.; Kim, J.; Shi, S.-F.; Zhang, Y.; Jin, C.; Sun, Y.; Tongay, S.; Wu, J.; Zhang, Y.; Wang, F., Ultrafast charge transfer in atomically thin MoS₂/WS₂ heterostructures. *Nature Nanotechnology* **2014**, *9*, 682.
82. Zhu, H.; Wang, J.; Gong, Z.; Kim, Y. D.; Hone, J.; Zhu, X. Y., Interfacial Charge Transfer Circumventing Momentum Mismatch at Two-Dimensional van der Waals Heterojunctions. *Nano Letters* **2017**, *17* (6), 3591-3598.
83. Ceballos, F.; Bellus, M. Z.; Chiu, H.-Y.; Zhao, H., Probing charge transfer excitons in a MoSe₂-WS₂ van der Waals heterostructure. *Nanoscale* **2015**, *7* (41), 17523-17528.
84. Ji, Z.; Hong, H.; Zhang, J.; Zhang, Q.; Huang, W.; Cao, T.; Qiao, R.; Liu, C.; Liang, J.; Jin, C.; Jiao, L.; Shi, K.; Meng, S.; Liu, K., Robust Stacking-Independent Ultrafast Charge Transfer in MoS₂/WS₂ Bilayers. *ACS Nano* **2017**, *11* (12), 12020-12026.
85. Zheng, Q.; Saidi, W. A.; Xie, Y.; Lan, Z.; Prezhdo, O. V.; Petek, H.; Zhao, J., Phonon-Assisted Ultrafast Charge Transfer at van der Waals Heterostructure Interface. *Nano Letters* **2017**, *17* (10), 6435-6442.
86. Zhang, J.; Hong, H.; Lian, C.; Ma, W.; Xu, X.; Zhou, X.; Fu, H.; Liu, K.; Meng, S., Interlayer-State-Coupling Dependent Ultrafast Charge Transfer in MoS₂/WS₂ Bilayers. *Advanced Science* **2017**, *4* (9), 1700086.
87. Zhou, H.; Zhao, Y.; Zhu, H., Dielectric Environment-Robust Ultrafast Charge Transfer Between Two Atomic Layers. *The Journal of Physical Chemistry Letters* **2019**, *10* (2), 150-155.

88. Wang, K.; Huang, B.; Tian, M.; Ceballos, F.; Lin, M.-W.; Mahjouri-Samani, M.; Boulesbaa, A.; Poretzky, A. A.; Rouleau, C. M.; Yoon, M.; Zhao, H.; Xiao, K.; Duscher, G.; Geohegan, D. B., Interlayer Coupling in Twisted WSe₂/WS₂ Bilayer Heterostructures Revealed by Optical Spectroscopy. *ACS Nano* **2016**, *10* (7), 6612-6622.
89. Rigosi, A. F.; Hill, H. M.; Li, Y.; Chernikov, A.; Heinz, T. F., Probing Interlayer Interactions in Transition Metal Dichalcogenide Heterostructures by Optical Spectroscopy: MoS₂/WS₂ and MoSe₂/WSe₂. *Nano Letters* **2015**, *15* (8), 5033-5038.
90. Long, R.; Prezhd, O. V., Quantum Coherence Facilitates Efficient Charge Separation at a MoS₂/MoSe₂ van der Waals Junction. *Nano Letters* **2016**, *16* (3), 1996-2003.
91. Wang, H.; Bang, J.; Sun, Y.; Liang, L.; West, D.; Meunier, V.; Zhang, S., The role of collective motion in the ultrafast charge transfer in van der Waals heterostructures. *Nature Communications* **2016**, *7*, 11504.
92. Chen, H.; Wen, X.; Zhang, J.; Wu, T.; Gong, Y.; Zhang, X.; Yuan, J.; Yi, C.; Lou, J.; Ajayan, P. M.; Zhuang, W.; Zhang, G.; Zheng, J., Ultrafast formation of interlayer hot excitons in atomically thin MoS₂/WS₂ heterostructures. *Nature Communications* **2016**, *7*, 12512.
93. Rivera, P.; Schaibley, J. R.; Jones, A. M.; Ross, J. S.; Wu, S.; Aivazian, G.; Klement, P.; Seyler, K.; Clark, G.; Ghimire, N. J.; Yan, J.; Mandrus, D. G.; Yao, W.; Xu, X., Observation of long-lived interlayer excitons in monolayer MoSe₂-WSe₂ heterostructures. *Nature Communications* **2015**, *6*, 6242.
94. Okada, M.; Kutana, A.; Kureishi, Y.; Kobayashi, Y.; Saito, Y.; Saito, T.; Watanabe, K.; Taniguchi, T.; Gupta, S.; Miyata, Y.; Yakobson, B. I.; Shinohara, H.; Kitaura, R., Direct and Indirect Interlayer Excitons in a van der Waals Heterostructure of hBN/WS₂/MoS₂/hBN. *ACS Nano* **2018**, *12* (3), 2498-2505.
95. Hanbicki, A. T.; Chuang, H.-J.; Rosenberger, M. R.; Hellberg, C. S.; Sivaram, S. V.; McCreary, K. M.; Mazin, I. I.; Jonker, B. T., Double Indirect Interlayer Exciton in a MoSe₂/WSe₂ van der Waals Heterostructure. *ACS Nano* **2018**, *12* (5), 4719-4726.
96. Nagler, P.; Plechinger, G.; Ballottin, M. V.; Mitioglu, A.; Meier, S.; Paradiso, N.; Strunk, C.; Chernikov, A.; Christianen, P. C. M.; Schüller, C.; Korn, T., Interlayer exciton dynamics in a dichalcogenide monolayer heterostructure. *2D Materials* **2017**, *4* (2), 025112.
97. Miller, B.; Steinhoff, A.; Pano, B.; Klein, J.; Jahnke, F.; Holleitner, A.; Wurstbauer, U., Long-Lived Direct and Indirect Interlayer Excitons in van der Waals Heterostructures. *Nano Letters* **2017**, *17* (9), 5229-5237.

98. Kunstmann, J.; Mooshammer, F.; Nagler, P.; Chaves, A.; Stein, F.; Paradiso, N.; Plechinger, G.; Strunk, C.; Schüller, C.; Seifert, G.; Reichman, D. R.; Korn, T., Momentum-space indirect interlayer excitons in transition-metal dichalcogenide van der Waals heterostructures. *Nature Physics* **2018**, *14* (8), 801-805.
99. Nayak, P. K.; Horbatenko, Y.; Ahn, S.; Kim, G.; Lee, J.-U.; Ma, K. Y.; Jang, A. R.; Lim, H.; Kim, D.; Ryu, S.; Cheong, H.; Park, N.; Shin, H. S., Probing Evolution of Twist-Angle-Dependent Interlayer Excitons in MoSe₂/WSe₂ van der Waals Heterostructures. *ACS Nano* **2017**, *11* (4), 4041-4050.
100. Baranowski, M.; Surrente, A.; Kłopotowski, L.; Urban, J. M.; Zhang, N.; Maude, D. K.; Wiwatowski, K.; Mackowski, S.; Kung, Y. C.; Dumcenco, D.; Kis, A.; Plochocka, P., Probing the Interlayer Exciton Physics in a MoS₂/MoSe₂/MoS₂ van der Waals Heterostructure. *Nano Letters* **2017**, *17* (10), 6360-6365.
101. Rivera, P.; Seyler, K. L.; Yu, H.; Schaibley, J. R.; Yan, J.; Mandrus, D. G.; Yao, W.; Xu, X., Valley-polarized exciton dynamics in a 2D semiconductor heterostructure. *Science* **2016**, *351* (6274), 688.
102. Surrente, A.; Kłopotowski, Ł.; Zhang, N.; Baranowski, M.; Mitioglu, A. A.; Ballottin, M. V.; Christianen, P. C. M.; Dumcenco, D.; Kung, Y.-C.; Maude, D. K.; Kis, A.; Plochocka, P., Intervalley Scattering of Interlayer Excitons in a MoS₂/MoSe₂/MoS₂ Heterostructure in High Magnetic Field. *Nano Letters* **2018**, *18* (6), 3994-4000.
103. Tongay, S.; Fan, W.; Kang, J.; Park, J.; Koldemir, U.; Suh, J.; Narang, D. S.; Liu, K.; Ji, J.; Li, J.; Sinclair, R.; Wu, J., Tuning Interlayer Coupling in Large-Area Heterostructures with CVD-Grown MoS₂ and WS₂ Monolayers. *Nano Letters* **2014**, *14* (6), 3185-3190.
104. Ross, J. S.; Rivera, P.; Schaibley, J.; Lee-Wong, E.; Yu, H.; Taniguchi, T.; Watanabe, K.; Yan, J.; Mandrus, D.; Cobden, D.; Yao, W.; Xu, X., Interlayer Exciton Optoelectronics in a 2D Heterostructure p-n Junction. *Nano Letters* **2017**, *17* (2), 638-643.
105. Jiang, C.; Xu, W.; Rasmita, A.; Huang, Z.; Li, K.; Xiong, Q.; Gao, W.-b., Microsecond dark-exciton valley polarization memory in two-dimensional heterostructures. *Nature Communications* **2018**, *9* (1), 753.
106. Yuan, L.; Wang, T.; Zhu, T.; Zhou, M.; Huang, L., Exciton Dynamics, Transport, and Annihilation in Atomically Thin Two-Dimensional Semiconductors. *The Journal of Physical Chemistry Letters* **2017**, *8* (14), 3371-3379.
107. Cui, Q.; Ceballos, F.; Kumar, N.; Zhao, H., Transient Absorption Microscopy of Monolayer and Bulk WSe₂. *ACS Nano* **2014**, *8* (3), 2970-2976.

108. Cadiz, F.; Robert, C.; Courtade, E.; Manca, M.; Martinelli, L.; Taniguchi, T.; Watanabe, K.; Amand, T.; Rowe, A. C. H.; Paget, D.; Urbaszek, B.; Marie, X., Exciton diffusion in WSe₂ monolayers embedded in a van der Waals heterostructure. *Applied Physics Letters* **2018**, *112* (15), 152106.
109. Kumar, N.; Cui, Q.; Ceballos, F.; He, D.; Wang, Y.; Zhao, H., Exciton diffusion in monolayer and bulk MoSe₂. *Nanoscale* **2014**, *6* (9), 4915-4919.
110. Kulig, M.; Zipfel, J.; Nagler, P.; Blanter, S.; Schüller, C.; Korn, T.; Paradiso, N.; Glazov, M. M.; Chernikov, A., Exciton Diffusion and Halo Effects in Monolayer Semiconductors. *Physical Review Letters* **2018**, *120* (20), 207401.
111. Cordovilla Leon, D. F.; Li, Z.; Jang, S. W.; Cheng, C.-H.; Deotare, P. B., Exciton transport in strained monolayer WSe₂. *Applied Physics Letters* **2018**, *113* (25), 252101.
112. Bettis Homan, S.; Sangwan, V. K.; Balla, I.; Bergeron, H.; Weiss, E. A.; Hersam, M. C., Ultrafast Exciton Dissociation and Long-Lived Charge Separation in a Photovoltaic Pentacene–MoS₂ van der Waals Heterojunction. *Nano Letters* **2017**, *17* (1), 164-169.
113. Huang, Y. L.; Zheng, Y. J.; Song, Z.; Chi, D.; Wee, A. T. S.; Quek, S. Y., The organic–2D transition metal dichalcogenide heterointerface. *Chemical Society Reviews* **2018**, *47* (9), 3241-3264.
114. Kafle, T. R.; Kattel, B.; Lane, S. D.; Wang, T.; Zhao, H.; Chan, W.-L., Charge Transfer Exciton and Spin Flipping at Organic–Transition-Metal Dichalcogenide Interfaces. *ACS Nano* **2017**, *11* (10), 10184-10192.
115. Zhang, L.; Sharma, A.; Zhu, Y.; Zhang, Y.; Wang, B.; Dong, M.; Nguyen, H. T.; Wang, Z.; Wen, B.; Cao, Y.; Liu, B.; Sun, X.; Yang, J.; Li, Z.; Kar, A.; Shi, Y.; Macdonald, D.; Yu, Z.; Wang, X.; Lu, Y., Efficient and Layer-Dependent Exciton Pumping across Atomically Thin Organic–Inorganic Type-I Heterostructures. *Advanced Materials* **2018**, *30* (40), 1803986.
116. Liu, X.; Gu, J.; Ding, K.; Fan, D.; Hu, X.; Tseng, Y.-W.; Lee, Y.-H.; Menon, V.; Forrest, S. R., Photoresponse of an Organic Semiconductor/Two-Dimensional Transition Metal Dichalcogenide Heterojunction. *Nano Letters* **2017**, *17* (5), 3176-3181.
117. Jariwala, D.; Howell, S. L.; Chen, K.-S.; Kang, J.; Sangwan, V. K.; Filippone, S. A.; Turrisi, R.; Marks, T. J.; Lauhon, L. J.; Hersam, M. C., Hybrid, Gate-Tunable, van der Waals p–n Heterojunctions from Pentacene and MoS₂. *Nano Letters* **2016**, *16* (1), 497-503.
118. Sun, J.; Choi, Y.; Choi, Y. J.; Kim, S.; Park, J.-H.; Lee, S.; Cho, J. H., 2D–Organic Hybrid Heterostructures for Optoelectronic Applications. *Advanced Materials* **2019**, *0* (0), 1803831.

119. Zhu, T.; Yuan, L.; Zhao, Y.; Zhou, M.; Wan, Y.; Mei, J.; Huang, L., Highly mobile charge-transfer excitons in two-dimensional WS₂/tetracene heterostructures. *Science Advances* **2018**, *4* (1), eaao3104.
120. Zeng, H.; Liu, G.-B.; Dai, J.; Yan, Y.; Zhu, B.; He, R.; Xie, L.; Xu, S.; Chen, X.; Yao, W.; Cui, X., Optical signature of symmetry variations and spin-valley coupling in atomically thin tungsten dichalcogenides. *Scientific Reports* **2013**, *3*, 1608.
121. Hu, P.; Li, H.; Li, Y.; Jiang, H.; Kloc, C., Single-crystal growth, structures, charge transfer and transport properties of anthracene-F4TCNQ and tetracene-F4TCNQ charge-transfer compounds. *CrystEngComm* **2017**, *19* (4), 618-624.
122. Chong, S.; Min, W.; Xie, X. S., Ground-State Depletion Microscopy: Detection Sensitivity of Single-Molecule Optical Absorption at Room Temperature. *The Journal of Physical Chemistry Letters* **2010**, *1* (23), 3316-3322.
123. Wong, C. T. O.; Lo, S. S.; Huang, L., Ultrafast Spatial Imaging of Charge Dynamics in Heterogeneous Polymer Blends. *The Journal of Physical Chemistry Letters* **2012**, *3* (7), 879-884.
124. Mak, K. F.; Sfeir, M. Y.; Wu, Y.; Lui, C. H.; Misewich, J. A.; Heinz, T. F., Measurement of the Optical Conductivity of Graphene. *Physical Review Letters* **2008**, *101* (19), 196405.
125. Baugher, B. W. H.; Churchill, H. O. H.; Yang, Y.; Jarillo-Herrero, P., Optoelectronic devices based on electrically tunable p-n diodes in a monolayer dichalcogenide. *Nature Nanotechnology* **2014**, *9*, 262.
126. Sundaram, R. S.; Engel, M.; Lombardo, A.; Krupke, R.; Ferrari, A. C.; Avouris, P.; Steiner, M., Electroluminescence in Single Layer MoS₂. *Nano Letters* **2013**, *13* (4), 1416-1421.
127. Peimyoo, N.; Shang, J.; Cong, C.; Shen, X.; Wu, X.; Yeow, E. K. L.; Yu, T., Nonblinking, Intense Two-Dimensional Light Emitter: Monolayer WS₂ Triangles. *ACS Nano* **2013**, *7* (12), 10985-10994.
128. Jo, S.; Ubrig, N.; Berger, H.; Kuzmenko, A. B.; Morpurgo, A. F., Mono- and Bilayer WS₂ Light-Emitting Transistors. *Nano Letters* **2014**, *14* (4), 2019-2025.
129. Fontana, M.; Deppe, T.; Boyd, A. K.; Rinzan, M.; Liu, A. Y.; Paranjape, M.; Barbara, P., Electron-hole transport and photovoltaic effect in gated MoS₂ Schottky junctions. *Scientific Reports* **2013**, *3*, 1634.
130. Yin, Z.; Li, H.; Li, H.; Jiang, L.; Shi, Y.; Sun, Y.; Lu, G.; Zhang, Q.; Chen, X.; Zhang, H., Single-Layer MoS₂ Phototransistors. *ACS Nano* **2012**, *6* (1), 74-80.
131. Ramasubramaniam, A., Large excitonic effects in monolayers of molybdenum and tungsten dichalcogenides. *Physical Review B* **2012**, *86* (11), 115409.

132. Qiu, D. Y.; da Jornada, F. H.; Louie, S. G., Optical Spectrum of MoS₂: Many-Body Effects and Diversity of Exciton States. *Physical Review Letters* **2013**, *111* (21), 216805.
133. Ugeda, M. M.; Bradley, A. J.; Shi, S.-F.; da Jornada, F. H.; Zhang, Y.; Qiu, D. Y.; Ruan, W.; Mo, S.-K.; Hussain, Z.; Shen, Z.-X.; Wang, F.; Louie, S. G.; Crommie, M. F., Giant bandgap renormalization and excitonic effects in a monolayer transition metal dichalcogenide semiconductor. *Nature Materials* **2014**, *13*, 1091.
134. Xiao, D.; Liu, G.-B.; Feng, W.; Xu, X.; Yao, W., Coupled Spin and Valley Physics in Monolayers of MoS₂ and Other Group-VI Dichalcogenides. *Physical Review Letters* **2012**, *108* (19), 196802.
135. Gong, Z.; Liu, G.-B.; Yu, H.; Xiao, D.; Cui, X.; Xu, X.; Yao, W., Magnetoelectric effects and valley-controlled spin quantum gates in transition metal dichalcogenide bilayers. *Nature Communications* **2013**, *4*, 2053.
136. Kormányos, A.; Burkard, G.; Gmitra, M.; Fabian, J.; Zólyomi, V.; Drummond, N. D.; Fal'ko, V., k·p theory for two-dimensional transition metal dichalcogenide semiconductors. *2D Materials* **2015**, *2* (2), 022001.
137. Liu, G.-B.; Shan, W.-Y.; Yao, Y.; Yao, W.; Xiao, D., Three-band tight-binding model for monolayers of group-VIB transition metal dichalcogenides. *Physical Review B* **2013**, *88* (8), 085433.
138. Qiu, D. Y.; Cao, T.; Louie, S. G., Nonanalyticity, Valley Quantum Phases, and Lightlike Exciton Dispersion in Monolayer Transition Metal Dichalcogenides: Theory and First-Principles Calculations. *Physical Review Letters* **2015**, *115* (17), 176801.
139. Echeverry, J. P.; Urbaszek, B.; Amand, T.; Marie, X.; Gerber, I. C., Splitting between bright and dark excitons in transition metal dichalcogenide monolayers. *Physical Review B* **2016**, *93* (12), 121107.
140. Zhang, X.-X.; You, Y.; Zhao, S. Y. F.; Heinz, T. F., Experimental Evidence for Dark Excitons in Monolayer WSe₂. *Physical Review Letters* **2015**, *115* (25), 257403.
141. Molas, M. R.; Faugeras, C.; Slobodeniuk, A. O.; Nogajewski, K.; Bartos, M.; Basko, D. M.; Potemski, M., Brightening of dark excitons in monolayers of semiconducting transition metal dichalcogenides. *2D Materials* **2017**, *4* (2), 021003.
142. Baranowski, M.; Surrente, A.; Maude, D. K.; Ballottin, M.; Mitioglu, A. A.; Christianen, P. C. M.; Kung, Y. C.; Dumcenco, D.; Kis, A.; Plochocka, P., Dark excitons and the elusive valley polarization in transition metal dichalcogenides. *2D Materials* **2017**, *4* (2), 025016.

143. Zhang, X.-X.; Cao, T.; Lu, Z.; Lin, Y.-C.; Zhang, F.; Wang, Y.; Li, Z.; Hone, J. C.; Robinson, J. A.; Smirnov, D.; Louie, S. G.; Heinz, T. F., Magnetic brightening and control of dark excitons in monolayer WSe₂. *Nature Nanotechnology* **2017**, *12*, 883.
144. Korn, T.; Heydrich, S.; Hirmer, M.; Schmutzler, J.; Schüller, C., Low-temperature photocarrier dynamics in monolayer MoS₂. *Applied Physics Letters* **2011**, *99* (10), 102109.
145. Kozawa, D.; Kumar, R.; Carvalho, A.; Kumar Amara, K.; Zhao, W.; Wang, S.; Toh, M.; Ribeiro, R. M.; Castro Neto, A. H.; Matsuda, K.; Eda, G., Photocarrier relaxation pathway in two-dimensional semiconducting transition metal dichalcogenides. *Nature Communications* **2014**, *5*, 4543.
146. Chernikov, A.; Ruppert, C.; Hill, H. M.; Rigosi, A. F.; Heinz, T. F., Population inversion and giant bandgap renormalization in atomically thin WS₂ layers. *Nature Photonics* **2015**, *9*, 466.
147. Wang, H.; Zhang, C.; Rana, F., Ultrafast Dynamics of Defect-Assisted Electron–Hole Recombination in Monolayer MoS₂. *Nano Letters* **2015**, *15* (1), 339-345.
148. Pogna, E. A. A.; Marsili, M.; De Fazio, D.; Dal Conte, S.; Manzoni, C.; Sangalli, D.; Yoon, D.; Lombardo, A.; Ferrari, A. C.; Marini, A.; Cerullo, G.; Prezzi, D., Photo-Induced Bandgap Renormalization Governs the Ultrafast Response of Single-Layer MoS₂. *ACS Nano* **2016**, *10* (1), 1182-1188.
149. Ceballos, F.; Cui, Q.; Bellus, M. Z.; Zhao, H., Exciton formation in monolayer transition metal dichalcogenides. *Nanoscale* **2016**, *8* (22), 11681-11688.
150. Moody, G.; Schaibley, J.; Xu, X., Exciton dynamics in monolayer transition metal dichalcogenides. *Journal of the Optical Society of America B* **2016**, *33* (7), C39-C49.
151. Ruppert, C.; Chernikov, A.; Hill, H. M.; Rigosi, A. F.; Heinz, T. F., The Role of Electronic and Phononic Excitation in the Optical Response of Monolayer WS₂ after Ultrafast Excitation. *Nano Letters* **2017**, *17* (2), 644-651.
152. Lagarde, D.; Bouet, L.; Marie, X.; Zhu, C. R.; Liu, B. L.; Amand, T.; Tan, P. H.; Urbaszek, B., Carrier and Polarization Dynamics in Monolayer MoS₂. *Physical Review Letters* **2014**, *112* (4), 047401.
153. Palummo, M.; Bernardi, M.; Grossman, J. C., Exciton Radiative Lifetimes in Two-Dimensional Transition Metal Dichalcogenides. *Nano Letters* **2015**, *15* (5), 2794-2800.
154. Klimov, V. I.; Mikhailovsky, A. A.; McBranch, D. W.; Leatherdale, C. A.; Bawendi, M. G., Quantization of Multiparticle Auger Rates in Semiconductor Quantum Dots. *Science* **2000**, *287* (5455), 1011.

155. Hyeon-Deuk, K.; Prezhd, O. V., Time-Domain ab Initio Study of Auger and Phonon-Assisted Auger Processes in a Semiconductor Quantum Dot. *Nano Letters* **2011**, *11* (4), 1845-1850.
156. Huang, L.; Krauss, T. D., Quantized Bimolecular Auger Recombination of Excitons in Single-Walled Carbon Nanotubes. *Physical Review Letters* **2006**, *96* (5), 057407.
157. Ma, Y.-Z.; Valkunas, L.; Dexheimer, S. L.; Bachilo, S. M.; Fleming, G. R., Femtosecond Spectroscopy of Optical Excitations in Single-Walled Carbon Nanotubes: Evidence for Exciton-Exciton Annihilation. *Physical Review Letters* **2005**, *94* (15), 157402.
158. Htoon, H.; Hollingsworth, J. A.; Dickerson, R.; Klimov, V. I., Effect of Zero- to One-Dimensional Transformation on Multiparticle Auger Recombination in Semiconductor Quantum Rods. *Physical Review Letters* **2003**, *91* (22), 227401.
159. Robel, I.; Bunker, B. A.; Kamat, P. V.; Kuno, M., Exciton Recombination Dynamics in CdSe Nanowires: Bimolecular to Three-Carrier Auger Kinetics. *Nano Letters* **2006**, *6* (7), 1344-1349.
160. Yang, Y.; Rodríguez-Córdoba, W.; Lian, T., Multiple Exciton Generation and Dissociation in PbS Quantum Dot-Electron Acceptor Complexes. *Nano Letters* **2012**, *12* (8), 4235-4241.
161. Sim, S.; Park, J.; Song, J.-G.; In, C.; Lee, Y.-S.; Kim, H.; Choi, H., Exciton dynamics in atomically thin MoS₂: Interexcitonic interaction and broadening kinetics. *Physical Review B* **2013**, *88* (7), 075434.
162. Salehzadeh, O.; Tran, N. H.; Liu, X.; Shih, I.; Mi, Z., Exciton Kinetics, Quantum Efficiency, and Efficiency Droop of Monolayer MoS₂ Light-Emitting Devices. *Nano Letters* **2014**, *14* (7), 4125-4130.
163. Sun, D.; Rao, Y.; Reider, G. A.; Chen, G.; You, Y.; Brézin, L.; Harutyunyan, A. R.; Heinz, T. F., Observation of Rapid Exciton-Exciton Annihilation in Monolayer Molybdenum Disulfide. *Nano Letters* **2014**, *14* (10), 5625-5629.
164. Mouri, S.; Miyauchi, Y.; Toh, M.; Zhao, W.; Eda, G.; Matsuda, K., Nonlinear photoluminescence in atomically thin layered WSe₂ arising from diffusion-assisted exciton-exciton annihilation. *Physical Review B* **2014**, *90* (15), 155449.
165. Lee, Y.; Ghimire, G.; Roy, S.; Kim, Y.; Seo, C.; Sood, A. K.; Jang, J. I.; Kim, J., Impeding Exciton-Exciton Annihilation in Monolayer WS₂ by Laser Irradiation. *ACS Photonics* **2018**, *5* (7), 2904-2911.
166. Gutiérrez, H. R.; Perea-López, N.; Elías, A. L.; Berkdemir, A.; Wang, B.; Lv, R.; López-Urías, F.; Crespi, V. H.; Terrones, H.; Terrones, M., Extraordinary Room-Temperature Photoluminescence in Triangular WS₂ Monolayers. *Nano Letters* **2013**, *13* (8), 3447-3454.

167. Mitioglu, A. A.; Plochocka, P.; Jadcak, J. N.; Escoffier, W.; Rikken, G. L. J. A.; Kulyuk, L.; Maude, D. K., Optical manipulation of the exciton charge state in single-layer tungsten disulfide. *Physical Review B* **2013**, *88* (24), 245403.
168. Ross, J. S.; Wu, S.; Yu, H.; Ghimire, N. J.; Jones, A. M.; Aivazian, G.; Yan, J.; Mandrus, D. G.; Xiao, D.; Yao, W.; Xu, X., Electrical control of neutral and charged excitons in a monolayer semiconductor. *Nature Communications* **2013**, *4*, 1474.
169. Shi, H.; Yan, R.; Bertolazzi, S.; Brivio, J.; Gao, B.; Kis, A.; Jena, D.; Xing, H. G.; Huang, L., Exciton Dynamics in Suspended Monolayer and Few-Layer MoS₂ 2D Crystals. *ACS Nano* **2013**, *7* (2), 1072-1080.
170. Perebeinos, V.; Tersoff, J.; Avouris, P., Radiative Lifetime of Excitons in Carbon Nanotubes. *Nano Letters* **2005**, *5* (12), 2495-2499.
171. Mortimer, I. B.; Nicholas, R. J., Role of Bright and Dark Excitons in the Temperature-Dependent Photoluminescence of Carbon Nanotubes. *Physical Review Letters* **2007**, *98* (2), 027404.
172. Zhu, Z.; Crochet, J.; Arnold, M. S.; Hersam, M. C.; Ulbricht, H.; Resasco, D.; Hertel, T., Pump-Probe Spectroscopy of Exciton Dynamics in (6,5) Carbon Nanotubes. *The Journal of Physical Chemistry C* **2007**, *111* (10), 3831-3835.
173. Liu, G.-B.; Xiao, D.; Yao, Y.; Xu, X.; Yao, W., Electronic structures and theoretical modelling of two-dimensional group-VIB transition metal dichalcogenides. *Chemical Society Reviews* **2015**, *44* (9), 2643-2663.
174. Wang, Q.; Ge, S.; Li, X.; Qiu, J.; Ji, Y.; Feng, J.; Sun, D., Valley Carrier Dynamics in Monolayer Molybdenum Disulfide from Helicity-Resolved Ultrafast Pump-Probe Spectroscopy. *ACS Nano* **2013**, *7* (12), 11087-11093.
175. Bao, W.; Borys, N. J.; Ko, C.; Suh, J.; Fan, W.; Thron, A.; Zhang, Y.; Buyanin, A.; Zhang, J.; Cabrini, S.; Ashby, P. D.; Weber-Bargioni, A.; Tongay, S.; Aloni, S.; Ogletree, D. F.; Wu, J.; Salmeron, M. B.; Schuck, P. J., Visualizing nanoscale excitonic relaxation properties of disordered edges and grain boundaries in monolayer molybdenum disulfide. *Nature Communications* **2015**, *6*, 7993.
176. Amani, M.; Lien, D.-H.; Kiriya, D.; Xiao, J.; Azcatl, A.; Noh, J.; Madhvapathy, S. R.; Addou, R.; Kc, S.; Dubey, M.; Cho, K.; Wallace, R. M.; Lee, S.-C.; He, J.-H.; Ager, J. W.; Zhang, X.; Yablonovitch, E.; Javey, A., Near-unity photoluminescence quantum yield in MoS₂. *Science* **2015**, *350* (6264), 1065.
177. Amani, M.; Taheri, P.; Addou, R.; Ahn, G. H.; Kiriya, D.; Lien, D.-H.; Ager, J. W.; Wallace, R. M.; Javey, A., Recombination Kinetics and Effects of Superacid Treatment in Sulfur- and Selenium-Based Transition Metal Dichalcogenides. *Nano Letters* **2016**, *16* (4), 2786-2791.

178. Kim, H.; Lien, D.-H.; Amani, M.; Ager, J. W.; Javey, A., Highly Stable Near-Unity Photoluminescence Yield in Monolayer MoS₂ by Fluoropolymer Encapsulation and Superacid Treatment. *ACS Nano* **2017**, *11* (5), 5179-5185.
179. Atallah, T. L.; Wang, J.; Bosch, M.; Seo, D.; Burke, R. A.; Moneer, O.; Zhu, J.; Theibault, M.; Brus, L. E.; Hone, J.; Zhu, X. Y., Electrostatic Screening of Charged Defects in Monolayer MoS₂. *The Journal of Physical Chemistry Letters* **2017**, *8* (10), 2148-2152.
180. Carozo, V.; Wang, Y.; Fujisawa, K.; Carvalho, B. R.; McCreary, A.; Feng, S.; Lin, Z.; Zhou, C.; Perea-López, N.; Elías, A. L.; Kabius, B.; Crespi, V. H.; Terrones, M., Optical identification of sulfur vacancies: Bound excitons at the edges of monolayer tungsten disulfide. *Science Advances* **2017**, *3* (4), e1602813.
181. Liu, X.; Hu, J.; Yue, C.; Della Fera, N.; Ling, Y.; Mao, Z.; Wei, J., High Performance Field-Effect Transistor Based on Multilayer Tungsten Disulfide. *ACS Nano* **2014**, *8* (10), 10396-10402.
182. Shaw, P. E.; Ruseckas, A.; Samuel, I. D. W., Exciton Diffusion Measurements in Poly(3-hexylthiophene). *Advanced Materials* **2008**, *20* (18), 3516-3520.
183. Beal, A. R.; Liang, W. Y.; Hughes, H. P., Kramers-Kronig analysis of the reflectivity spectra of 3R-WS₂ and 2H-WSe₂. *Journal of Physics C: Solid State Physics* **1976**, *9* (12), 2449-2457.
184. Haug, A., Band-to-band Auger recombination in semiconductors. *Journal of Physics and Chemistry of Solids* **1988**, *49* (6), 599-605.
185. Robel, I.; Gresback, R.; Kortshagen, U.; Schaller, R. D.; Klimov, V. I., Universal Size-Dependent Trend in Auger Recombination in Direct-Gap and Indirect-Gap Semiconductor Nanocrystals. *Physical Review Letters* **2009**, *102* (17), 177404.
186. Schaller, R. D.; Klimov, V. I., High Efficiency Carrier Multiplication in PbSe Nanocrystals: Implications for Solar Energy Conversion. *Physical Review Letters* **2004**, *92* (18), 186601.
187. Kumar, N.; Cui, Q.; Ceballos, F.; He, D.; Wang, Y.; Zhao, H., Exciton-exciton annihilation in MoSe₂ monolayers. *Physical Review B* **2014**, *89* (12), 125427.
188. Taylor, R. A.; Adams, R. A.; Ryan, J. F.; Park, R. M., Exciton recombination dynamics in ZnCdSeZnSe quantum wells. *Journal of Crystal Growth* **1996**, *159* (1), 822-825.
189. Hangleiter, A., Recombination of correlated electron-hole pairs in two-dimensional semiconductors. *Physical Review B* **1993**, *48* (12), 9146-9149.

190. Stier, A. V.; McCreary, K. M.; Jonker, B. T.; Kono, J.; Crooker, S. A., Exciton diamagnetic shifts and valley Zeeman effects in monolayer WS₂ and MoS₂ to 65 Tesla. *Nature Communications* **2016**, *7*, 10643.
191. Snoke, D.; Denev, S.; Liu, Y.; Pfeiffer, L.; West, K., Long-range transport in excitonic dark states in coupled quantum wells. *Nature* **2002**, *418*, 754.
192. Remeika, M.; Graves, J. C.; Hammack, A. T.; Meyertholen, A. D.; Fogler, M. M.; Butov, L. V.; Hanson, M.; Gossard, A. C., Localization-Delocalization Transition of Indirect Excitons in Lateral Electrostatic Lattices. *Physical Review Letters* **2009**, *102* (18), 186803.
193. Gärtner, A.; Holleitner, A. W.; Kotthaus, J. P.; Schuh, D., Drift mobility of long-living excitons in coupled GaAs quantum wells. *Applied Physics Letters* **2006**, *89* (5), 052108.
194. Kato, T.; Kaneko, T., Transport Dynamics of Neutral Excitons and Trions in Monolayer WS₂. *ACS Nano* **2016**, *10* (10), 9687-9694.
195. Yuan, L.; Huang, L., Exciton dynamics and annihilation in WS₂ 2D semiconductors. *Nanoscale* **2015**, *7* (16), 7402-7408.
196. Ovchinnikov, D.; Allain, A.; Huang, Y.-S.; Dumcenco, D.; Kis, A., Electrical Transport Properties of Single-Layer WS₂. *ACS Nano* **2014**, *8* (8), 8174-8181.
197. Basu, P. K.; Ray, P., Calculation of the mobility of two-dimensional excitons in a GaAs/GaAl_xGa_{1-x}As quantum well. *Physical Review B* **1991**, *44* (4), 1844-1849.
198. Jin, Z.; Li, X.; Mullen, J. T.; Kim, K. W., Intrinsic transport properties of electrons and holes in monolayer transition-metal dichalcogenides. *Physical Review B* **2014**, *90* (4), 045422.
199. Kim, S.; Konar, A.; Hwang, W.-S.; Lee, J. H.; Lee, J.; Yang, J.; Jung, C.; Kim, H.; Yoo, J.-B.; Choi, J.-Y.; Jin, Y. W.; Lee, S. Y.; Jena, D.; Choi, W.; Kim, K., High-mobility and low-power thin-film transistors based on multilayer MoS₂ crystals. *Nature Communications* **2012**, *3*, 1011.
200. Fivaz, R., Theory of layer structures. *Journal of Physics and Chemistry of Solids* **1967**, *28* (5), 839-845.
201. Kaasbjerg, K.; Thygesen, K. S.; Jacobsen, K. W., Phonon-limited mobility in n-type single-layer MoS₂ from first principles. *Physical Review B* **2012**, *85* (11), 115317.
202. Li, S.-L.; Wakabayashi, K.; Xu, Y.; Nakaharai, S.; Komatsu, K.; Li, W.-W.; Lin, Y.-F.; Aparecido-Ferreira, A.; Tsukagoshi, K., Thickness-Dependent Interfacial Coulomb Scattering in Atomically Thin Field-Effect Transistors. *Nano Letters* **2013**, *13* (8), 3546-3552.

203. Ma, N.; Jena, D., Charge Scattering and Mobility in Atomically Thin Semiconductors. *Physical Review X* **2014**, *4* (1), 011043.
204. Das, S.; Chen, H.-Y.; Penumatcha, A. V.; Appenzeller, J., High Performance Multilayer MoS₂ Transistors with Scandium Contacts. *Nano Letters* **2013**, *13* (1), 100-105.
205. Sui, Y.; Appenzeller, J., Screening and Interlayer Coupling in Multilayer Graphene Field-Effect Transistors. *Nano Letters* **2009**, *9* (8), 2973-2977.
206. Radisavljevic, B.; Kis, A., Mobility engineering and a metal-insulator transition in monolayer MoS₂. *Nature Materials* **2013**, *12*, 815.
207. Butler, S. Z.; Hollen, S. M.; Cao, L.; Cui, Y.; Gupta, J. A.; Gutiérrez, H. R.; Heinz, T. F.; Hong, S. S.; Huang, J.; Ismach, A. F.; Johnston-Halperin, E.; Kuno, M.; Plashnitsa, V. V.; Robinson, R. D.; Ruoff, R. S.; Salahuddin, S.; Shan, J.; Shi, L.; Spencer, M. G.; Terrones, M.; Windl, W.; Goldberger, J. E., Progress, Challenges, and Opportunities in Two-Dimensional Materials Beyond Graphene. *ACS Nano* **2013**, *7* (4), 2898-2926.
208. Bernardi, M.; Palumbo, M.; Grossman, J. C., Semiconducting Monolayer Materials as a Tunable Platform for Excitonic Solar Cells. *ACS Nano* **2012**, *6* (11), 10082-10089.
209. Britnell, L.; Ribeiro, R. M.; Eckmann, A.; Jalil, R.; Belle, B. D.; Mishchenko, A.; Kim, Y. J.; Gorbachev, R. V.; Georgiou, T.; Morozov, S. V.; Grigorenko, A. N.; Geim, A. K.; Casiraghi, C.; Neto, A. H. C.; Novoselov, K. S., Strong Light-Matter Interactions in Heterostructures of Atomically Thin Films. *Science* **2013**, *340* (6138), 1311.
210. Yu, W. J.; Liu, Y.; Zhou, H.; Yin, A.; Li, Z.; Huang, Y.; Duan, X., Highly efficient gate-tunable photocurrent generation in vertical heterostructures of layered materials. *Nature Nanotechnology* **2013**, *8*, 952.
211. Jariwala, D.; Sangwan, V. K.; Lauhon, L. J.; Marks, T. J.; Hersam, M. C., Emerging Device Applications for Semiconducting Two-Dimensional Transition Metal Dichalcogenides. *ACS Nano* **2014**, *8* (2), 1102-1120.
212. Li, M.-Y.; Shi, Y.; Cheng, C.-C.; Lu, L.-S.; Lin, Y.-C.; Tang, H.-L.; Tsai, M.-L.; Chu, C.-W.; Wei, K.-H.; He, J.-H.; Chang, W.-H.; Suenaga, K.; Li, L.-J., Epitaxial growth of a monolayer WSe₂-MoS₂ lateral p-n junction with an atomically sharp interface. *Science* **2015**, *349* (6247), 524.
213. Yu, J. H.; Lee, H. R.; Hong, S. S.; Kong, D.; Lee, H.-W.; Wang, H.; Xiong, F.; Wang, S.; Cui, Y., Vertical Heterostructure of Two-Dimensional MoS₂ and WSe₂ with Vertically Aligned Layers. *Nano Letters* **2015**, *15* (2), 1031-1035.

214. Massicotte, M.; Schmidt, P.; Violla, F.; Schädler, K. G.; Reserbat-Plantey, A.; Watanabe, K.; Taniguchi, T.; Tielrooij, K. J.; Koppens, F. H. L., Picosecond photoresponse in van der Waals heterostructures. *Nature Nanotechnology* **2015**, *11*, 42.
215. Cheng, R.; Li, D.; Zhou, H.; Wang, C.; Yin, A.; Jiang, S.; Liu, Y.; Chen, Y.; Huang, Y.; Duan, X., Electroluminescence and Photocurrent Generation from Atomically Sharp WSe₂/MoS₂ Heterojunction p–n Diodes. *Nano Letters* **2014**, *14* (10), 5590-5597.
216. Lopez-Sanchez, O.; Alarcon Llado, E.; Koman, V.; Fontcuberta i Morral, A.; Radenovic, A.; Kis, A., Light Generation and Harvesting in a van der Waals Heterostructure. *ACS Nano* **2014**, *8* (3), 3042-3048.
217. He, J.; Kumar, N.; Bellus, M. Z.; Chiu, H.-Y.; He, D.; Wang, Y.; Zhao, H., Electron transfer and coupling in graphene–tungsten disulfide van der Waals heterostructures. *Nature Communications* **2014**, *5*, 5622.
218. Yu, Y.; Hu, S.; Su, L.; Huang, L.; Liu, Y.; Jin, Z.; Purezky, A. A.; Geohegan, D. B.; Kim, K. W.; Zhang, Y.; Cao, L., Equally Efficient Interlayer Exciton Relaxation and Improved Absorption in Epitaxial and Nonepitaxial MoS₂/WS₂ Heterostructures. *Nano Letters* **2015**, *15* (1), 486-491.
219. Kozawa, D.; Carvalho, A.; Verzhbitskiy, I.; Giustiniano, F.; Miyauchi, Y.; Mouri, S.; Castro Neto, A. H.; Matsuda, K.; Eda, G., Evidence for Fast Interlayer Energy Transfer in MoSe₂/WS₂ Heterostructures. *Nano Letters* **2016**, *16* (7), 4087-4093.
220. Hill, H. M.; Rigosi, A. F.; Raja, A.; Chernikov, A.; Roquelet, C.; Heinz, T. F., Exciton broadening in WS₂/graphene heterostructures. *Physical Review B* **2017**, *96* (20), 205401.
221. Heo, H.; Sung, J. H.; Cha, S.; Jang, B.-G.; Kim, J.-Y.; Jin, G.; Lee, D.; Ahn, J.-H.; Lee, M.-J.; Shim, J. H.; Choi, H.; Jo, M.-H., Interlayer orientation-dependent light absorption and emission in monolayer semiconductor stacks. *Nature Communications* **2015**, *6*, 7372.
222. Ghorbani-Asl, M.; Bristowe, P. D.; Koziol, K.; Heine, T.; Kuc, A., Effect of compression on the electronic, optical and transport properties of MoS₂/graphene-based junctions. *2D Materials* **2016**, *3* (2), 025018.
223. Du, A.; Sanvito, S.; Li, Z.; Wang, D.; Jiao, Y.; Liao, T.; Sun, Q.; Ng, Y. H.; Zhu, Z.; Amal, R.; Smith, S. C., Hybrid Graphene and Graphitic Carbon Nitride Nanocomposite: Gap Opening, Electron–Hole Puddle, Interfacial Charge Transfer, and Enhanced Visible Light Response. *Journal of the American Chemical Society* **2012**, *134* (9), 4393-4397.

224. Coy Diaz, H.; Avila, J.; Chen, C.; Addou, R.; Asensio, M. C.; Batzill, M., Direct Observation of Interlayer Hybridization and Dirac Relativistic Carriers in Graphene/MoS₂ van der Waals Heterostructures. *Nano Letters* **2015**, *15* (2), 1135-1140.
225. Jin, W.; Yeh, P.-C.; Zaki, N.; Chenet, D.; Arefe, G.; Hao, Y.; Sala, A.; Mentis, T. O.; Dadap, J. I.; Locatelli, A.; Hone, J.; Osgood, R. M., Tuning the electronic structure of monolayer graphene/MoS₂ van der Waals heterostructures via interlayer twist. *Physical Review B* **2015**, *92* (20), 201409.
226. Chung, T. F.; Shen, T.; Cao, H.; Jauregui, L. A.; Wu, W. E. I.; Yu, Q.; Newell, D.; Chen, Y. P., Synthetic Graphene Grown by Chemical Vapor Deposition on Copper Foils. *International Journal of Modern Physics B* **2013**, *27* (10), 1341002.
227. Kim, K. S.; Zhao, Y.; Jang, H.; Lee, S. Y.; Kim, J. M.; Kim, K. S.; Ahn, J.-H.; Kim, P.; Choi, J.-Y.; Hong, B. H., Large-scale pattern growth of graphene films for stretchable transparent electrodes. *Nature* **2009**, *457*, 706.
228. Li, X.; Cai, W.; An, J.; Kim, S.; Nah, J.; Yang, D.; Piner, R.; Velamakanni, A.; Jung, I.; Tutuc, E.; Banerjee, S. K.; Colombo, L.; Ruoff, R. S., Large-Area Synthesis of High-Quality and Uniform Graphene Films on Copper Foils. *Science* **2009**, *324* (5932), 1312.
229. Bian, G.; Chung, T.-F.; Chen, C.; Liu, C.; Chang, T.-R.; Wu, T.; Belopolski, I.; Zheng, H.; Xu, S.-Y.; Sanchez, D. S.; Alidoust, N.; Pierce, J.; Quilliams, B.; Barletta, P. P.; Lorcy, S.; Avila, J.; Chang, G.; Lin, H.; Jeng, H.-T.; Asensio, M.-C.; Chen, Y. P.; Hasan, M. Z., Experimental observation of two massless Dirac-fermion gases in graphene-topological insulator heterostructure. *2D Materials* **2016**, *3* (2), 021009.
230. Mak, K. F.; Shan, J.; Heinz, T. F., Seeing Many-Body Effects in Single- and Few-Layer Graphene: Observation of Two-Dimensional Saddle-Point Excitons. *Physical Review Letters* **2011**, *106* (4), 046401.
231. Catti, M.; Pavese, A.; Dovesi, R.; Saunders, V. R., Static lattice and electron properties of MgCO₃ (magnesite) calculated by ab initio periodic Hartree-Fock methods. *Physical Review B* **1993**, *47* (15), 9189-9198.
232. Lichanot, A.; Aprà, E.; Dovesi, R., Quantum Mechanical Hartree-Fock Study of the Elastic Properties of Li₂S and Na₂S. *physica status solidi (b)* **1993**, *177* (1), 157-163.
233. Corà, F.; Patel, A.; Harrison, N. M.; Dovesi, R.; Catlow, C. R. A., An ab Initio Hartree-Fock Study of the Cubic and Tetragonal Phases of Bulk Tungsten Trioxide. *Journal of the American Chemical Society* **1996**, *118* (48), 12174-12182.
234. Perdew, J. P.; Burke, K.; Ernzerhof, M., Generalized Gradient Approximation Made Simple. *Physical Review Letters* **1996**, *77* (18), 3865-3868.

235. Grimme, S., Semiempirical GGA-type density functional constructed with a long-range dispersion correction. *Journal of Computational Chemistry* **2006**, *27* (15), 1787-1799.
236. Kresse, G.; Furthmüller, J., Efficient iterative schemes for ab initio total-energy calculations using a plane-wave basis set. *Physical Review B* **1996**, *54* (16), 11169-11186.
237. Blöchl, P. E., Projector augmented-wave method. *Physical Review B* **1994**, *50* (24), 17953-17979.
238. Kresse, G.; Joubert, D., From ultrasoft pseudopotentials to the projector augmented-wave method. *Physical Review B* **1999**, *59* (3), 1758-1775.
239. Heyd, J.; Scuseria, G. E.; Ernzerhof, M., Hybrid functionals based on a screened Coulomb potential. *The Journal of Chemical Physics* **2003**, *118* (18), 8207-8215.
240. Huo, N.; Wei, Z.; Meng, X.; Kang, J.; Wu, F.; Li, S.-S.; Wei, S.-H.; Li, J., Interlayer coupling and optoelectronic properties of ultrathin two-dimensional heterostructures based on graphene, MoS₂ and WS₂. *Journal of Materials Chemistry C* **2015**, *3* (21), 5467-5473.
241. Kobayashi, Y.; Sasaki, S.; Mori, S.; Hibino, H.; Liu, Z.; Watanabe, K.; Taniguchi, T.; Suenaga, K.; Maniwa, Y.; Miyata, Y., Growth and Optical Properties of High-Quality Monolayer WS₂ on Graphite. *ACS Nano* **2015**, *9* (4), 4056-4063.
242. Das, A.; Pisana, S.; Chakraborty, B.; Piscanec, S.; Saha, S. K.; Waghmare, U. V.; Novoselov, K. S.; Krishnamurthy, H. R.; Geim, A. K.; Ferrari, A. C.; Sood, A. K., Monitoring dopants by Raman scattering in an electrochemically top-gated graphene transistor. *Nature Nanotechnology* **2008**, *3*, 210.
243. Zhou, K.-G.; Withers, F.; Cao, Y.; Hu, S.; Yu, G.; Casiraghi, C., Raman Modes of MoS₂ Used as Fingerprint of van der Waals Interactions in 2-D Crystal-Based Heterostructures. *ACS Nano* **2014**, *8* (10), 9914-9924.
244. Hu, X.; Yasaei, P.; Jokisaari, J.; Ögüt, S.; Salehi-Khojin, A.; Klie, R. F., Mapping Thermal Expansion Coefficients in Freestanding 2D Materials at the Nanometer Scale. *Physical Review Letters* **2018**, *120* (5), 055902.
245. Yoon, D.; Son, Y.-W.; Cheong, H., Negative Thermal Expansion Coefficient of Graphene Measured by Raman Spectroscopy. *Nano Letters* **2011**, *11* (8), 3227-3231.
246. Lee, J. E.; Ahn, G.; Shim, J.; Lee, Y. S.; Ryu, S., Optical separation of mechanical strain from charge doping in graphene. *Nature Communications* **2012**, *3*, 1024.
247. Khalil, H. M. W.; Khan, M. F.; Eom, J.; Noh, H., Highly Stable and Tunable Chemical Doping of Multilayer WS₂ Field Effect Transistor: Reduction in Contact Resistance. *ACS Applied Materials & Interfaces* **2015**, *7* (42), 23589-23596.

248. Cunningham, P. D.; Hanbicki, A. T.; McCreary, K. M.; Jonker, B. T., Photoinduced Bandgap Renormalization and Exciton Binding Energy Reduction in WS₂. *ACS Nano* **2017**, *11* (12), 12601-12608.
249. Ulstrup, S.; Čabo, A. G.; Miwa, J. A.; Riley, J. M.; Grønberg, S. S.; Johannsen, J. C.; Cacho, C.; Alexander, O.; Chapman, R. T.; Springate, E.; Bianchi, M.; Dendzik, M.; Lauritsen, J. V.; King, P. D. C.; Hofmann, P., Ultrafast Band Structure Control of a Two-Dimensional Heterostructure. *ACS Nano* **2016**, *10* (6), 6315-6322.
250. Raja, A.; Chaves, A.; Yu, J.; Arefe, G.; Hill, H. M.; Rigosi, A. F.; Berkelbach, T. C.; Nagler, P.; Schüller, C.; Korn, T.; Nuckolls, C.; Hone, J.; Brus, L. E.; Heinz, T. F.; Reichman, D. R.; Chernikov, A., Coulomb engineering of the bandgap and excitons in two-dimensional materials. *Nature Communications* **2017**, *8*, 15251.
251. Schmitt-Rink, S.; Chemla, D. S.; Miller, D. A. B., Theory of transient excitonic optical nonlinearities in semiconductor quantum-well structures. *Physical Review B* **1985**, *32* (10), 6601-6609.
252. Sie, E. J.; Steinhoff, A.; Gies, C.; Lui, C. H.; Ma, Q.; Rösner, M.; Schönhoff, G.; Jahnke, F.; Wehling, T. O.; Lee, Y. H.; Kong, J.; Jarillo-Herrero, P.; Gedik, N., Observation of Exciton Redshift–Blueshift Crossover in Monolayer WS₂. *Nano Letters* **2017**, *17* (7), 4210-4216.
253. Massicotte, M.; Schmidt, P.; Violla, F.; Watanabe, K.; Taniguchi, T.; Tielrooij, K. J.; Koppens, F. H. L., Photo-thermionic effect in vertical graphene heterostructures. *Nature Communications* **2016**, *7*, 12174.
254. Liu, Y.; Stradins, P.; Wei, S.-H., Van der Waals metal-semiconductor junction: Weak Fermi level pinning enables effective tuning of Schottky barrier. *Science Advances* **2016**, *2* (4), e1600069.
255. Forti, S.; Rossi, A.; Büch, H.; Cavallucci, T.; Bisio, F.; Sala, A.; Menteş, T. O.; Locatelli, A.; Magnozzi, M.; Canepa, M.; Müller, K.; Link, S.; Starke, U.; Tozzini, V.; Coletti, C., Electronic properties of single-layer tungsten disulfide on epitaxial graphene on silicon carbide. *Nanoscale* **2017**, *9* (42), 16412-16419.
256. Wu, K.; Chen, J.; McBride, J. R.; Lian, T., Efficient hot-electron transfer by a plasmon-induced interfacial charge-transfer transition. *Science* **2015**, *349* (6248), 632.
257. Perebeinos, V.; Tersoff, J.; Avouris, P., Scaling of Excitons in Carbon Nanotubes. *Physical Review Letters* **2004**, *92* (25), 257402.
258. Raja, A.; Montoya–Castillo, A.; Zultak, J.; Zhang, X.-X.; Ye, Z.; Roquelet, C.; Chenet, D. A.; van der Zande, A. M.; Huang, P.; Jockusch, S.; Hone, J.; Reichman, D. R.; Brus, L. E.; Heinz, T. F., Energy Transfer from Quantum Dots to Graphene and MoS₂: The Role of Absorption and Screening in Two-Dimensional Materials. *Nano Letters* **2016**, *16* (4), 2328-2333.

259. Liang, Y.; Huang, S.; Soklaski, R.; Yang, L., Quasiparticle band-edge energy and band offsets of monolayer of molybdenum and tungsten chalcogenides. *Applied Physics Letters* **2013**, *103* (4), 042106.
260. Miyazaki, J.; Kawasumi, K.; Kobayashi, T., Resolution improvement in laser diode-based pump-probe microscopy with an annular pupil filter. *Opt. Lett.* **2014**, *39* (14), 4219-4222.
261. Tan, J. Y.; Avsar, A.; Balakrishnan, J.; Koon, G. K. W.; Taychatanapat, T.; O'Farrell, E. C. T.; Watanabe, K.; Taniguchi, T.; Eda, G.; Castro Neto, A. H.; Özyilmaz, B., Electronic transport in graphene-based heterostructures. *Applied Physics Letters* **2014**, *104* (18), 183504.
262. Tielrooij, K. J.; Piatkowski, L.; Massicotte, M.; Woessner, A.; Ma, Q.; Lee, Y.; Myhro, K. S.; Lau, C. N.; Jarillo-Herrero, P.; van Hulst, N. F.; Koppens, F. H. L., Generation of photovoltage in graphene on a femtosecond timescale through efficient carrier heating. *Nature Nanotechnology* **2015**, *10*, 437.
263. Jailaubekov, A. E.; Willard, A. P.; Tritsch, J. R.; Chan, W.-L.; Sai, N.; Gearba, R.; Kaake, L. G.; Williams, K. J.; Leung, K.; Rossky, P. J.; Zhu, X. Y., Hot charge-transfer excitons set the time limit for charge separation at donor/acceptor interfaces in organic photovoltaics. *Nature Materials* **2012**, *12*, 66.
264. Vandewal, K.; Albrecht, S.; Hoke, E. T.; Graham, K. R.; Widmer, J.; Douglas, J. D.; Schubert, M.; Mateker, W. R.; Bloking, J. T.; Burkhard, G. F.; Sellinger, A.; Fréchet, J. M. J.; Amassian, A.; Riede, M. K.; McGehee, M. D.; Neher, D.; Salleo, A., Efficient charge generation by relaxed charge-transfer states at organic interfaces. *Nature Materials* **2013**, *13*, 63.
265. Falke, S. M.; Rozzi, C. A.; Brida, D.; Maiuri, M.; Amato, M.; Sommer, E.; De Sio, A.; Rubio, A.; Cerullo, G.; Molinari, E.; Lienau, C., Coherent ultrafast charge transfer in an organic photovoltaic blend. *Science* **2014**, *344* (6187), 1001.
266. Jakowetz, A. C.; Böhm, M. L.; Sadhanala, A.; Huettner, S.; Rao, A.; Friend, R. H., Visualizing excitations at buried heterojunctions in organic semiconductor blends. *Nature Materials* **2017**, *16*, 551.
267. Britnell, L.; Gorbachev, R. V.; Jalil, R.; Belle, B. D.; Schedin, F.; Mishchenko, A.; Georgiou, T.; Katsnelson, M. I.; Eaves, L.; Morozov, S. V.; Peres, N. M. R.; Leist, J.; Geim, A. K.; Novoselov, K. S.; Ponomarenko, L. A., Field-Effect Tunneling Transistor Based on Vertical Graphene Heterostructures. *Science* **2012**, *335* (6071), 947.

268. Mishchenko, A.; Tu, J. S.; Cao, Y.; Gorbachev, R. V.; Wallbank, J. R.; Greenaway, M. T.; Morozov, V. E.; Morozov, S. V.; Zhu, M. J.; Wong, S. L.; Withers, F.; Woods, C. R.; Kim, Y. J.; Watanabe, K.; Taniguchi, T.; Vdovin, E. E.; Makarovskiy, O.; Fromhold, T. M.; Fal'ko, V. I.; Geim, A. K.; Eaves, L.; Novoselov, K. S., Twist-controlled resonant tunnelling in graphene/boron nitride/graphene heterostructures. *Nature Nanotechnology* **2014**, *9*, 808.
269. Cho, E. H.; Song, W. G.; Park, C. J.; Kim, J.; Kim, S.; Joo, J., Enhancement of photoresponsive electrical characteristics of multilayer MoS₂ transistors using rubrene patches. *Nano Research* **2015**, *8* (3), 790-800.
270. Yang, F.; Cheng, S.; Zhang, X.; Ren, X.; Li, R.; Dong, H.; Hu, W., 2D Organic Materials for Optoelectronic Applications. *Advanced Materials* **2018**, *30* (2), 1702415.
271. Liu, X.; Wei, Z.; Balla, I.; Mannix, A. J.; Guisinger, N. P.; Luijten, E.; Hersam, M. C., Self-assembly of electronically abrupt borophene/organic lateral heterostructures. *Science Advances* **2017**, *3* (2), e1602356.
272. Lee, Y. T.; Jeon, P. J.; Han, J. H.; Ahn, J.; Lee, H. S.; Lim, J. Y.; Choi, W. K.; Song, J. D.; Park, M.-C.; Im, S.; Hwang, D. K., Mixed-Dimensional 1D ZnO–2D WSe₂ van der Waals Heterojunction Device for Photosensors. *Advanced Functional Materials* **2017**, *27* (47), 1703822.
273. Deotare, P. B.; Chang, W.; Hontz, E.; Congreve, D. N.; Shi, L.; Reuswig, P. D.; Modtland, B.; Bahlke, M. E.; Lee, C. K.; Willard, A. P.; Bulović, V.; Van Voorhis, T.; Baldo, M. A., Nanoscale transport of charge-transfer states in organic donor–acceptor blends. *Nature Materials* **2015**, *14*, 1130.
274. Bernardo, B.; Cheyons, D.; Verreet, B.; Schaller, R. D.; Rand, B. P.; Giebink, N. C., Delocalization and dielectric screening of charge transfer states in organic photovoltaic cells. *Nature Communications* **2014**, *5*, 3245.
275. Athanasopoulos, S.; Tscheuschner, S.; Bässler, H.; Köhler, A., Efficient Charge Separation of Cold Charge-Transfer States in Organic Solar Cells Through Incoherent Hopping. *The Journal of Physical Chemistry Letters* **2017**, *8* (9), 2093-2098.
276. Wan, Y.; Guo, Z.; Zhu, T.; Yan, S.; Johnson, J.; Huang, L., Cooperative singlet and triplet exciton transport in tetracene crystals visualized by ultrafast microscopy. *Nature Chemistry* **2015**, *7*, 785.
277. Guo, Z.; Wan, Y.; Yang, M.; Snaider, J.; Zhu, K.; Huang, L., Long-range hot-carrier transport in hybrid perovskites visualized by ultrafast microscopy. *Science* **2017**, *356* (6333), 59.

278. Lee, C.-H.; Schiros, T.; Santos, E. J. G.; Kim, B.; Yager, K. G.; Kang, S. J.; Lee, S.; Yu, J.; Watanabe, K.; Taniguchi, T.; Hone, J.; Kaxiras, E.; Nuckolls, C.; Kim, P., Epitaxial Growth of Molecular Crystals on van der Waals Substrates for High-Performance Organic Electronics. *Advanced Materials* **2014**, *26* (18), 2812-2817.
279. Chen, R., Apparent stretched-exponential luminescence decay in crystalline solids. *Journal of Luminescence* **2003**, *102-103*, 510-518.
280. Lu, S.; Madhukar, A., Nonradiative Resonant Excitation Transfer from Nanocrystal Quantum Dots to Adjacent Quantum Channels. *Nano Letters* **2007**, *7* (11), 3443-3451.
281. Peumans, P.; Forrest, S. R., Separation of geminate charge-pairs at donor-acceptor interfaces in disordered solids. *Chemical Physics Letters* **2004**, *398* (1), 27-31.
282. Rowland, C. E.; Fedin, I.; Zhang, H.; Gray, S. K.; Govorov, A. O.; Talapin, D. V.; Schaller, R. D., Picosecond energy transfer and multiexciton transfer outpaces Auger recombination in binary CdSe nanoplatelet solids. *Nature Materials* **2015**, *14*, 484.
283. Prins, F.; Goodman, A. J.; Tisdale, W. A., Reduced Dielectric Screening and Enhanced Energy Transfer in Single- and Few-Layer MoS₂. *Nano Letters* **2014**, *14* (11), 6087-6091.
284. Zang, H.; Routh, P. K.; Huang, Y.; Chen, J.-S.; Sutter, E.; Sutter, P.; Cotlet, M., Nonradiative Energy Transfer from Individual CdSe/ZnS Quantum Dots to Single-Layer and Few-Layer Tin Disulfide. *ACS Nano* **2016**, *10* (4), 4790-4796.
285. Li, Y.; Chernikov, A.; Zhang, X.; Rigosi, A.; Hill, H. M.; van der Zande, A. M.; Chenet, D. A.; Shih, E.-M.; Hone, J.; Heinz, T. F., Measurement of the optical dielectric function of monolayer transition-metal dichalcogenides: MoS₂, MoSe₂, WS₂, and WSe₂. *Physical Review B* **2014**, *90* (20), 205422.
286. Pavesi, L.; Ceschini, M., Stretched-exponential decay of the luminescence in porous silicon. *Physical Review B* **1993**, *48* (23), 17625-17628.
287. Lee, C. K.; Shi, L.; Willard, A. P., A Model of Charge-Transfer Excitons: Diffusion, Spin Dynamics, and Magnetic Field Effects. *The Journal of Physical Chemistry Letters* **2016**, *7* (12), 2246-2251.
288. Berrehar, J.; Delannoy, P.; Schotta, M., Drift mobility of holes in crystalline tetracene. *physica status solidi (b)* **1976**, *77* (2), K119-K122.
289. Kuc, A.; Zibouche, N.; Heine, T., Influence of quantum confinement on the electronic structure of the transition metal sulfide TS₂. *Physical Review B* **2011**, *83* (24), 245213.
290. Lebègue, S.; Eriksson, O., Electronic structure of two-dimensional crystals from ab initio theory. *Physical Review B* **2009**, *79* (11), 115409.

291. Ramakrishna Matte, H. S. S.; Gomathi, A.; Manna, A. K.; Late, D. J.; Datta, R.; Pati, S. K.; Rao, C. N. R., MoS₂ and WS₂ Analogues of Graphene. *Angewandte Chemie International Edition* **2010**, *49* (24), 4059-4062.
292. Zhang, Y.; Chang, T.-R.; Zhou, B.; Cui, Y.-T.; Yan, H.; Liu, Z.; Schmitt, F.; Lee, J.; Moore, R.; Chen, Y.; Lin, H.; Jeng, H.-T.; Mo, S.-K.; Hussain, Z.; Bansil, A.; Shen, Z.-X., Direct observation of the transition from indirect to direct bandgap in atomically thin epitaxial MoSe₂. *Nature Nanotechnology* **2013**, *9*, 111.
293. Komsa, H.-P.; Krasheninnikov, A. V., Effects of confinement and environment on the electronic structure and exciton binding energy of MoS₂ from first principles. *Physical Review B* **2012**, *86* (24), 241201.
294. Cheiwchanchamnangij, T.; Lambrecht, W. R. L., Quasiparticle band structure calculation of monolayer, bilayer, and bulk MoS₂. *Physical Review B* **2012**, *85* (20), 205302.
295. Molina-Sánchez, A.; Sangalli, D.; Hummer, K.; Marini, A.; Wirtz, L., Effect of spin-orbit interaction on the optical spectra of single-layer, double-layer, and bulk MoS₂. *Physical Review B* **2013**, *88* (4), 045412.
296. Kośmider, K.; González, J. W.; Fernández-Rossier, J., Large spin splitting in the conduction band of transition metal dichalcogenide monolayers. *Physical Review B* **2013**, *88* (24), 245436.
297. Wang, Z.; Molina-Sánchez, A.; Altmann, P.; Sangalli, D.; De Fazio, D.; Soavi, G.; Sassi, U.; Bottegoni, F.; Ciccacci, F.; Finazzi, M.; Wirtz, L.; Ferrari, A. C.; Marini, A.; Cerullo, G.; Dal Conte, S., Intravalley Spin-Flip Relaxation Dynamics in Single-Layer WS₂. *Nano Letters* **2018**, *18* (11), 6882-6891.
298. Sun, Z.; Martinez, A.; Wang, F., Optical modulators with 2D layered materials. *Nature Photonics* **2016**, *10*, 227.
299. Sarkar, D.; Xie, X.; Liu, W.; Cao, W.; Kang, J.; Gong, Y.; Kraemer, S.; Ajayan, P. M.; Banerjee, K., A subthermionic tunnel field-effect transistor with an atomically thin channel. *Nature* **2015**, *526*, 91.
300. Nagler, P.; Ballottin, M. V.; Mitioglu, A. A.; Mooshammer, F.; Paradiso, N.; Strunk, C.; Huber, R.; Chernikov, A.; Christianen, P. C. M.; Schüller, C.; Korn, T., Giant magnetic splitting inducing near-unity valley polarization in van der Waals heterostructures. *Nature Communications* **2017**, *8* (1), 1551.
301. Sun, Z.; Gu, J.; Ghazaryan, A.; Shotan, Z.; Considine, C. R.; Dollar, M.; Chakraborty, B.; Liu, X.; Ghaemi, P.; Kéna-Cohen, S.; Menon, V. M., Optical control of room-temperature valley polaritons. *Nature Photonics* **2017**, *11*, 491.

302. Kim, J.; Jin, C.; Chen, B.; Cai, H.; Zhao, T.; Lee, P.; Kahn, S.; Watanabe, K.; Taniguchi, T.; Tongay, S.; Crommie, M. F.; Wang, F., Observation of ultralong valley lifetime in WSe₂/MoS₂ heterostructures. *Science Advances* **2017**, *3* (7), e1700518.
303. Onga, M.; Zhang, Y.; Ideue, T.; Iwasa, Y., Exciton Hall effect in monolayer MoS₂. *Nature Materials* **2017**, *16*, 1193.
304. Schaibley, J. R.; Rivera, P.; Yu, H.; Seyler, K. L.; Yan, J.; Mandrus, D. G.; Taniguchi, T.; Watanabe, K.; Yao, W.; Xu, X., Directional interlayer spin-valley transfer in two-dimensional heterostructures. *Nature Communications* **2016**, *7*, 13747.
305. Benítez, L. A.; Sierra, J. F.; Savero Torres, W.; Arrighi, A.; Bonell, F.; Costache, M. V.; Valenzuela, S. O., Strongly anisotropic spin relaxation in graphene–transition metal dichalcogenide heterostructures at room temperature. *Nature Physics* **2018**, *14* (3), 303-308.
306. Garcia, J. H.; Vila, M.; Cummings, A. W.; Roche, S., Spin transport in graphene/transition metal dichalcogenide heterostructures. *Chemical Society Reviews* **2018**, *47* (9), 3359-3379.
307. Safeer, C. K.; Ingla-Aynés, J.; Herling, F.; Garcia, J. H.; Vila, M.; Ontoso, N.; Calvo, M. R.; Roche, S.; Hueso, L. E.; Casanova, F., Room-Temperature Spin Hall Effect in Graphene/MoS₂ van der Waals Heterostructures. *Nano Letters* **2019**, *19* (2), 1074-1082.
308. Latini, S.; Winther, K. T.; Olsen, T.; Thygesen, K. S., Interlayer Excitons and Band Alignment in MoS₂/hBN/WSe₂ van der Waals Heterostructures. *Nano Letters* **2017**, *17* (2), 938-945.
309. Ceballos, F.; Bellus, M. Z.; Chiu, H.-Y.; Zhao, H., Ultrafast Charge Separation and Indirect Exciton Formation in a MoS₂–MoSe₂ van der Waals Heterostructure. *ACS Nano* **2014**, *8* (12), 12717-12724.
310. Ceballos, F.; Ju, M.-G.; Lane, S. D.; Zeng, X. C.; Zhao, H., Highly Efficient and Anomalous Charge Transfer in van der Waals Trilayer Semiconductors. *Nano Letters* **2017**, *17* (3), 1623-1628.
311. Calman, E. V.; Fogler, M. M.; Butov, L. V.; Hu, S.; Mishchenko, A.; Geim, A. K., Indirect excitons in van der Waals heterostructures at room temperature. *Nature Communications* **2018**, *9* (1), 1895.
312. Zhang, C.; Chuu, C.-P.; Ren, X.; Li, M.-Y.; Li, L.-J.; Jin, C.; Chou, M.-Y.; Shih, C.-K., Interlayer couplings, Moiré patterns, and 2D electronic superlattices in MoS₂/WSe₂ hetero-bilayers. *Science Advances* **2017**, *3* (1), e1601459.

313. Xue, J.; Sanchez-Yamagishi, J.; Bulmash, D.; Jacquod, P.; Deshpande, A.; Watanabe, K.; Taniguchi, T.; Jarillo-Herrero, P.; LeRoy, B. J., Scanning tunnelling microscopy and spectroscopy of ultra-flat graphene on hexagonal boron nitride. *Nature Materials* **2011**, *10*, 282.
314. Yu, H.; Liu, G.-B.; Tang, J.; Xu, X.; Yao, W., Moiré excitons: From programmable quantum emitter arrays to spin-orbit-coupled artificial lattices. *Science Advances* **2017**, *3* (11), e1701696.
315. Zhang, N.; Surrente, A.; Baranowski, M.; Maude, D. K.; Gant, P.; Castellanos-Gomez, A.; Plochocka, P., Moiré Intralayer Excitons in a MoSe₂/MoS₂ Heterostructure. *Nano Letters* **2018**, *18* (12), 7651-7657.
316. Kang, J.; Li, J.; Li, S.-S.; Xia, J.-B.; Wang, L.-W., Electronic Structural Moiré Pattern Effects on MoS₂/MoSe₂ 2D Heterostructures. *Nano Letters* **2013**, *13* (11), 5485-5490.
317. Decker, R.; Wang, Y.; Brar, V. W.; Regan, W.; Tsai, H.-Z.; Wu, Q.; Gannett, W.; Zettl, A.; Crommie, M. F., Local Electronic Properties of Graphene on a BN Substrate via Scanning Tunneling Microscopy. *Nano Letters* **2011**, *11* (6), 2291-2295.
318. Tong, Q.; Liu, F.; Xiao, J.; Yao, W., Skyrmions in the Moiré of van der Waals 2D Magnets. *Nano Letters* **2018**, *18* (11), 7194-7199.
319. Ni, G. X.; Wang, H.; Wu, J. S.; Fei, Z.; Goldflam, M. D.; Keilmann, F.; Özyilmaz, B.; Castro Neto, A. H.; Xie, X. M.; Fogler, M. M.; Basov, D. N., Plasmons in graphene moiré superlattices. *Nature Materials* **2015**, *14*, 1217.
320. Wu, S.; Wang, L.; Lai, Y.; Shan, W.-Y.; Aivazian, G.; Zhang, X.; Taniguchi, T.; Watanabe, K.; Xiao, D.; Dean, C.; Hone, J.; Li, Z.; Xu, X., Multiple hot-carrier collection in photo-excited graphene Moiré superlattices. *Science Advances* **2016**, *2* (5), e1600002.
321. Yankowitz, M.; Jung, J.; Laksono, E.; Leconte, N.; Chittari, B. L.; Watanabe, K.; Taniguchi, T.; Adam, S.; Graf, D.; Dean, C. R., Dynamic band-structure tuning of graphene moiré superlattices with pressure. *Nature* **2018**, *557* (7705), 404-408.
322. Shi, Z.; Jin, C.; Yang, W.; Ju, L.; Horng, J.; Lu, X.; Bechtel, H. A.; Martin, M. C.; Fu, D.; Wu, J.; Watanabe, K.; Taniguchi, T.; Zhang, Y.; Bai, X.; Wang, E.; Zhang, G.; Wang, F., Gate-dependent pseudospin mixing in graphene/boron nitride moiré superlattices. *Nature Physics* **2014**, *10*, 743.
323. Tran, K.; Moody, G.; Wu, F.; Lu, X.; Choi, J.; Kim, K.; Rai, A.; Sanchez, D. A.; Quan, J.; Singh, A.; Embley, J.; Zepeda, A.; Campbell, M.; Autry, T.; Taniguchi, T.; Watanabe, K.; Lu, N.; Banerjee, S. K.; Silverman, K. L.; Kim, S.; Tutuc, E.; Yang, L.; MacDonald, A. H.; Li, X., Evidence for moiré excitons in van der Waals heterostructures. *Nature* **2019**.

324. Seyler, K. L.; Rivera, P.; Yu, H.; Wilson, N. P.; Ray, E. L.; Mandrus, D. G.; Yan, J.; Yao, W.; Xu, X., Signatures of moiré-trapped valley excitons in MoSe₂/WSe₂ heterobilayers. *Nature* **2019**.
325. Jin, C.; Regan, E. C.; Yan, A.; Iqbal Bakti Utama, M.; Wang, D.; Zhao, S.; Qin, Y.; Yang, S.; Zheng, Z.; Shi, S.; Watanabe, K.; Taniguchi, T.; Tongay, S.; Zettl, A.; Wang, F., Observation of moiré excitons in WSe₂/WS₂ heterostructure superlattices. *Nature* **2019**.
326. Gong, Y.; Lei, S.; Ye, G.; Li, B.; He, Y.; Keyshar, K.; Zhang, X.; Wang, Q.; Lou, J.; Liu, Z.; Vajtai, R.; Zhou, W.; Ajayan, P. M., Two-Step Growth of Two-Dimensional WSe₂/MoSe₂ Heterostructures. *Nano Letters* **2015**, *15* (9), 6135-6141.
327. Chen, K.; Wan, X.; Wen, J.; Xie, W.; Kang, Z.; Zeng, X.; Chen, H.; Xu, J.-B., Electronic Properties of MoS₂-WS₂ Heterostructures Synthesized with Two-Step Lateral Epitaxial Strategy. *ACS Nano* **2015**, *9* (10), 9868-9876.
328. Liu, K.; Zhang, L.; Cao, T.; Jin, C.; Qiu, D.; Zhou, Q.; Zettl, A.; Yang, P.; Louie, S. G.; Wang, F., Evolution of interlayer coupling in twisted molybdenum disulfide bilayers. *Nature Communications* **2014**, *5*, 4966.
329. Hsu, W.-T.; Zhao, Z.-A.; Li, L.-J.; Chen, C.-H.; Chiu, M.-H.; Chang, P.-S.; Chou, Y.-C.; Chang, W.-H., Second Harmonic Generation from Artificially Stacked Transition Metal Dichalcogenide Twisted Bilayers. *ACS Nano* **2014**, *8* (3), 2951-2958.
330. Yin, X.; Ye, Z.; Chenet, D. A.; Ye, Y.; O'Brien, K.; Hone, J. C.; Zhang, X., Edge Nonlinear Optics on a MoS₂ Atomic Monolayer. *Science* **2014**, *344* (6183), 488.
331. Chae, W. H.; Cain, J. D.; Hanson, E. D.; Murthy, A. A.; Dravid, V. P., Substrate-induced strain and charge doping in CVD-grown monolayer MoS₂. *Applied Physics Letters* **2017**, *111* (14), 143106.
332. Vögele, X. P.; Schuh, D.; Wegscheider, W.; Kotthaus, J. P.; Holleitner, A. W., Density Enhanced Diffusion of Dipolar Excitons within a One-Dimensional Channel. *Physical Review Letters* **2009**, *103* (12), 126402.
333. Rapaport, R.; Chen, G.; Simon, S. H., Nonlinear dynamics of a dense two-dimensional dipolar exciton gas. *Physical Review B* **2006**, *73* (3), 033319.

PUBLICATIONS

1. Tong Zhu, Jordan M. Snaider, **Long Yuan**, and Libai Huang, Ultrafast Dynamic Microscopy of Carrier and Exciton Transport, *Annu. Rev. Phys. Chem.* 2019. 70, 249–74
2. Enzheng Shi, Shibin Deng, Biao Yuan, Yao Gao, Akriti, **Long Yuan**, Chelsea S. Davis, Dmitry Zemlyanov, Yi Yu, Libai Huang, and Letian Dou, Extrinsic and Dynamic Edge States of Two-Dimensional Lead Halide Perovskites, *ACS Nano*, 2019, 13, 635–1644
3. Tuning the interfacial and energetic interactions between a photoexcited conjugated polymer and open-shell small molecules, Daniel A. Wilcox, Jordan Snaider, Sanjoy Mukherjee, **Long Yuan**, Libai Huang, Brett M. Savoiea and Bryan W. Boudouris, *Soft Matter*, 2019,15, 1413-1422
4. **Long Yuan**#, Ting-Fung Chung#, Agnieszka Kuc#, Yan Wan, Yang Xu, Yong P. Chen, Thomas Heine, and Libai Huang*, Photocarrier Generation from Interlayer Charge-Transfer Transitions in WS₂-Graphene Heterostructures, *Science Advance*, 2018, 4, e1700324. (#: Co-first authors).
5. Tong Zhu#, **Long Yuan**#, Yan Zhao, Yan Wan, Jianguo Mei, Libai Huang*, Highly Mobile Charge-Transfer Excitons in Two-Dimensional Tetracene-WS₂ Heterostructures, *Science Advance*, 2018, 4, eaao3104. (#: Co-first authors).
6. Jordan M. Snaider, Zhi Guo, Ti Wang, Mengjin Yang, **Long Yuan**, Kai Zhu, and Libai Huang*, Ultrafast Imaging of Carrier Transport across Grain Boundaries in Hybrid Perovskite Thin Films. *ACS Energy Lett.* 2018, 3, 1402–1408.
7. Yan Zhao, Aristide Gumyusenge, Jiazhi He, Ge Qu, **Long Yuan**, Xikang Zhao, Hongyi Zhang, Libai Huang, Ying Diao, Jianguo Mei*, Continuous Melt-Drawing of Highly Aligned Semiconducting Microfibers for Flexible and Stretchable Electronics, *Advanced Functional Materials*, 2018, 28, 1705584.
8. **Long Yuan**, Ti Wang, Tong Zhu, Mingwei Zhou, and Libai Huang*, Exciton Dynamics, Transport, and Annihilation in Atomically Thin 2D Semiconductor, *Journal of Physical Chemistry Letters*, 2017, 8, 3371–3379.

9. Jingyu Sun, Zhaolong Chen, **Long Yuan**, Yubin Chen, Jing Ning, Shuwei Liu, Donglin Ma, Xiuju Song, Manish K. Priyadarshi, Alicja Bachmatiuk, Mark H. Rummeli, Tianbao Ma, Linjie Zhi, Libai Huang, Yanfeng Zhang*, and Zhongfan Liu*, Direct Chemical-Vapor-Deposition-Fabricated, Large-Scale Graphene Glass with High Carrier Mobility and Uniformity for Touch Panel Applications, *ACS Nano* 2016, 10, 11136–11144.

10. **Long Yuan** and Libai Huang*, Exciton Dynamics and Annihilation in WS₂ 2D Semiconductor, *Nanoscale*, 2015, 7, 7402-7408.



Cite this: *Nanoscale*, 2015, 7, 7402

Exciton dynamics and annihilation in WS₂ 2D semiconductors†

Long Yuan and Libai Huang*

Received 19th January 2015,
Accepted 19th March 2015
DOI: 10.1039/c5nr00383k
www.rsc.org/nanoscale

We systematically investigate the exciton dynamics in monolayered, bilayered, and trilayered WS₂ two-dimensional (2D) crystals by time-resolved photoluminescence (TRPL) spectroscopy. The exciton lifetime when free of exciton annihilation was determined to be 806 ± 37 ps, 401 ± 25 ps, and 332 ± 19 ps for WS₂ monolayer, bilayer, and trilayer, respectively. By measuring the fluorescence quantum yields, we also establish the radiative and nonradiative lifetimes of the direct and indirect excitons. The exciton decay in monolayered WS₂ exhibits a strong excitation density-dependence, which can be described using an exciton–exciton annihilation (two-particle Auger recombination) model. The exciton–exciton annihilation rate for monolayered, bilayered, and trilayered WS₂ was determined to be 0.41 ± 0.02 , $(6.00 \pm 1.09) \times 10^{-3}$ and $(1.88 \pm 0.47) \times 10^{-3}$ cm² s⁻¹, respectively. Notably, the exciton–exciton annihilation rate is two orders of magnitude faster in the monolayer than in the bilayer and trilayer. We attribute the much slower exciton–exciton annihilation rate in the bilayer and trilayer to reduced many-body interaction and phonon-assisted exciton–exciton annihilation of indirect excitons.

Introduction

Semiconducting atomically thin layers of transition metal dichalcogenides (TMDs) such as MoS₂, MoSe₂, WS₂, and WSe₂ have attracted much research interest due to their unique electronic structures and optical properties.^{1,2} These properties led to potential applications in optoelectronics and electronics,^{3,4} including field-effect transistors,^{5–9} atomically thin photovoltaic devices^{10–13} and ultrasensitive photodetectors.^{14,15}

One of the unique properties of these atomically-thin 2D semiconductors is the indirect to direct bandgap transition and the extraordinarily large exciton binding energy at the monolayer limit.^{16,17} The atomically-thin nature of the monolayer also leads to a strong enhancement of the Coulomb interaction between the electron and the hole. As a result, the bound electron–hole pairs, also known as excitons, dominate the optical and electrical properties of these materials. Recent theoretical calculations and experimental measurements showed that the exciton binding energy is in the range of 0.3–1.0 eV for the TMD monolayers,^{18–23} an order of magnitude larger than other previously investigated 2D excitonic structures, such as quantum wells. Such a large exciton binding energy results in strongly bound excitons at room temperature, providing an ideal platform to study exciton

behaviors in 2D systems. Although exciton dynamics have been investigated in these 2D semiconductor,^{24,25} large variations in sample qualities due to different preparation methods have prevented intrinsic radiative and nonradiative lifetimes of excitons from being conclusively established.

Another hallmark of low-dimensional electronic systems is the enhanced many-body interaction due to a reduced dimensionality. Upon the generation of a high density of electrons and holes, many-body scattering processes such as Auger recombination and exciton–exciton annihilation play an important role in nonradiative relaxation. These nonradiative recombination processes define the upper limit of excitation density and ultimately the efficiency for applications such as semiconductor lasers and light-emitting diodes. Exciton–exciton annihilation and Auger recombination have been intensively investigated in quantum dots,^{26,27} carbon nanotubes^{28,29} and semiconductor nanowires.^{30–32} While recent studies on MoS₂, MoSe₂ and WSe₂ monolayers have shown the existence of exciton–exciton annihilation at high excitation density,^{33–38} how quantum confinement of 2D excitons impacts the many-body exciton interaction is still elusive.

In this paper, we investigate exciton dynamics and many-body exciton interactions in monolayered, bilayered, and trilayered exfoliated WS₂. We choose WS₂ as a model system because of the relatively low defect density in WS₂ as manifested by the higher photoluminescence (PL) quantum yield (QY) than other 2D semiconductors (~6% in WS₂, compared to ~0.1% of MoS₂). We measure exciton dynamics in both low and high exciton density regimes. Our results demonstrate

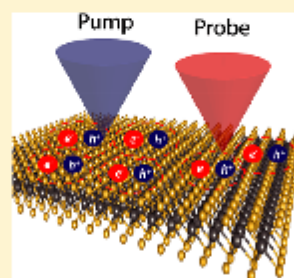
Department of Chemistry, Purdue University, West Lafayette, Indiana 47907, USA.
E-mail: libai-huang@purdue.edu
† Electronic supplementary information (ESI) available. See DOI: 10.1039/c5nr00383k

Exciton Dynamics, Transport, and Annihilation in Atomically Thin Two-Dimensional Semiconductors

Long Yuan, Ti Wang, Tong Zhu, Mingwei Zhou, and Libai Huang*

Department of Chemistry, Purdue University, West Lafayette, Indiana 47907, United States

ABSTRACT: Large binding energy and unique exciton fine structure make the transition metal dichalcogenides (TMDCs) an ideal platform to study exciton behaviors in two-dimensional (2D) systems. While excitons in these systems have been extensively researched, there currently lacks a consensus on mechanisms that control dynamics. In this Perspective, we discuss extrinsic and intrinsic factors in exciton dynamics, transport, and annihilation in 2D TMDCs. Intrinsically, dark and bright exciton energy splitting is likely to play a key role in modulating the dynamics. Extrinsic, defect scattering is prevalent in single-layer TMDCs, which leads to rapid picosecond decay and limits exciton transport. The exciton–exciton annihilation process in single-layer TMDCs is highly efficient, playing an important role in the nonradiative recombination rate in the high exciton density regime. Future challenges and opportunities to control exciton dynamics are discussed.



Atomically thin and two-dimensional (2D) transition metal dichalcogenides (TMDCs) are layered structures where adjacent layers are held by van der Waals force.¹ Because the interlayer coupling is relatively weak, the electrons and holes are confined in the layer plane. Bound electron–hole pairs, or excitons, dominate the optical properties of these materials.^{2,3} Recent experimental measurements showed that the exciton binding energy is in the range of 0.3–0.7 eV for the TMDCs monolayers, more than an order of magnitude larger than other previously investigated 2D excitonic structures such as semiconducting quantum wells.^{4–6} These 2D excitons are neither strictly Wannier nor Frenkel type, but have exciton radii (~2 nm)⁶ in the intermediate regime. The stable excitons at room temperature make the TMDCs an ideal platform to study exciton behaviors in 2D systems.

Exciton fine structure in monolayers of TMDCs results from strong spin–orbit coupling, broken inversion symmetry, and quantum confinement effects.

Exciton fine structure in monolayers of TMDCs results from strong spin–orbit coupling, broken inversion symmetry, and quantum confinement effects. As the number of layer reduces to single layer, the band structure of TMDCs undergoes indirect-to-direct band transition.^{7,7,8} Valence band edge splits into two spin-polarized bands at inequivalent valleys (K/K') in the Brillouin zone due to strong spin–orbit coupling effect,⁹ which has an energy difference of a few hundred millielectronvolts.^{10–14} Spin–orbit coupling also leads to a splitting in the conduction band, albeit much smaller, from several millielectronvolts to tens of millielectronvolts, leading to

close-lying spin-allowed bright and spin-forbidden dark exciton levels.^{12,15–19}

Exciton dynamics in monolayer TMDCs have been extensively studied;^{20–27} however, the interpretation of these measurements varies with exciton lifetime ranging from a few picoseconds to nanoseconds.²⁶ Dark and bright exciton states are expected to play a key role in the dynamics of the 2D excitons;^{17,28} however, how such exciton fine structure affects dynamics is not fully addressed in the current literature. Because the dark states could lie either above or below the bright states depending on the materials,^{16,28} the lack of understanding of the dark states is likely one of the reasons for the widespread of exciton lifetimes measured. For instance, time-resolved photoluminescence (PL) spectroscopy and transient absorption (TA) spectroscopy, the two most widely used tools to study exciton dynamics, could be sensitive to different exciton populations. Both experimental and theoretical efforts to address the dynamics of dark and bright excitons will be necessary for realizing electronic and optoelectronic applications of TMDCs. In addition, there currently lacks a comprehensive understanding of exciton transport in the TMDCs materials. It will be useful to establish the intrinsic limit of exciton transport, which is highly relevant for applications such as photovoltaics. Previous reports on exciton transport have shown contradicting results: the exciton diffusion coefficient is higher for single layer than for bulk WSe_2 ²⁹ but the opposite is true for MoSe_2 .³⁰

In this Perspective, we discuss the intrinsic and extrinsic factors that control exciton dynamics and transport in 2D TMDCs. This Perspective is not meant to be a comprehensive

Received: April 12, 2017

Accepted: June 29, 2017

Published: June 29, 2017

PHYSICS

Photocarrier generation from interlayer charge-transfer transitions in WS₂-graphene heterostructuresLong Yuan,^{1*} Ting-Fung Chung,^{2,3*} Agnieszka Kuc,^{4,5*} Yan Wan,¹ Yang Xu,^{2,3} Yong P. Chen,^{2,3,6} Thomas Heine,^{4,5} Libai Huang^{1†}

Efficient interfacial carrier generation in van der Waals heterostructures is critical for their electronic and optoelectronic applications. We demonstrate broadband photocarrier generation in WS₂-graphene heterostructures by imaging interlayer coupling-dependent charge generation using ultrafast transient absorption microscopy. Interlayer charge-transfer (CT) transitions and hot carrier injection from graphene allow carrier generation by excitation as low as 0.8 eV below the WS₂ bandgap. The experimentally determined interlayer CT transition energies are consistent with those predicted from the first-principles band structure calculation. CT interactions also lead to additional carrier generation in the visible spectral range in the heterostructures compared to that in the single-layer WS₂ alone. The lifetime of the charge-separated states is measured to be ~1 ps. These results suggest that interlayer interactions make graphene-two-dimensional semiconductor heterostructures very attractive for photovoltaic and photodetector applications because of the combined benefits of high carrier mobility and enhanced broadband photocarrier generation.

INTRODUCTION

Nanostructured materials hold great promise as building blocks to create new architectures for electronic and optoelectronic devices. Atomically thin van der Waals layers (1) represent a new two-dimensional (2D) material class with unusual optical and electronic properties emerging at the single- or few-layer limit (2–7), which provide opportunities to design new functionalities. Specifically, heterostructures can be formed by artificially stacking layers of different 2D materials, because traditional restrictions in heterostructure growth such as lattice-matching conditions and atom interdiffusion are no longer required (8–11). In the past few years, heterostructures constructed from graphene, hexagonal boron nitride, and semiconducting transition metal dichalcogenides (TMDCs) have established a remarkable platform for photoactive applications, including photodetectors, light-emitting diodes, and atomically thin photovoltaics (9, 12–20).

Efficient photocarrier generation at the interfaces remains a central challenge for many of the abovementioned applications of 2D heterostructures. The structural tunability of 2D nanostructures along with atomically thin and sharp 2D interfaces provides new opportunities for controlling charge-transfer (CT) interactions at the interfaces (21, 22). Charge transfer at 2D interfaces has been demonstrated to be very rapid, occurring on time scales ranging from 50 fs to a few picoseconds (23–29), and interlayer CT exciton transitions have been observed (30, 31). Graphene is a versatile component to couple to TMDCs because of its high carrier mobility in combination with chemical inertness, high thermal conductance, and extraordinary stability. Heterostructures constructed from graphene and TMDCs also provide opportunities to achieve broadband charge separation below the semiconductor bandgap by using hot carrier injection from graphene (32). These heterostruc-

tures maintain the high mobility of graphene, which suggests that efficient extraction of carriers can be achieved at the interfaces (20, 33, 34).

A largely unexplored question is how interlayer CT interactions contribute to interfacial charge generation and separation in 2D heterostructures. Charge separation could take place directly by exciting CT transitions at the interface. Because the interlayer distance between the graphene layer and the 2D semiconductor layer could be as small as 3 Å, interlayer interactions beyond London dispersion are apparent, leading to modification of optical absorption and band structures (34–38). In addition, because practically every atom is on the surface, interfacial charge transfer is expected to play a much more important role in 2D heterostructures than in those formed by bulk materials. Although emission from interlayer CT excitons has been observed in 2D heterostructures (30, 31), no direct excitation of these CT states has been reported partly due to relatively weak oscillator strengths (39). Here, we present a joint experimental and theoretical investigation to address charge generation from interlayer CT transitions in TMDC/graphene heterostructures. We use spatial ultrafast transient absorption microscopy (TAM) to directly compare charge generation at different interlayer coupling strengths to elucidate the role of CT transitions in WS₂-graphene heterostructures. These results demonstrate effective broadband carrier generation by excitations below the bandgap in TMDC/graphene heterostructures.

RESULTS AND DISCUSSION

Interlayer coupling-dependent charge transfer from WS₂ to graphene

The top and side views of heterostructures formed by a WS₂ layer and a graphene layer are schematically depicted in Fig. 1A. The optical micrograph of a heterostructure constructed from an exfoliated bilayer WS₂ (2L-WS₂) flake and a chemical vapor deposition (CVD)-grown graphene (G) layer on a Si/SiO₂ substrate is shown in Fig. 1B. From the atomic force microscopy (AFM) image (Fig. 1C), significant spatial heterogeneity in the contact between the 2L-WS₂ layer and the graphene layer can be observed, which is common for heterostructures fabricated by transfer methods. Specifically, there is an area with very flat morphology (area 1), whereas another area has many ripples (area 2), which indicates good contact between the graphene layer and the WS₂

¹Department of Chemistry, Purdue University, West Lafayette, IN 47907, USA. ²Department of Physics and Astronomy, Purdue University, West Lafayette, IN 47907, USA. ³Blick Nanotechnology Center, Purdue University, West Lafayette, IN 47907, USA. ⁴Wilhelm-Ostwald-Institut für Physikalische und Theoretische Chemie, Universität Leipzig, 04103 Leipzig, Germany. ⁵Department of Physics & Earth Science, Jacobs University Bremen, 28759 Bremen, Germany. ⁶School of Electrical and Computer Engineering, Purdue University, West Lafayette, IN 47907, USA.

*These authors contributed equally to this work.

†Corresponding author. Email: libai-huang@purdue.edu

PHYSICS

Highly mobile charge-transfer excitons in two-dimensional WS₂/tetracene heterostructures

Tong Zhu,* Long Yuan,* Yan Zhao, Mingwei Zhou, Yan Wan, Jianguo Mei, Libai Huang†

Charge-transfer (CT) excitons at heterointerfaces play a critical role in light to electricity conversion using organic and nanostructured materials. However, how CT excitons migrate at these interfaces is poorly understood. We investigate the formation and transport of CT excitons in two-dimensional WS₂/tetracene van der Waals heterostructures. Electron and hole transfer occurs on the time scale of a few picoseconds, and emission of interlayer CT excitons with a binding energy of ~0.3 eV has been observed. Transport of the CT excitons is directly measured by transient absorption microscopy, revealing coexistence of delocalized and localized states. Trapping-detapping dynamics between the delocalized and localized states leads to stretched-exponential photoluminescence decay with an average lifetime of ~2 ns. The delocalized CT excitons are remarkably mobile with a diffusion constant of ~1 cm² s⁻¹. These highly mobile CT excitons could have important implications in achieving efficient charge separation.

INTRODUCTION

Charge transfer and separation at heterointerfaces play a key role in determining the efficiency of light to electricity conversion using organic and nanostructured materials (1–5). In these systems, charge separation occurs when an exciton created in one material is dissociated into a spatially separated electron-hole (e-h) pair across the interface. Semiconducting transition metal dichalcogenides (TMDCs) are versatile building blocks for fabricating two-dimensional (2D) van der Waals (vdW) heterostructures with atomically thin and sharp interfaces, allowing for applications such as photovoltaics and photodetectors (6–10). Molecular and polymeric semiconductors can also be integrated with 2D TMDCs to form vdW heterostructures (11–15), and charge generation at organic-TMDC interfaces has been recently demonstrated (14).

Charge transfer at the interface of TMDC heterostructures has been found to be extremely rapid, as short as 50 fs (15–19). However, because of the inefficient screening of the interfacial Coulomb potential, the spatially separated e-h pair are not free but bound with energy on the order of hundreds of millielectron volts (20), leading to the formation of charge-transfer (CT) excitons also known as interlayer excitons in TMDC heterostructures (such as MoS₂/WS₂) (16–18, 21–24). When incorporated with molecular semiconductors, the nature of the interfacial CT states following CT events remains elusive at the 2D organic-TMDC interfaces. Although CT excitons have been inferred in recent studies (14, 15), no direct experimental evidence has been provided.

CT exciton diffusion has been proposed as a mechanism for the electrons and holes to escape the large interfacial Coulomb potential to achieve charge separation (25). However, the CT states so far have been mostly studied in largely disordered systems such as organic solar cells (1–3, 25–27), where measurements are averaged over many different kinds of interfaces making it difficult to obtain the upper limit of CT exciton transport. To overcome this difficulty, we use heterostructures that integrate exfoliated WS₂ layers with tetracene thin films as a model system with 2D crystalline organic-inorganic interfaces. Another challenge is that direct measurements of CT exciton transport require quantitative information in both spatial and temporal domains. Recent photoluminescence (PL) microscopy measurements have revealed that CT excitons move 5 to 10 nm in space at disordered organic-organic

interfaces (25). However, a drawback for PL-based techniques is that only emissive species are investigated, whereas many of the CT states are nonemissive. To address this challenge, we use transient absorption microscopy (TAM) that is capable of imaging both emissive and nonemissive excitons with ~200 fs temporal resolution and ~50-nm spatial precision (28). The measurements on WS₂/Tc heterostructures presented here reveal highly mobile CT excitons with a diffusion constant of ~1 cm² s⁻¹, which could be an important factor in achieving efficient charge separation at 2D organic-TMDC interfaces.

RESULTS AND DISCUSSION

CT excitons emission and dynamics

Figure 1 shows the construction of a heterostructure from a single-layer WS₂ (1L-WS₂) and a tetracene (Tc) thin film. The optical image of the exfoliated 1L-WS₂ flake before the Tc deposition is shown in Fig. 1A, and the reflection spectrum is shown in fig. S1. Polycrystalline Tc thin film is deposited onto the WS₂ flakes by physical vapor deposition, as detailed in the Supplementary Materials. A film thickness of ~20 nm is determined using atomic force microscopy (AFM) (Fig. 1B and fig. S2). The Tc molecules are likely to pack edge-on in the herringbone structure on WS₂, as schematically shown in Fig. 1C (29).

Figure 1D compares the steady-state PL spectra from the 1L-WS₂/Tc heterostructure, a Tc-only region of the film, and the 1L-WS₂ before deposition of Tc, with photoexcitation at 2.8 eV exciting both the 1L-WS₂ and the Tc film. The 1L-WS₂ shows an emission peak near 2.0 eV corresponding to the direct interband recombination of the A exciton (30). An additional low-energy emission peak at 1.7 eV from the heterostructure is observed in addition to the emission of the A exciton of WS₂ and the singlet exciton of Tc. We have confirmed this low-energy emission peak in all the 1L-WS₂/Tc heterostructures fabricated. The intensity of the low-energy emission could vary significantly from sample to sample, probably due to the variations in morphology of different samples.

The 1L-WS₂ and the Tc molecules form a type II heterojunction, as schematically shown in Fig. 1C. The conduction band minimum (~3.4 eV) (31) of the 1L-WS₂ lies lower than the lowest unoccupied molecular orbital level (~2.4 eV) (32) of Tc molecules allowing electron transfer from Tc to WS₂, whereas the valence band maximum (VBM; ~5.8 eV) (31) of WS₂ is located lower than the highest occupied molecular orbital (HOMO) level of Tc (~5.4 eV) (32), facilitating hole

Copyright © 2018
The Authors, some
rights reserved;
exclusive licensee
American Association
for the Advancement
of Science. No claim to
original U.S. Government
Works. Distributed
under a Creative
Commons Attribution
Non-Commercial
License 4.0 (CC BY-NC).

Downloaded from <http://advances.sciencemag.org/> on March 16, 2018

Department of Chemistry, Purdue University, West Lafayette, IN 47907, USA.

*These authors contributed equally to this work.
†Corresponding author. Email: libai-huang@purdue.edu